
Doctoral Dissertations


Student Theses and Dissertations

Spring 2019

Three-dimensional nanotube arrays for solar energy harvesting and production of solar fuels

Wipula P. R. Liyanage

Follow this and additional works at: https://scholarsmine.mst.edu/doctoral_dissertations

 Part of the [Inorganic Chemistry Commons](#), and the [Materials Science and Engineering Commons](#)
Department: Chemistry

Recommended Citation

Liyanage, Wipula P. R., "Three-dimensional nanotube arrays for solar energy harvesting and production of solar fuels" (2019). *Doctoral Dissertations*. 3103.

https://scholarsmine.mst.edu/doctoral_dissertations/3103

This thesis is brought to you by Scholars' Mine, a service of the Missouri S&T Library and Learning Resources. This work is protected by U. S. Copyright Law. Unauthorized use including reproduction for redistribution requires the permission of the copyright holder. For more information, please contact scholarsmine@mst.edu.

THREE-DIMENSIONAL NANOTUBE ARRAYS FOR SOLAR ENERGY

HARVESTING AND PRODUCTION OF SOLAR FUELS

by

WIPULA PRIYA RASIKA LIYANAGE

A DISSERTATION

Presented to the Faculty of the Graduate School of the

MISSOURI UNIVERSITY OF SCIENCE AND TECHNOLOGY

In Partial Fulfillment of the Requirements for the Degree

DOCTOR OF PHILOSOPHY

in

CHEMISTRY

2019

Approved by:

Dr. Manashi Nath, Advisor
Dr. Amitava Choudhury
Dr. Jeffery G. Winiarz
Dr. Nicholas Leventis
Dr. Edward C. Kinzel

© 2019

Wipula Priya Rasika Liyanage

All Rights Reserved

PUBLICATION DISSERTATION OPTION

This dissertation consists of six published articles and two unpublished articles which have been submitted for publication as follows:

Paper I: pages 32—56 has published in ‘Nanomaterials and Energy’.

Paper II: pages 57—82 has published in ‘Solar Energy Materials and Solar Cells’.

Paper III: pages 83—96 has published in ‘ECS Transactions’.

Paper IV: pages 97—131 has published in ‘Journal of Materials Chemistry A’.

Paper V: pages 132—159 has been submitted to ‘Materials Science & Engineering: B’.

Paper VI: pages 160—194 has published in ‘ACS Applied Energy Materials’.

Paper VII: pages 195—216 has published in ‘RSC Advances’.

Paper VIII: pages 217—242 has been submitted to ‘International Journal of Hydrogen Energy’.

ABSTRACT

Over the past decade extensive research has been carried out on photovoltaic semiconductors to provide a solution towards a renewable energy future. Fabricating high-efficiency photovoltaic devices largely rely on nanostructuring the photoabsorber layers due to the ability of improving photoabsorption, photocurrent generation and transport in nanometer scale. Vertically aligned, highly uniform nanorods and nanowire arrays for solar energy conversion have been explored as potential candidates for solar energy conversion and solar-fuel generation owing to their enhanced photoconversion efficiencies.

However, controlled fabrication of nanorod and especially nanotube arrays with uniform size and shape and a pre-determined distribution density is still a significant challenge. In this research work, we demonstrate how to address this issue by fabricating nanotube arrays by confined electrodeposition on lithographically patterned nanoelectrodes defined through electron beam as well as nanosphere photolithography. This simple technique can lay a strong foundation for the study of novel photovoltaic devices because successful fabrication of these devices will enhance the ability to control structure-property relationships. The nanotube patterns fabricated by this method could produce an equivalent amount of photocurrent density produced by a thin film like device while having less than 10% of semiconducting material coverage. This project also focused on solar fuel generation through photoelectrocatalytic water splitting for which efficient electrocatalysts were developed from non-precious elements. Lastly, a protocol was developed to disperse these electrocatalysts into a butadiene based polymeric catalytic ink and further processing to yield free-standing catalytic film applicable for water electrolysis.

ACKNOWLEDGMENTS

I would like to express my deepest appreciation to my adviser, Dr. Manashi Nath, for accepting me as her student and for guiding and encouraging me all the way through the course of my academic progress. Without her persistence, guidance and help through her excellent expertise in chemistry, this dissertation would not have been possible. I especially acknowledge with thanks the sincere support and consideration received to overcome my difficulties during hard times. She truly holds a position of a mentor.

I am using this opportunity to express my sincere gratitude to my committee members, Dr. Amitava Choudhury, Dr. Nicholas Leventis, Dr. Jeffery G. Winiarz, and Dr. Edward C. Kinzel, for their continuous support and assistance. I would like to thank the Materials Research Center for their numerous supports provided through characterization techniques. I am especially thankful to the Department of Chemistry for providing a teaching assistantship during my graduate studies. I really appreciate my lab mates, friends, and all of those who supported me in numerous ways during the completion of my projects.

I also express my gratitude to Dr. David Prendergast, director of the theory facility at Molecular Foundry, who facilitated to carry out my project during my internship in Lawrence Berkeley National Laboratory. It was a great chance for learning and professional development and his research group's support and advice was priceless.

This journey would have been impossible without the unconditional love and encouragement from my wife, Umanga De Silva, my parents, my brother and sister, in-law parents and two brothers in-law. I would like to dedicate this dissertation to them.

TABLE OF CONTENTS

	Page
PUBLICATION DISSERTATION OPTION.....	iii
ABSTRACT.....	iv
ACKNOWLEDGMENTS	v
LIST OF ILLUSTRATIONS.....	xv
LIST OF TABLES.....	xix
 SECTION	
1. INTRODUCTION.....	1
1.1. NANOSTRUCTURING THE PHOTOABSORBER.....	5
1.2. REDUCTION OF MATERIAL COST & USAGE BY NANO- STRUCTURING.....	5
1.3. INCREASING EFFICIENCY LIMITS.....	8
1.4. ENHANCEMENT OF PHOTO ABSORPTION: THEORETICAL STUDIES.....	10
1.5. ENHANCEMENT OF PHOTOABSORPTION: EXPERIMENTAL STUDIES.....	11
1.6. ENHANCING CHARGE CARRIER COLLECTION.....	13
1.7. PERFORMANCE OF AN ARRAY OF NANOTUBES.....	14
1.8. CONFINED ELECTRODEPOSITION ON LITHOGRAPHICALLY PATTERNED NANOELECTRODES.....	16
1.9. SOLAR-TO-FUEL ENERGY CONVERSION	17
1.9.1. Brief Overview of Photoelectrocatalytic (PEC) Water Splitting.....	18
1.9.2. Photoabsorbers and Photoanodes.	21

1.9.3. Coupling Electrocatalysts with Photoanodes: The Backbone of PEC Water Splitting.	22
1.9.4. High-efficiency Selenide and Telluride based OER Electrocatalysts: The Effect of Covalency.....	23
1.9.5. Effect of Nanostructuring on Photoabsorber Properties.....	25
1.9.6. Assembling the Nanotubes/nanowires as Arrays: The Practical Challenge.	28
1.9.7. Efforts to Grow Ordered Arrays of Nanotubes on Large Scale Through Bottom-up Methods.....	30

PAPER

I. PATTERNED ELECTRODEPOSITION OF CdTe NANOROD AND NANOTUBE ARRAYS FOR SOLAR CELLS.....	32
ABSTRACT	32
1. INTRODUCTION.....	33
2. EXPERIMENTAL	36
2.1. MATERIALS	36
2.2. CHARACTERIZATIONS.....	37
2.2.1. Powder X-ray Diffraction (PXRD).	37
2.2.2. Scanning Electron Microscopy (SEM).....	37
2.2.3. Electron Beam Lithography (EBL)	37
2.2.4. Photoelectrochemical (PEC) Measurements	38
3. METHODS.....	38
3.1. SAMPLE PREPARATION BY EBL	38
3.2. SAMPLE PREPARATION BY NSP	39
3.3. ELECTRODEPOSITION OF NANOWIRES.....	39
4. RESULTS AND DISCUSSION	40

4.1. CHARACTERIZATION OF THE NANOROD ARRAYS FABRICATED THROUGH EBL.....	41
4.2. LARGE AREA GROWTH OF CDTE NANOWIRES	43
4.2.1. Pattern Definition by NSP.....	43
4.2.2. Characterization of the Nanorod Arrays Fabricated through NSP.....	45
4.3. PEC RESPONSE MEASUREMENTS	47
4.4. GROWTH OF CDTE NANOTUBE ARRAYS AND ENHANCED PHOTOCURRENT	50
5. CONCLUSION	52
ACKNOWLEDGEMENTS	53
REFERENCES	53
II. FABRICATION OF CdTe NANOROD ARRAYS OVER LARGE AREA THROUGH PATTERNED ELECTRODEPOSITION FOR EFFICIENT SOLAR ENERGY CONVERSION	57
ABSTRACT	57
1. INTRODUCTION.....	58
2. MATERIAL & METHODS.....	62
2.1. MATERIALS	62
2.2. METHODS	62
2.3. NANOSPHERE PHOTO-LITHOGRAPHY (NPL).....	64
2.4. LARGE AREA NANO-ELECTRODE PATTERN DEFINITION BY NPL.....	66
2.5. ELECTRODEPOSITION OF NANOWIRES.....	67
2.6. CHARACTERIZATIONS.....	68
2.6.1. Powder X-ray diffraction.....	68

2.6.2. SEM and EDS	68
2.6.3. Photoelectrochemical measurements	69
3. RESULTS AND DISCUSSION	69
3.1. MORPHOLOGY OF THE ELECTRODEPOSITED CdTe.....	69
3.2. PHOTOELECTROCHEMICAL RESPONSE MEASUREMENTS.....	72
4. CONCLUSION	77
ACKNOWLEDGEMENTS	78
SUPPORTING INFORMATION	78
REFERENCES	79
III. GROWTH OF ORDERED NANOSTRUCTURE ARRAYS INCLUDING NANOTUBES AND NANORODS FOR HIGH EFFICIENCY SOLAR CELLS.....	83
ABSTRACT	83
1. INTRODUCTION.....	84
2. EXPERIMENTAL DETAILS.....	86
2.1. MATERIALS AND TECHNIQUES.....	86
2.2. PREPARATION OF SAMPLES BY EBL.....	86
2.3. ELECTRODEPOSITION OF NANOTUBES/NANORODS	87
3. RESULTS AND DISCUSSION	89
3.1. PROPERTIES OF NANOTUBES AND NANORODS.....	89
3.2. ENHANCED PHOTOELECTROCHEMICAL (PEC) RESPONSE	91
4. CONCLUSION	94
ACKNOWLEDGEMENTS	95
REFERENCES	95

IV. CdS–CdTe HETEROJUNCTION NANOTUBE ARRAYS FOR EFFICIENT SOLAR ENERGY CONVERSION	97
ABSTRACT	98
1. INTRODUCTION	99
2. EXPERIMENTAL	101
2.1. MATERIALS AND METHODS	101
2.1.1. Chemicals.	101
2.1.2. Nanotube and Nanorod Growth.	102
2.1.3. Deposition of CdS Layer by CBD.....	103
2.1.4. Definition of nanoelectrodes by lithography.....	103
2.1.5. Electrodeposition of CdTe.....	105
3. CHARACTERIZATION.....	106
4. RESULTS & DISCUSSION	107
4.1. MORPHOLOGY & COMPOSITION.....	107
4.2. PHOTOELECTROCHEMICAL ANALYSIS	114
5. CONCLUSIONS	123
ACKNOWLEDGEMENTS	125
SUPPLEMENTARY INFORMATION.....	125
REFERENCES.....	129
V. CuInSe ₂ NANOTUBE ARRAYS FOR EFFICIENT SOLAR ENERGY CONVERSION	132
ABSTRACT	132
1. INTRODUCTION	133
2. EXPERIMENTAL SECTION	135

2.1. GROWTH OF NANOTUBES.....	135
3. CHARACTERIZATION OF NANOTUBES	137
4. RESULTS AND DISCUSSION	138
4.1. COMPOSITION, MORPHOLOGY AND CRYSTAL STRUCTURE.....	138
4.2. OPTICAL PROPERTIES.....	142
4.3. PHOTOELECTROCHEMICAL (PEC) STUDY OF THE NANOTUBE ARRAY	144
5. CONCLUSIONS	151
ACKNOWLEDGEMENTS	152
SUPPLEMENTARY INFORMATION.....	152
REFERENCES.....	153
VI. COPPER SELENIDES AS HIGH-EFFICIENCY ELECTROCATALYSTS FOR OXYGEN EVOLUTION REACTION.....	160
ABSTRACT	161
1. INTRODUCTION.....	162
2. EXPERIMENTAL SECTION	164
2.1. MATERIALS	164
2.2. ELECTRODEPOSITION OF COPPER SELENIDE (Cu ₂ Se).....	165
2.3. HYDROTHERMAL SYNTHESIS OF COPPER SELENIDE (Cu ₂ Se)	165
2.4. CHEMICAL VAPOR DEPOSITION (CVD) OF COPPER SELENIDE.....	166
2.5. ELECTRODE PREPARATION.....	167
3. RESULTS AND DISCUSSION	167
3.1. STRUCTURAL AND MORPHOLOGICAL CHARACTERIZATION.....	167

3.2. TESTING OF EVOLVED GAS AND FARADAIC EFFICIENCY.....	180
4. CONCLUSIONS	182
ACKNOWLEDGEMENTS	183
SUPPLEMENTARY INFORMATION.....	183
REFERENCES.....	190
VII. FABRICATION OF MULTIFUNCTIONAL FERROMAGNETIC Au ₃ Pd–CoSe NANOPARTICLES.....	195
ABSTRACT	195
1. INTRODUCTION.....	196
2. EXPERIMENTAL	198
2.1. MATERIALS & METHODS.....	198
2.2. SYNTHESIS OF Au ₃ Pd–CoSe COMPOSITE NANOPARTICLES	198
2.3. CHARACTERIZATION TOOLS & TECHNIQUES	199
2.3.1. Powder X-ray diffraction.....	199
2.3.2. Electron microscopy characterizations.....	200
2.3.3. Magnetic characterizations.....	201
2.3.4. Optical characterizations.....	201
3. RESULTS & DISCUSSION	202
3.1. MORPHOLOGY AND STRUCTURAL CHARACTERIZATION	202
3.2. OPTICAL PROPERTIES	205
3.3. MAGNETIC PROPERTY MEASUREMENT	208
3.4. MECHANISM OF FORMATION	211
4. CONCLUSIONS	212
ACKNOWLEDGEMENTS	212

SUPPLEMENTARY INFORMATION.....	213
REFERENCES.....	214
VIII. A FREE STANDING CATALYST FILM FOR ELECTROCATALYTIC APPLICATIONS.....	217
ABSTRACT.....	217
1. INTRODUCTION.....	218
2. EXPERIMENTAL.....	221
2.1. MATERIALS.....	221
2.2. FABRICATION OF CATALYST FILM.....	222
2.2.1. Preparation of Conducting Carbon Dispersion.....	222
2.2.2. Preparation of the Catalyst Dispersion.....	222
2.2.3. Preparation of Catalyst Ink-Base.....	222
2.2.4. Preparation of Catalyst Ink.....	224
2.2.5. Preparation of Substrate Supported Catalyst Films.....	224
2.2.6. Preparation of Free Standing Catalyst Film.....	225
2.2.7. Preparation of Free Standing Films with Electrodeposited Catalyst Layers.....	225
3. CHARACTERIZATION OF FREE STANDING CATALYST FILM.....	226
3.1. EVALUATION OF CATALYTIC ACTIVITY.....	227
4. RESULTS AND DISCUSSION.....	229
4.1. ELECTRICAL CONDUCTIVITY.....	229
4.2. SCANNING ELECTRON MICROSCOPY (SEM).....	231
4.3. EVALUATION OF CATALYTIC PROPERTIES.....	234
5. CONCLUSIONS.....	237

ACKNOWLEDGEMENTS 237

REFERENCES 238

SECTION

2. CONCLUSION 243

BIBLIOGRAPHY 247

VITA 265

LIST OF ILLUSTRATIONS

Figure	Page
SECTION	
1.1. Schematic diagrams of photovoltaic devices.....	2
1.2. Schematic diagram of energy bands.....	3
1.3. Relationship between power conversion efficiency, module area costs and cost per peak watt (in \$/Wp).....	4
1.4. Schematic representation of nanowire structures used in photovoltaic applications.....	8
1.5. Schematic representations of (a) nanorod (b) nanohole and (c) nanotube arrays.....	15
1.6. Schematic diagram of (a) a typical fabrication process and (b) growing nanotube and nanorod arrays.....	16
1.7. Schematic representation of the proposed PEC water splitting device.....	19
PAPER I	
1. A schematic diagram showing the steps for generating CdTe nanorod arrays through PatED.....	40
2. (a) SEM image (top view) and (b) PXRD pattern of CdTe nanorods.....	41
3. SEM images.....	43
4. NSP patterns.....	44
5. Morphology and crystal structure.....	46
6. Generation of photocurrent.....	48
7. PEC characteristics of nanotubes.....	51
PAPER II	
1. Schematic showing the steps for generating CdTe nanorod arrays.....	64

2. Results of Nanosphere Photolithography.....	65
3. The NPL process.....	68
4. CdTe nanowire arrays.....	71
5. PEC measurements.....	75

PAPER III

1. Schematic representation of the EBL process.....	88
2. Morphology and crystal structure.....	90
3. Generated photocurrent at an applied bias of -0.4 V.....	92

PAPER IV

1. An illustration of the growth of (a) nanotube and (b) nanorod arrays.....	102
2. An illustration of the growth of nanotube arrays by patterned electrodeposition protocol.....	104
3. XRD pattern collected from the patterned CdS–CdTe nanotube arrays where the CdTe was grown on top of CdS.....	108
4. CdS CdTe nanotube arrays.....	110
5. CdS CdTe nanorod arrays.....	111
6. Morphology of the patterns.....	113
7. PEC characterization of nanotube array.....	116
8. PEC characterization of nanorod array.....	118
9. Photoconversion efficiency.....	120
10. PEC study of thin films.....	122

PAPER V

1. Morphology and composition.....	139
2. HRTEM image and SAED pattern showing dominant (112) crystal lattice fringes of CISE.....	141

3. XRD pattern of an array of CISE nanotubes.	142
4. Absorption spectrum of the CISE nanotube arrays.	143
5. PEC characterization.....	146
6. A comparison of the photo current voltage (JV) performance of the CISE nanotube array and thin film devices.	147
7. Electrochemical Impedance Spectroscopy.	150

PAPER VI

1. PXRD patterns of Cu ₂ Se.	168
2. TEM images of Cu ₂ Se.....	171
3. OER polarization curves of Cu ₂ Se.....	174
4. Stability studies of the catalyst.	178
5. Plots for the ORR-OER reaction.....	180

PAPER VII

1. Crystal structure and morphology.....	203
2. Elemental mapping of the Au–CoSe nanoparticles.	204
3. TEM images of nanoparticles.	206
4. HRTEM images of a single nanoparticles.	206
5. Absorbance spectra from Au ₃ Pd–CoSe bifunctional nanoparticles.....	207
6. The magnetization behaviour of Au ₃ Pd–CoSe nanoparticles.	209

PAPER VIII

1. Schematic representation of preparing the free standing catalyst film-base.....	223
2. Free standing catalyst film.	226
3. Effect of carbon content to the electrical conductivity of composite films.	231
4. SEM images of free standing catalyst base films prepared in Table 1.	232

5. Free standing catalyst film prepared with Ni_3Te_2 catalyst.	233
6. Evaluation of free standing catalyst film.	235
7. Evaluation of HER and catalytic activity of free standing catalyst film.....	236

LIST OF TABLES

Table	Page
PAPER IV	
1. Photovoltaic performance data of the fabricated devices	121
PAPER V	
1. Summary of PV performance and impedance parameters of the CISE devices	148
PAPER VI	
1. Comparison of OER activities at different Cu-based electrocatalysts.....	177
PAPER VIII	
1. Electrical and mechanical properties of catalyst ink base films	230

1. INTRODUCTION

Solar energy is becoming an essential source of renewable energy as an alternative to the conventional fossil fuel based sources of power. Due to the ever increasing demand and the non-renewable nature, fossil fuels are not expected to last long and in addition, the use of the fossil fuels has already contributed to a great extent for the global warming, pollution and other environmental issues. Therefore, global communities has focused to take initiatives for the implementation of renewable, clean and promising energy sources such as solar energy.^{1,2} As a result, the field of solar photovoltaic research has increased significantly along with the rapid development of the semiconductor industry showing the increasing interest in this field.³ Solar energy is renewable and as shown in Figure 1.1, can be collected by using solar cells⁴, photoelectrochemical(PEC) cells⁵ and photo catalysts.⁶

Utilizing the photovoltaic effect, solar energy can directly be converted to electricity with a solar cells.⁷ Solar cell completes two necessary and successive tasks in this process: photogeneration of charge carriers in a light absorbing material and separation of the charge carriers to a selective contact that will transmit electricity.⁸ photogeneration of charge carriers happens by the absorption of photons with higher energy than that of the band gap of the semiconducting material and then separation takes place at the p-n junction. A p-n junction is the interphase between p-type doped and n-type doped semiconducting materials. The p-type doped region contains excess of holes (Fermi level close to the valance band) and the n-type doped region contains excess of electrons (Fermi level close to the conduction band) respectively. When the two sides are

brought together, electrons flow from n- side to the p-side and holes flow from p-side to the n-side until thermodynamic equilibrium is achieved by the system and the Fermi level become same in both sides. Due to the alignment of the Fermi level, both conduction band and the valance band bend at the p-n junction and create an electrostatic potential difference which induces a drift current opposite to the diffusion current at the junction.

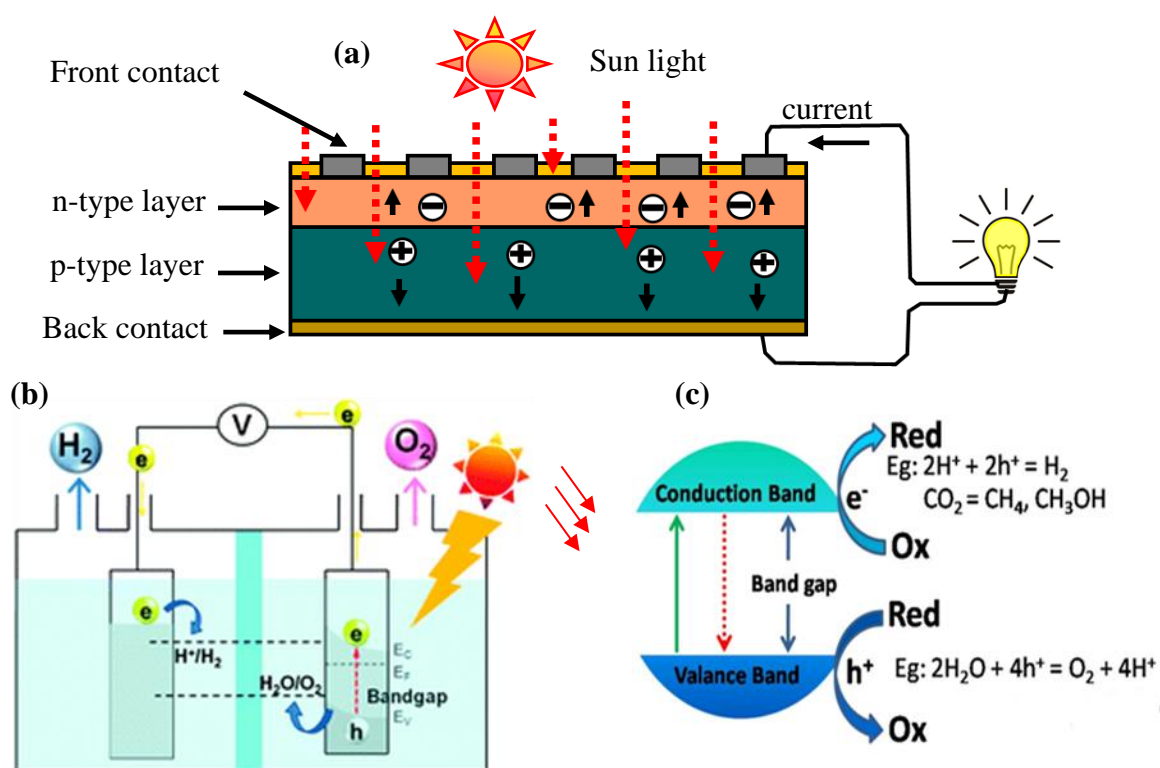


Figure 1.1. Schematic diagrams of photovoltaic devices. **a)** solar cell **b)** PEC cell **c)** photocatalyst for CO₂ conversion.

This potential gradient brings on an electric field and the affected region by the electric field is called the depletion region. Then, the charge carriers generated within the

depletion region by photoabsorption separate into n-type region and p-type regions. Electrons drift to the n- doped region and vice versa for the holes to produce voltage, v and current, I thus power ($P = V \times I$). Figure 1. 2 shows a schematic band diagram for n-type and p-type regions before and after forming the interphase.⁹

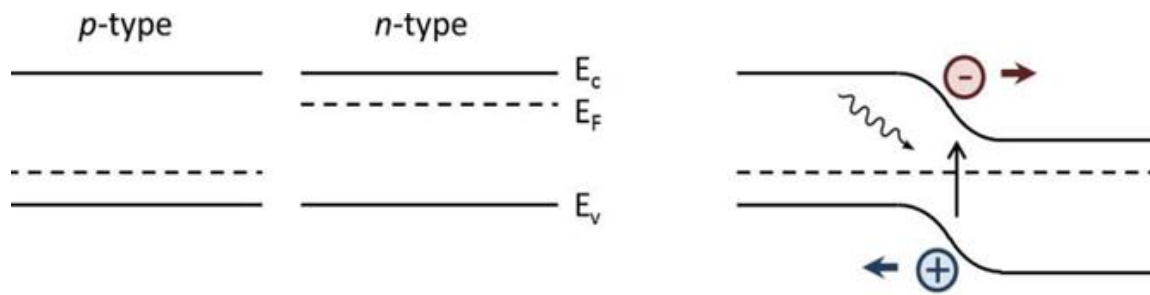


Figure 1.2. Schematic diagram of energy bands. (a) p-type and n-type semiconductors and (b) separation of photogenerated charge carriers at the p-n junction.

According to the detailed analysis carried out by Shockley–Queisser it has shown that the maximum photo conversion efficiency that can be achieved by a thin film like single p-n junction photovoltaic device is about 33%.¹⁰ Since the introduction of the first silicon based solar cell by Russel Ohl¹¹ in 1941, which had less than 1% efficiency, photo conversion efficiency has progressively approached the Shockley–Queisser limit due to the advancements in the material processing, material quality and device configurations. As an example, the highest confirmed current efficiencies for crystalline Si is 25.6%, while for GaAs thin film solar cells it is 28.8%.¹²

However, the adoption of energy from photovoltaic devices by household and industrial entities depend on its cost compared with that of available conventional energy

sources.¹³ Besides the recent cost reduction of the solar panel modules and reaching grid parity, it has seen that it is unlikely to displace a larger fraction of energy usage from fossil fuels by photovoltaic since the fossil fuel infrastructure is substantial and well established. It has predicted that the cost of the solar modules should be reduced to a half or a third of the average grid costs (that is 0.05 to 0.03 \$/kWh) in the US for widespread usage of solar electricity.¹⁴ To achieve this target, for example, 40% efficient module with a cost of 160 \$/m² or a 30% efficient module with a cost of 120 \$/m² need to be available with a useful life time of 10-15 years without degradation.¹³ Figure 1.3 shows the relationship between cost per unit area, rated module efficiency and operating cost (\$/kWh)¹³.

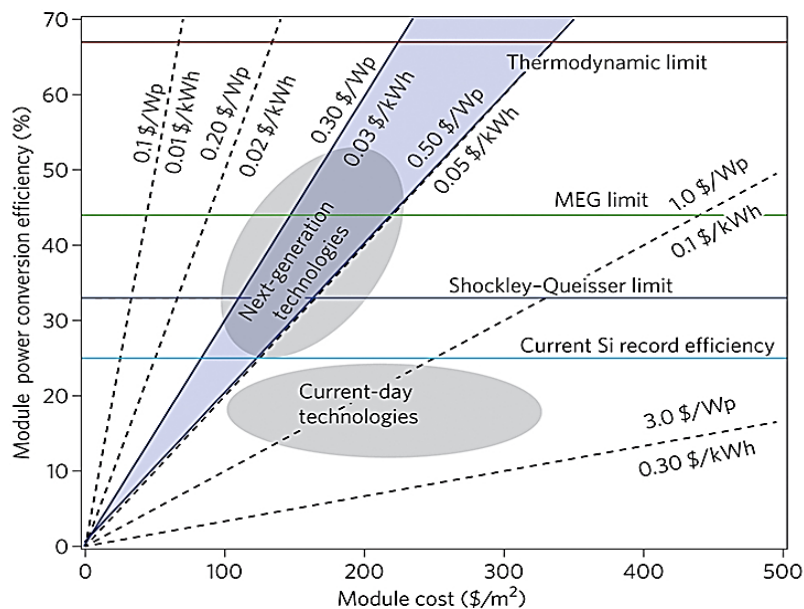


Figure 1.3. Relationship between power conversion efficiency, module area costs and cost per peak watt (in \$/Wp).

The light blue line represents the current laboratory record efficiency for bulk crystal silicon while the blue horizontal line is the Shockley–Queisser limit for single-junction devices. The limiting efficiency for third-generation device concepts (Multiple Exciton Generation) is indicated as the green line. For next-generation technologies the goal is to reach the area denoted by the blue shaded region.¹³

1.1. NANOSTRUCTURING THE PHOTOABSORBER

It is well known when a given material is fabricated in the form of nanostructures, the new system shows different properties than a bulk structure or thin film fabricated from the same compound.¹⁵ These phenomena have triggered researchers to investigate new avenues of approaching solar energy conversion for the generation of electricity or fuels. While the large surface to volume ratio of nanomaterials can provide various benefits,¹⁶ sufficiently small objects with size of ~1 to 20 nm can also possess quantization effects.¹⁷ Nanomaterials have explored in photo conversion process towards achieving two broad approaches: (1) significant reduction in material usage;¹⁸ (2) obtain a higher efficiency than Shockley–Queisser limit.¹⁹ Both approaches can lead to reduce the cost per kwh.

1.2. REDUCTION OF MATERIAL COST & USAGE BY NANO-STRUCTURING

Conventional crystalline silicon solar cells typically reflect about 30% of the incident light.²⁰ Since the reflected light cannot be absorbed by the photoactive components, it cannot be converted into electricity. Therefore, antireflective coatings are applied at an additional cost on silicon surface to reduce the reflection to about 3-4%.²¹ It

has shown that nanostructured surfaces can significantly reduce the reflection losses.²²⁻²⁴ If those nanostructures are made of photovoltaic materials, the antireflective coatings are not needed. Furthermore, nanostructures can be fabricated as periodic patterns to capture even more light through phenomena such as light trapping and therefore, less material is needed to capture the sun light.^{25,26}

For indirect band gap semiconductors such as silicon, a thick absorber film is needed to absorb all the light. Therefore, high purity materials with long carrier lifetime are required to make sure all the carriers are collected over the large thickness. This also increase the material cost. One of the approaches for this problem is the usage of semiconductor as nanocrystals or quantum dots. Their most important characteristics for the solar cell application are the dependent of the bandgap on their size.²⁷

The bandgap of the nanocrystals determine which photons can be absorbed and therefore, can control the cell voltage.²⁸ Since only the photons with higher energy than the bandgap can be absorbed, narrow bandgap semiconductors are capable of absorbing photons in a wide range of energy and produce a higher photocurrent. However, output voltage is less because the voltage is proportional to the bandgap. Wide bandgap semiconductors, on the other hand, capable of delivering high voltages but the photocurrent produced is low.²⁸

Hence, there is an optimum bandgap that can produce the highest efficiency as shown by Shockley–Queisser analysis, which lies in the region of 1.2 to 1.4 eV.¹⁰ Usually, semiconductors with less than 1 eV is not employed in single junction solar cells however, due to the quantum confinement effect, quantum dots can increase the band gap by more than 1 eV compared to the bulk materials thus making more semiconducting

materials available for photovoltaic applications as nanocrystals or quantum dots. As an example, bulk PbS have a band gap of 0.4 eV but nanocrystalline PbS can have a band gap from ~0.6 eV to ~2 eV depending on their size.²⁹⁻³¹ In addition, these nanocrystals can be synthesized and processed into nanocrystalline thin films at low temperatures which enables low manufacturing costs.³² PbS nanocrystal solar cells have shown much progress and now has approached ~9% efficiency limit with crystals having bandgap of 1.25-1.4 eV.^{33,34} Other examples include quantum dots made from CdTe,³⁵ CdSe³⁶ and copper indium gallium selenide (CIGS).³⁷ Other emerging type of solar cells developed from nanostructured device concept are solution processed perovskite solar cells.³⁸ However, their efficiencies are significantly limited by the recombination losses due to the electron scattering and trapping at nanoparticle boundaries³⁹ and also the Shockley–Queisser limit unless incorporated into a multi junction architecture.

Radial p-n junction nanowires have been explored to minimize such material costs.^{40, 41} In this structure, the p-n junction lies along the length of the nanowire as indicated in Figure 1.4. When charge carriers are generated at the junction, they only need to travel the diameter of the wire to be collected. Since less rigorous conditions are required on charge carrier lifetime, lower grade material can be used. Therefore, when light trapping and reduced minority carrier lifetime are introduced, the quality of the material and the amount of material used can be greatly reduced.

Usually, in bulk solar cells, large dielectric constant of the material is utilized to separate electron and holes generated as a result of photoabsorption by the semiconductor thus preventing the interaction of each other which facilitate recombination and loss of carriers. Nanostructuring has identified as a way to bypass the requirement of high

dielectric constant of the materials and therefore, allow new class of low cost material and device design.⁴²

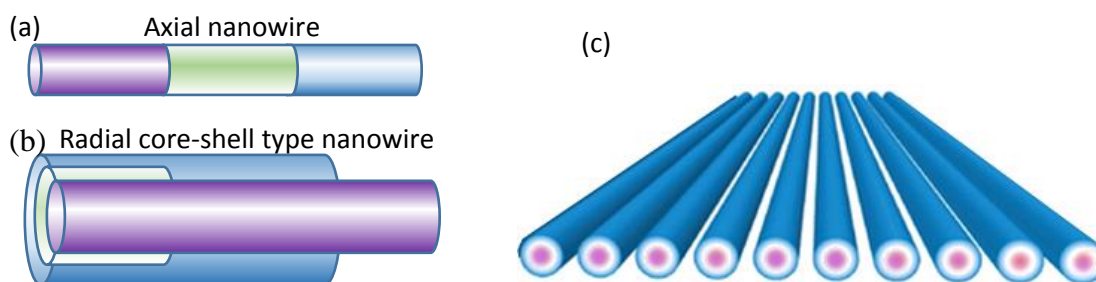


Figure 1.4. Schematic representation of nanowire structures used in photovoltaic applications. (a) axial junctions (b) and radial junctions. (c) Schematic of nanowires prepared to form a thin solar cell device.⁴¹

As an example, two different materials where one is n-type and the other is p-type, can be intermixed in nanoscale morphology. In this case rapid charge transfer has observed after light produces the electron hole pairs thus minimizing their recombination.⁴³

1.3. INCREASING EFFICIENCY LIMITS

Emerging photovoltaic technologies strive to achieve efficiencies beyond Shockley–Queisser limit (~33%) in addition to the reduction of component costs. In a single junction solar cell, excited electrons generated by photons with high energy than the band gap of the semiconductor loses their energy as heat when they are relaxed to the conduction band edge. Therefore, the amount of energy of the photons with energy greater than the bandgap is lost as heat. On the other hand, the fraction of photons having

energy less than that of the bandgap are not absorbed and cannot support to the photocurrent.⁴⁴

In the efforts of achieving higher efficiencies, attempts are made to capture high energy photons more efficiently and also recover low energy photons that are normally not absorbed. One of the approaches is using multijunction solar cells where stacking of p-n junctions made in the order of decreasing bandgap to cover most of the solar spectrum. The theoretical photoconversion efficiency for multijunction solar cells lies close to 58% at 1 sun illumination.⁴⁵

Conversion efficiency of 34.1% has obtained with a triple junction solar cell¹² and efficiency of 46% has achieved with a solar concentration equivalent to 500 suns.⁴⁶ However, these types of solar cells are extremely expensive to be available as a commercial product and stringent production conditions need to be employed for manufacturing them. Therefore, material and device structure innovation has become the cutting edge of the current photovoltaic research.

Specifically, extensive studies have shown that fabricating conventional semiconductor materials as three dimensional nanostructure arrays such as nanowires,^{47,48} nanopillars,^{49,50} nanocones,^{51,52} etc both photo absorption and photogenerated carrier collection can be significantly improved. Among these structures, nanowires are highly appreciated because they provide many degrees of freedom. In fact, recent studies have shown that vertically aligned nanowire arrays not only improve photoabsorption by light trapping but also improve the carrier collection by orthogonalizing the light propagation and carrier collection.^{53,54}

1.4. ENHANCEMENT OF PHOTO ABSORPTION: THEORETICAL STUDIES

Many research groups have extensively studied the photoabsorption of nanowire arrays targeting to achieve optimized design for efficient photoconversion.⁵⁵⁻⁵⁸

Theoretical understanding of the device can greatly assist design of optimal photovoltaic structures. In particular, Chen and the co-workers reported the numerical modeling of optical absorption of periodic nanostructures including silicon nanowire arrays, nanohole arrays and nano-pyramid arrays.^{59,60} The effects of nanowire diameter, length, and filling ratio on the optical absorption of nanowire arrays were systematically analyzed using transfer matrix method (TMM).⁵⁹ They have showed that the electromagnetic interaction between nanowires are very important, and nanowire structures showed higher absorption than thin films made by the same material, mostly at high-frequency regione.⁵⁹

Expanding their work into next level, silicon nanohole arrays have investigated as light harvesting structures and compared them to nanorod arrays. It has shown that similar to the above observation, nanohole arrays also have superior efficiencies than nanorod or thin film like geometries at practical thicknesses.⁶⁰

Further simulations have shown that absorption at $\lambda = 670$ nm increases as the filling ratio decreases in both nanohole as well as nanorod arrays as a result of the smaller optical density, which has created an antireflection effect. Moreover, nanohole arrays have shown better optical absorption than nanorod arrays over the entire range of the investigated filling fraction, which has attributed to both effective light coupling as well as the large density of waveguide modes.⁶⁰

In many cases, light trapping has identified as the effect of increasing optical path of photons inside nanostructures by Lambertian scattering, which has a theoretical limit

of $4n^2$, where n is the refractive index of the material.⁶¹ Recently, Han and Chen have designed a nonsymmetric tapered two-dimensional gratings structure to examine light trapping in thin silicon nanostructures for photovoltaic applications.⁶¹ They, have shown absorption close to the Lambertian limit at normal incidence and also have demonstrated that rod array structures with nonsymmetric tapered tops can show absorption close to the Lambertian limit even when averaged over all directions of incidence. These effects indicate a possibility to reduce thickness of crystalline Si wafer by 2 orders of magnitude while maintain the same optical absorption capability.⁶¹

1.5. ENHANCEMENT OF PHOTOABSORPTION: EXPERIMENTAL STUDIES

Apart from the theoretical studies, many experiments have performed to fabricate 3D nanostructure arrays to study their optical behavior for photovoltaic applications. In general, fabrication method of nanostructure arrays fall into two broad categories: (1) top down approach (2) bottom up approach. Top down approach mainly refer to the methods that usually etch the bulk substrates followed by patterning with a suitable method to obtain the nanostructure array.

The etching process shapes the bulk substrate into a nanostructured array.⁶²⁻⁶⁶ In the bottom up fabrication method, growth of the nanostructures starting from atomic scale takes place. Common bottom up fabrication techniques involves, for example, vapor-liquid-solid growth (VLS),⁶⁷⁻⁶⁹ vapor solid growth (VS),^{70,71} electrochemical growth,⁷²⁻⁷⁴ etc. In practice, bottom up approach is preferred since it is low cost compared to the top down approach and in some cases shape of the nanostructure arrays can be well controlled by bottom up approach.⁷⁵⁻⁷⁸

Growth and characterization of silicon based nanowire arrays have been extensively studied since silicon is the dominant material in the solar cell industry. As an example, ordered array of silicon nanowire arrays have been fabricated with self-assembled silica beads followed by deep reactive ion etching on silicon substrates as illustrated in literature⁷⁹ and also by VLS growth technique.⁸⁰

Optical transmittance studies have shown that nanowire arrays reduce the intensity of the transmitted light compared to the planar sample, indicating a strong light trapping effect of the nanowire arrays.⁷⁹ Light-trapping path length enhancement factor, which is defined as the apparent optical thickness of the structure divided by its actual thickness, was determined to be increased by 73 times for the nanowire array compared to a planar substrate and that is even higher than the previously mentioned Lambertian light trapping limit, due to the photonic crystal enhancement effects in the devices.⁷⁹ Etching of silicon to obtain nanowire arrays is a costly process since it requires defect free epitaxial silicon wafers and also patterning of the substrate before the etching process. Therefore, large efforts have taken to fabricate nanowire arrays by bottom up approach using typical catalytic VLS method.⁸⁰ They have shown that arrays having less than 5% areal fraction of wires can achieve up to 96% peak absorption, and that they can absorb up to 85% of day-integrated, above-bandgap direct sunlight. In fact, it has further observed that these arrays show enhanced near-infrared absorption, which allows their overall sunlight absorption to exceed the ray-optics light-trapping absorption limit per volume of silicon compared to planar geometry of silicon.

Use of anodized alumina as a template is another method for the fabrication of semiconductor nanowire arrays for photovoltaic applications.⁸¹⁻⁸⁴ As an example,

germanium nanowire arrays were assembled in the anodic alumina membrane (AAM) via catalytic VLS growth method, while the AAM was fabricated by multiple-step etching and anodization. Compared to the Ge blank film with only 53% light absorption, the Ge nanowire array has achieved a much improved (99%) optical absorption.⁸⁵ While AAM technique provides fabrication of nanowire arrays over larger area the difficulty of controlling the distance between two adjacent nanowires and the requirement of harsh acidic or basic conditions to remove the template to reveal the nanowire arrays are some of the disadvantages of this technique. Especially, template removal process can be detrimental to the semiconducting nanostructures.

1.6. ENHANCING CHARGE CARRIER COLLECTION

Light absorption and photogenerated carrier collection are two key aspects of an efficient solar cell device. Besides enhancing light capturing capability, well designed nanostructures can also improve photogenerated carrier collection. Especially, short collection lengths can facilitate the efficient collection of photogenerated carriers in materials with low minority-carrier diffusion lengths. In this regard, vertically aligned photovoltaic structures consisting of vertically aligned arrays of radial p-n junction nanorod solar cells have shown a significant improvement.⁸⁶⁻⁸⁹

As shown in literature,⁹⁰ each nanorod in the array has a shallow p-n junction acting as a tiny solar cell, in which photoexcited minority carriers only have to travel across a short pathway to reach the p-n junction which then separates the charges. Such a rod geometry device allows high charge collection efficiency even using low quality films, leading to lower material cost in solar cells. This configuration separates the

direction of photon absorption and carrier collection, and open up new opportunities for further optimization.

Following this concept, many nanowire solar cell structures have been developed to orthogonalize the light absorption and carrier collection directions and seen a significant efficiency in quantum yield.⁹¹⁻⁹³ However, semiconducting photovoltaic materials with a high surface recombination velocity is preferable to fabricate as large diameter wire arrays to reduce surface-to-volume ratio to reduce surface recombination.^{26,80,94,95}

It has seen that increasing the wire diameter is cost effective than introducing an additional passivation layer to minimize surface recombination losses in InP nanowire arrays. On the other hand, it has been also found that catalyst like Au used in conventional Si nanowire VLS growth process introduces impurity states in the bandgap reducing the minority carrier life time and hence device performance.⁹⁶

1.7. PERFORMANCE OF AN ARRAY OF NANOTUBES

Motivated by the improvements seen in nanowire arrays and nanohole arrays, it was our understanding that if we combine these two geometries a better geometry that facilitates light harvesting could be obtained. For example, if a nanohole is drilled into a nanorod or nanowire then the resulting geometry is a nanotube as shown in Figure 1.5. Hence, fabricating nanotube arrays would be a way to see the combined or synergistic effect of both nanorods and nanoholes. That is the motivation behind the creation of these nanotube arrays.

One of the significant challenges present in this area of research is the lack of ability to control the morphological parameters such as nanotube diameter, wall thickness, length and distribution density such as in the case of fabrication of nanotube arrays. Anodic aluminum oxide are often used as hard templates for directing the morphology of nanowires and nanorods but one of the disadvantage of this method is its inability to fully control the physical parameters as desired and often the removal of the hard template using acidic or basic conditions can create negative effects on fabricated nanowires.

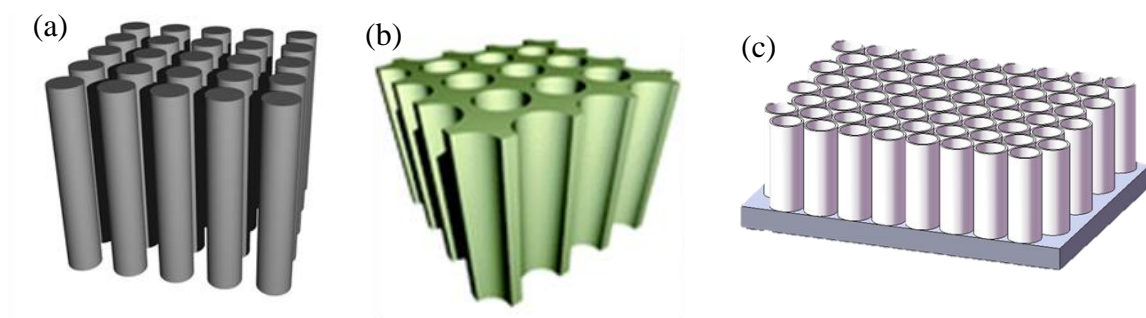


Figure 1.5. Schematic representations of (a) nanorod (b) nanohole and (c) nanotube arrays.

Besides, it is not a direct fabrication method for nanotube arrays. Hence, hard template free, controlled fabrication method, specially, for the fabrication of nanotube arrays will be very useful for a systematic study of structure property relationships since the success of such fabricated device solely depend on the ability to control the desired structural parameters with a high degree of precision and reproducibility.

1.8. CONFINED ELECTRODEPOSITION ON LITHOGRAPHICALLY PATTERNED NANOELECTRODES

In this report, we present a direct fabrication protocol to grow semiconducting nanotube arrays such as CdTe, CuInSe₂, CoSe₂, etc with a high degree of monodispersity with morphological control. Figure 1.6 shows a schematic representation of the fabrication process. In a typical sample preparation process, a conducting substrate such as Indium Tin Oxide (ITO) coated glass is coated with a layer of polymethyl methacrylate polymer (PMMA) and baked in an oven at 180 °C for 3 minutes.

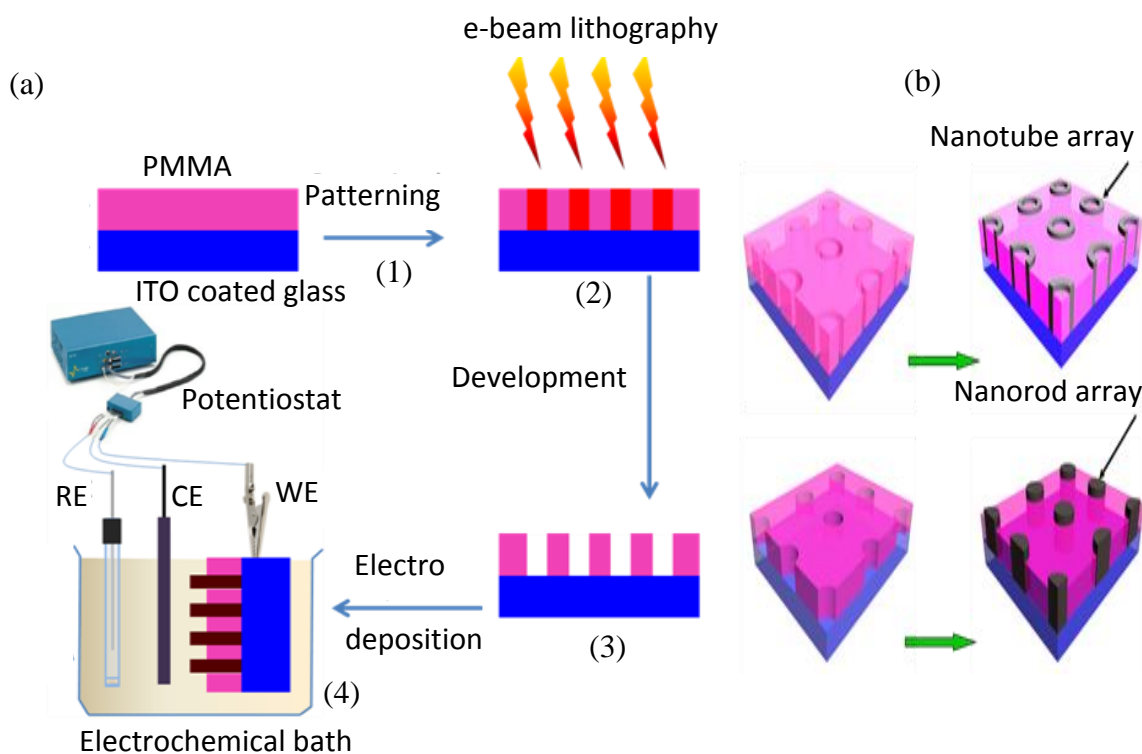


Figure 1.6. Schematic diagram of (a) a typical fabrication process and (b) growing nanotube and nanorod arrays.

Next, the sample is exposed to an electron beam at selected areas as shown in step 2. After that, the sample is dipped in a solvent mixture of methyl isobutyl ketone : isopropyl alcohol (1:3) for 1 minutes and air dried. In this step, the polymer exposed to the electron beam dissolves in the solvent mixture revealing a nanoelectrode pattern on the conducting substrate. The polymer not exposed to the electron beam remain intact as seen in step 3. Finally, electrodeposition of the desired material performs on the sample using it as the working electrode in a typical three electrode electrochemical setup. Electrodeposition exclusively takes place, as seen in step 4, on exposed nanoelectrodes since rest of the polymer is an insulator. Depending on the exposed pattern nanorods or nanotubes can be fabricated. The photovoltaic nanorod and nanotube arrays fabricated by using this protocol exhibited significant photocurrent densities compared to thin film like morphologies demonstrating the effectiveness of the technique.⁹⁷⁻¹⁰⁰

1.9. SOLAR-TO-FUEL ENERGY CONVERSION

Over the past several decades, photoelectrochemical (PEC) water splitting using solar radiation to generate oxygen and hydrogen fuels has become one of the most promising techniques for solar fuel generation.¹⁰¹⁻¹¹⁴ However, practical application of such solar-to-fuel energy conversion systems has been limited by several technical challenges, which includes materials composition and device architecture. The key challenges that must be addressed for increasing system level performance of PEC devices are: (i) maximizing carrier generation through optical absorption by the photoabsorber layer in the visible wavelength region; (ii) efficient separation of photogenerated electron-hole pairs with minimal recombination from the bulk of the

photoabsorber to the reaction site at the electrode surface; (iii) rapid surface reaction for consumption of the photogenerated charge carriers through water oxidation/reduction with minimum overpotential. Above all, stability of the PEC device under operational condition is an unwritten requirement which is desirable for any practical device. For a functional PEC device, these issues of charge carrier generation, separation, transport and injection, are integrally inter-related and cannot be effectively addressed in isolation. In this research work focus was aimed to design a hierarchical composite integrating a co-catalyst with a textured photoabsorber layer, specifically a photoabsorber layer comprising of an array of tubular structures decorated with cocatalyst nanostructures as shown in Figure 1.7, where each of these potential issues will be addressed and the efficiency will be maximized through proper choice of materials composition and/or morphology. For photoelectrochemical water splitting, the main challenge lies in the anodic oxygen evolution reaction (OER). Hence, in this project we will concentrate on the photoanode-OER-electrocatalyst composite.

1.9.1. Brief Overview of Photoelectrocatalytic (PEC) Water Splitting.

Photoelectrocatalytic (PEC) water splitting is one of the most promising and sustainable, solar-to-fuel energy conversion approaches that has been developed over decades.¹⁰¹⁻¹¹⁴ In the simplest design, the device consists of a photoabsorber layer that absorbs solar radiation and transfers the charge carriers to the electrode-electrolyte interface where water oxidation/reduction takes place through charge injection from the electrode to the reactants (H_2O) in the electrolyte, to produce O_2 (oxygen evolution reaction, OER) and H_2 (hydrogen evolution reaction, HER) at the photoanode and photocathode, respectively.

Another design aspect that becomes very crucial for a functional PEC is the separation and transport of the photogenerated charge carriers, i.e. electrons and holes with minimal recombination.

To mitigate this problem, the photoanode is typically coated with a *p*-type material which acts as hole transport layer (HTL) that allows holes to move through, while blocking electrons. Hence, there can be effective spatial separation of electron-hole pair minimizing recombination. The holes are then transferred to the electrocatalyst from where they are injected to the redox species in the electrolyte ($\text{H}_2\text{O} \rightarrow \text{O}_2$), while electrons are collected in the back electrode and are transferred to the cathode through external circuit. It is imperative therefore, that for an efficient PEC water splitting system, all three of these processes, i.e. photoexcited charge carrier generation, charge transport and charge injection has to be optimal and moreover, the respective valence band edges for each layer has to be compatible in energy. Of these, the photoexcited charge carrier generation and charge injection are the two factors that has the maximum influence on the efficiency of the PEC water splitting system.

Hence, in this project we will focus on gaining a fundamental understanding of the structure-property relationship of the individual components, i.e. nanostructured photoabsorber arrays, and OER cocatalysts, and their interplay in the integrated device. Only with such knowledge can further device architecture be designed leading to better performance. Such improvements will be significant, since even slight increases in efficiency of solar-to-fuel energy conversion, leads to a reductions in the cost of the module and increased sustainability.

1.9.2. Photoabsorbers and Photoanodes. Although single crystalline and polycrystalline Si has been the material of choice as solar photoabsorption,¹¹⁵ recently, several other inorganic compounds have shown significant promise as thin film photovoltaic materials with a proper band gap lying in the solar absorption region. In particular, binary chalcogenides such as CdTe, CdSe, CuSe have shown potential for efficient power generation.¹¹⁶⁻¹¹⁸ The photoconversion efficiency of these systems has been very promising, for example, First Solar reported a record high efficiency of 20.4% for CdTe photovoltaic solar cell which beat the previous record of 19.6% conversion efficiency set by GE Global Research.¹¹⁹

Ternary (CuInSe₂ [CISe], CuGaSe₂, CuInS₂ [CIS]) and quaternary compounds (Cu(In_{1-x}Ga_x)Se₂ [CIGS], CuIn(Se_{1-x}S_x)₂) have also attracted considerable interest due to their outstanding electro optical properties.^{120,121} The I-III-VI₂ chalcopyrite semiconductors (exemplified by Cu(In,Ga)Se₂) are among the most promising light-absorbing materials for photovoltaic applications because of their appropriate band gaps, high absorption coefficients, and good radiation stability.¹²²⁻¹²⁵ Chalcopyrite CuInSe₂, with a direct band gap of 1.04 eV, has a high absorption coefficient over the UV-vis range, which is on the order of 10⁵ cm⁻¹ for the bulk and 10⁴ cm⁻¹ for thin films.³² The band gap of CuInS₂ (1.53 eV) is also well-matched to the solar spectrum for optimum photovoltaic performance. The advantage of using direct bandgap semiconductor is that they have high absorption coefficient leading to better efficiency even with less material in the absorber layer. For a PEC water splitting device, in addition to high absorption coefficient, a photoabsorber should also fulfil some other requirements to effectively function as photoanode/photocathode. For example, for efficient solar water splitting,

ideal bandgap of the photoabsorber should be in the range of 1.4 – 2.0 eV. In addition, the material should show stability against photocorrosion under continuous operation in aqueous electrolyte. Apart from optimal bandgap, the alignment of the valence band edge with the water oxidation level is also of utmost importance for an effective photoanode. A large separation between the redox level in the electrolyte and the valence states of the photoanode leads to high overpotential which reduces the rate of charge injection across the semiconductor-electrolyte interaction thereby slowing down the water oxidation reaction. Apart from the above mentioned photoabsorbers, variety of other semiconductors has been applied as photoanodes in solar water splitting, the most notable being BiVO₄,^{127,128} WO₃,¹²⁹ Fe₂O₃,¹³⁰⁻¹³³ and Ta₃N₅.¹³⁴⁻¹³⁶

1.9.3. Coupling Electrocatalysts with Photoanodes: The Backbone of PEC

Water Splitting. Although a variety of photoabsorbers has been applied as photoanodes for solar water splitting, most of them suffer serious drawbacks mainly due to compromised stability under long-term operation, and the band edge positions not being aligned with water oxidation level which leads to application of large bias voltage and less efficient charge injection. These issues have been addressed by sensitizing the photoanode with cocatalysts responsible for water oxidation. Nocera and other researchers have extensively studied the PEC water splitting with molecular OER catalysts coupled with photoanodes which shows moderately high efficiency.^{110,137,138}

However, the extended stability of molecular catalysts against photodegradation limits the applicability of these systems. Inorganic solids have also been used as cocatalysts with variety of photoanodes.^{104,113,139,140} A proper cocatalyst should be highly active for OER, be impervious to light absorption, stable in aqueous electrolyte and more

importantly, have proper band alignment with the photoanode as well as water oxidation level. Hence, the integration of cocatalyst with photoabsorber cannot be done arbitrarily, but rather involves understanding of their core materials chemistry. Our aim is to integrate the highly active selenide and telluride based OER electrocatalysts with the selenide and telluride based photoabsorbers, hypothesizing that such assembly will lead to more efficient charge transfer and injection, due to better alignment of the valence band edges.

1.9.4. High-efficiency Selenide and Telluride based OER Electrocatalysts:

The Effect of Covalency. While the literature for OER electrocatalysts is over-populated with transition metal oxides, from materials chemistry point of view, one can readily anticipate how the catalytic efficiency can be further improved by changing the coordination environment around the catalytically active metal center. It had been discussed earlier that increasing covalency in the metal-oxygen bond led to better catalytic efficiency.¹⁴¹ According to Fajan's rule, for a specific metal ion, the covalency increases with increasing anion size and since the chalcogenides are bigger than the oxides, it can be expected that metal-chalcogen bonds will have a greater degree of covalent character than the metal oxides.¹⁴²

Hence chemically it is quite intuitive that replacing the oxide coordination sphere with chalcogenide coordinations (chalcogen = S, Se, Te) will change the degree of covalency around the transition metal center. Additionally, such change in the transition metal's coordination environment will also affect the bonding nature and correspondingly the electronic properties of the solid.¹⁴² Typically it has been observed that while the transition metal oxides are wide bandgap and mostly insulating, transition metal

chalcogenides have narrower bandgap, semiconducting nature and some of them are even semimetal or metals with zero bandgap.¹⁴³⁻¹⁴⁶ For example, while NiO has a bandgap of 3.5 eV, NiS₂ and NiSe₂ have much smaller bandgaps of 0.35 eV and 0.0 eV, respectively.^{143,144} Typically in these transition metal oxides/chalcogenides, in the simplest bonding scheme, the valence band edge is composed of the σ -bonding interaction with chalcogen s and p – orbitals with the metal d -orbitals (e_g symmetric $d_{x^2-y^2}$ and d_{z^2}) while the bottom of the conduction band has more contribution from the anti-bonding σ^* orbitals centered preferentially on the metal.¹⁴⁴ The d -orbitals of the transition metal (forming the t_{2g} and e_g^* sets) lie in the inter-band region where the splitting between them is determined by simple consideration of ligand field theory. As the anions are changed from O to Te, i.e. down the chalcogen series, the valence band edge is expected to rise higher in energy due to decreasing electronegativity of the chalcogen atom and higher covalency. Additionally, the crystal field splitting of the d -orbitals is also affected by changing the chalcogen atoms which changes the ligand field strength. These changes in the orbital energy levels will directly influence their alignment with respect to the water oxidation and reduction levels, which in turn will affect charge transfer between the catalyst and water. For PEC water splitting catalysts, one of the most influential factors in light of electronic band structure is that water oxidation-reduction levels are bracketed within the valence and conduction band edges of the catalyst. In these electrocatalytic systems charge injection occurs at the semiconductor (catalyst)-electrolyte interface which is influenced by relative energy levels of the semiconductor and aqueous electrolyte, and efficient charge transfer will occur when these two levels are closer in energy. The separation between the band edges and the water oxidation-

reduction levels is reflected in the measured overpotential for OER/HER. From previous band structure studies, it has been shown that valence band edge of the transition metal oxide are highly oxidizing compared to the water oxidation level, e.g. TiO_2 ,¹⁴⁵ whereas that of the chalcogenide band edges being much higher up are less oxidizing, which also means that they are closer to the water oxidation level. Such closeness expectedly will lead to better charge injection, reducing overpotential, thereby facilitating the catalysis mechanism as proposed above.

Hence, from chemistry point of view, selenides and tellurides can be expected to show better OER catalytic activity. In fact, a big boost for these non-precious metal based non-oxide OER electrocatalysts has been provided by the discovery of several transition metal sulfides and selenides which have shown much better electrocatalytic activity, both in terms of overpotential (at the benchmark current density of 10 mA/cm^2) and current density, compared to the corresponding oxides.¹⁴⁶⁻¹⁷⁴ Several of these selenides and telluride have also been synthesized in the our laboratory.¹⁴⁶⁻¹⁵⁴ Apart from results reported from the our lab, several other researchers have confirmed that indeed selenides show high activity for OER in alkaline medium.¹⁵⁵⁻¹⁷³ So, there is no doubt that the selenides can indeed outperform some of the conventional OER electrocatalysts.

1.9.5. Effect of Nanostructuring on Photoabsorber Properties. Recent research has shown that increasing the aspect ratio of the photovoltaic material increases the photoconversion efficiency.¹⁷⁶⁻¹⁷⁸ This has led to a renewed interest in photoabsorber geometries such as nanowires and nanorods.

For example, high-aspect-ratio (length/diameter) nanorods allow the use of a sufficient thickness of material to obtain good optical absorption (lower reflection

relative to planar geometries) while simultaneously providing short collection lengths for excited carriers in a direction normal to the light absorption.¹⁷⁹⁻¹⁸⁰ These two effects are complimentary for improving the overall efficiency and are particularly significant for materials with defects or imperfect crystallinity. Improving the carrier transport characteristics is key to increasing photoconversion efficiency which improves performance and reduces material consumption.¹⁷⁶⁻¹⁷⁸

An ideal absorber should have a columnar grain structure to aid carrier collection and transport and minimize loss due to grain boundary scattering and recombination. For example, ordered arrays of silicon nanowires increase the path length of incident solar radiation by up to a factor of 73.¹⁷⁹ Similarly, there are encouraging recent reports of increased efficiency in nanowire solar cells constructed with the pnictides, InP and GaAs semiconductors.¹⁸⁰⁻¹⁸¹ including efficiencies normalized to the active area of the device that exceeds the Shockley-Queisser limit. This requires the nanowires to act as nanoantennas, locally concentrating the incident light. With the InP nanowire arrays it was observed that with a very small coverage (12%), photocurrent obtained was higher than in a conventional thin film device.¹⁸⁰ and the optimal coverage with the nanowires were determined to be 10 – 15% for this system.

This behavior has also been reproduced with perovskite nanowires.¹⁸¹ While several attempts to grow CISE and CIGS nanostructures have been reported,¹⁸²⁻¹⁸⁶ efforts to grow nanowire arrays with uniform diameter and length are very limited in the literature and will be advanced in the proposed work. One of the biggest advantages of using nanowires in lieu of planar films is that the enhanced photo-conversion efficiency

of the nanowires significantly reduces the use of expensive semiconducting materials thereby drastically decreasing the cost of raw materials.

Other nanoarchitectures such as nanohole arrays, have also shown significant promising for photovoltaics.¹⁸⁷⁻¹⁹⁶ For example nanohole arrays with hole diameters of 10s to 100s of nanometers and are an antireflective coating.¹⁸⁹⁻¹⁹⁰ Surface reflective losses has been a long-standing issue in solar energy research and various approaches of antireflective coating on the photoabsorber surface has been adapted to suppress this loss, including surface texturing. Recent research has indicated that replacing the surface texturing with periodic arrays of nanostructures can lead to drastic reduction of the optical loss.¹⁸⁷⁻¹⁹¹

The antireflective property could be also obtained in the nanopillar arrays,¹⁹¹ however, by introducing the central porous architectures (nanoholes) reflectance of the photoabsorber layer could be further reduced and multiple the nanohole/nanowire arrays have been shown to produce low reflectance¹⁸⁹⁻¹⁹² and most of them showed very low reflectance. Most importantly nanostructured array can be designed by varying the diameter along the length to produce broadband antireflective properties,¹⁹¹ similar to the classic moth's eye effect and significantly lower overall reflectance than equivalent planar films. The improved light absorption acts in concert with the improved carrier extraction to enhance overall solar cell efficiency.

This research will investigate the influence of nanostructured arrays (particularly nanotubes) on enhancing optical absorption as well as photo carrier generation and collection. Understanding the phenomena will allow the synthesis of morphologies that can simultaneously maximize both. It is expected that the nanotube can effectively trap

light through internal reflection and scattering thereby, reducing reflective losses similar to the nanohole arrays. This reduces the need for external antireflective coatings.

Accordingly, we will produce nanoarchitectures of different photoabsorbers including CdTe, CISE, and CZTS with proper $p-n$ junctions to investigate the effect of geometric parameters, in the presence of electrodeposited microstructure/defects, on photoconversion efficiency. There is limited literature on nanotube arrays as photoabsorbers and understanding the structure/property relationships for these systems will address significant knowledge gaps for photovoltaics.

1.9.6. Assembling the Nanotubes/nanowires as Arrays: The Practical

Challenge. One of the most significant challenge in this semiconductor nanostructure research is their assembly with precise control of their properties. Although conceptually the photovoltaic nanowire and nanotube arrays seem very attractive as photoabsorbers, the construction of such complex architectures from the nanoscale building blocks by a bottom-up synthesis technique is extremely challenging.

This is especially true for nanotubes/nanowires of complex ternary and quaternary compositions. The use of a sacrificial template, where the morphology-directing template is consumed as one of the reactants, provides better dimension control. However, the target compositions for the nanotubes will be limited by the reactivity of the sacrificial templates. The lack of rational synthesis protocols severely hinders the progress of the field by not providing opportunities to build scientific knowledge regarding the dependence of efficiency on the dimensions and morphology of the semiconductor nanostructures and their arrays. While it is feasible to synthesize multi-component complex architectures of nanomaterials, it is significantly more difficult to

manufacture a nanostructured device over the large areas at costs required for practical devices. The utility of semiconductor nanowires in photovoltaic devices relies on electron transport across the nanowires and at the nanowire electrode interfaces. These two factors define in large the effectiveness of the nanowire device. Poor contact at the nanowire electrode interface leads to a large Schottky barrier with huge contact resistance across the interface inhibiting carrier transport.¹³⁸

Achievement of reproducible nanowire-electrode interfaces requires careful analysis of the chemistry and physics at the interface. Another bottleneck to success with semiconductor nanowire devices is created by the extreme difficulty of assembling nanowires into well-defined arrays. Integrating mass-produced nanostructures into devices requires very challenging post-synthesis assembly involving several laborious steps and lengthy procedures. Additionally, the length scale of these nanostructures magnifies the electrostatic forces and Brownian motion. Chemical field flow in an electrical field is under instigation industry (e.g., SolVac) for vertically aligning pnictide nanowires on the surface without any physical adherence.¹⁹⁷ However, while these techniques produces some alignment, they are nowhere near optimal or reproducible and hence have very low throughput.

This compromise the economic viability for creating ordered nanowire devices. Apart from the obvious advantage of site specific growth, nanopatterning also offers precise control of the size uniformity, dimensionality, growth direction, and dopant distribution in these nanostructures. The latter is of particular importance, since, these parameters ultimately define charge transfer efficiency of these nanowires. Development of new assembly methods for integration and growth of nanotubes/nanowires on a

substrate by confining growth region with suitable bottom-up techniques producing high density of nanowires is very advantageous. Direct electrochemical growth of the nanotubes/nanowires on electrodes, ensures robustness of the contact at nanowire-electrode interface with reduced contact resistance.

1.9.7. Efforts to Grow Ordered Arrays of Nanotubes on Large Scale Through Bottom-up Methods. Although, the nanowire arrays have been commonly produced through template approach using anodic aluminum oxide membranes (AAO),¹⁹⁸ nanotube arrays surprisingly have not been fabricated in large party due to the complexity of the morphology control. Nanohole arrays have been made on Si layer through subtractive processes including, ion-beam sputtering, wet etching and shadow mask etching.¹⁸⁷⁻¹⁹¹ In these processes the pre-deposited photoabsorber layer is textured with the aid of preferential etching where the process is most commonly carried out in ultra-high vacuum chambers.

While this method produces uniform arrays, frequently impurity atoms, mostly metals, are incorporated into the photoabsorber layer which can act as recombination centers leading to carrier loss.¹⁹⁰ Additionally creating nanotube architectures using such etching process will be far more complex and questionable with regards to feasibility. An additive process more closer to the *bottom-up* approach, and not requiring ultra-high vacuum capabilities, might be more desirable since it will reduce the complexity of the fabrication process as well as be amenable to other complex photoabsorbers such as CdTe, CISE, CuSe, and so on.

Electrodeposition is one such *bottom-up* additive process which can be done under ambient conditions on rigid as well as flexible substrates, and can be scaled up to

any desirable length scale. Protocol proposed by the this research might be one of the most versatile and unique method to create nanotube arrays with controllable dimensions including length, pore diameter, wall thickness, pitch and distribution pattern over a large area. Through the proposed hypothesis driven materials chemistry research we will address both charge carrier generation and transport by creating vertically ordered nanotube arrays of optimal composition and morphology for high photoconversion efficiency.

PAPER**I. PATTERNED ELECTRODEPOSITION OF CdTe NANOROD AND NANOTUBE ARRAYS FOR SOLAR CELLS**

Nanomaterials and Energy, 3.5 (2014): 167-176

Wipula P. R. Liyanage,^a Sukhada Mishra,^a Jacob A. Wilson,^b E. Kinzel,^b Manashi Nath^{*a}

^a Department of Chemistry, Missouri University of Science and Technology, 142 Schrenk Hall, 400 W 11th Street, Rolla, MO 65401-USA.

^b Department of Mechanical and Aerospace Engineering, Missouri University of Science and Technology, Toomey Hall, 400 W 11th Street, Rolla, MO 65401-USA

KEYWORDS: CdTe, nanofabrication, nanotube arrays, nanowire solar cells, photovoltaics, solar cells

ABSTRACT

CdTe nanorod and nanotube arrays have been grown on indium tin oxide-coated glass slides through confined electrodeposition on lithographically patterned nanoelectrodes. While pattern definition by e-beam lithography yielded thinner nanorods and nanotubes, pattern definition by nanosphere photolithography using polystyrene spheres as lenses was successful in creating these nanowire arrays over a large area exceeding several sq-cm in a single step. The successful creation of clean arrays of nanotubes with uniform diameters underlined the versatility and uniqueness of the protocol. The photoconversion efficiencies of the nanorod/nanotube arrays were determined through photoelectrochemical response under UV light excitation. The observed photocurrent density of the fabricated nanorod device was more than two times

higher than that of thin films fabricated under similar conditions, in spite of having a much lesser surface coverage for the nanorod device (~12% compared to the thin-film device). In addition to the potential of improved solar energy conversion efficiency by the nanorod and nanotube arrays, reduced material consumption due to lower coverage and simplicity of the fabrication technique make this approach ideal for the production of high-efficiency photovoltaic devices at commercial scale.

1. INTRODUCTION

Due to the tremendous costs and impacts to the environment associated with traditional energy sources, technology related to the development of high-efficiency solar cells plays a major role in low-carbon energy power generation.¹ Although single crystal and polycrystalline silicon (Si) solar cells dominate the world of solar cell production, large-scale implementation of Si-based solar cells is still not economically the best solution although the cost of Si solar cells has fallen recently. This is attributable to the fact that the energy payback time for their production is much longer, thus limiting their productions at larger scales.² On the other hand, several semiconducting inorganic compounds such as CuInSe₂, Cu(In,Ga)Se₂ and CdTe have shown promise as photovoltaic materials for efficient power generation.³ Thin-film solar cells of Cu(In_{1-x}Ga_x)Se₂ have achieved record conversion efficiencies as high as 21.5%.⁴ With an ideal bandgap of 1.45 eV lying in the solar absorption region and having the ability to be in both n-type and p-type conductivities, CdTe is a material of great importance for application in solar energy conversion.^{5,6}

Recent progresses in the area of photovoltaics utilize the semiconductor nanostructures for solar energy conversion due to their ability to regulate electronic properties by means of composition, size and shape.^{1,7} It has been shown that due to the nanoscale characteristics of absorption of radiation and generation of the photocurrent, controlling semiconducting materials in the nanometer dimension provide new opportunities for the development of future generation solar cells.⁸ Parallel assembly of nanowires and nanorods has gained renewed interest over nanoparticles and thin films since high aspect ratio of nanowires and nanorods provides sufficient thickness for optical absorption while naturally providing a direct path for the transport of excited carriers along the length of the rod or the wire.^{8,9} An added advantage of using nanowires in lieu of planar films is the improved efficiency achieved per unit volume of the semiconductor caused by increased light absorption, trapping and charge collection in the nanowires. Another factor that plays a significant role in determining the efficiency of the solar cell device is the grain size of the absorber material.¹⁰ An ideal absorber should have a columnar grain structure to aid carrier collection, transport and minimize loss due to grain boundary scattering and recombination.¹¹ Semiconducting nanowire arrays have been shown to have low reflective losses compared to planar semiconductors leading to higher optical absorption.¹² It has been predicted that nanometric geometry might also play a constructive role in increasing the effectiveness of the photovoltaic device, by virtue of increasing the surface area and providing an unhindered transport path.⁸ Increased efficiency in nanowire solar cells constructed with InP and GaAs has been recently reported and, with InP nanowire arrays, it has been reported that even with a very small coverage (12%) photocurrent obtained was better than that of a conventional

thin film.^{12,13} These reports claim that these nanowire solar cells can even beat the Shockley–Queisser limit with the nanowires acting as solar concentrators. It has also been observed that the photocurrent efficiency can be amplified by growing very high density of vertically ordered semiconducting nanowires over any defined area on a conducting surface.¹⁴ Although conceptually the photovoltaic nanowire arrays seem very attractive for solar cells, the construction of such complex architectures from the nanoscale building blocks by the bottom-up synthesis technique is extremely challenging. In this report, we demonstrate that these challenges can be overcome and present a simple and scalable method for growing nanorod and nanotube arrays on a transparent conducting substrate at desired locations through patterned electrodeposition (PatED) and demonstrate the feasibility of growing both thinner nanowires as well as thicker nanowire arrays over large area exceeding several sq-cm. We demonstrate the concept using CdTe as the semiconducting material and indium tin oxide (ITO)-coated glass as the conducting substrate, where the growth of nanorod and nanotube was achieved by the electrodeposition on nanoelectrodes patterned on ITO-coated glass by electron beam lithography (EBL) and nanosphere photolithography (NSP). While pattern definition by EBL yielded very small nanoelectrodes, which eventually led to nanorods less than several hundreds of nanometers in diameter albeit covering smaller areas, repeated pattern definition by EBL with small lateral shift between patterns could successfully translate these smaller nanowire arrays over areas larger than those obtained by single-step EBL. NSP process, on the other hand, actually led to the growth of CdTe nanorod arrays over large areas approaching commercial manufacturing scale in a single step. By a subtle variation in the pattern definition in EBL, we could also grow arrays of CdTe

nanotubes. Previous researchers have used both potentiostatic and galvanostatic electrodeposition to prepare CdTe films for efficient solar cells.¹⁵ Aqueous electrodeposition is an attractive preparative method for CdTe films because it is not only scalable to large area depositions but also a widely used industrial technique. Although there are reports of CdTe nanowire arrays,^{16–19} electrodeposition of CdTe thin films,^{15,20} VLS growth of nanowires through chemical vapour deposition,^{21,22} seeded growth process²³ and closed-space sublimation,¹⁸ most of them are not economically viable due to low throughput or the use of hard templates like AAO.^{16,18,19} Typically removal of these hard, rigid templates requires treatment with either acids or bases. Under such conditions, semiconducting nanomaterials such as CdTe and CuInSe₂ are highly susceptible to decomposition and hydrolysis leading to compositional degradation of the nanowires that affects its photovoltaic performance. The simplicity and reproducibility of the scalable method proposed here provide an opportunity to explore the synthesis of nanowires with variable chemical compositions as well as the nanowire–electrode interphase and study their effect on the performance of the nanodevices. The photovoltaic nanorod and nanotube arrays fabricated by using the above protocol exhibited significant photoconversion efficiencies demonstrating the effectiveness of the technique.

2. EXPERIMENTAL

2.1. MATERIALS

Polymethylmethacrylate (PMMA, mol. wt. 450K and 950K, supplied by Microchem, Newton, MA, USA) was used as the insulating e-beam resist. ITO-coated

conducting glass substrates used for nanowire growth were purchased from Sigma Aldrich and had a surface resistance of 60Ω . Electrodeposition was performed with IvumStat potentiostat.

A positive-tone photoresist S-1805 was purchased from Microchem (Newton, MA, USA) and used as is. Size-selected polystyrene microspheres used as lenses for NSP were purchased from Bangs Laboratories (Fishers, IN, USA). Chemicals used for lithography and electrodeposition, that is, Triton X-100, CdSO_4 , TeO_2 , H_2SO_4 , were used as purchased from Fisher Chemicals.

2.2. CHARACTERIZATIONS

2.2.1. Powder X-ray Diffraction (PXRD). PXRD patterns were taken with PANalytical's X'Pert PRO Materials Research Diffractometer (MRD, CuK_α 1.5418 \AA). As-grown CdTe nanowires on the ITO-coated glass substrates were used for data collection. The PXRD was collected at grazing angles in thin-film geometry (GI mode with Göbel mirrors).

2.2.2. Scanning Electron Microscopy (SEM). SEM imaging was taken using Helios NanoLab 600 equipped with energy-dispersive X-Ray spectroscopy (EDS) detector (Oxford Instruments, Abingdon, UK) for elemental analysis. Elemental analysis was performed by both linescan mode and selected area elemental mapping.

2.2.3. Electron Beam Lithography (EBL). Electron beam lithography was performed with the in-built lithography facility available with a Helios NanoLab 600 DualBeam FIB microscope.

2.2.4. Photoelectrochemical (PEC) Measurements. Photoconductivity was measured through PEC measurements performed with IvumStat potentiostat. A 400 W Xe lamp operating in UVA range (320–390 nm) with the intensity of 100 mW/cm² was used to illuminate the nanorod device.

3. METHODS

3.1. SAMPLE PREPARATION BY EBL

The first step of pattern definition by EBL on ITO-coated glass substrate consisted of coating the substrate with PMMA layer (mol. wt. 450K) by spin-coating. This PMMA layer was then baked at 180°C for 6 min. A second layer of PMMA (mol. wt. 950k) was spin coated on top of the 1st layer followed by baking at 180°C.

The total film thickness of the resist layer was ~0.3 μm. The PMMA layers were then selectively exposed to the e-beam during EBL. Typically, the hole sizes for EBL were maintained in the 200–1000 nm range. After e-beam exposure, the exposed polymer was removed by developing in MIBK-IPA (1:3) solution for 45 s according to a standard reported procedure,²⁴ while the unexposed PMMA remained unaltered. Post-lithography treatment also exposed the underlying ITO through the lithographically patterned holes, thus forming nanoelectrode islands on the substrate. The remaining unexposed PMMA, by virtue of its electrically insulating properties, acted as a soft mask during the electrodeposition of the semiconducting material inhibiting deposition in the non-patterned regions. Figure 1 shows a schematic representation of the experimental protocol.

3.2. SAMPLE PREPARATION BY NSP

Nanosphere photolithography (NSP) was also used to pattern the nanoelectrodes onto ITO-coated glass slides. The substrate was spin coated with 450 nm of S-1805 photoresist. The photoresist was then soft-baked at 115°C for 90 s. Following this step, a solution of size-selected polystyrene nanospheres was spin coated onto surface. The nanosphere solution (10% by weight) was 1.7 μm polystyrene microspheres from Bangs Laboratories. This was mixed 7:1 with 1:400 Triton X-100 to methanol surfactant solution. During spin coating, the nanospheres self-assemble onto the surface of the photoresist to form a hexagonal close-packed (HCP) lattice.

The spheres were exposed using an i-line mask aligner for 0.7 s at 10 mW/cm². Following the exposure, the photoresist was developed in MF-319 developer for 30 s and rinsed in deionized water, before hard-baking at 145°C for 30 min. During the development process, the microspheres are washed away leaving the hole array pattern in the photoresist, with open channels to the ITO layer. Following patterning, electrodeposition is performed following the same procedure as with EBL.

3.3. ELECTRODEPOSITION OF NANOWIRES

The nanowires were grown by electrodeposition on confined nanoelectrodes exposed through the lithographic processing. IviumStat electrochemical interface instrument under constant potential (chronoamperometric) conditions was used and the deposition was carried out in an electrochemical bath containing a solution of 0.1 M CdSO₄ and 0.001 M TeO₂ using a reported procedure for thin-film deposition of CdTe.^{25,26} Temperature was maintained at 65°C while the pH of the electrolytic bath was

adjusted to 1.8 using 0.1 M H₂SO₄. Following the electrodeposition, the substrate was washed thoroughly with distilled water in order to remove the excess reactants from the substrate.

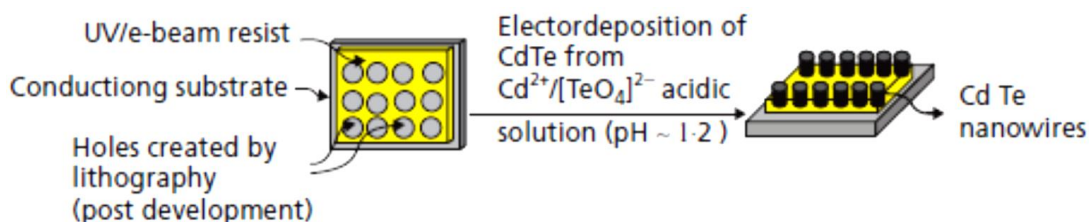


Figure 1. A schematic diagram showing the steps for generating CdTe nanorod arrays through PatED

4. RESULTS AND DISCUSSION

The nanowire arrays for this study were grown by PatED on ITO-coated conducting glass slides. The novelty of the technique lies in the fact that most of the commonly used polymeric resists are insulating in nature. Hence when periodically arranged sections of the polymeric resist were removed post-exposure to the e-beam, it created holes in the polymeric layer that uncovered the underlying ITO thereby creating nanoelectrodes embedded in an insulating matrix. The nanoelectrode is further confined within a nanochannel formed by the surrounding polymeric layer. Since electrodeposition occurs selectively on the electrodes, in subsequent steps deposition of CdTe on the nanoelectrodes along with confined growth within the nanochannels expectedly leads to nanowires or nanorods depending on the deposition time and the thickness of the resist

layer. The authors had previously obtained CdTe nanowire arrays by using this protocol. In the current manuscript, the authors have shown that this method of confined electrodeposition is not specific to only EBL. The protocol also works very well with UV lithography, which increases the versatility of the production process.

4.1. CHARACTERIZATION OF THE NANOROD ARRAYS FABRICATED THROUGH EBL

When the electrodeposited substrates with the CdTe nanorods were investigated in SEM, it was clearly seen that the deposition of nanorods had taken place only over the nanoelectrodes defined by the EBL, which is apparent from the top view of the substrate (Figure 2(a)). Although the nanorod diameter was approximately 400 nm in this particular image, it was observed that the diameter could be varied over a range of 200–800 nm by altering the nanoelectrode dimension during EBL. The polymer surface left intact by the e-beam remained very clean indicating the novelty and specificity of this approach. The PXRD spectra (Figure 2(b)) revealed that as-synthesized CdTe nanorods crystallized in the cubic zinc-blende phase (JCPDS file, card number 00-015-0770).

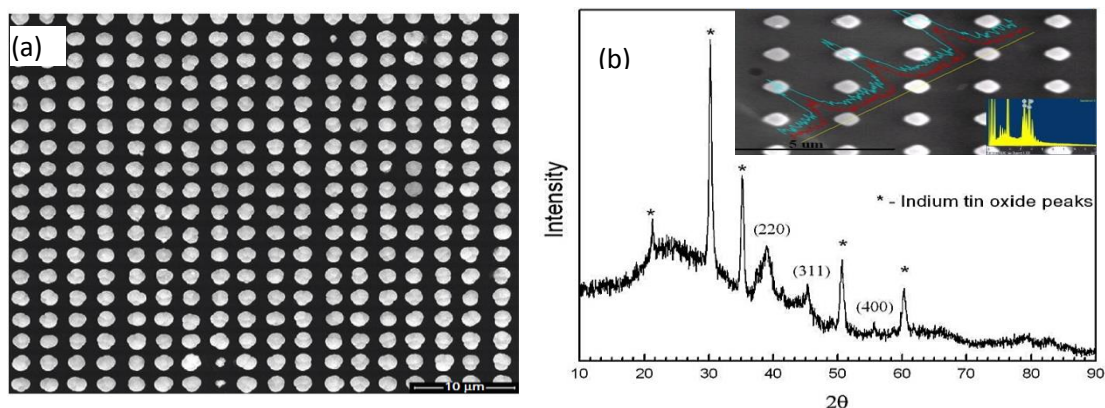


Figure 2. (a) SEM image (top view) and (b) PXRD pattern of CdTe nanorods

EDS analysis carried out of the nanorods confirmed that the elemental composition of Cd and Te is approximately in the ratio of 1:1 with slight excess of Te, which points out that the CdTe nanorods might be p-type.²⁶ The nanorods grown by this method have similar composition and uniform aspect ratio across the entire pattern showing the effectiveness of this simple technique that is very important since the properties of the nanomaterials are size-dependent, and nanodevices rely on the uniformity of the nanostructures in terms of composition and morphology. This would very hardly be achieved by non-direct growth nanofabrication strategies. Further exploitation of the EBL technique revealed that stepwise lithography can be performed to write these individual patterns one after the other over a large area by moving the sample stage by a fixed distance to maintain the separation between two neighboring patterns. Figure 3 shows two examples of uniform nanorod arrays with different nanorod densities created over a larger area by PatED following sequential EBL with the same uniformity being carried over all the patterns. Hence, this method discloses a promise to deliver thinner-diameter nanorod arrays over large areas for practical usage.

Apart from being a flexible patterning technique, high reliability and the ability to write reproducible structures over considerably large areas are some of the characteristics of EBL. Another advantage of the EBL for the definition of nanoelectrode patterns is the excellent resolution due to the small wavelength of the electrons and the size of the electron beam.²⁷ During direct patterning on a substrate, a small e-beam spot is manipulated with respect to the substrate to expose the resist one pixel at a time, eliminating the expensive and time-consuming production of masks and other peripherals required for pattern generation by most of the other available methods. The writing area

is typically governed by the maximum deflection range of the electron beam that is of the order of a few hundred micrometers. Production of larger patterns over a wide area requires the movements of the stage, which often times needs to be very accurate in order to correctly stitch consecutive writing fields.²⁸

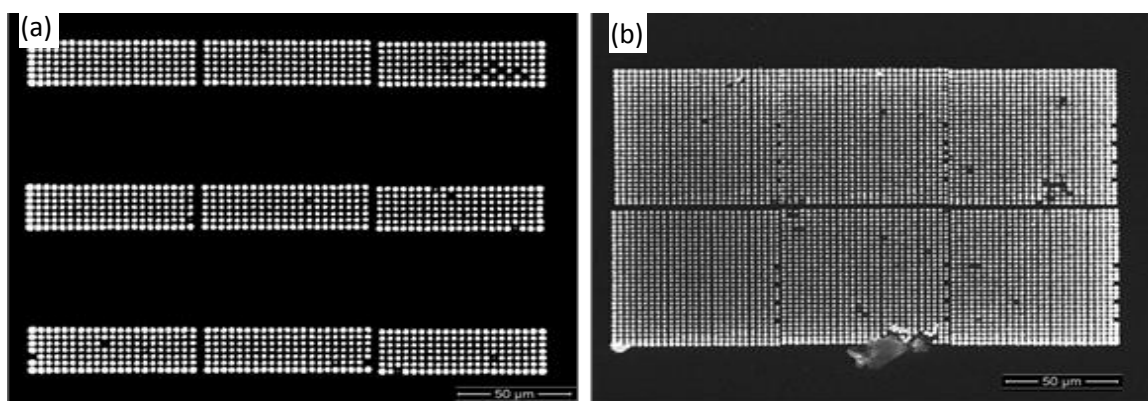


Figure 3. SEM images. Large-scale (a) low-density, (b) high-density nanorod pattern generation through electrodeposition followed by EBL

4.2. LARGE AREA GROWTH OF CDTE NANOWIRES

4.2.1. Pattern Definition by NSP. Nanosphere photolithography (NSP) is an inexpensive high throughput nanofabrication technique developed by the Mohseni group.^{29,30} It can be thought of as a combination of two established nanofabrication technologies: (a) NSP that consists of using a self-assembled HCP nanosphere array to pattern a substrate, typically using the spheres as a shadow mask during evaporation^{31–33} and (b) the photonic jet formed adjacent to a nanosphere.^{34–36}

In NSP, nanospheres serve as an array of microlenses that expose the photoresist directly under the nanospheres. This technique is capable of producing HCP arrays of either holes or pillars in positive- or negative-tone photoresists, respectively. Figure 4 shows the representative results of this technique. It is important to note that spinning the spheres onto the photoresist leads to defects and discrete crystal-like domains forming around defects caused by large particles (false color in Figure 4(a)). Alternative techniques exist for generating HCP sphere arrays, for example, following the Langmuir–Blodgett method.³³ However, for creating nanowire arrays this is not necessary, and this work demonstrates that the simpler spin-coating approach still generates viable nanowire arrays with enhanced photocurrent. In the present research work, this technique was utilized with a positive-tone photoresist to define positions of holes on a photoresist that was spin coated upon a conducting ITO substrate.

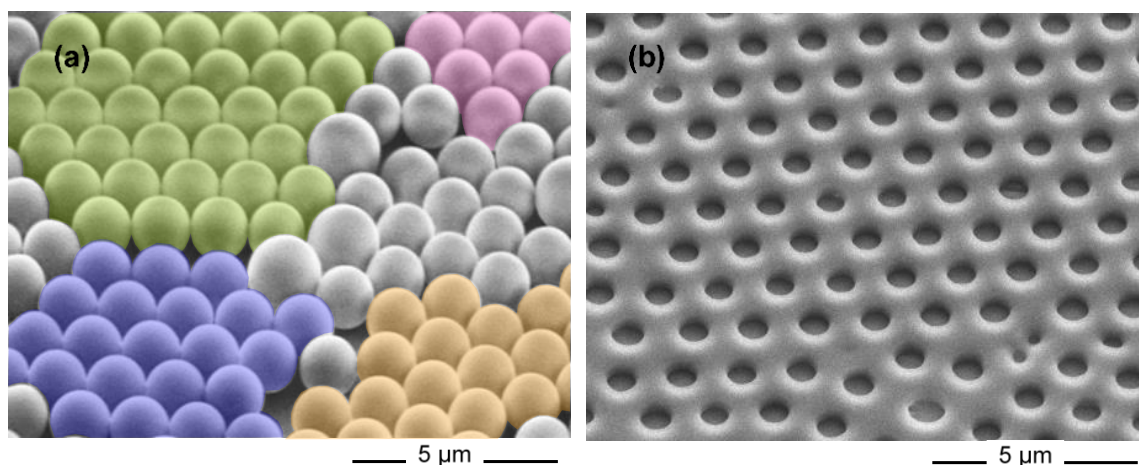


Figure 4. NSP patterns. (a) shows nanospheres on the photoresist with crystal domains highlighted and (b) shows exposed holes in the photoresist

During the development procedure, the photoresist was removed at the positions of the holes defined by the photolithography process exposing the underlying conducting ITO substrate (Figure 4(b)). These exposed areas were used as nanoelectrodes for the electrodeposition process. The remaining polymer on the ITO substrate acts as supporting channels through which nanorods of CdTe can be grown by electrodeposition.

4.2.2. Characterization of the Nanorod Arrays Fabricated through NSP.

Figure 5 shows the SEM images of nanorod arrays prepared by this method on ITO substrates to evaluate the effectiveness of this technique. The deposited films adhered strongly to the substrates and had excellent coverage. It is very clear from Figure 5(a) that monodispersed array of nanorods can be obtained over a significantly larger area and the inset of Figure 5(a) shows the EDS elemental mapping of the as-synthesised nanorod arrays confirming the presence of Cd and Te solely in the nanorods. The formation of CdTe on the substrates was further confirmed by PXRD (Figure 5(b), which showed that the as-grown CdTe nanorods crystallized in the cubic zinc-blende phase structure (JCPDS: 15-0770).

It has been reported that enhanced crystal quality of CdTe semiconductor films can be achieved by carrying out the electrodeposition at elevated temperatures.^{5,26} Ionic liquid was also used to obtain crystalline semiconductor films through direct electrodeposition at higher temperatures without subsequent annealing.²⁸ For the CdTe nanorod arrays obtained by PatED, it was observed that the intensity of diffraction lines increases with the increase in deposition temperature (Figure 5(b)). The weakest diffraction lines for CdTe were observed for the nanorods deposited at 50°C while the strongest lines were observed for the nanorods deposited at 90°C.

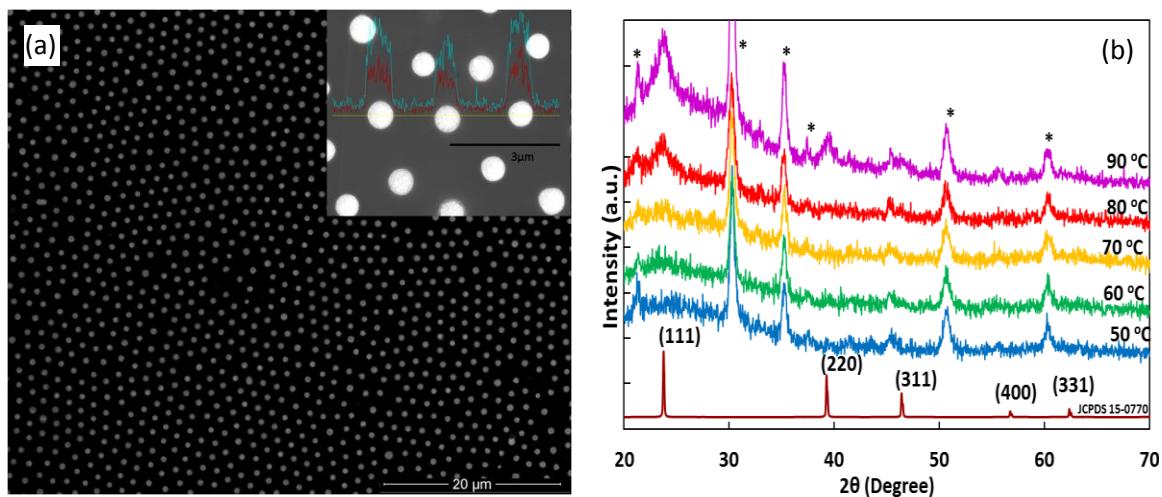


Figure 5. Morphology and crystal structure. (a) SEM of nanorod arrays prepared by NSP showing the excellent monodispersed nanorod arrays. Inset: EDS elemental analysis showing Cd and Te composition on nanorods. (b) PXRD pattern of CdTe nanorods deposited at different temperatures

Hence, it is clear that the crystallinity of nanorods can be increased by increasing the deposition temperature. However, deposition at higher temperatures also increased the rate of deposition and resulted in clustered growth and overgrowth of CdTe that spilled outside the nanochannels. This kind of overgrowth can be detrimental to the photoconversion efficiency. Hence, a temperature in mid-range ($\sim 65^{\circ}\text{C}$) was chosen for subsequent electrodeposition, such that there was balance between considerable crystallinity and minimal overgrowth of CdTe.

Considerable broadening of the (111) peak was observed in the PXRD pattern, which indicated that the CdTe nanorods were polycrystalline with domains of $\sim 39 \text{ \AA}$ in size as calculated from the Scherer equation. Similar to the patterns prepared by EBL (Figure 2), the polymer not affected during photolithography remained very clean proving the effectiveness of this technique. The most interesting feature of NSP over

EBL is the scalability of the technique to cover very large areas³⁷ such as a whole Si wafer at a given time.

4.3. PEC RESPONSE MEASUREMENTS

The bandgap of the CdTe nanorod arrays was measured by UV–Vis spectroscopy in the solid state. The UV–Vis spectra obtained from blank ITO and PMMA-coated ITO were used as references and were subtracted from the spectra obtained from the sample to isolate the absorption peak solely due to CdTe. From the absorption spectra, a bandgap of 1.4 eV was estimated for the CdTe nanorod device (Figure S1 in supplementary information). As-synthesized CdTe nanorods arrays grown on ITO substrate using NSP were used for investigating the photocurrent generation according to a reported procedure³⁸ using the three-electrode system with a Ag/AgCl reference electrode, platinum counter electrode and the substrate with the nanorod arrays as the working electrode.

A buffer solution containing 0.1 M acetic acid, 0.1 M sodium acetate and 0.1 M sodium sulfite and having a pH of 4.6 was used as the electrolyte solution. A 400W Xe lamp operating in UVA range (320–390 nm) with the intensity of 100 mW/cm² was used to illuminate the nanorod device. PEC measurements in illuminated and dark conditions were also performed on CdTe thin film on ITO in addition to the CdTe nanorod arrays on ITO for comparison. For the controlled experiment, a PMMA-coated ITO substrate (blank) was also characterized through PEC measurements to demonstrate that PMMA itself does not show appreciable photocurrent under these conditions.

The applied potential was varied from 0 to 0.8 V using linear sweep technique at a scan rate of 0.005 V/s. It has been demonstrated^{12, 14} that the nanorod devices can generate a high current density in spite of their low coverage compared to a thin-film device. Figure 6(a) shows the current response obtained under illuminated and dark conditions for the fabricated nanorod arrays, and Figure 6(b) shows the same response for the fabricated thin-film device.

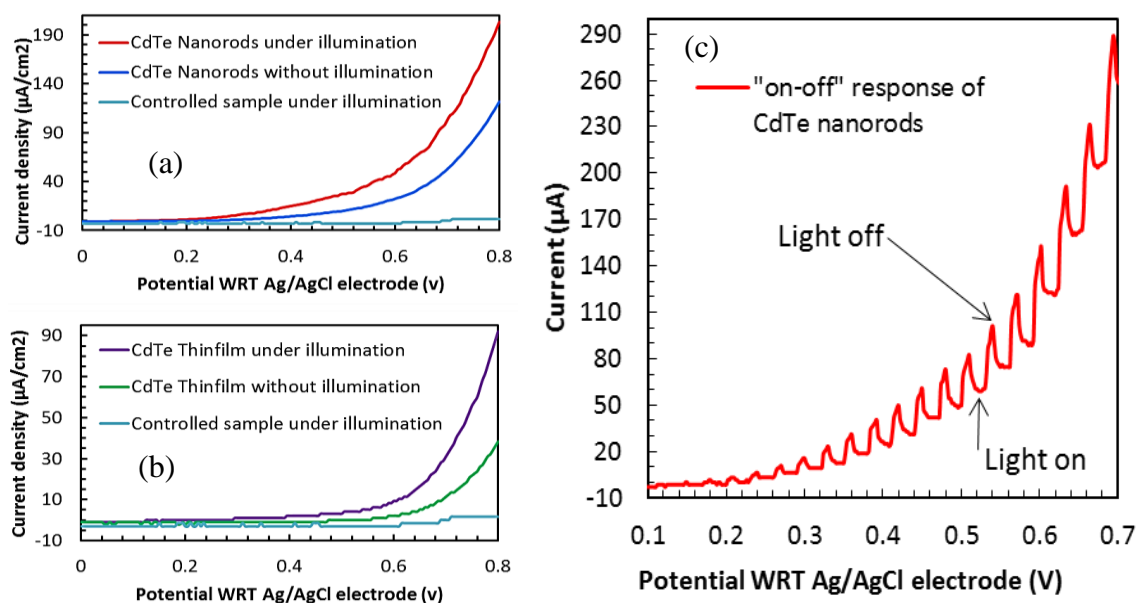


Figure 6. Generation of photocurrent. (a) Photocurrent density under illuminated and dark conditions of the nanorod device fabricated from NSP technique. (b) Generated photocurrent of the thin film under similar conditions. (c) Photocurrent generation of the nanorod device when the light source is turned on and off periodically.

The thickness of the deposited active material remained the same in both cases by maintaining the same electrodeposition parameters. The blank sample, which does not contain the active material, showed no significant photocurrent under the experimental

conditions. The ‘on-off’ response of the nanorod device shown in Figure 6(c) was recorded by turning on the light for 5 s and turning off the light for 15 s periodically. The CdTe nanorod device shows a photocurrent density of $203 \mu\text{A}/\text{cm}^2$, which was more than two times of the current density comparable to the $92 \mu\text{A}/\text{cm}^2$ obtained from the CdTe thin film, however, the coverage of the active material of the nanodevice is $\sim 12\%$ compared to the thin-film device. This clearly showed that the photocurrent comparable to that of a thin film can be generated with a fraction of the active material. These observations are very similar to the ones recently reported for vertically aligned InP nanorod arrays.¹²

Photocurrent enhancement in the nanorod arrays can be caused by several factors. If the sizes of the nanorods are below the ray optics limit, the light absorption in the nanorods can be significantly enhanced through resonant light trapping,¹² which leads to better photocurrent generation. Vertically aligned nanorod arrays having a three-dimensional geometric configuration can also exhibit reduced surface optical reflection leading to enhanced absorption.³⁹ On the other hand, for thicker nanorods, a more predominant factor comes into play. Each nanorod acts as a resistor and the current output from a parallel series of resistors is amplified heavily according to Ohm’s law. Thus for thicker nanorods, increasing the packing density of the vertically ordered nanorods amplifies the photocurrent output even though light absorption is not necessarily enhanced. In these CdTe nanorod arrays, the size of individual nanorod is slightly bigger than that required for enhanced light absorption. Hence, photocurrent enhancement is most probably caused by the parallel arrangement of the nanorods within a small space and higher volume of the photoabsorber.

4.4. GROWTH OF CDTE NANOTUBE ARRAYS AND ENHANCED PHOTOCURRENT

The concept of PatED to produce nanorod arrays was further extended to investigate the possibility of fabricating novel nanostructure architectures like vertically aligned nanotube arrays for solar energy conversion. Nanotubes have recently shown promise in various energy-related applications like dye-sensitized solar cells as well as photovoltaics.⁴⁰ The nanotube geometry will be especially helpful for photoconversion due to larger accessible surface area compared to the nanorods, which further enhances the photoconversion efficiency achieved per unit volume of the semiconductor. However, making such vertically ordered nanotube arrays has been very challenging and has been achieved with very limited cases mostly confined to the oxides like Al₂O₃ and TiO₂ that are grown by anodisation.⁴¹ Reports of CdTe or other chalcogenides nanotube arrays are very rare, and typically they involve the use of a morphology-directing hard template that has to be removed after CdTe growth.⁴⁰ Such multi-step processes hamper the large-scale production of these nanoarchitectures and also affect the compositional purity of the device. With the current protocol reported here, we could modify the pattern for EBL and, instead of writing an array of circles, we designed the pattern features such that it writes an array of shells with the e-beam. After the development and removal of polymer, doughnut-like nanoelectrodes were formed on the ITO-PMMA substrate where the center of the doughnut was still filled with unexposed PMMA. Confined electrodeposition on these doughnut-shaped nanoelectrodes was expected to give nanotubular architectures in a single step. Figure 7(a) shows the SEM image of uniform nanotube arrays produced by this technique. The novelty of the protocol can be appreciated by looking at the cleanliness of the CdTe deposition (the PMMA surface in between the nanotubes does

not have any CdTe deposition or overgrowth) and uniformity of the nanotubular architectures in terms of both tube-wall thickness and outer diameter. Large-area pattern creation through sequential EBL involving lateral translation of the sample stage in between the patterns could deliver the nanotube arrays over much larger area similar to the ones shown in Figure 3. The PEC response of the as-grown nanotube arrays under UV-light excitation was tested under similar conditions as described for the nanorod arrays and the result is shown in Figure 7(b).

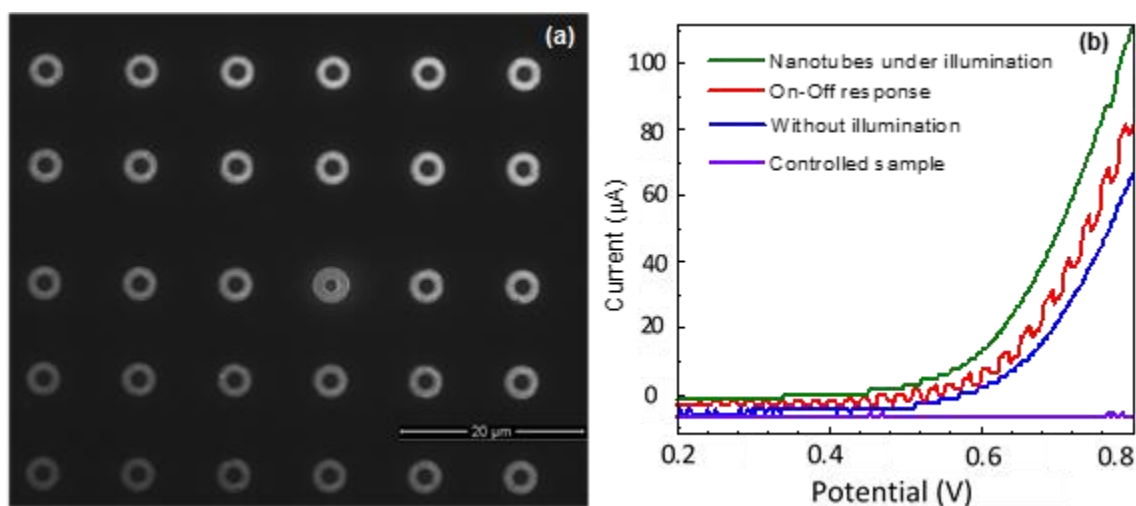


Figure 7. PEC characteristics of nanotubes. (a) Vertically aligned CdTe nanotube arrays (viewed from top along the axis of tube-growth). Inset shows the zoomed in cross-sectional view of the individual CdTe nanotubes. (b) PEC response of the as-grown nanotubes

The PEC response indicates that a similar photocurrent can be generated from nanotubes having a total coverage even lower than that of the nanorods. This observation is clearly indicative of the fact that higher surface area in the nanotube arrays, as

compared to that of the nanorods, delivers a better efficiency per semiconductor volume. The creation of nanotubular architectures through this simple PatED protocol is a very novel concept, since the process is independent of nanostructure composition and ideally any type of nanotubes can be electrodeposited in these doughnut-shaped nanoelectrodes.

5. CONCLUSION

We demonstrate that the concept of PatED on lithographically created nanoelectrodes can successfully be extended for producing nanorod/nanotube arrays covering a large area. These semiconducting nanorod and nanotube arrays can be effectively used as nanowire solar cells offering high photoconversion efficiencies at low surface coverage. It was also revealed that this model of PatED of nanorod/nanowire arrays can be further extended to an inexpensive, high-throughput, commercial-scale manufacturing process with the aid of NSP that makes the production process more cost-effective. Less usage of active material to obtain a comparable efficiency to a thin-film device promotes the idea that a significant cost reduction of the manufactured device can be achieved by fabricating vertically aligned nanorod or nanotube arrays for solar energy conversion. The use of any promising technology for solar energy conversion should strike a balance between lowering the systems costs, meeting the demands for high efficiency and promising capability for large-scale fabrication with minimal cost. The protocols reported here attempt to find that balance by delivering high-efficiency nanowire solar cells that are amenable for widespread deployment in a cost-effective way. Since electrodeposition is a simple, reproducible and scalable technique amenable

to deposition of a large variety of materials, the PatED process can be very significant for solar energy research as it can deliver nanorod and nanotube arrays of even complex photovoltaic materials like the ternary/quaternary chalcogenides as well as the recently discovered perovskite solar cells.⁴² The soft matrix of polymer present in the fabricated device also makes the whole composite less rigid and hence the entire nanodevice can be grown on either rigid or flexible substrates, which is an added advantage of the described protocol.

ACKNOWLEDGEMENTS

The authors would like to acknowledge the Materials Research Center at Missouri S&T and the UM Research Board for financial support.

REFERENCES

1. Darling, S. B.; Fengqi, Y. The case for organic photovoltaics. *RSC Advances* **2013**, 3, 17633–17648.
2. Tao, M. Inorganic photovoltaic solar cells: silicon and beyond. *The Electrochemical Society Interface* **2008**, 17 (4), 30–35.
3. Romeo, A.; Terheggen, M.; Abou-Ras, D., et al. Development of thin-film Cu(In,Ga)Se₂ and CdTe solar cells. *Progress in Photovoltaics: Research and Applications* **2004**, 12 (2–3), 93–111.
4. Ward, J. S.; Ramanathan, K.; Hasoon, F. S., et al. A 21.5% efficient Cu(In,Ga)Se₂ thin-film concentrator solar cell. *Progress in Photovoltaics: Research and Applications* **2002**, 10 (1), 41–46.
5. Golgovici, F.; Visan, T. Electrodeposition Behaviour of Cadmium Telluride from Choline Chloride-Urea Ionic Liquids. *Chalcogenide Letters* **2012**, 9 (4), 165–174.

6. Lincot, D. Electrodeposition of semiconductors. *Thin Solid Films* **2005**, 487 (1–2), 40–48.
7. Kamat, P. V. Quantum Dot Solar Cells. The Next Big Thing in Photovoltaics. *Journal of Physical Chemistry Letters* **2013**, 4 (6), 908–918.
8. Huynh, W. U.; Dittmer, J. J.; Alivisatos, A. P. Hybrid nanorod-polymer solar cells. *Science* **2002**, 295, 2425–2427.
9. Garnett, E.; Yang, P. Light trapping in silicon nanowire solar cells. *Nano Letters* **2010**, 10 (3), 1082–1087.
10. Tena-Zaera, R.; Ryan, M. A.; Katty, A., et al. Fabrication and characterization of ZnO nanowires/CdSe/CuSCN eta-solar cell. *Comptes Rendus Chimie* **2006**, 9 (5–6), 717–729.
11. Weil, B. D.; Connor, S. T.; Cui, Y. CuInS₂ solar cells by air-stable ink rolling. *Journal of the American Chemical Society* **2010**, 132 (19), 6642–6643.
12. Wallentin, J.; Anttu, N.; Asoli, D., et al. InP nanowire array solar cells achieving 13.8% efficiency by exceeding the ray optics limit. *Science* **2013**, 339 (6123), 1057–1060.
13. Tajik, N.; Peng, Z.; Kuyanov, P.; LaPierre, R. R. Sulfur passivation and contact methods for GaAs nanowire solar cells. *Nanotechnology* **2011**, 22 (22), 225402.
14. Mishra, S.; Nath, M. Growth of vertically aligned CdTe nanorod arrays through patterned electrodeposition. *Nano Energy* **2013**, 2 (6), 1207–1213.
15. Romeo, N.; Bosio, A.; Canevari, V.; Podestà, A. Recent progress on CdTe/CdS thin film solar cells. *Solar Energy* **2004**, 77 (6), 795–801.
16. Tsakalakos, L.; Balch, J.; Fronheiser, J., et al. Silicon nanowire solar cells. *Applied Physics Letters* **2007**, 91 (23), 233117.
17. Law, M.; Greene, L. E.; Johnson, J. C.; Saykally, R.; Yang, P. Nanowire dye-sensitized solar cells. *Nature Materials* **2005**, 4 (6), 455–459.
18. Zubía, D.; López, C.; Rodríguez, M., et al. Ordered CdTe/Cds arrays for high-performance solar cells. *Journal of Electronic Materials* **2007**, 36 (12), 1599–1603.
19. Dongsheng, X.; Yuguo, G.; Dapeng, Y. Highly ordered and well-oriented single-crystal CdTe nanowire arrays by direct-current electrodeposition. *Journal of Materials Research* **2002**, 17 (7), 1711–1714.

20. Britt, J.; Ferekides, C. Thin-film CdS/CdTe solar cell with 15.8% efficiency. *Applied Physics Letters* **1993**, 62 (22), 2851–2852.
21. Yang, P.; Yan, H.; Mao, S., et al. Controlled growth of ZnO nanowires and their optical properties. *Advanced Functional Materials* **2002**, 12 (5), 323–331.
22. Zhao, A. W.; Meng, G. W.; Zhang, L. D., et al. Electrochemical synthesis of ordered CdTe nanowire arrays. *Applied Physics A* **2003**, 76 (4), 537–539.
23. Sima, M.; Enculescu, I.; Trautmann, C.; Neumann, R. Electrodeposition of CdTe nanorods in ion track membranes. *Journal of Optoelectronics and Advanced Materials* **2004**, 6 (1), 121–125.
24. Greeneich, J. S. Developer Characteristics of Poly-(Methyl Methacrylate) Electron Resist. *Journal of the Electrochemical Society* **1975**, 122 (7), 970–976.
25. Ferekides, C.; Britt, J. CdTe solar cells with efficiencies over 15%. *Solar Energy Materials and Solar Cells* **1994**, 35, 255–262.
26. Panicker, M. P. R.; Knaster, M.; Kroger, F. A. Cathodic Deposition of CdTe from Aqueous Electrolytes. *Journal of the Electrochemical Society* **1978**, 125, 566–572.
27. Fontana, R. E.; Katine, J.; Rooks, M., et al. E-beam writing: a next-generation lithography approach for thin-film head critical features. *IEEE Transactions on Magnetics* **2002**, 38 (1), 95–100.
28. Grigorescu, A. E.; Hagen, C. W. Resists for sub-20-nm electron beam lithography with a focus on HSQ: state of the art. *Nanotechnology* **2009**, 20 (29), 292001.
29. Wu, W.; Katsnelson, A.; Memis, O. G.; Mohseni, H. A deep sub-wavelength process for the formation of highly uniform arrays of nanoholes and nanopillars. *Nanotechnology* **2007**, 18, 485302.
30. Wu, W.; Dey, D.; Memis, O. G.; Katsnelson, A.; Mohseni, H. Fabrication of Large Area Periodic Nanostructures Using Nanosphere Photolithography. *Nanoscale Research Letters* **2008**, 3, 351–354.
31. Fischer, U. C.; Zingsheim, H. P. Submicroscopic pattern replication with visible light. *Journal of Vacuum Science & Technology* **1981**, 19, 881–885.
32. Deckman, H. W.; Dunsmuir, J. H. Applications of surface textures produced with natural lithography. *Journal of Vacuum Science & Technology B* **1983**, 1, 1109–1112.

33. Hsu, C.-M.; Conner, S. T.; Tang, M. X.; Cui, Y. Wafer-scale silicon nanopillars and nanocones by Langmuir-Blodgett assembly and etching. *Applied Physics Letters* **2008**, 93, 133109.
34. Heifetz, A.; Kong, S.-C.; Sahakian, A. V.; Taflove, A.; Backman, V. Photonic Nanojets. *Journal of Computational and Theoretical Nanoscience* **2009**, 6, 1979–1992.
35. Lecler, S.; Takakura, Y.; Meyrueis, P. Properties of a three-dimensional photonic jet. *Optics Letters* 2005, 30, 2641–2643.
36. Pan, H.; Hwang, D. J.; Ko, S. H., et al. High-Throughput Near-Field Optical Nanoprocessing of Solution-Deposited Nanoparticles. *Small* **2010**, 6 (16), 1812–1821.
37. Li, H.; Wu, N. A large-area nanoscale gold hemisphere pattern as a nanoelectrode array. *Nanotechnology* **2008**, 19 (27), 275301.
38. Miyake, M.; Murase, K.; Hirato, T.; Awakura, Y. Electrical properties of CdTe layers electrodeposited from ammoniacal basic electrolytes. *Journal of the Electrochemical Society* **2003**, 150 (6), C413–C419.
39. Fan, Z.; Ruebusch, D. J.; Rathore, A. A., et al. Challenges and prospects of nanopillar-based solar cells. *Nano Research* **2009**, 2 (11), 829–843.
40. Wang, X.; Li, G.; Zhu, H., et al. Vertically aligned CdTe nanotube arrays on indium tin oxide for visible-light-driven photocatalysis. *Applied Catalysis B: Environmental* **2014**, 147, 17–21.
41. Regonini, D.; Bowen, C. R.; Jaroenworarluck, A.; Stevens, R. A review of growth mechanism, structure and crystallinity of anodized TiO₂ nanotubes. *Materials Science and Engineering Reports* **2013**, 74 (12), 377–406.
42. Liu, M.; Johnston, M. B.; Snaith, H. J. Efficient planar heterojunction perovskite solar cells by vapour deposition. *Nature* **2013**, 501, 395–398.

II. FABRICATION OF CdTe NANOROD ARRAYS OVER LARGE AREA THROUGH PATTERNED ELECTRODEPOSITION FOR EFFICIENT SOLAR ENERGY CONVERSION

Solar Energy Materials and Solar Cells, 133 (2015): 260-267

Wipula P.R. Liyanage ^a, Jacob S. Wilson ^b, Edward C. Kinzel ^b, Brandon K. Durant ^c, Manashi Nath ^{a,*}

^a Department of Chemistry, Missouri University of Science and Technology, 400W 11th Street, Rolla, MO 65409, USA

*e-mail: nathm@mst.edu

^b Department of Mechanical and Aerospace Engineering, Missouri University of Science and Technology, 400W 13th Street, Rolla, MO 65409, USA

^c Department of Chemistry, University of Wyoming, 1000 E. University Ave, Laramie, WY 82071, USA

KEYWORDS: CdTe nanorods, Solar cells, Patterned growth, Nanorod arrays, Photovoltaic

ABSTRACT

Development of solar energy conversion devices based on nano-fabrication techniques is the key to next generation photovoltaics. However, low throughput and complicated production procedures have limited their emergence at commercially relevant scales. In this article we report an inexpensive, high-throughput, versatile and reproducible technique for fabrication of vertically aligned CdTe nanorod arrays with coverage over a significantly large area through selective electrodeposition (PatED) on lithographically patterned nanoelectrodes. The nanoelectrodes are patterned using the Nanosphere Photolithography (NPL) technique which uses size-controlled polystyrene

spheres as microlenses to focus light into photonic jets on an underlying photoresist. The nanorod diameter and pitch could be controlled through optimization of the NPL process. This generalized technique provides a way for production of wafer-scale nanorod arrays on conducting surfaces for solar energy conversion. Observed photocurrent density from the nanorod device is more than two times higher than thin films fabricated under similar conditions, in spite of actual coverage for the nanorod device being ~12% compared to the thin film. In addition to improved photocurrent generation, reduced material consumption due to enhanced effectiveness at lower coverage and simplicity of the fabrication technique makes this process ideal for the cost-effective production of high efficiency solar cells at commercial scale.

1. INTRODUCTION

In today's solar energy research, single crystal and polycrystalline Si solar cells dominate the world solar cell production. The last 50 years have seen the development of commercial silicon photovoltaics which can convert sunlight into electricity at efficiencies around 20% and provide the most feasible carbon-neutral route to displacing terawatts (TW) of nonrenewable power consumed worldwide [1]. However, despite falling costs large scale deployment of Si based solar cells is still not economically viable. The reason is that the energy payback time for their production is much longer than that for thin film solar cells which limits their productions at larger scales. On the other hand, several inorganic compounds, especially chalcogenides, have shown promise as photovoltaic materials with a band gap suitable for absorbing in the solar absorption

region. Of these materials, binary chalcogenides such as CdTe, CdSe, ternary compounds (CuInSe₂ [CISE], CuGaSe₂, CuInS₂ [CIS]) and quaternary compounds (Cu(In_{1-x}Ga_x)Se₂ [CIGS], CuIn(S_{e1-x}S_x)₂) have shown promise to outperform Si for efficient power generation owing to their outstanding electro-optical properties [2–7]. Very recently First Solar reported a record high efficiency of 20.4% for CdTe photovoltaic solar cell which beat the previous record of 19.6% conversion efficiency set by GE Global Research [8].

Another aspect of solar energy research depends on the morphology dependence of the solar-to-energy conversion efficiency. For the photovoltaic devices, recent advances in research has shown that increasing the aspect ratio of the photovoltaic material (i.e. the absorber) increases efficiency of the device and in that respect nanowires and nanorods have gained renewed interest [9–11]. High-aspect ratio (length/diameter) nanowires provide sufficient thickness of the absorber layer to obtain good optical absorption while simultaneously minimizing collection lengths for excited carriers in a direction normal to the light absorption [12,13], thereby, increasing the effectiveness of the photovoltaic device. The columnar grain structure of the absorber material also works in favor of increasing the solar cell efficiency by facilitating carrier collection and transport and minimizing loss due to grain boundary scattering and recombination. Additionally, semiconducting nanowire arrays have been shown to have low reflective losses compared to planar semiconductors leading to higher optical absorption. It has been predicted that nanometric geometry might also play a constructive role in increasing the effectiveness of the photovoltaic device merely by increasing the surface area and providing an unhindered transport path [9–11]. Accordingly, ordered arrays of silicon nanowires increase the path length of incident solar radiation by up to a

factor of 73 [14]. Recently there have been some very encouraging reports of increased efficiency in nanowire solar cells constructed with the pnictides, InP and GaAs semiconductors [15,16]. These reports claim that these nanowire solar cells can even beat the Shockley-Queisser limit with the nanowires acting as solar concentrators. One of the biggest advantages of using nanowires in lieu of planar films is that the higher surface area in the nanowires significantly reduces the use of expensive semiconducting materials thereby drastically decreasing the cost of raw materials. This is indeed significant since with even a slight increase in efficiency of the solar cell, in the long run, it will lead to a reduction in the functional cost of the module. With the InP nanowire arrays it was observed that even with a very small coverage (12%), photocurrent obtained was better than a conventional thin film [15]. In fact, the optimal coverage with the nanowires was determined to be 10–15%. This behavior has been reproduced with the GaAs nanowire arrays also [16].

Although conceptually the photovoltaic nanowire arrays seem very attractive for solar cells, the construction of such complex architectures from the nanoscale building blocks by the bottom-up synthesis technique is extremely challenging. Among the most common methods to grow ordered arrays of nanowires, the use of porous hard templates such as anodic aluminum oxide (AAO) is very prevalent [17]. Growth inside AAO templates produces assembled arrays of monodisperse nanowires of uniform composition, however, it suffers from major drawbacks one of them being template removal which requires etching of the alumina in a highly basic (NaOH) or acidic solution. Most inorganic compounds such as the chalcogenides (e.g. CdTe, CuInSe₂ etc.), are very susceptible to decomposition and hydrolysis under such basic conditions thereby

leading to compositional degradation of the nanowires which affects its photovoltaic performance. In this article we report a very simple, reproducible and cost-effective technique to grow CdTe nanorod arrays over a large area through patterned electrodeposition (PatED) on nanoelectrodes created through nanosphere photolithography (NPL). These nanorod arrays were characterized through photoelectrochemical measurements in liquid junction electrolytes which have the advantages of being conformal to the nanostructures, non-destructive and allow access to the junction to investigate the effects of surface treatments. A low-intensity green laser was used to illuminate the device whereby, the vertically ordered nanorod arrays exhibit a photocurrent density twice as higher as that obtained from a film-like morphology electrodeposited under similar conditions. Although there are reports for synthesis of CdTe nanowire arrays [18–21], electrodeposition of CdTe thin films [22,23], VLS growth of nanowires through chemical vapor deposition [24,25], seeded growth process [26] and close space sublimation [20,27] some of these methods are not economically viable due to low throughput or the use of hard templates such as AAO, which seriously thwarts the widespread application of this potentially transformative photovoltaic material. The protocol described in this article produces monodisperse nanorod arrays over close-to-industrial length scales through one-step electrodeposition process, which is very cost-effective and reproducible. Moreover, the generalized protocol reported here is independent of the nanorod composition and ideally can be extrapolated to grow nanorod arrays of other solar cell materials as well including the ternary and quaternary chalcogenides.

2. MATERIAL & METHODS

2.1. MATERIALS

ITO coated conducting glass substrates used for nanowire growth were purchased from Sigma Aldrich and had a surface resistivity of $60 \Omega/\text{sq}$. Electrodeposition was performed with IvumStat potentiostat. S-1805 purchased from Microchem was used as the photoresist. Chemicals used for lithography and electrodeposition, i.e. Triton X100 (laboratory grade), CdSO_4 (>99% purity), TeO_2 (>99% purity), H_2SO_4 , were used as purchased without further purification. Size-selected polystyrene microspheres (1.7 μm nominal diameter) were purchased from Bangs Laboratories.

2.2. METHODS

The nanorod arrays for this study was grown by patterned electrodeposition (PatED) on ITO coated conducting glass substrates, whereby, the growth centers (i.e. nanoelectrodes) were defined through nanosphere photolithography (NPL). The novelty of the technique lies in the fact that most of the polymeric resists used for lithographic techniques including photoresists are electrically insulating, thereby not functioning as an active electrode surface during electrodeposition.

Hence, when patterns are written on the polymeric resist and developed through proper treatment which removes the exposed polymer, holes created in the resist layer exposes the underlying substrate (i.e. nanoelectrode) forming a nanochannel-like geometry where the walls of the channel are formed by the polymeric resist confining the exposed nanoelectrode at the floor of the channel. This concept was utilized for designing

the current protocol, where an electrically conducting ITO layer was chosen as the substrate.

In that case, lithographic patterning will create an arrays of nanoelectrodes (exposed ITO blocks) confined within an insulating polymeric matrix (photoresist). The patterned substrate containing the nanoelectrodes was then connected as cathode in an electrochemical set-up and CdTe was electrodeposited on the confined nanoelectrodes. Figure 1 shows a schematic representation of the PatED process using NPL. This process is similar to using a soft, flexible template and yields very clean deposition. The feasibility of this approach was demonstrated previously by the authors by producing CdTe nanowire arrays on nanoelectrodes created through e-beam lithography (EBL) [17]. However, even though thin nanorods could be produced by the EBL, the major drawback of that is the scalability issue and cost-effectiveness.

Hence, the authors are trying to expand this protocol to other lithographic techniques, especially photolithography, which can create large area patterns in a single step and also uses cheaper fabrication tools thereby increasing the cost effectiveness. In this article, the authors report a unique approach to create the patterned substrates by using polystyrene nanospheres as masks for photolithography, which further simplifies the process without compromising on the quality of the nanorod arrays and device performance. Another interesting feature of the NPL aided electrodeposition process reported by the authors is that the diameter of the nanorods (and nanoelectrodes) could be controlled by varying the UV exposure time and the authors could make the nanoelectrodes as small as 180 nm.

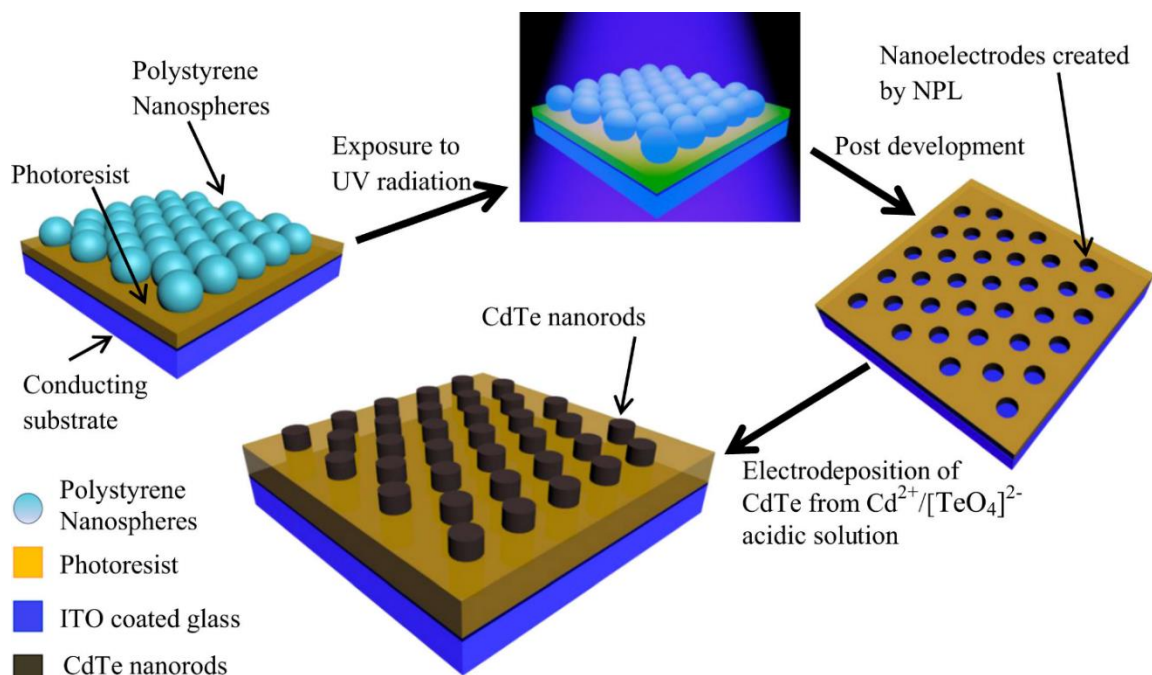


Figure 1. Schematic showing the steps for generating CdTe nanorod arrays. They were fabricated on nano-electrodes through electrodeposition on nano-electrodes defined on ITO coated glass through nanosphere photolithographic process.

2.3. NANOSPHERE PHOTOLITHOGRAPHY (NPL)

Nanosphere Photolithography (NPL) is a rapid parallel fabrication strategy for the patterning of large scale arrays. When UV radiation is incident on a nanosphere of the right index it is focused to a photonic jet [28–30]. When the nanosphere sits in-contact with a layer of photoresist, the photonic jet exposes a sub-wavelength hole. NPL uses a self-assembled array of nanospheres to pattern the photoresist in parallel. This technique was originally developed by H. Mohseni and coworkers [31–34]. The NPL approach is similar to conventional nanosphere lithography, which uses the Hexagonal Close-Packed (HCP) array as a shadow mask for physical processing of the underlying substrate [35,36]. Instead of patterning at the interstitial points in the array, NPL patterns the area

directly beneath each nanosphere. This proves to be advantageous around defects in the lattice which are not exposed because the light is not focused there. The NPL approach can produce HCP arrays of holes in positive tone resists and pillars in negative tone resists, adding to its versatility. The concept is similar to UV lithography, however, instead of using hard masks, the nanospheres themselves act as soft masks leading to selective exposure and pattern definition on the surface of the photoresist. Several different techniques can be used to deposit the microspheres including, spin-coating and the Langmuir-Blodgett method [37]. Spin coating is the simplest approach and produces discrete crystal like domains (shown by the red dotted line in Figure 2a) in the HCP lattice. The current work demonstrates that this technique generates viable nanowire arrays with well-controlled and uniform diameter despite defects in the array.

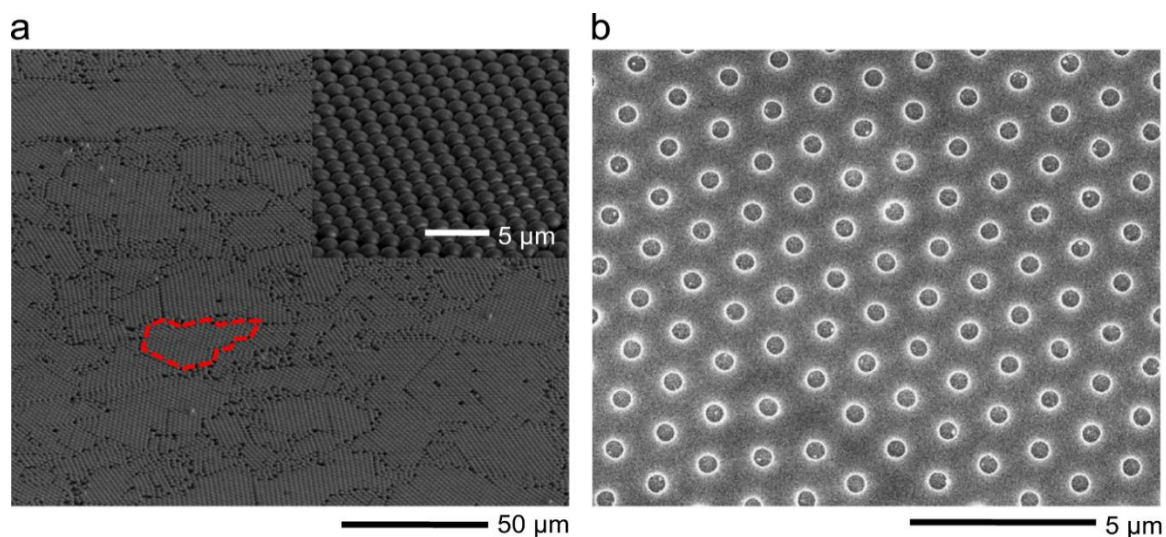


Figure 2. Results of Nanosphere Photolithography. (a) Ordered crystalline domains of polystyrene nanospheres on photoresist. Dotted line shows an individual crystalline domain. Inset shows close-up of crystal domains showing extensive homogeneity. (b) Nanoelectrodes created on the photoresist through NPL after removal of the polystyrene spheres.

2.4. LARGE AREA NANO-ELECTRODE PATTERN DEFINITION BY NPL

Nanosphere Photolithography (NPL) was used to pattern nanoelectrodes onto ITO coated slides. Initially the ITO coated glass substrates were cleaned with piranha solution (a mixture of conc. H_2SO_4 and 30% H_2O_2 in 3:1 v/v ratio) to remove any surface contaminants, especially organic impurities. Following this the substrates were further rinsed in water and methanol followed by drying in air. Spin coating was used to deposit 450 nm of S-1805 (positive tone photoresist) onto the substrates (5000 rpm for 1 min). This was followed by soft-baking at 115 °C for 90 s.

A solution of polystyrene nanospheres was then spin-coated onto the surface. The nanosphere solution was 10% by weight of 1.7 μm (nominal diameter) polystyrene microspheres from Bangs Laboratories which was mixed with a 1:400 Triton X-100 to methanol surfactant solution in 7:1 volume ratio. During spin coating, the nanospheres self-assemble onto the surface of the photoresist to form a hexagonal close-packed lattice. The photoresist was exposed by illuminating the nanospheres with UV light from an i-line mask aligner for 0.7 s at 10 mW/cm^2 . Following exposure the photoresist was developed in MF-319 developer solution for 30 s and rinsed in DI water, before hard baking at 145 °C for 30 min. During the development process the microspheres were washed away along with the exposed photoresist leaving the hole array pattern in the photoresist, with open channels to the ITO layer. Figure 3 depicts patterning the photoresist using NPL, along with a frequency domain finite-element domain method simulation (HFSS) of the electric field at different depths of the photoresist. The diameter of the holes is determined by the exposure time, with holes as small as 130 nm in diameter possible under coherent laser illumination. Controlling the exposure dose

provides control over the diameter of the nanoelectrodes and subsequently on the diameter of the electrodeposited nanorods.

2.5. ELECTRODEPOSITION OF NANOWIRES

The nanowires were grown by electrodeposition on confined nanoelectrodes exposed through the lithographic processing (Figure 1). While generally, electrodeposition is normally performed under a potential sweep, for the present protocol, electrodeposition was performed under constant potential (chronoamperometric) conditions from an electrochemical bath containing a solution of 0.1 M CdSO₄ and 0.001 M solution of TeO₂ using a reported procedure for thin film deposition of CdTe [38,39]. Temperature of the electrolytic bath was maintained at 65 °C while the pH of the electrolytic bath was adjusted to 1.8 using 0.1 M H₂SO₄. Electrodeposition was typically done for 15 s without agitating the solution. Plating current was typically negative and showed an initial decrease which then plateaued with increasing deposition time.

The chronoamperometric conditions were found to be very critical for the growth of columnar nanostructures as opposed to cluster growth obtained under potential sweep [17]. The potential for chronoamperometric deposition was maintained at -0.55 V against Ag/AgCl reference electrode. It was observed that increasing the temperature helped to increase the crystallinity of the deposited CdTe nanorods, however, it also increased the Te content in the nanorods. Accordingly, a bath temperature of 60–70 °C was found to be optimal for the nanorod growth. Following electrodeposition the substrate was washed thoroughly with distilled water in order to remove the excess reactants from the substrate.

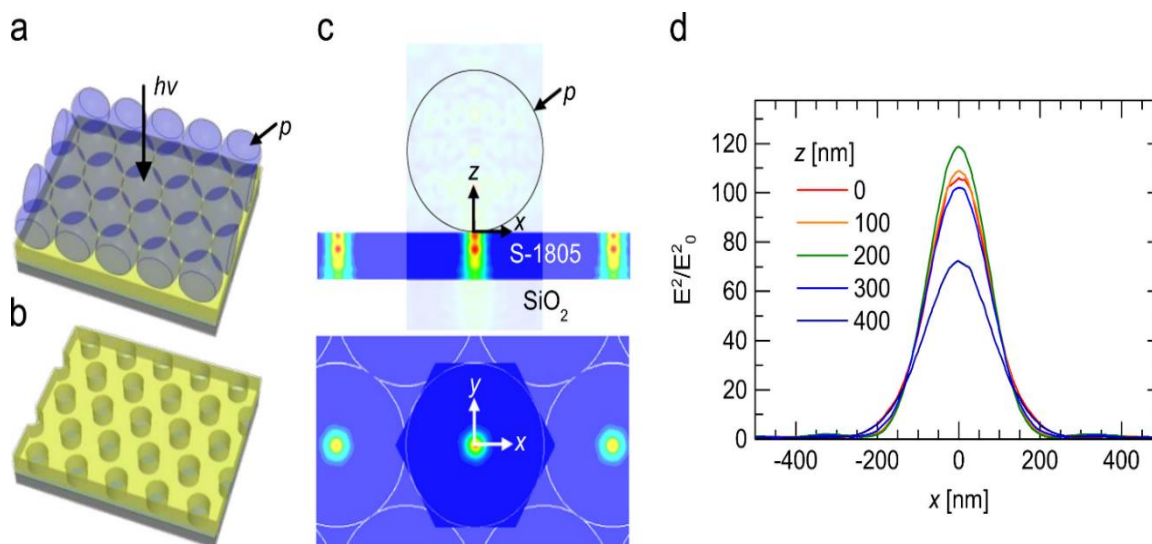


Figure 3. The NPL process. Illustrations of (a) nanospheres self-assembled on photoresist surface and (b) exposed hole array. (c) Simulated electric field intensity inside photoresist and (d) normalized to incident intensity at different depths within photoresist.

2.6. CHARACTERIZATIONS

2.6.1. Powder X-ray diffraction. Powder X-ray diffraction patterns (pxrd) were taken by PANalytical's X'Pert PRO Materials Research Diffractometer (MRD, $\text{CuK}\alpha$ 1.5418 Å). The pxrd was collected at grazing angles in thin film geometry (GI mode with Göbel mirrors).

2.6.2. SEM and EDS. Scanning electron microscopy (SEM) imaging was taken using Helios Nanolab- 600 equipped with Energy Dispersive Spectrometry (EDS) detector (Oxford Instrument) for elemental analysis. Detailed composition analysis was carried out qualitatively and quantitatively using EDS under the line mode as well as under the area mode.

2.6.3. Photoelectrochemical measurements. Photoconductivity was measured through photoelectrochemical measurements performed with IvumStat potentiostat. (Details about the measurement and experimental set-up have been provided in Section 3.2).

3. RESULTS AND DISCUSSION

3.1. MORPHOLOGY OF THE ELECTRODEPOSITED CdTe

As expected, under PatED conditions electrodeposition occurred only on the nanoelectrodes and the CdTe grew as columnar nanorods on the nanoelectrodes whereby lateral growth was restricted by the polymeric resist forming the walls of the nanochannel surrounding the nanoelectrode. Figure 4a shows the FESEM image of top view of the patterned substrate with the CdTe nanorods grown on 400 nm nanoelectrodes. It clearly depicts the immaculate deposition of CdTe only over the nanoelectrodes defined through lithography. The rest of the resist surface looks absolutely clean, thereby, underlining the novelty of this approach. The deposited films adhered strongly to the substrates and had excellent coverage. The most significant advantage of NPL over the e-beam lithography is the scalability of the technique to cover very large area such as a whole silicon wafer of 4 in. diameter at a given time [40]. Hence another notable feature of the PatED process is uniform deposition over an area exceeding several cm² in coverage in a single step. The formation of CdTe on the substrates was further confirmed by pXRD (Figure 4c), which showed that the as-grown CdTe nanorods crystallized the cubic zinc-blende phase structure (JCPDS: 15-0770). The diffraction peak corresponding to (111) lattice planes

were the most visible in the pXRD pattern. Considerable broadening of the (111) diffraction peak indicated that the CdTe nanorods were polycrystalline with individual crystalline domains in the range of 10 nm (as calculated from Scherrer equation) [41]. The pXRD pattern also showed prominent peaks corresponding to ITO from the conducting surface. The enhanced intensity of the ITO diffraction peaks masked some of the CdTe diffraction intensities. High crystallinity from the ITO background also created obstructive scattering noise from the substrate.

It was observed that the intensity of diffraction peaks corresponding to CdTe increased with the increasing deposition temperature leading to better crystallinity of the nanorods [38]. The weakest diffraction lines for CdTe were observed for the nanorods deposited at 50 °C and the strongest lines were observed for the same deposited at 90 °C (see Supplementary Figure S1). Hence, it was concluded that the crystallinity of the nanorods can be improved by increasing the deposition temperature. However, it was also observed that increasing the deposition temperature led to considerable over-growth and cluster formation of the electrodeposited CdTe. Accordingly the most suitable temperature for CdTe nanorod growth was found to be ~60–70 °C in the current set-up.

The composition of the nanorods were also confirmed by EDS which shows the presence of Cd and Te in the nanorods in approximately 1:1.4 ratio with slight excess of Te which indicates that the CdTe nanorods might be p-type [38]. There is very minimal lateral growth of the deposited CdTe under chronoamperometric conditions. Figure 4b shows the elemental mapping of Cd and Te across the nanorods, which proves beyond doubt the presence of Cd and Te exclusively in the nanorods.

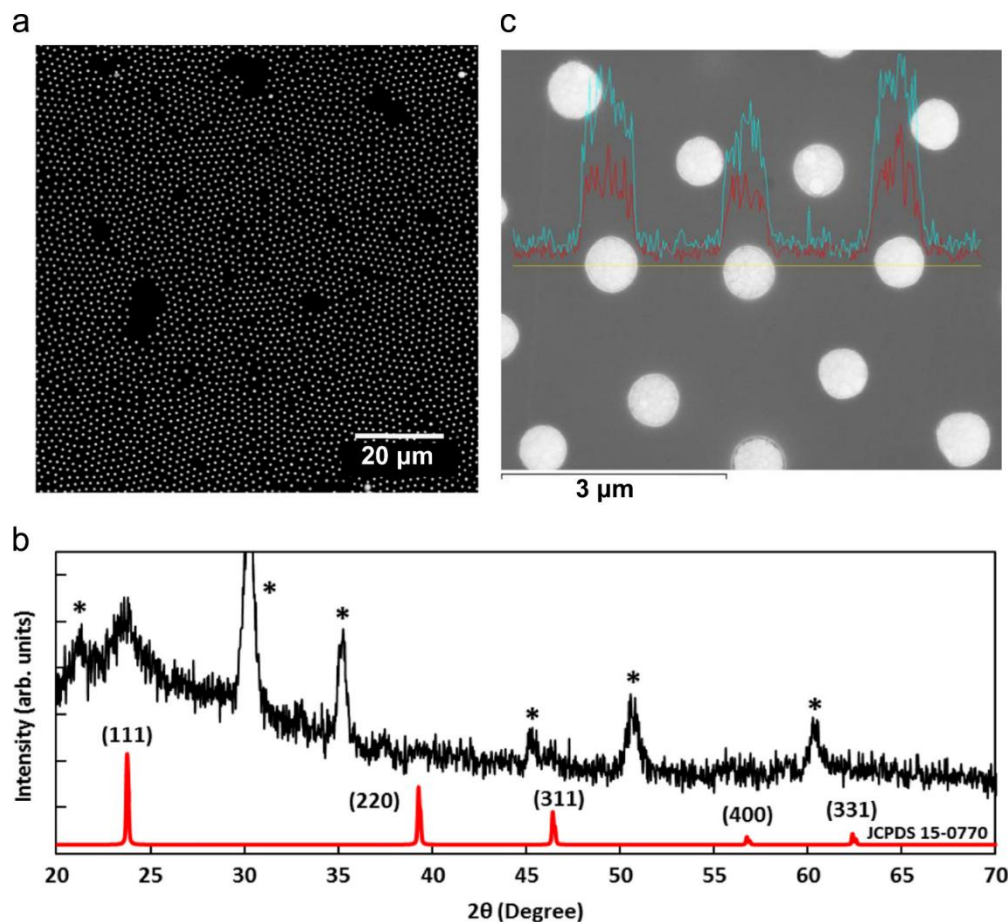


Figure 4. CdTe nanowire arrays. (a) produced on large area through NPL and PatED. (b) Elemental mapping of Cd and Te across the nanorods. (c) Pxd pattern of as-grown CdTe nanorods grown at 80 °C. Red plot shows the standard diffraction pattern for CdTe while asterix (*) indicate the ITO peaks.

The length of the nanorods could be varied by varying the thickness of the photoresist, while the diameter could be controlled through fine-tuning the nanoelectrode dimension. Another notable feature is that since the nanoelectrodes inherently pack in a HCP array reminiscent of the close-packing of the nanospheres, the resulting nanorods also show hexagonal close packing which is the most efficient way of packing individual units in a given volume. The nanorods grown by the chronoamperometric deposition exhibited similar stoichiometry and uniform aspect ratio across the entire pattern. This is

of huge technological importance since, the properties of the nanomaterials are very much size-dependent and the effectiveness of the nanodevice rests on the monodispersity of the functional nano-structures in terms of size and morphology. It is very difficult to grow nanorods of exact same diameter and length by non-directed growth strategies. This simple approach outlined here was able to produce nanorods with uniform aspect ratio over $4 \times 4 \text{ cm}^2$ area as shown in the SEM images. The diameters of these nanowires are expected to affect the properties especially related to the solar energy absorption and carrier mobility.

The protocol described above provides the opportunity to control the aspect ratio of the nanorods through controlling the nanoelectrode diameter and thickness of the polymeric resist. The nanoelectrodes diameter could be varied by altering the exposure time during NPL. The thickness of polymeric resist on the other hand, determines the length of the nanorod and the authors have previously observed that with EBL, increasing the resist thickness to about $1 \text{ }\mu\text{m}$ yielded micrometer long nanowires [17]. Other factors such as nanorod packing density and nanorod-electrode interface can also affect the device performance and the nanowire arrays fabricated by this method can be easily manipulated to study above-mentioned dependencies and lead to formulation of a better efficiency device. Hence the method outlined here can actually deliver nanorod arrays for practical usage.

3.2. PHOTOELECTROCHEMICAL RESPONSE MEASUREMENTS

Photoelectrochemical characterization of the CdTe nanorods arrays were obtained by illuminating with a green Nd-YAG laser operating at 532 nm , where the light intensity

was $\sim 45 \text{ mWcm}^{-2}$ as measured by a powermeter. The PEC measurements were done in a three-cell electrode set-up with Pt-wire and Ag/AgCl as the counter and reference electrodes, respectively. An aqueous $0.1 \text{ M Eu}(\text{NO}_3)_3 \cdot 6\text{H}_2\text{O}$ solution ($\text{pH}=3$), which acts as a redox mediator and electron scavenger was used as the redox electrolyte. The laser beam was chopped at regular intervals to assess the current under illuminated and dark conditions. Photoelectrochemical measurements in illuminated and dark conditions were also performed on CdTe thin film on ITO in addition to the CdTe nanorod arrays for comparison. The thickness of the deposited active material (CdTe) was maintained to be the same in both cases by maintaining the same electrodeposition parameters. For the control experiment, a S-1805 coated ITO substrate (blank) was also characterized through PEC measurements to demonstrate that polymeric resist itself does not show appreciable photocurrent under these conditions. The applied potential was varied from 0 V to -0.5 V using linear sweep technique at the scan rate of 0.02 V/s . The resist layer was not removed prior to PEC measurements.

A cathodic photocurrent was obtained from these CdTe nanorod arrays. Figure 5(a) shows the current response obtained under illumination and dark conditions with the fabricated nanorod arrays and Figure 5(b) shows the same response for the fabricated thin film device. From Figure 5(a) it can be seen that the control sample, which does not contain the active material, shows no significant photocurrent under the experimental conditions. Negative photocurrent indicates p-type conductivity of the CdTe nanorod arrays. A total current density of $\sim 240 \mu\text{A cm}^{-2}$ was obtained under 41 mWcm^{-2} front illumination of the CdTe nanorod arrays, while CdTe bulk film showed a current density in the range of $85 \mu\text{Acm}^{-2}$. The photocurrent could be switched on and off by

intermittently shutting off the light source (chopping) approximately at 2 s intervals. The chopped photocurrent obtained from the CdTe nanorod device at an applied bias of -0.3 V has been shown in Figure 5(c) which also shows the stability of the photocurrent against time.

An interesting observation was that the CdTe nanorod arrays exhibited a current density more than twice of that obtained from the bulk-like film. It should also be noted that the coverage of the electrode with the active material was much smaller ($\sim 12\%$) in the nanorod array device as compared to the thin film device. Comparison between electrode coverage with the active photovoltaic material is better represented in Figure 5d which shows a graphical representation of the comparison between the electrodes containing the CdTe film and the nanorod arrays used for photocurrent measurement. In both cases the ITO-coated glass (i.e. the working electrode) was dipped almost halfway into the electrolyte solution to measure the photocurrent and the electrode area is represented by the blue boxes in the Figure. But, while the continuous CdTe film was grown uniformly over an electrode area of approximately $1 \times 0.5 \text{ cm}^2$, the CdTe nanorod arrays were covering an area of $0.12 \times 0.06 \text{ cm}^2$ (combining the orangish circles representing the CdTe nanorods in inset of Figure 5d).

In this nanodevice, average radii of the nanorods were of 310 nm and the array pitch was maintained at 960 nm with an average packing density of $\sim 0.4 \text{ rods}/\mu\text{m}^2$. Hence, the actual area of coverage for the CdTe nanorods would be approximately 1/8th of the CdTe film. This indicates that the CdTe nanorod arrays can generate a photocurrent density as high as CdTe thin film but with less than 10% surface coverage as compared to the film.

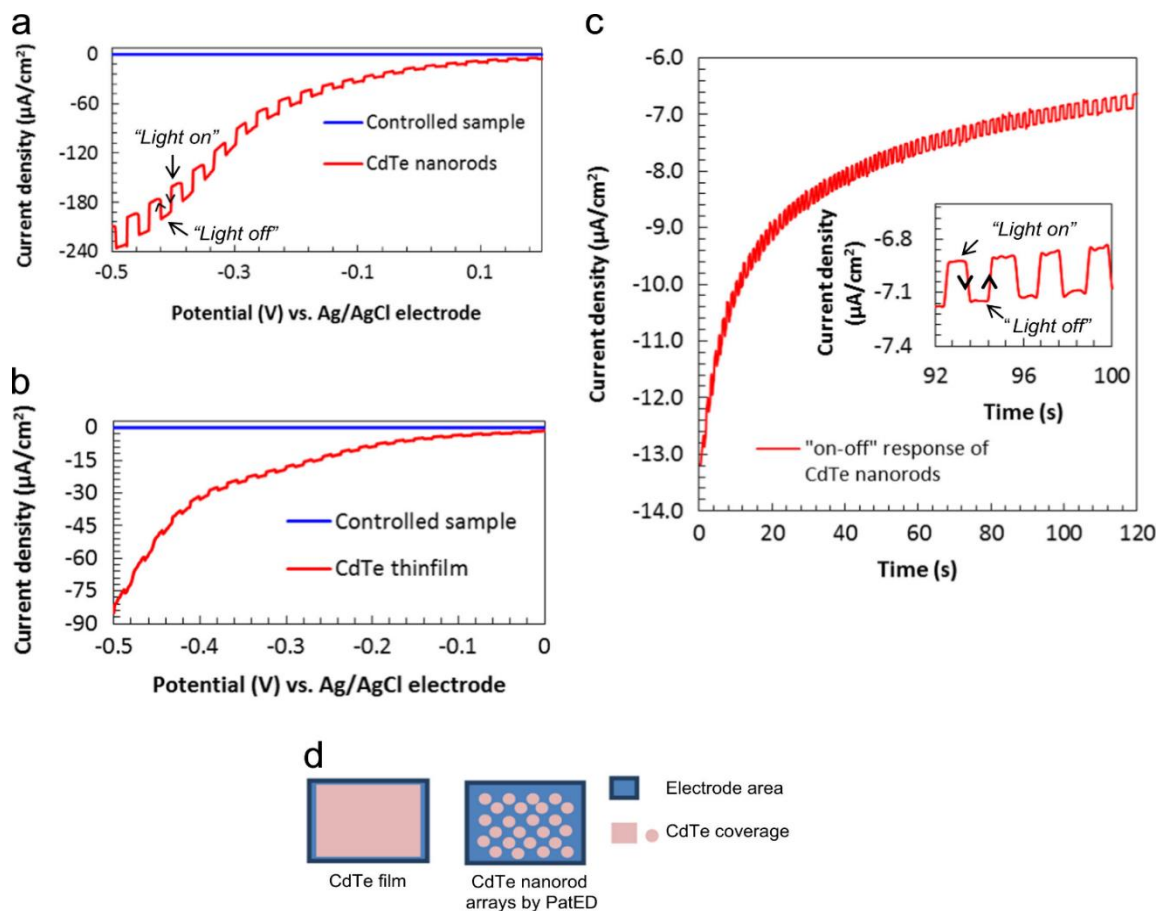


Figure 5. PEC measurements. (a) Photocurrent density under illumination and dark conditions of the nanorod device fabricated from nanosphere photolithography technique. (b) Generated photocurrent of the thin film under similar conditions. (c) Photocurrent generation of the nanorod device when the light source is turned on and off periodically. (d) Comparison between the electrodes containing the CdTe film and the nanorod arrays.

This observation is very similar to the InP nanowire arrays reported recently by Wallentin et al. [15] Previous researchers have reported photocurrent obtained from individual CdTe nanowires contacted by two Au electrodes [42,43]. These photocurrents were mostly in the pA to nA range [41,43] as would be expected from these extremely thin, extremely small current carriers. However, the aligned nanorod arrays grown by this

confined electrodeposition contains large density of nanorods in parallel orientation acting like a parallel series of resistors. This clearly shows the generation of a photocurrent comparable to a thin film can be achieved with a small quantity of the active material.

Low usage of active material to obtain a comparable efficiency to a thin film device promotes the idea that a significant reduction of materials cost can be achieved by fabricating vertically aligned nanorod arrays for solar energy conversion. Another notable feature is that such high efficiencies with low coverage by nanostructures will eventually lead to less usage of expensive semiconducting materials. Three dimensional geometric configuration of vertically aligned nanorod arrays can account for reduced surface optical reflection and enhanced absorption [44].

According to Figure 5 it is clear that the nanorod arrays of CdTe can effectively produce higher photocurrent by virtue of parallel placement of the nanorods, even if the diameter of the individual nanorods might be above the threshold for resonant light trapping. Numerical simulations of the process predict that further reduction of the nanorod diameter will lead to electromagnetic resonances in the nanorods. This leads to enhanced optical absorption with higher carrier collection by the nanorod arrays which can potentially increase the photocurrent generation even further.

This can be augmented by reducing the pitch to increase the density of nanowires per unit area. Both of these factors can increase the device efficiency by orders of magnitude. The authors are currently trying to produce nanorod arrays through this PatED process with thinner nanorods (~150 nm) and study the efficiency for photocurrent generation.

4. CONCLUSION

We have successfully developed a protocol of growing CdTe nanorod arrays over large area on conducting surfaces by simple electrochemical methods coupled with lithographic patterning. The nanorod arrays produced over several cm² area was exceptionally monodisperse in terms of nanorod diameter, length and composition. The photocurrent obtained from the vertically aligned CdTe nanorod arrays grown by this method was better than that obtained from a CdTe film electrodeposited over a similar area thereby underlining the potential of this technique for producing high efficiency miniaturized devices.

This method will be especially useful for making solar cell devices, since, the efficiency of the solar cells nowadays, depends strongly on the materials chosen to absorb the solar radiation and also on the design of the cells. This protocol provides ample opportunity to investigate the effect of each external parameter such as nanorod diameter, array packing density, shape, and morphology on the device performance. The primary requirement for this technique is the embedded nanoelectrodes, which can be obtained by lithography on any conducting surface, including flexible substrates. In principle, any functional material can be grown by electrodeposition in the confined nanoelectrodes. The use of NPL as the patterning tool also amplifies the versatility of the approach. NPL is a very cost-effective, reproducible and scalable technique that can produce uniform patterns in a single step over large area. The combination of NPL and electrodeposition, both of which are cheap methods, makes this protocol very attractive for large scale implementation. The PatEd process would be significantly helpful for growing nanowire

arrays of the ternary and quaternary chalcogenides such as the CIGS, CIS where morphology control is extremely challenging, given the complexity of the systems. The versatility of this approach is currently being tested with other photovoltaic and semiconductor systems. Authors are also trying to measure the spectral response profile for photocurrent generation of the CdTe nanorod arrays.

ACKNOWLEDGEMENTS

MN, WPRL, SM, JW and EK will like to thank Materials Research Center at Missouri S&T for equipment usage. The authors will also like to thank Prof. Bruce Parkinson (University of Wyoming) for help with the photoelectrochemical measurements. MN and EK would like to thank UM research board for supporting this work.

SUPPORTING INFORMATION

Supplementary data associated with this article can be found in the online version at <http://dx.doi.org/10.1016/j.solmat.2014.11.022>.

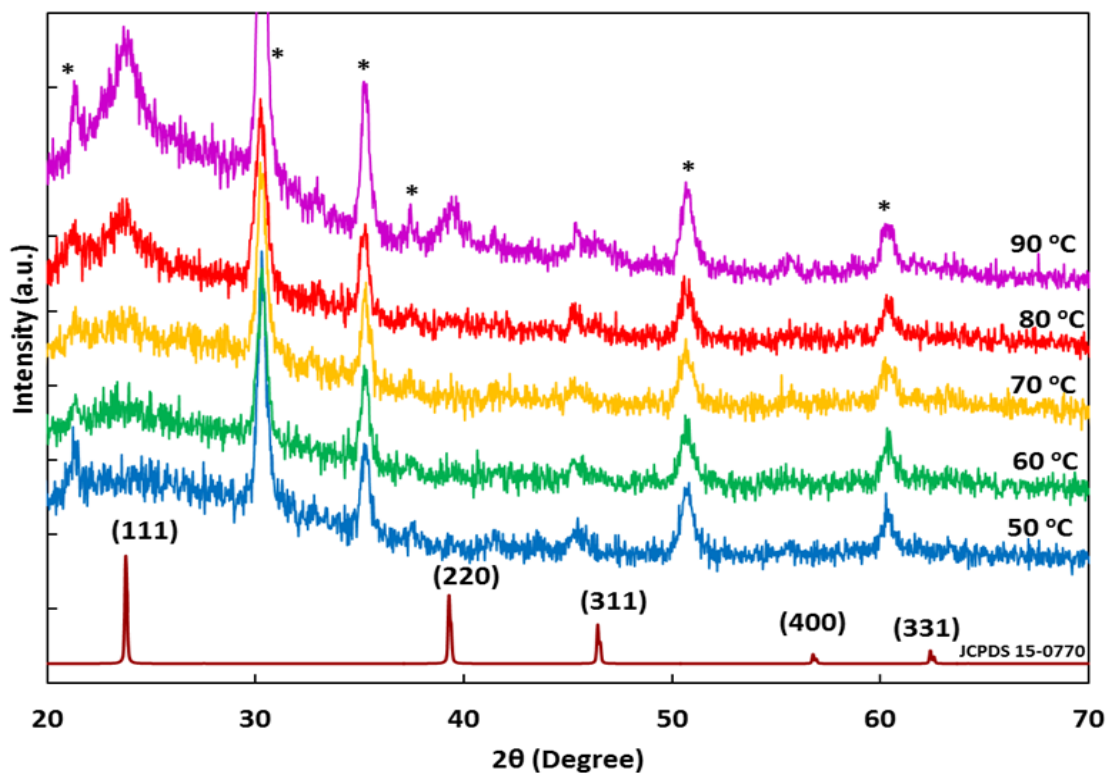


Figure S1. XRD pattern of CdTe nanorods deposited at different temperatures

REFERENCES

1. N.S. Lewis, D.G. Nocera, Powering the planet: chemical challenges in solar energy utilization *Proc. Natl. Acad. Sci. USA*, 103 (2006), 15729-15735.
2. R.W. Birkmire, E. Eser, Polycrystalline thin film solar cells: present status and future potential *Annu. Rev. Mater. Sci.*, 27 (1997), 625-653.
3. X. Wu, High-efficiency polycrystalline CdTe thin-film solar cells, *Sol. Energy*, 77 (2004), 803-814.
4. K.W. Frese, A high-efficiency single-crystal CdSe photoelectrochemical solar cell and an associated loss mechanism, *Appl. Phys. Lett.*, 40 (1982), 275-277.
5. W.S. Chen, J.M. Stewart, R.A. Mickelsen, Chemical deposition and characterization of Cu₃Se₂ and CuSe thin films, *Appl. Phys. Lett.*, 46 (1985), 1095-1098.

6. A. Miguel, M.A. Contreras, B. Egaas, K. Ramanathan, J. Hiltner, A. Swartzlander, F. Hasoon, R. Noufi Progress toward 20% efficiency in Cu(InGa)Se₂ polycrystalline thin-film solar cells, *Prog. Photovolt.: Res. Appl.*, 7 (1999), 311-316.
7. M.A. Green, Thin-film solar cells: review of materials, technologies and commercial status *J. Mater. Sci.: Mater. Electron*, 18 (2007), S15-S19.
8. First Solar Press Release, First solar sets world record for CdTe solar cell efficiency. (<http://investor.firstsolar.com/releases.cfm>) (Accessed 25.02.14).
9. I. Gur, N.A. Fromer, M.L. Geier, A.P. Alivisatos, Air-stable all-inorganic nanocrystal solar cells processed from solution, *Science*, 310 (2005), 462.
10. N. Anttu, H.Q. Xu, Coupling of light into nanowire arrays and subsequent absorption *J. Nanosci. Nanotechnol.*, 10 (2010), 7183-7187.
11. B. Kannan, K. Castelino, A. Majumdar, Design of nanostructured heterojunction polymer photovoltaic devices, *Nano Lett.*, 3 (2003), 1729-1733.
12. B.M. Kayes, H.A. Atwater, N.S. Lewis, Comparison of the device physics principle of planar and radial p-n junction nanorod solar cells, *J. Appl. Phys.*, 97 (2005), 114302-114313.
13. D. Biello, Solar power lightens up with thin film technology, *Sci. Am.* (<http://www.sciam.com/article.cfm?id=solar-power-lightens-up-with-thin-film-cells>) (accessed 25.04.2008).
14. E Garnett, P. Yang, Light trapping in silicon nanowire solar cells, *Nano Lett.*, 10 (2010), 1082-1087.
15. J. Wallentin, N. Anttu, D. Asoli, M. Huffman, I. Aberg, M.H. Magnusson, G. Siefert, P.F. Kailuweit, F. Dimroth, B. Witzigmann, H.Q. Xu, L. Samuelson, K. Depert, M.T. Borgstrom, InP nanowire array solar cells achieving 13.8% efficiency by exceeding the ray optics limit, *Science*, 339 (2013), 1057-1060.
16. P. Krogstrup, H.I. Jorgensen, M. Heiss, O. Demichel, J.V. Holm, M. Aagesen, J. Nygard, A.F. Morral Single nanowire solar cells beyond the Shockley-Queisser limit, *Nat. Photonics* (2013), 10.1038/nphoton.2013.32.
17. S. Mishra, M. Nath, Growth of vertically aligned CdTe nanorod arrays through patterned electrodeposition, *Nano Energ.*, 2 (6) (2013), 1207-1213.
18. M.C. Kum, B.Y. Yoo, Y.W. Rheem, K.N. Bozhilov, W. Chen, A. Mulchandani, N.V. Myung Synthesis and characterization of CdTe nanowire, *Nanotechnology*, 19 (2008), 325711-325718.

19. Y. Ye, L. Dai, T. Sun, L.P. You, R. Zhu, J.Y. Gao, R.M. Peng, D.P. Yu, G.G. Qin, High-quality CdTe Nanowires, Synthesis characterization and application in photoresponsive devices, *J. Appl. Phys.*, 108 (2010), 044301.
20. C. Ferekides, J. Britt, CdTe solar cells with efficiencies over 15%, *Sol. Energy Mater. Sol. Cells*, 35 (1994), 255-262.
21. D. Zubía, C. López, M. Rodríguez, Ordered CdTe/CdS arrays for high-performance solar cells *Electron. Mater.*, 36 (2007), 1599-1603.
22. X. Dongsheng, Y. Yuguo Guo, D. Yu, Highly ordered and well-oriented single-crystal CdTe nanowire arrays by direct-current electrodeposition, *J. Mater. Res.*, 17 (07) (2002), 1711-1714.
23. B.M. Basol, Electrodeposited CdTe and HgCdTe solar cells, *Solar Cells*, 23 (1988), 69-88.
24. D. Cunningham, M. Rubcich, D. Skinner, Cadmium telluride PV module manufacturing at BP Solar, *Prog. Photovolt: Res. Appl.*, 10 (2002), 159-168.
25. Y. Peidong, H. Yan, S. Mao, Controlled growth of ZnO nanowires and their optical properties *Adv. Funct. Mater.*, 12 (5) (2002), 323.
26. A.W. Zhao, G.W. Meng, L.D. Zhang, Electrochemical synthesis of ordered CdTe nanowire arrays *Appl. Phys. A*, 76 (4) (2003), 537-539.
27. M. Sima, I Enculescu, C Trautmann, Electrodeposition of CdTe nanorods in ion track membranes *J. Optoelectron. Adv. Mater.*, 6 (1) (2004), 121-125.
28. A. Heifetz, S.-C. Kong, A.V. Sahakian, A. Taflove, V. Backman, Photonic nanojets, *J. Computational and Theoretical Nanosci.*, 6 (2009), 1979-1992.
29. S. Leeler, Y. Takakura, P. Meyrucis, Properties of a 3D photonic jet, *Opt. Lett.*, 30 (2005), 2651 (2643).
30. H. Pan, D.J. Hwang, S.H. Ko, T.A. Clem, J.M.J. Frechet, D. Bauerle, C.P. Grigoropoulos, High-throughput near-field optical nanoprocessing of solution-deposited nanoparticles, *Small*, 6 (16) (2010), 1812-1821.
31. W. Wu, A. Katsnelson, O.G. Memis, H. Mohseni, A deep sub-wavelength process for the formation of highly uniform arrays of nanoholes and nanopillars, *Nanotechnol.*, 18 (2007), 485302.
32. W. Wu, D. Dey, O.G. Memis, A. Katsnelson, H. Mohseni, A novel self-aligned and maskless process for formation of highly uniform arrays of nanoholes and nanopillars, *Nanoscale Res. Lett.*, 3 (2008), 123.

33. W. Wu, D. Dey, A. Katsnelson, O.G. Memis, H. Mohseni, Large areas of periodic nanoholes perforated in multistacked films produced by lift-off, *J. Vac. Sci. Technol. B*, 26 (2008), 1745-1747.
34. W. Wu, D. Dey, O.G. Memis, A. Katsnelson, H. Mohseni, Fabrication of large area periodic nanostructures using nanosphere photolithography, *Nanoscale Res. Lett.*, 3 (2008), 351-354.
35. U.C. Fischer, H.P. Zingsheim, Submicroscopic pattern replication with visible light, *J. Vac. Sci. Technol.*, 19 (1981), 881-885.
36. H.W. Deckman, J.H. Dunsmuir, Applications of surface textures produced with natural lithography *J. Vac. Sci. Technol. B*, 1 (1983), 1109-1112.
37. C.-M. Hsu, S.T. Conner, M.X. Tank, Y. Cui, Wafer-scale silicon nanopillars and nanocones by Langmuir-Blodgett assembly and etching, *Appl. Phys. Lett.*, 93 (2008), 133109.
38. M.P.R. Panicker, M Knaster, F.A. Kroger, Cathodic deposition of CdTe from aqueous electrolytes *J. Electrochem. Soc.*, 125 (1978), 566-572.
39. B.M. Basol, Electrodeposited CdTe and HgCdTe solar cells, *Solar Cells*, 23 (1988), 69-88.
40. H. Li, N. Wu, A large-area nanoscale gold hemisphere pattern as a nanoelectrode array *Nanotechnol.*, 19 (27) (2008), 275301.
41. A.L. Patterson, The Scherrer formula for X-ray particle size determination, *Phys. Rev.*, 56 (1939), 978-982.
42. M.C. Kum, B.Y. Yoo, Y.W. Rheem, K.N. Bozhilov, W. Chen, A. Mulchandani, N.V. Myung Synthesis and characterization of cadmium telluride nanowire, *Nanotechnol.*, 19 (2008), 325711-325718.
43. Z. Fan, H. Razavi, J.W. Do, A. Moriwaki, O. Ergen, Y.L. Chueh, P.W. Leu, J.C. Ho, T. Takahashi, L.A. Reichertz, S. Neale, K. Yu, M. Wu, J.W. Ager, A. Javey, Three-dimensional nanopillar-array photovoltaics on low-cost and flexible substrates, *Nat. Mater.*, 8 (2009), 648-653.
44. F. Zhiyong, D.J. Ruebusch, A.A. Rathore, Challenges and prospects of nanopillar-based solar cells *Nano Res*, 2 (11) (2009), 829-843.

III. GROWTH OF ORDERED NANOSTRUCTURE ARRAYS INCLUDING NANOTUBES AND NANORODS FOR HIGH EFFICIENCY SOLAR CELLS

ECS Transactions, 66 (40) 1-7 (2015)

Wipula. P. R. Liyanage, Manashi Nath*

Department of Chemistry, Missouri University of Science and Technology, 400W 11th Street, Rolla, MO 65409, USA

*e-mail: nathm@mst.edu

ABSTRACT

A simple and straightforward approach has been described for the fabrication of CdTe nanotube and nanorod arrays with a high degree of precision through confined electrodeposition on lithographically patterned nanoelectrodes. This technique has the potential of growing these nanotube/nanowire arrays with extreme uniformity over a significantly large area. The desired nanoelectrode pattern was defined through electron beam lithography on indium tin oxide coated glass, and electrodeposition of the semiconducting material of interest (CdTe) on the nanoelectrodes produced the nanotubes/nanowires. It is interesting to note that the measured photocurrent density of nanotube device created by this protocol exceeds that obtained from a thin film device fabricated under similar conditions by several orders of magnitude. The ability to fine tune all the physical dimensions and distribution density of the nanostructures, make this method a versatile tool to fabricate and investigate nano-structured photovoltaic devices and study their structure-property relationship. Additionally the ability to create uniform

nano-feature arrays in addition to nanotube/nanorod arrays through one-step electrodeposition makes this protocol unique.

1. INTRODUCTION

Research and development in the field of high efficiency solar energy conversion relies heavily on the fabrication of the photo absorber materials as nanowire or nanotubular architectures, since these morphologies gives better photocurrent output with lese coverage of the active material.¹ High aspect ratio of nanostructures has an added advantage over nanoparticles and thin films since it provides appropriate thickness for light absorption while presenting an unhindered straight path for the transport of excited carriers along the length of the nanostructure.^{2,3} Moreover, in the presence of nanowires or nanorods like architectures, the efficiency achieved by a unit volume of the semiconducting material is increased by improved light absorption, light trapping and carrier collection.

However, fabrication of the nanostructured semiconducting materials as vertically aligned, highly ordered nanowire or nanotubular arrays with precise distribution of size and shape over a defined location is still remains a significant technical challenge. Although there are reported methods to make ordered nanowire arrays like vapor liquid solid (VLS) growth by chemical vapor transport,^{4,5} seeded growth process⁶ and closed-space sublimation,⁷ Most popular procedure for growing arrays of nanowires is by using hard templates like anodized aluminum,^{8,9} however, it suffers from the disadvantage that this rigid template need to be removed using bases or acids to reveal the nanostructures

and that process makes the semiconducting nanostructure susceptible for decomposition and hydrolysis and that can affect the photovoltaic performance of the entire device. On the other hand, shape, as well as the physical dimensions and distribution density of nanostructures cannot be controlled as desired by this method. The simple protocol described in this report produces precise and reproducible results that provide an opportunity to explore the fabrication of ordered nanostructure arrays including nanowires and nanotubes with variable chemical compositions and a variety of nanostructure-electrode interphase to study their effect on the performance of the nanodevices.

We demonstrate this concept using CdTe as the semiconducting material and indium tin oxide (ITO) coated glass as the transparent conducting substrate, where the growth of nanostructures were accomplished by electrodeposition on nanoelectrodes created on ITO coated glass substrate through electron beam lithography (EBL). By small variations of the EBL pattern definition process, arrays of nanorods, nanotubes and other interesting nanofeatures can be achieved.

Electrodeposition of CdTe from aqueous solutions is a well-studied technique because it is not only scalable to larger area but also a well-established industrial process. Both galvanostatic and potentiostatic methods have been utilized to produce CdTe photovoltaic thin films¹⁰ and nanorod arrays.^{11, 12} In this report, the fabrication process was explained and the effectiveness of this technique was demonstrated by the enhancement in photo conversion efficiencies of the fabricated photovoltaic nanotube and nanorod arrays by using this method.

2. EXPERIMENTAL DETAILS

2.1. MATERIALS AND TECHNIQUES

All chemicals used for preparing solutions were of analytical grade. CdSO₄ and TeO₂ were purchased from Sigma Aldrich and used without further purification. Polymethylmethacrylate (PMMA, mol. wt. 450K and 950K, supplied by Microchem, Newton, MA, USA) was used as the insulating e-beam resist. ITO-coated conducting glass substrates were purchased from Sigma Aldrich and had a surface resistance of 60Ω/sq. Electrodeposition was performed with IvumStat potentiostat. Powder X-ray diffraction (PXRD) patterns were taken with PANalytical's X'Pert PRO Materials Research Diffractometer (MRD, CuKα 1.5418 Å). Scanning Electron Microscope (SEM) imaging was taken using Helios NanoLab 600 equipped with energy-dispersive X-Ray spectroscopy (EDS) detector (Oxford Instruments, Abingdon, UK) for elemental analysis. EBL was performed with the in-built lithography facility available with a Helios NanoLab 600 DualBeam FIB microscope. Photoconductivity was measured through Photoelectrochemical (PEC) measurements performed with IvumStat potentiostat. A 400 W Xe lamp operating in UVA range (320–390 nm) with the intensity of 100 mW/cm² was used to illuminate the nanorod device.

2.2. PREPARATION OF SAMPLES BY EBL

For the pattern definition on the ITO substrate by EBL, the e-beam resist was prepared by spin coating two layers of PMMA polymer on ITO coated conducting glass. First PMMA layer (mol. wt. 495K) was spin coated and backed for 3 minutes on a

hotplate at 180°C and allowed to cool to room temperature before coating the second PMMA layer (mol. wt. 950K). Substrate was again baked for 3 minutes on a hotplate at 180°C and allowed to cool to room temperature. As prepared resist layer has a thickness about 300 nm. These PMMA layers are selectively exposed to the electron beam in the EBL process. After that the exposed area of the polymer can be removed by dipping the substrate in MIBK-IPA (1:3) solution for 55 seconds according to a reported procedure,¹³ while unexposed polymer remained intact. During this pattern development process, the underlying ITO layer is exposed through the nanofeatures defined by EBL thus forming nanoelectrode islands on the substrate. During electrodeposition of the semiconducting materials on this substrate, deposition takes place exclusively on the exposed ITO through the nanofeatures while the remaining unexposed polymer acts as a soft mask inhibiting the deposition in the non-patterned areas. The experimental protocol was illustrated in Figure 1.

2.3. ELECTRODEPOSITION OF NANOTUBES/NANORODS

The growth of the nanotubes and nanorods were achieved by electrodeposition on confined nanoelectrodes exposed through the EBL process. IviumStat potentiostat with standard three electrode system was used under constant potential (chronoamperometric) conditions to for the electrodeposition and an electrochemical bath containing a solution of 1.0 M CdSO₄ and 0.001 M TeO₂ was used according to a reported procedure for thin-film deposition of CdTe.^{14,15} The deposition potential was optimum at -0.55V against Ag/AgCl reference electrode. It was seen that when the temperature was increased in the

deposition bath, the crystallinity of the deposit was increased however, Te content of the deposit increases with increasing temperature.

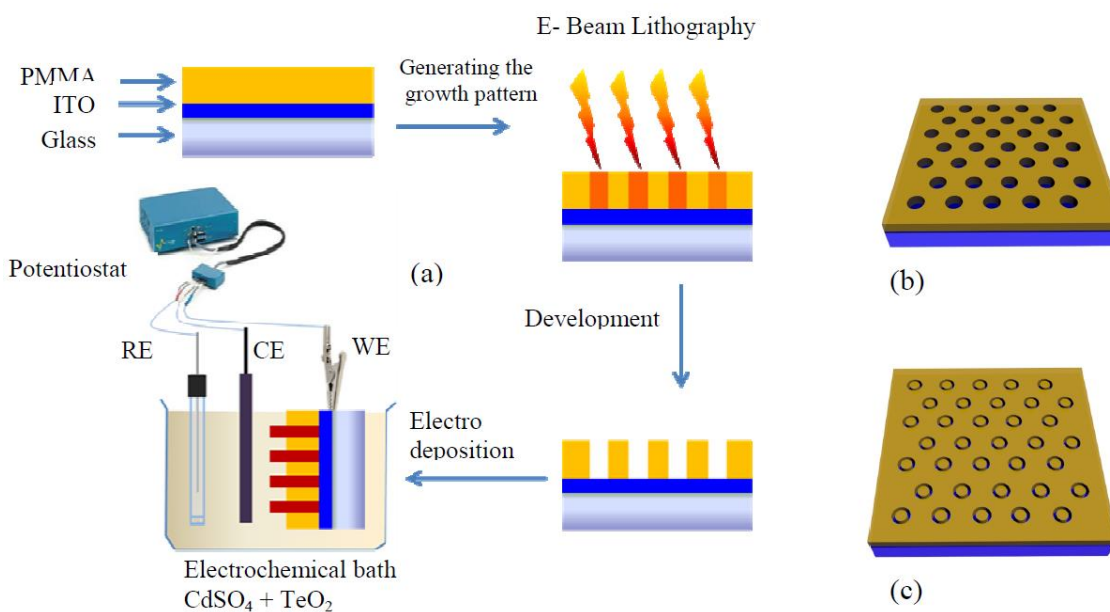


Figure 1. Schematic representation of the EBL process. (a) electrodeposition for generating CdTe nanotube and nanorod arrays on ITO coated conducting glass substrates. RE stands for reference electrode, CE stands for counter electrode and WE stands for working electrode. Representation of prepared substrate for the deposition of (b) nanorod arrays (c) nanotube arrays.

Therefore, a bath temperature of 60 – 70 °C was found to be optimum for the deposition of nanotube and nanorods. In the current process bath temperature was maintained at 65°C while the pH was adjusted to 1.8 using 1 M H₂SO₄. As prepared substrates were rinsed thoroughly after the electrodeposition with distilled water in order to remove the excess reactants from the substrate and dried under a stream of nitrogen in room temperature.

3. RESULTS AND DISCUSSION

3.1. PROPERTIES OF NANOTUBES AND NANORODS

During the electrodeposition, CdTe was deposited only on the nanoelectrodes created by the EBL process. The surrounding polymer acts as an insulating matrix preventing the deposition of the semiconducting material outside of the exposed nanoelectrodes. In addition, the growth of the nanorods or the nanotubes was guided by the polymeric nanochannel surrounding the nanoelectrode and that prevent any lateral growth of the nanorods or nanotubes thus the columnar shape of the nanotube or the nanorods remain unchanged during the growth conditions depending on the thickness of the polymer layer and the deposition time. Rest of the polymer resist remains very clean indicating the novelty of this approach. When the electrodeposited samples were investigated in the SEM, it clearly shows the deposition has only taken place on the nanoelectrodes defined by EBL. Figure 2 shows the top view of the pattern with CdTe nanorod and nanotube arrays. The deposition of CdTe on the substrate was further confirmed by PXRD, which shows that the deposition has taken place in cubic zinc blende crystal structure.

However, at higher temperature deposition is very rapid and that lead to the overgrowth of nanorods and nanotubes outside of the nanochannels which alters the highly ordered nanostructure and hence deposition temperature was maintained at 65 °C. In addition, it also was seen that more tellurium tends to deposit at higher temperatures.

The pxrd pattern also shows prominent peaks of ITO which are coming from the background conducting substrate and the enhanced peak intensity of ITO mask some of

the diffraction peak from CdTe. EDX line scan was performed to confirm the elemental composition of the deposit and that shows Cd and Te on as deposited nanotubes and nanorods with 1: 1.4 ratios with slight excess of tellurium which indicate the nanostructures might be p-type.¹⁵

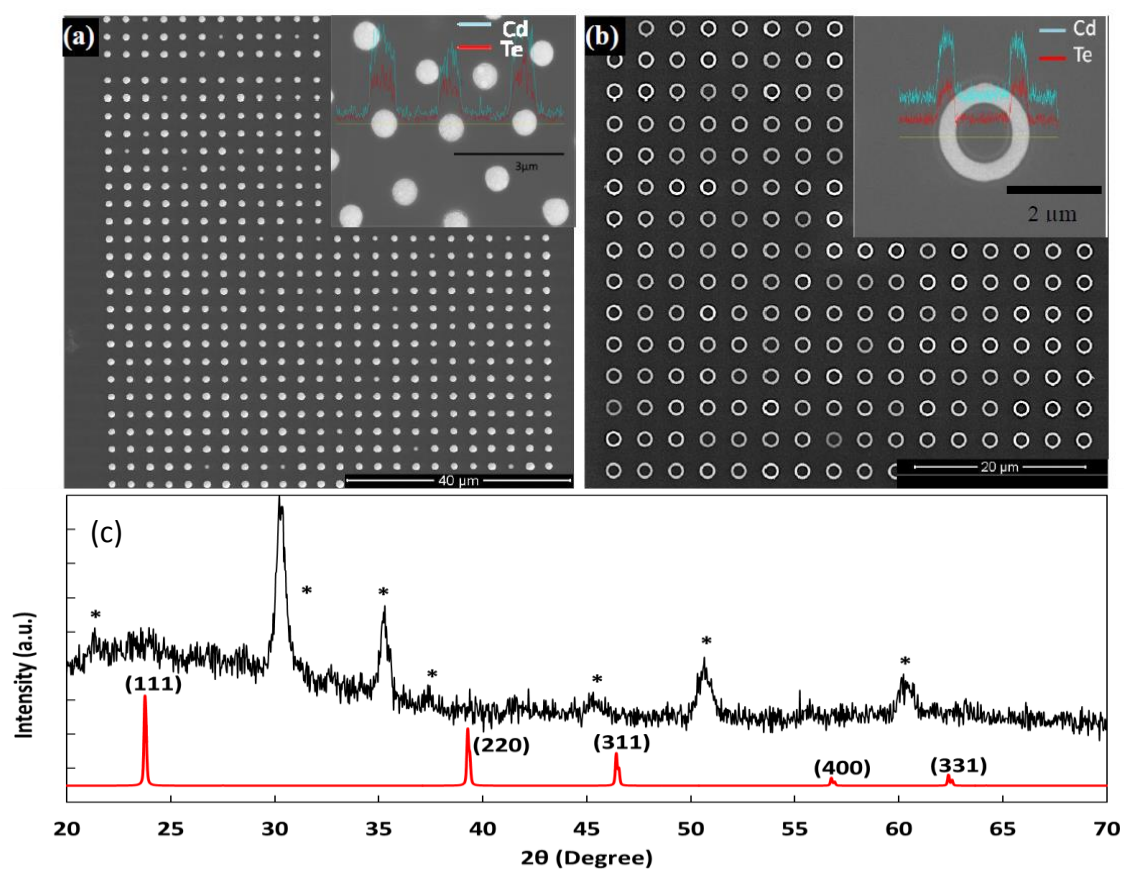


Figure 2. Morphology and crystal structure. SEM image of CdTe (a) nanorod arrays (b) nanotube arrays fabricated by this method. Inset shows the EDX elemental line scan across the nanostructures confirming the presence of Cd and Te in the nanorods and nanotubes, respectively. (c) PXRD pattern of nanorods compared with a standard sample of CdTe. ITO peaks from the background is indicated by an asterisk (*).

The length of the nanotubes or nanorods can be controlled by controlling the thickness of the polymer and also the deposition time while the diameter and wall thickness of nanotubes can be fine-tuned by changing the size of the nanoelectrode defined through EBL process. As grown nanotubes and nanorods shows similar elemental composition and aspect ratio over the entire pattern. In technological point of view, this is an added advantage because the properties of the nanodevice very much depend on the size and shape of the individual functional nanostructures.

3.2. ENHANCED PHOTOELECTROCHEMICAL (PEC) RESPONSE

Generation of the photocurrent was monitored as shown in Figure 3 by photoelectrochemical response measurements of the nanotube and nanorod arrays according to a reported procedure.¹⁷

Three electrode system containing the substrate with nanorod arrays as the working electrode, Ag/AgCl reference electrode and Pt counter electrode was used in a buffer solution of 0.1 M acetic acid, 0.1 M sodium acetate and 0.1 M sodium sulfite and having a pH of 4.6 as the electrolyte medium. The device was illuminated with a 400W Xe lamp operating in UVA range (320–390 nm) with the intensity of 100 mW/cm². To monitor the difference between photocurrent and the dark current the light source was chopped at regular intervals to provide a light on-off environment. Figure 3 shows a comparison of generated photo current from the nanodevices and a thin film device fabricated under similar conditions.

Same measurements were carried out on a thin film of CdTe grown on ITO substrate under similar electrodeposition parameters to obtain a comparison of

photocurrent with the nanodevice. As a controlled experiment, PMMA coated ITO substrate (blank sample) was also used for the measurement of the photocurrent to demonstrate that blank sample generate no noticeable photocurrent under these experimental conditions.

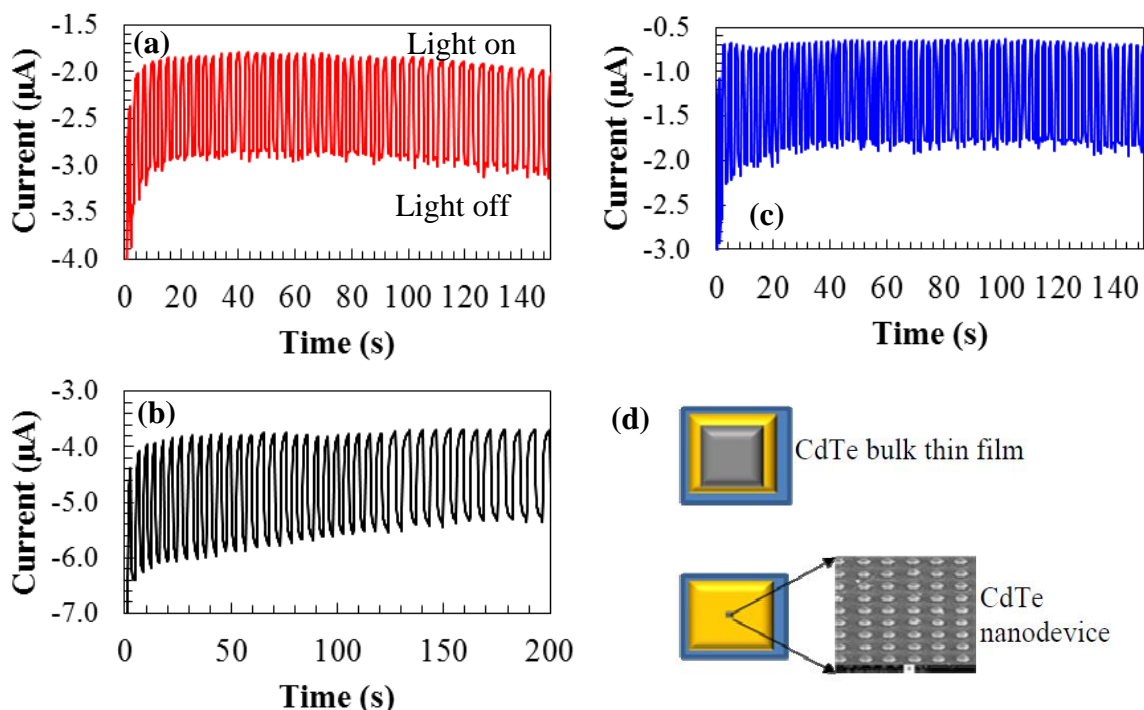


Figure 3. Generated photocurrent at an applied bias of -0.4 V. (a) from the nanotube device (b) nanorod device and (c) thin film device under similar testing conditions. (d) shows a graphical comparison of the area from which the photocurrent was generated. Total area covered by the photoactive material of nanodevice is about 12% compared to the coverage of the thin film.

The negative photocurrents obtained from the devices indicate that the deposited CdTe is p-type conductivity. It was noted that CdTe nanorod arrays showed a photocurrent density more than twice of that obtained from the thin film device besides

the actual coverage of the active material in the nanorod device is much smaller (12%) compared to the thin film device. PEC measurements of the nanotube array device shows that a similar photocurrent to the nanorod device can be achieved with even less area of total coverage compared to the nanorod device. Nanotube arrays will especially be useful for photo conversion due to the larger available surface area compared to nanorod arrays, which can improve photocurrent generation per unit volume of the semiconducting material. The above observation confirms that having larger surface area of nanotubes delivers better efficiency than nanorods per unit volume. However, fabricating such vertically aligned nanotube arrays are very challenging and reports of CdTe or other semiconducting nanotube arrays are very limited. The fabrication of nanotube arrays described in this protocol is a novel concept and it is independent of the material need to be deposited or the conducting substrate. Typically any type of semiconducting material can be electrodeposited on a given conducting substrate using this protocol. The novelty of this method can be appreciated by looking at the cleanliness of the deposit, uniformity of the nanotube diameter and the wall thickness throughout the entire pattern as it was seen in Figure 2(b). These patterns can be generated over a larger area through a sequential EBL process.

Enhanced photocurrent can be attributed to several factors. If the nanorods or nanotubes are below the ray optics limit, significant light absorption can be achieved by resonance light trapping,¹ which can generate a higher photocurrent. Three dimensional geometry of the vertically aligned architecture can also direct to a reduced optical reflection leading to enhanced photo absorption.¹⁸ For thicker nanorods or nanotubes it can be considered as each nanorod or nanotube acts as a resistor and the current output

from a parallel series of resistors can be enhanced according to the Ohm's law. Hence, for vertically aligned thicker nanorod or nanotube arrays current can be amplified even though the photo absorption is not significantly enhanced. The physical dimensions of the CdTe nanorod and nanotube arrays are slightly larger than the threshold limit for resonance light trapping and therefore, most probably the enhancement of the photocurrent is due to the parallel arrangement of the nanostructures in a small space and a higher volume of the photoabsorber. Simulated results predict that further reduction of nanofeature size will lead to electromagnetic resonance in the nanorods and nanotubes. This will enhance photo absorbance and can potentially amplify the photocurrent generation. Authors are currently trying to fabricate thinner nanorod, nanotube and other types of nanostructure arrays with even smaller pitch and study the effect on the generation of the photocurrent.

4. CONCLUSION

We have successfully developed a protocol to fabricate ordered nanostructure arrays including nanotubes and nanorods by electrodeposition on lithographically patterned nanoelectrodes. As fabricated nanorod and nanotube arrays shows highly uniform physical dimensions and elemental composition. The photocurrent generate from the nanorod device is comparable to that of thin film device even though the coverage of the active material in the nanorod device is a fraction of the thin film device. Nanotube device produces a similar current with even lower coverage than that of the nanorod device thereby indicating the potential of this method to fabricate high efficiency

nanodevices. This protocol provide an opportunity to study the effect of the morphology to the photo absorption and photocurrent generation through fine tuning of each physical dimensions such as diameter of nanorod and nanotubes, nanotube wall thickness, the distance between adjacent nanotube or nanorods, packing density of the arrays and shape. The other advantage of this process is that these ordered arrays can be fabricated on any conducting substrate including flexible substrates. Since electrodeposition was employed for the growth of nanorod and nanotube arrays, complex structures like tandem solar cells can be easily achieved through sequential electrodeposition of the material of interest where morphology control is extremely challenging.

ACKNOWLEDGEMENTS

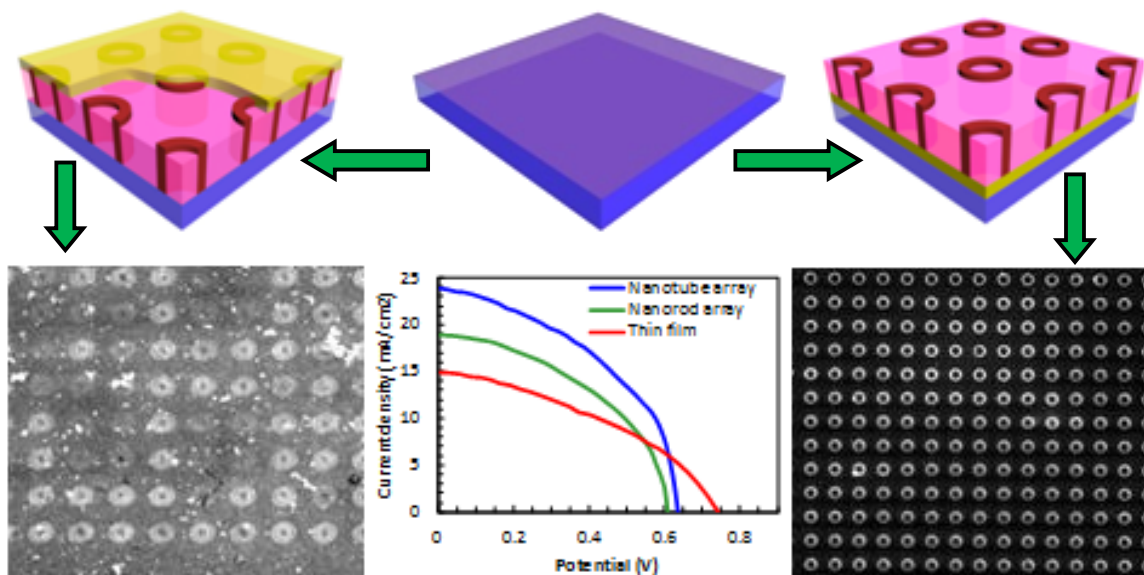
The authors would like to acknowledge the Materials Research Center at Missouri S&T and the UM Research Board for financial support.

REFERENCES

1. J. Wallentin, N. Anttu, D. Asoli, et al. *Science*, **339** (6123), 1057–1060(2013).
2. W. U. Huynh, J. Dittmer and A. P. Alivisatos, *Science*, **295**, 2425–2427(2002).
3. E. Garnett and P. Yang, *Nano Lett.*, **10** (3), 1082–1087 (2010).
4. P. Yang, H. Yan, S. Mao, et al. *Adv. Funct. Mater.*, **12** (5), 323–331(2002).
5. A. W. Zhao, G. W. Meng, L. D. Zhang, et al. *Appl. Phy. A*, **76** (4), 537–539(2003).

6. M. Sima, I. Enculescu, C. Trautmann, et al. *J. Optoelectron. and Adv. Mater.*, **6**(1), 121–125(2004).
7. D. Zubía, C. López, M. Rodríguez, et al. *J. Electronic Mater.*, **36** (12), 1599–1603(2007).
8. S. Dellis, A. Christoulaki, N. Spiliopoulos, et al. *J. Appl. Phy.*, **114**(16), 164308(2013).
9. L. Tsakalakos, J. Balch, J. Fronheiser, et al. *Appl. Phy. Lett.*, **91** (23), 233117(2007).
10. N. Romeo, A. Bosio, V. Canevari, et al. *Sol. Energy*, **77** (6), 795–801(2004).
11. S. Mishra, M. Nath, *Nano Energy*, **2** (6), 1207–1213 (2013).
12. W.P.R. Liyanage, E. C. Kinzel, M. Nath et al. *Sol. Energy Mater. and Sol. Cells*, **133**, 260-267(2015).
13. J. S. Greeneich, *J. Elec. Chem.. Soc.*, **122** (7), 970–976 (1975).
14. C. Ferekides, J. Britt, *Sol. Energy Mater. and Sol. Cells*, **35**, 255–262(1994).
15. M. P. R. Panicker, M. Knaster, F. A. Kroger, *J. Elec.chem. Soc.*, **125**, 566–572(1978).
16. A.L. Patterson, *Phys. Rev.*, **56**, 978–982(1939).
17. M. Miyake, K. Murase, T. Hirato, et al. *J. Elec.chem. Soc.*, **150** (6), C413–C419(2003).
18. Z. Fan, D. J. Ruebusch, A. A. Rathore, et al. *Nano Res.*, **2** (11), 829–843(2009).

IV. CdS–CdTe HETEROJUNCTION NANOTUBE ARRAYS FOR EFFICIENT SOLAR ENERGY CONVERSION



Journal of Materials Chemistry A, 2016, 4, 14637-14648

W. P. R. Liyanage and M. Nath*

Department of Chemistry, Missouri University of Science and Technology, 400W 11th Street, Rolla, MO 65409, USA

*e-mail: nathm@mst.edu

† Electronic supplementary information (ESI) available: SEM images of longer tubes grown through pulsed electrodeposition and showing changes in tube dimension by controlling lithographic parameters; XPS spectra of Cd and Te; electroimpedance spectroscopy; optical spectroscopy; chronoamperometry studies; PXRD of CdTe layer.

See DOI: 10.1039/c6ta03572h

ABSTRACT

We have established a protocol for the fabrication of CdTe–CdS, lateral p–n junction nanotube arrays, configured akin to either substrate or superstrate geometries. The protocol involves confined electrodeposition of p-type CdTe on lithographically patterned nanoelectrodes defined on conducting substrates, where the substrate surface has been coated with the n-type CdS layer deposited through chemical bath deposition. Post-lithography the underlying CdS layer could be revealed at selective positions, which is the key factor in defining the nature of the formed CdS–CdTe heterojunction. The aspect ratio of the CdTe nanotubes could be controlled by doing pulsed electrodeposition as well as altering the thickness of the polymeric resist used for lithography and tuning the diameter of the nanoelectrodes. Photoelectrochemical analysis in a liquid junction electrolyte has been performed to characterize the photoconductivity response of nanotube arrays. Both the substrate and superstrate p–n junction arrangements of CdS–CdTe nanotube arrays showed photocurrent comparable to that obtained from a bulk film covering a much larger surface area compared to the nanodevice. Typically it was observed that for the heterojunction CdS–CdTe nanotube device less than 10% coverage with the photoabsorber layer was required compared to the bulk film, in order to produce the same amount of photocurrent. Specifically, the photoconversion efficiency was increased by 50% on changing the morphology from bulk film (6.3%) to tubular (9.6%). Additionally, the advantage of the “holey” architecture in the photoabsorber layer was very evident as the photocurrent obtained from the nanotube arrays was larger than that obtained from the nanorod arrays electrodeposited under similar conditions. These

observation suggest that these nanotube architectures combining the advantages of both the “holey” and nanopillar geometries might lead to an optimal nanostructured solar cell. The growth method of the nanotube arrays is simple and versatile which can be readily adapted to produce complex photoabsorber layers including the ternary and quaternary chalcogenides.

1. INTRODUCTION

Over the past several decades solar energy research has led to numerous promising discoveries, efficiencies and expectations. Some of these promising materials include the p–n type heterojunction solar cells like CdS–CdTe thin film solar cells, where n-type CdS is applied as a window layer and p-type CdTe functions as an absorber layer. These CdS–CdTe thin film solar cells have shown photoconversion efficiencies in the range of 6–22% where currently, the record efficiency is reported to be 22.1%.^{1–3} Interests in this class of photovoltaics have been fuelled by several factors including their proper band gap alignment, cost-effective methods for large scale fabrication, and stability.⁴ CdS–CdTe thin film photovoltaics have been fabricated by several groups through methods ranging from closed space sublimation, chemical bath deposition (CBD), electrodeposition, metal organic chemical vapour deposition (MOCVD) and solution-based growth.^{5–10} In recent years nanostructured photoabsorbers, especially nanowires have boosted the performance of solar cells by enhancing optical absorption while simultaneously providing short collection lengths for excited carriers in a direction normal to the light absorption.¹¹ Recently this concept was also applied to CdS–CdTe

nanostructured solar cells by Javéy and co-workers where they constructed nanopillar solar cells containing CdS nanopillars within a matrix of CdTe and showing high efficiency.^{12,13} The growth of CdTe nanorod arrays in the CdS matrix has been demonstrated to provide a three dimensional morphology enabling high optical absorption, thereby, increasing the carrier collection efficiency.¹³ The CdS–CdTe nanopillar solar cells were made by employing anodic aluminium oxide (AAO) membranes, which even though produces uniform arrays of the nanopillars, is still not the most lucrative high-throughput method owing to the rigidity of the AAO, as well as the fact that template removal requires harsh chemical treatment in strong base which might be detrimental to the nanowire composition. An AAO-free method for producing the heterojunction nanowire arrays might be very useful for advancing the nanowire solar cells.

With respect to nanostructured solar cells, another morphology has gained importance based on some recent advances with Si solar cell, viz. the nanohole architecture.¹⁴ Recently, it has been observed that ordered arrays of submicron sized nanoholes etched on the surface of Si photoabsorber produces a reasonably high efficiency solar cell.¹⁴ The increased efficiencies in this “holey” architecture have been attributed mainly due to the enhanced light scattering induced by the holes and less reflectivity. A tubular geometry with inner diameter and tube wall thickness in the order of several hundred nanometres might offer the same advantages of a “holey” architecture coupled with short collection lengths and enhanced absorption. However, producing well-defined nanotube arrays through rational synthesis methods is even more challenging than creating nanorod arrays. Nanotube arrays have been mostly created through

anodization process or through growth on a template.¹⁵ However, these approaches are very system specific. Most of the nanohole architectures have been engineered through top-down subtractive manufacturing. An additive growth process on the other hand, focusing on the bottom-up assembly method will have much more advantage for growing these complex architectures with precise control over morphology and stoichiometry especially for the multipart photoabsorber compositions. Hence in this article we report a simple, AAO-free protocol to grow CdS–CdTe heterojunction nanotube arrays through confined electrodeposition on lithographically patterned nanoelectrodes with a precise control on nanotube dimensions including tube inner and outer diameters, wall thickness, length, and distribution density. We have also measured photoelectrochemical response of the nanotube arrays and have compared them with that obtained from nanorod arrays produced by a similar approach. It was observed that the nanotube arrays indeed showed better photoconversion efficiency than the nanorod arrays.

2. EXPERIMENTAL

2.1. MATERIALS AND METHODS

2.1.1. Chemicals. All chemicals for nanotube/nanorod growth, chemical bath deposition (CBD), e-beam lithography and photoelectrochemical measurements were used as purchased.

CdSO₄, CdCl₂, TeO₂, thiourea, NH₄Cl, methylisobutylketone (MIBK) and isopropanol (IPA) were purchased from Alfa Aesar.

Polymethylmethacrylate (PMMA) of molecular weight 495k and 950k were purchased as 3% solution in monochlorobenzene from Microchem™. Indium tin oxide (ITO) coated glass slides with a sheet resistance of 20 ohms sq^{-1} was purchased from Fisher scientific.

2.1.2. Nanotube and Nanorod Growth. The CdS–CdTe heterojunction nanotube arrays were fabricated on conducting ITO-coated glass substrates using a combination of chemical bath deposition (CBD) for CdS and CdTe electrodeposition. For growing nanotubes/nanorods, a modified version of the protocol recently developed by the authors and described as confined electrodeposition on lithographically patterned nanoelectrodes was used as shown in Figure 1.^{16–18}

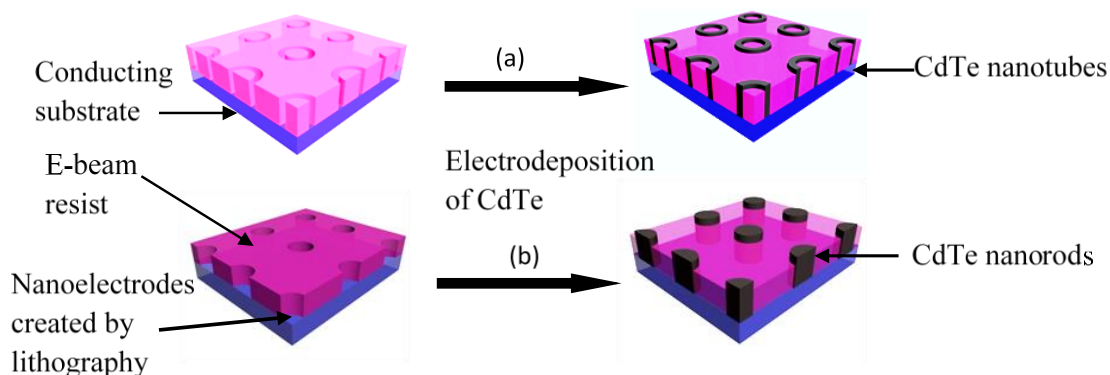


Figure 1. An illustration of the growth of (a) nanotube and (b) nanorod arrays.

The same procedure can be utilized to grow nanorod or nanowire arrays with a small modification of the lithographic pattern.

2.1.3. Deposition of CdS Layer by CBD. The CdS layers in these substrates were grown by CBD methods following a reported procedure.¹⁹ CBD is a simple, yet versatile technique which has been used extensively to grow semiconductor films on various substrates.²⁰ It is a low temperature method which involves dipping the substrate in a solution containing the precursor salts. The concentration of the solution, temperature and dipping time determines the thickness and morphology of the film. Well controlled CBD leads to formation of a very uniform layer of the semiconductor on the surface and the attachment of the film to the surface is very robust. Specifically, a CdS film of approximately 80–100 nm thickness was coated on the substrate by dipping it in an ammoniacal solution containing CdCl₂, thiourea, ammonium chloride (pH ≈ 11) for 20 min at ~80 °C. Lower temperature or lesser time for CBD growth leads to smaller thickness of the CdS films.

The CdS film could be grown both as under layer to the CdTe nanotubes or as a coating on top of the CdTe nanotubes. For the first case, a thin layer of n-type CdS was deposited on the ITO-coated glass which was then subjected to lithography and confined electrodeposition (vide infra). To compare the effectiveness of different configurations, another set of samples were prepared by depositing CdS as the last step of the process, i.e. on top of electrodeposited CdTe nanostructures.

2.1.4. Definition of nanoelectrodes by lithography. The ITO-CdS coated glass substrates were coated with polymethylmethacrylate (PMMA) which acted as an e-beam resist. During a typical e-beam resist coating process, PMMA 450k solution was spin coated at 4000 rpm for 50 seconds as the first step.

Then coated samples were baked on a hot plate at 180 °C for 3 minutes. PMMA 950k solution was then spin coated at 4500 rpm for 50 seconds and again baked at 180 °C for 3 minutes and allowed to cool to the room temperature. The desired patterns were written on the PMMA surface with e-beam lithography. In the next step, the patterns were developed in MIBK–IPA (1:3) solution which selectively dissolved the e-beam exposed PMMA, leaving the unexposed PMMA intact on the ITO surface.

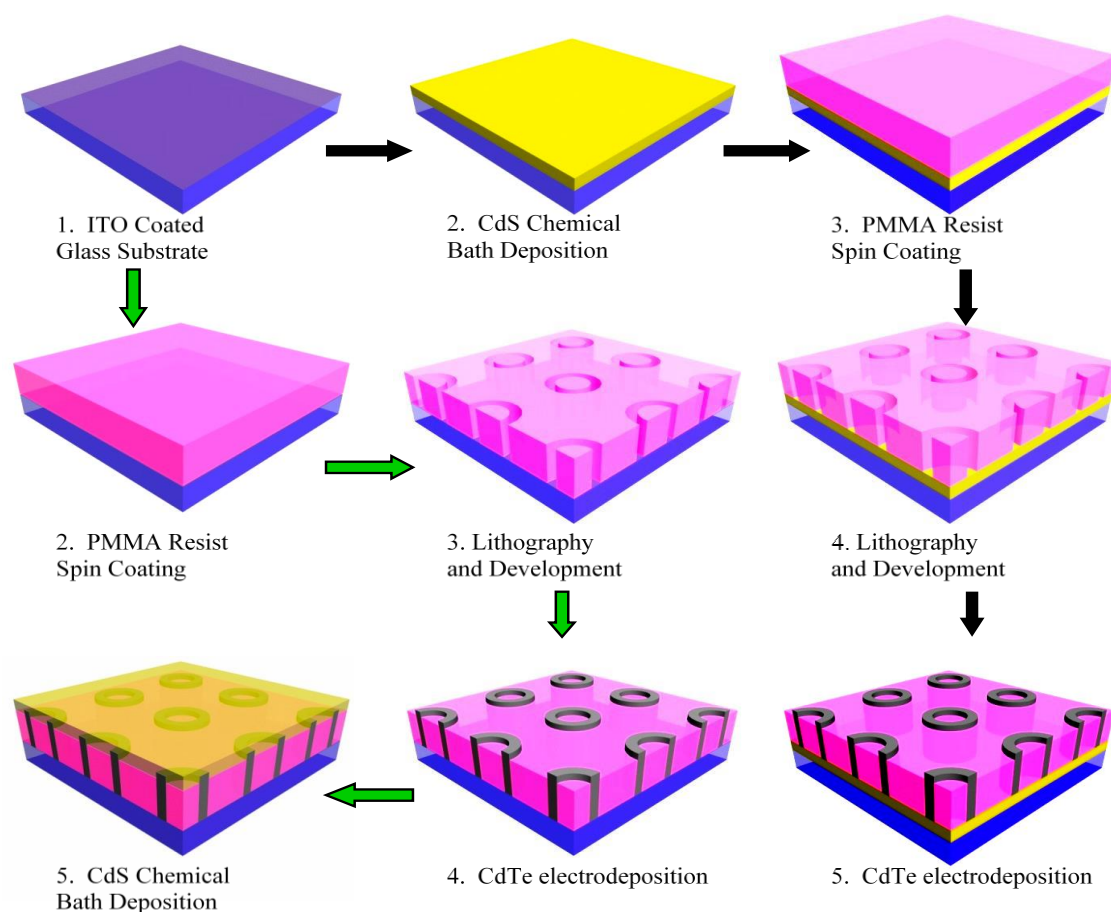


Figure 2. An illustration of the growth of nanotube arrays by patterned electrodeposition protocol. When the CBD process was carried out before the PMMA resist spin coating (path defined by black arrows), CdS layer is below the CdTe nanotubes. If the CBD process was carried out as the last step (path defined by green arrows), then the CdS layer is on top of the CdTe nanotubes.

Hence, following the development stage, two regions were defined on the substrate-surface: (i) the PMMA layer which was electrically insulating and (ii) the ITO-CdS layer exposed through the lithographically patterned holes which retained their electrical conductivity and hence acted as the nanoelectrodes. A novelty of the PMMA coated surfaces is that the PMMA coating protects the unexposed surface acting as a soft mask during the subsequent electrodeposition process. The entire protocol for CdS–CdTe nanotube growth has been described schematically in Figure 2.

2.1.5. Electrodeposition of CdTe. In the last step of the protocol, p-type CdTe was electrodeposited on the nanoelectrodes from a solution of 1 M CdSO₄ and 1 mM TeO₂ in an acidic pH of 1.8, following a reported procedure.²¹ The temperature of the electrolytic bath was maintained at 65 °C. Electrodeposition was done at a constant potential of –0.55 V using Ag/AgCl as the reference electrode under chronoamperometric conditions for 15–25 s.

During this process, CdTe was deposited solely on the nanoelectrodes with the surrounding PMMA being completely clean. A constant potential deposition was very crucial step as opposed to deposition under a potential sweep, since under those conditions it gave rise to clustered cauliflower-like morphology of the CdTe instead of nice columnar growth.¹⁶ Lengths of the CdTe nanotubes were determined by the thickness of the PMMA layer, while the diameters were defined by the nanoelectrode diameter. Typically, a length of 400 nm was readily achieved with a PMMA coating thickness of 350 nm. Interestingly, the length of the nanotubes could be increased through pulsed electrodeposition as shown in ESI Figure S1. Pulsed electrodeposition increased length of the nanotubes without compromising the diameters, providing a

unique way to precisely tailor length of the nanotubes and increase the exposed area for absorption and junction formation. Additionally, as observed by the authors previously, longer nanotubes/nanorods typically of the order of 1 μm could be also grown by the above protocol through increasing the PMMA layer thickness.¹⁶

It should be noted here that both p-type and n-type CdTe can be formed through electrodeposition.²¹ Previous studies by various groups have further confirmed that the deposition potential determines whether the electrodeposited film will be p- or n-type.^{21–23} Typically a lower deposition potential yields a more Te-rich film, thus making it a p-type semiconductor, while higher deposition potential gives rise to a more Cd-rich n-type film. In the present case, the deposition potential being small the films obtained were mostly Te-rich as observed with EDS (vide infra) thus making them a p-type layer. A lateral type p–n junction formed as the n-type CdS layer was deposited on p-type CdTe. These heterojunction nanostructures have been collectively referred to as CdS–CdTe henceforth. As mentioned above, two types of junction geometries were achieved, CdTe nanotubes/nanorods on CdS(ITO) layer and CdS layer on CdTe nanotube/nanorod layer.

3. CHARACTERIZATION

The CdS–CdTe heterojunction nanotube arrays were further characterized for the elemental composition and morphology analysis through powder X-ray diffraction (PXRD) using PANalytical's X'Pert PRO Materials Research Diffractometer (MRD, $\text{CuK}\alpha$ 1.5418 Å). Scanning electron microscopy (SEM) imaging was taken using Helios Nanolab-600 equipped with Energy Dispersive Spectrometry (EDS) detector (Oxford

Instrument) for elemental analysis. X-ray photoelectron spectroscopy (XPS). XPS measurements of the samples were performed using a KRATOS AXIS 165 X-ray Photoelectron Spectrometer using the monochromatic Al X-ray source. The impedance and photoconductivity measurements were carried out using a photoelectrochemical set-up under UV light excitation with an IviumStat potentiostat. Nanodevices were illuminated with A 400 W Xe lamp operating in UVA range (320–390 nm) with the intensity of 100 mW cm^{-2} . A mixture of 0.1 M solutions of sodium sulphite, sodium acetate and acetic acid at pH 4.6 was used as the electrolyte solution during the photoelectrochemical measurements.

4. RESULTS & DISCUSSION

4.1. MORPHOLOGY & COMPOSITION

PXRD pattern were obtained from the nanotube arrays grown by this patterned electrodeposition process without any further treatment. Typical PXRD pattern of the fully grown sample clearly showed the presence of CdS as shown in Figure 3. Both the nanotubes as well as nanorods fabricated by this method showed similar kind of PXRD patterns. However, the peaks corresponding to CdTe were of low intensity and were somewhat masked by the CdS as well as diffraction peaks from ITO which were also visible in the pattern, giving rise to a high background noise. This could be attributed to the fact that the CdTe nanorods covered only a region of $75 \times 75 \mu\text{m}^2$ area on the substrate from where the PXRD pattern was collected, while the CdS layer was spread on the entire substrate. Hence the cross-section of CdS exposed to the X-rays was much

higher than that of CdTe nanorod array. High crystallinity of the ITO background also created obstructive scattering noise from the substrate.

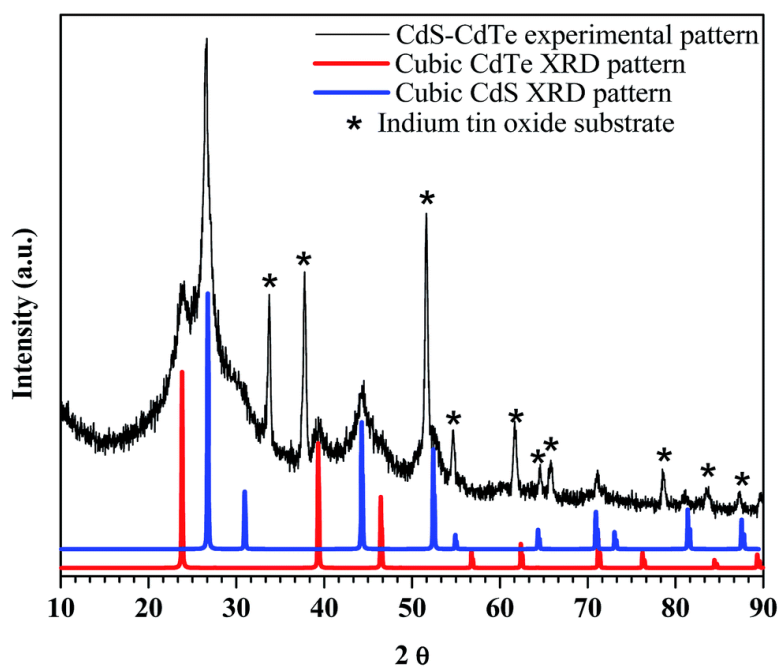


Figure 3. XRD pattern collected from the patterned CdS–CdTe nanotube arrays where the CdTe was grown on top of CdS. Standard plots for bulk CdS and CdTe has been included for comparison.

To confirm the formation of CdTe, PXRD pattern was collected independently from electrodeposited CdTe layer before the deposition of CdS. As shown in Figure S2, the PXRD pattern confirmed the formation of CdTe. The diffraction peaks corresponding to both CdS and CdTe were considerably broadened indicating that the crystallite sizes were smaller. Using Scherrer formula,²⁴ the crystallite size was estimated to be

approximately 50 nm for CdS indicating that CdS layer was polycrystalline where domain sizes were in the order of 50 nm.

Extensive SEM studies were carried out to investigate the morphology of the electrodeposited nanostructures. Figure 4a shows a typical low-magnification SEM image showing part of the nanotube arrays deposited over $70 \times 70 \mu\text{m}^2$ area containing approximately 225 nanotubes. The nanotubes were deposited entirely within the nanoelectrodes whereas the surrounding PMMA layer was completely clean. The SEM images also revealed that the nanotubes were extremely uniform in diameter and length over the entire pattern indicating the high degree of monodispersity in the nanostructures. Interestingly the wall thickness of the nanotubes could be controlled by tuning the area of pattern definition. Typically, lithographic writing of the pattern on a smaller area led to tubes with thicker walls and smaller diameters, while larger area of the pattern resulted in tubes with much thinner walls but larger outer diameter (ESI Figure S3). This kind of control might be very useful to optimize the photoconversion efficiency by tuning both the scattering (inner diameter of the tubes) as well as light absorption (controlling tube wall thickness). As mentioned above, length of the nanotubes could be altered through pulsed electrodeposition, through which longer nanotubes protruding out of the PMMA matrix could be grown (ESI Figure S1).

The composition and co-existence of Cd, S and Te in these nanostructures were investigated in details through EDS spectral analysis and elemental line scans which involved drawing a line across the nanostructure and following the elemental distribution of Cd, S, and Te along that line. From the line scan analysis shown in Figure 4b and d it was apparent that while the Cd and Te signals were higher in the nanostructure and

zeroed down in the valley between the nanostructures, the S signal showed a more or less uniform distribution across the lines, i.e. S was present both in the valley between the nanotubes and the tubes themselves.

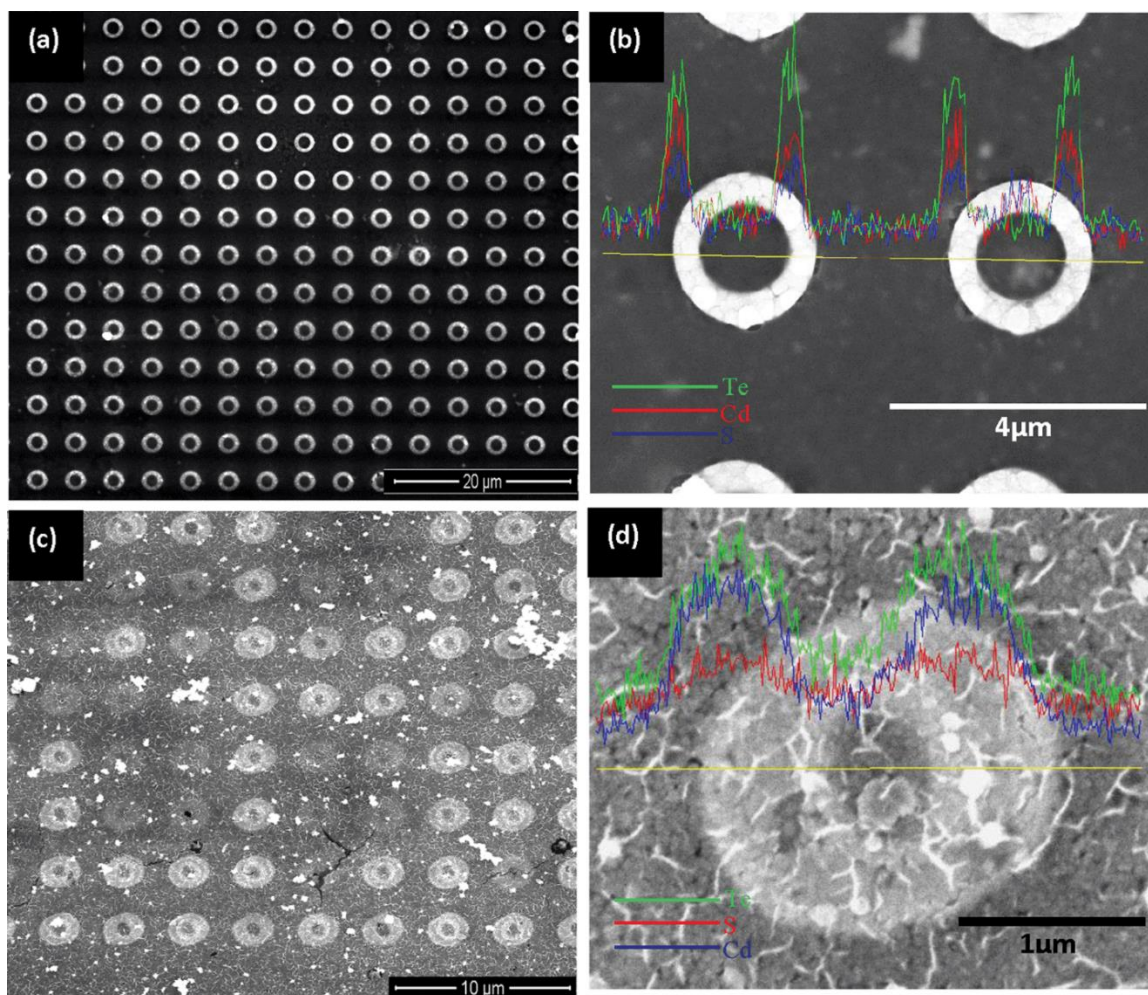


Figure 4. CdS/CdTe nanotube arrays. (a) SEM image of CdTe nanotubes grown on CdS layer similar to a pseudo-superstrate configuration. (b) Elemental analysis through EDX line scans showing maximization of Te and Cd within nanotube walls. (c) SEM image of CdS thin layer grown over CdTe nanotubes. Positions of the nanotubes beneath the CdS layer can still be identified. (d) Elemental analysis with EDX line scans on CdS layer grown on CdTe nanotubes.

Both S and Te had Cd associated with them. However, EDS being a depth-sensitive technique, the Cd associated with the Te showed up more prominently owing to the height of the nanotubes (~ 500 nm). Hence, Cd signal followed the Te signal.

Fabrication of nanorod arrays were also carried out following the same protocol used to prepare the nanotube arrays and Figure 5a shows a nanorod array covering an area of $70 \times 70 \mu\text{m}^2$ deposited on a thin layer of CdS.

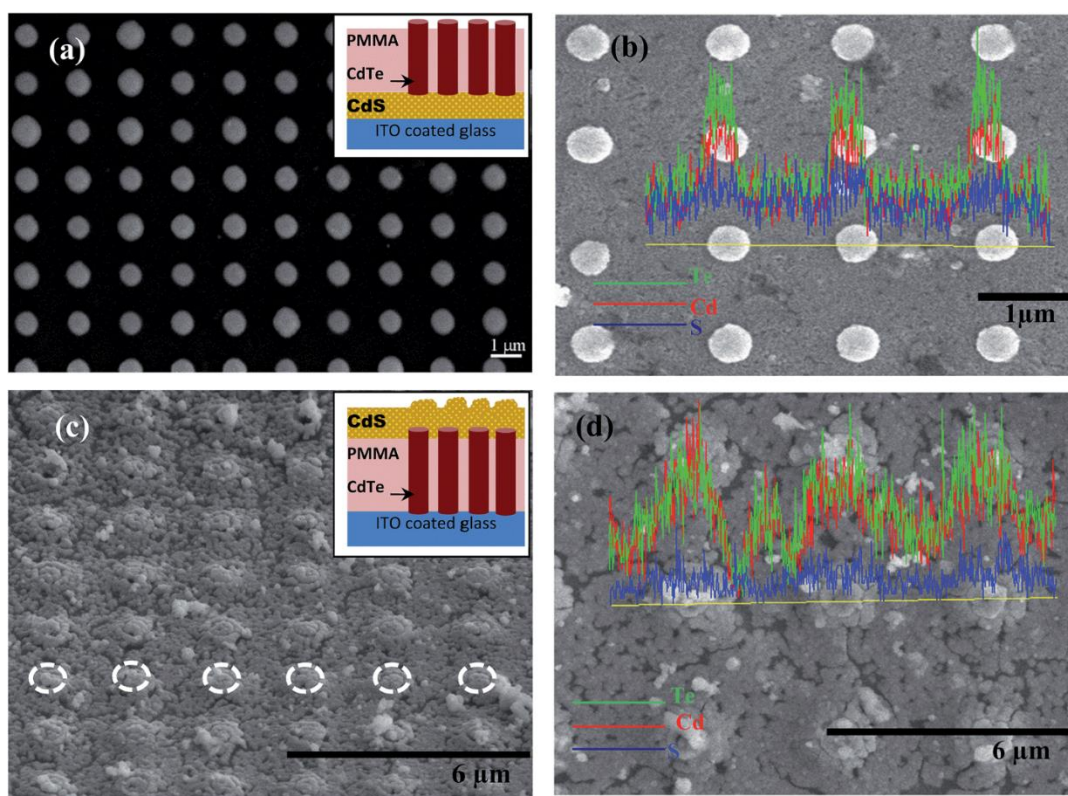


Figure 5. CdS/CdTe nanorod arrays. (a) SEM image of CdTe nanorods grown on CdS layer similar to a pseudo-superstrate heterojunction. Inset illustrates the schematic representation of the layer arrangement. (b) Elemental analysis through line scan showing maximization of Te and Cd within the nanorods while S is present uniformly over the entire region. (c) SEM image of CdS layer grown over CdTe nanorods. Dotted circles indicate the position of the nanorods beneath the CdS layer. Inset illustrates a cross sectional illustration of the layer arrangement. (d) Elemental analysis with EDS line scan.

There are 900 nanorods in the deposited pattern and similar to the nanotube patterns, a clean deposition of CdTe with a uniform distribution of size and shape can be observed in these nanorods patterns also. Another arrangement of the nanodevice was prepared by depositing CdS layer on top of CdTe nanorod pattern as shown in Figure 5c. EDX line scan was performed to locate the distribution of Cd, Te and S in the fabricated pattern as shown in Figure 5b and d.

The CdS–CdTe junction in these nanostructured arrays were also observed through cross-sectional SEM imaging of the CdTe-on-CdS superstrate configuration. For these purposes, the tubular architectures were redesigned such that instead of cylindrical tubes, a longitudinally sliced tube could be created such that the cross-section of the interface between underlying CdS layer and the growing CdTe tubes could be seen more clearly. Figure 6a and b shows the cross-sectional SEM images of the tubular and rod-like architectures of CdTe-on-CdS, respectively. As seen in Figure 6a, the CdTe maintains a uniform interface with the underlying CdS layer which continues throughout the thickness of the tube walls.

The CdS and CdTe layers has been highlighted in false color in the inset of Figure 6a. As can be seen clearly, the underlying CdS layers also maintains uniform thickness for each tubular structure throughout the entire array. The interface between CdS and CdTe maintains similar uniformity and continuity in the rod-like architectures as shown in Figure 6b. Inset in Figure 6b shows the CdS and CdTe layers in individual rods, and the thickness of the CdS layer is seen to be similar to that obtained for the tube-like architecture.

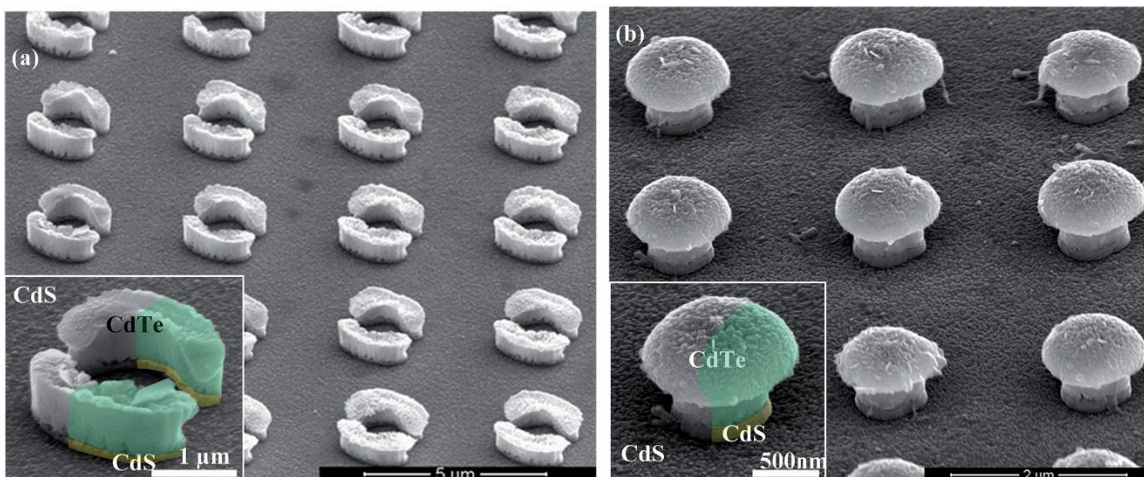


Figure 6. Morphology of the patterns. SEM image of (a) a CdTe pattern modified to write open tubular structures sliced longitudinally which exposes the growing edges thereby showing the cross sectional view. Inset shows close up image of an individual (open) tubular nanostructure. False color was used to show the CdTe and CdS sections. (b) CdTe rod pattern viewed at an angle to show the 3D structure and the interface. Inset: shows a close up view of an individual nanorod reinforced with false color to highlight the CdS and CdTe regions.

Detailed XPS analysis was also carried out on electrodeposited samples for further confirmation of formation of CdTe (ESI Figure S4). Cd 3d peaks were observed at 412.5 and 406.5 eV were similar to that observed in standard CdTe samples and confirmed the presence of Cd²⁺. Te 3d peaks were obtained at 573 and 583 eV which were also characteristic of CdTe.²⁵ The as-prepared devices were also characterized with optical absorption spectroscopy and the absorption spectra was analyzed for near band edge optical absorption using the classical relation $\alpha = A(h\nu - E_g)^n/h\nu$ where the symbols have their usual meanings, [A is a constant, n is 0.5 for direct transition, E_g is band gap and hν is photon energy]. Band gap was determined from the optical absorption data as shown in ESI Figure S5. The plot between $(\alpha h\nu)^2$ and hν become linear near the absorption edge. Extrapolating the linear portion of the plot to zero absorption coefficient

gives the band gap energy (E_g). It was observed that the CdTe nanotube arrays showed a band gap of 1.51 eV which is a 0.07 eV blue shift compared to the reported value for electrodeposited CdTe.²⁶ Band gap of CdS was determined as 2.31 eV (ESI Figure S5) which is comparable with the bandgap obtained for CdS prepared by chemical bath deposition.²⁷ The absorption spectra of the CdS–CdTe nanostructured device showed a cumulative effect of both the layers as shown in ESI Figure S5.

4.2. PHOTOELECTROCHEMICAL ANALYSIS

It is important to investigate the junction geometries before actual device formation. For this purpose, photoelectrochemical (PEC) measurements have been carried out, where the electrolyte containing a redox pair forming a junction with the top layer (CdS/CdTe) suffices for the top electrode of the actual device geometry. PEC studies in liquid electrolytes provide useful information about the junction interfaces since they provide conformal coverage across the junction topology. In this research project, the CdS–CdTe architectures were created in two specific configurations. It has been shown conventionally that CdS–CdTe solar cells can be fabricated either in superstrate or substrate geometries.²⁸ In superstrate configuration, the actual photoabsorber (CdTe) lies below the window layer formed by the CdS which in turn is capped by the TCO (transparent conducting oxide) electrode. The CdTe layer is contacted by a back electrode which is generally a metallic contact. In the substrate configuration however, CdTe is grown on a conducting electrode and the CdS layer is coated on top of CdTe. Conventionally, for CdTe solar cells, the superstrate configuration shows better solar energy conversion efficiency. However, the problem of high contact

resistance in the CdTe–metal interface as well as non-flexibility of the device has led researchers to investigate the substrate configuration also. Moreover, in the substrate configuration as CdTe is grown directly on the conducting electrode, the interface properties are expected to be much better. In the present case the CdTe nanotubes grown on top of CdS layer coated on ITO-glass can be considered closer to the superstrate configuration where the top electrode has been replaced with the liquid junction electrolyte. On the other hand, CdTe nanotubes grown directly on the ITO-coated glass and coated with CdS can be considered closer to the substrate configuration where the ITO-coated glass acts as both the growth substrate and the electrode, while the electrolyte forms the front contact.

PEC measurements were done on the as synthesized CdS–CdTe nanotube and nanorod arrays on ITO substrate in a liquid junction electrolytic set-up. Acetate buffer electrolyte was used in three electrode cell assembly containing Ag/AgCl as reference electrode, Pt mesh as counter electrode and substrates containing nanostructure arrays as working electrodes. Acetate buffer was prepared using 0.1 M acetic acid, 0.1 M sodium acetate and 0.1 M sodium sulphite and maintained at a pH of 4.6.²⁹ The nanodevice was illuminated with a 400 W Xe lamp operating in UVA range (320–390 nm) with intensity of 100 mW cm⁻².

Photoelectrochemical response of the nanodevices measured in illuminated and dark conditions were compared with that obtained from CdS–CdTe thin film electrodeposited on ITO by similar procedure (referred to as bulk film). A linear sweep was applied from 0 V to –0.5 V potential, at the scan rate of 0.01 V s⁻¹ and the current response from the sample was measured, while the light source was switched on and off

periodically. As expected the CdS–CdTe nanotubes and nanorods were very stable in the electrolyte solution and did not undergo degradation during the experiments.

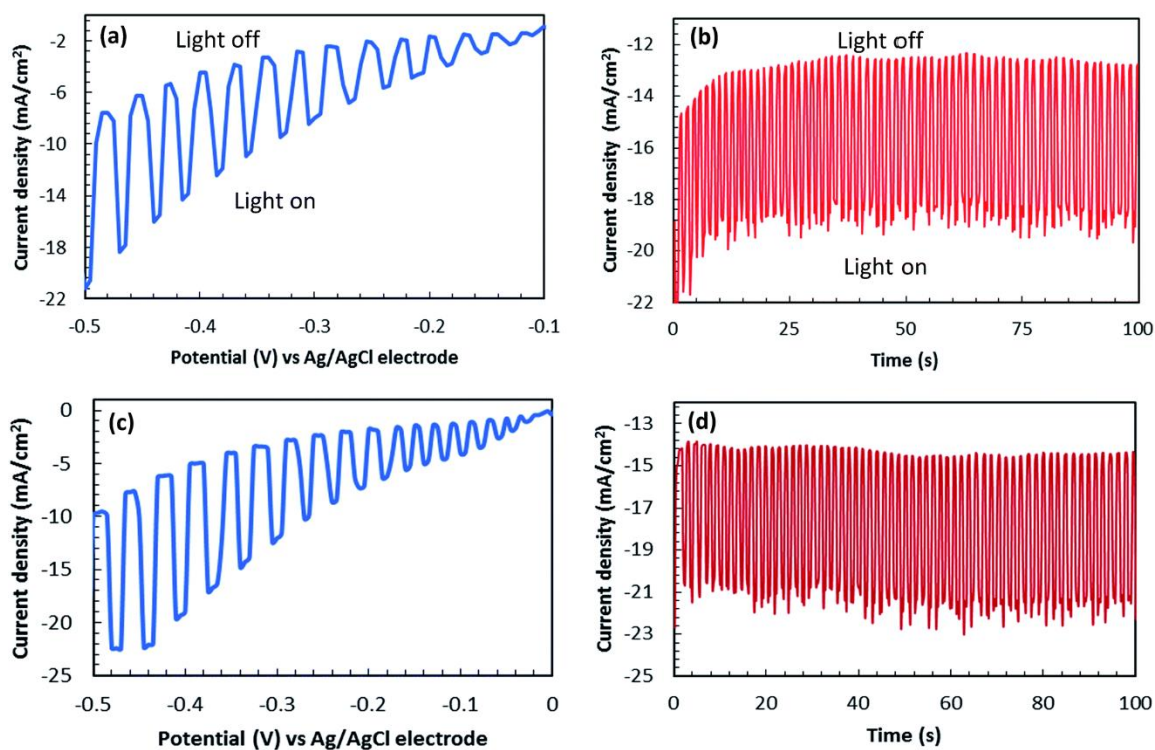


Figure 7. PEC characterization of nanotube array. (a) The on–off response of the photocurrent obtained under alternate illumination and dark conditions from the CdTe nanotube arrays grown on CdS layer during a potential scan. (b) Stability of the photocurrent measured at a constant potential of -0.4 V for extended time under intermittent exposure to the light source for CdTe nanotube grown on CdS. (c) The on–off response of the photocurrent obtained under alternate illumination and dark conditions from the CdS layer grown over CdTe nanotube arrays during a potential scan. (d) Stability of the photocurrent measured at a constant potential of -0.4 V for extended time under intermittent exposure to the light source for CdS layer grown over CdTe nanotube arrays.

The acetate buffer electrolyte composition works as a hole scavenger thereby, inhibiting degradation of the CdTe and formation of Te deposits which blocks the

nanostructure–electrolyte interface that can affect the cell performance.^{30,31} For these nanotube and nanorod arrays mostly cathodic photocurrent was observed. Figure 7a shows the on–off current response obtained from the lateral type p–n junction CdTe-on-CdS nanotube arrays under dark and illuminated conditions.

On the other hand, photocurrent generated from the CdTe nanotube arrays coated with CdS layer was very similar to the previous arrangement (Figure 7a and c, respectively). The photocurrent obtained was very stable as can be seen from the chronoamperometric measurements done at -0.4 V for extended period of time (Figure 7b, d and S6). However, as is apparent from Figure 7b and d, the CdTe nanotubes grown on CdS layers showed a slightly better photocurrent than the CdS coated CdTe nanotubes under chronoamperometric conditions.

As illustrated previously in Figure 1, nanorod or nanowire devices can be fabricated in addition to the nanotube devices by following same protocol. Figure 8 shows the on–off current response obtained from a nanorod lateral p–n junction device fabricated according to this procedure. It was observed that the device made by fabricating CdTe nanorods on CdS layer (Figure 8a) and CdS layer deposited on CdTe nanorod arrays (Figure 8c) produced comparable photocurrents to each other under the experimental conditions.

In all the above configurations it was observed that the photocurrent produced by CdTe nanotubes/nanorods electrodeposited on top of CdS layer was better than the CdS coated CdTe nanotubes/nanorods. As has been discussed previously, in the present case CdTe grown on top of CdS was closer to the superstrate configuration in liquid junction electrolyte, while the CdS coated CdTe nanotubes were similar to the substrate

configuration. It has been observed previously by various researchers that typically superstrate configuration produces better photoconversion efficiency possibly because of more efficient charge depletion and carrier transport.

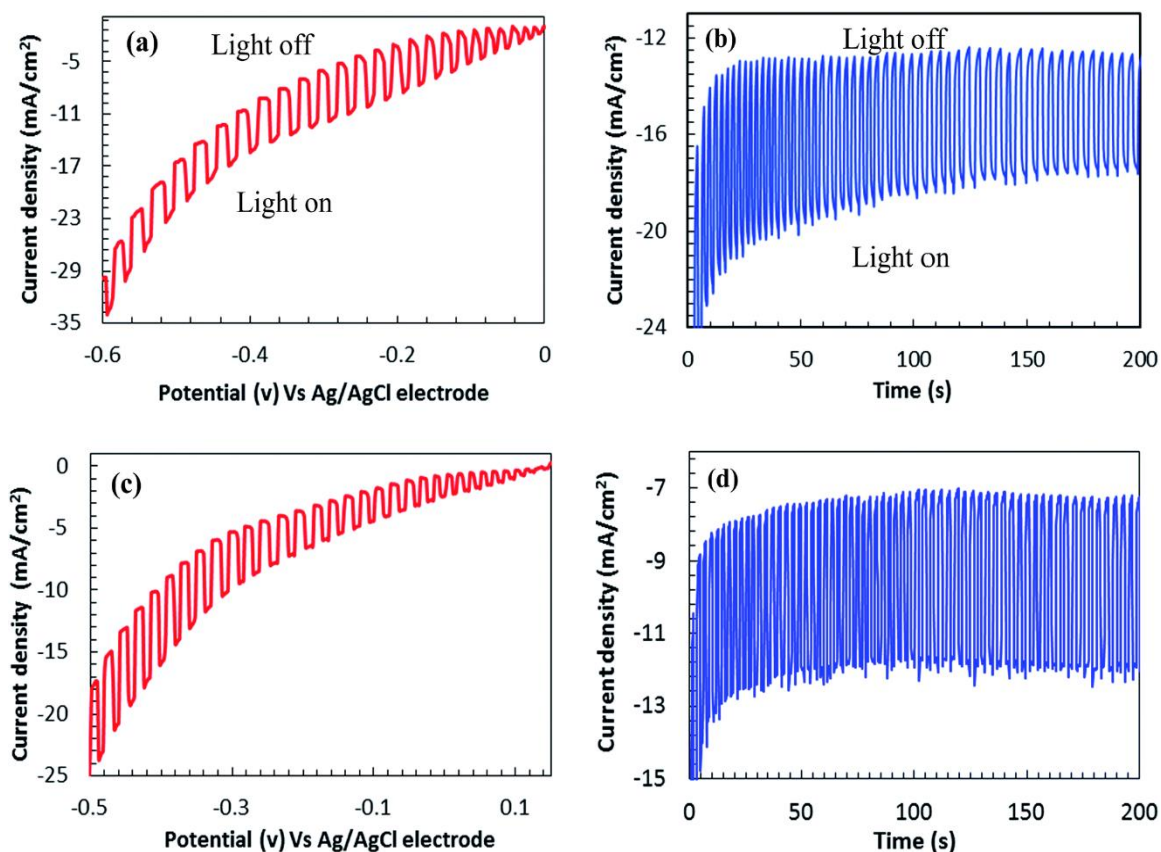


Figure 8. PEC characterization of nanorod array. (a) The on–off response of the photocurrent obtained under alternate illumination and dark conditions from the CdTe nanorod arrays grown on CdS layer. (b) Stability of the photocurrent measured at a constant potential of -0.4 V for extended time under intermittent exposure to the light source for CdTe nanorods grown on CdS. (c) The on–off response of the photocurrent obtained under alternate illumination and dark conditions from the CdS layer grown over CdTe nanorod arrays. (d) Stability of the photocurrent measured at a constant potential of -0.4 V for extended time under intermittent exposure to the light source for CdS layer grown over CdTe nanorod arrays.

Interestingly in these cases also, the pseudo-superstrate geometry exhibits a better photocurrent, thus highlighting the effectiveness of the growth protocol. To further investigate the effect of CdS layer on the photoconductor performance, PEC measurements were carried out with CdTe nanotubes arrays in the absence of a CdS layer. It was observed that there was ~25% increase of the photocurrent density in the presence of CdS layer (ESI Figure S7). This can be attributed to the efficient separation of generated charge carriers and improved collection efficiency in the presence of the electrostatic potential of the p–n junction created between CdS and CdTe. Additionally, in conventional thin film photovoltaics, one of the problems with the superstrate configuration deals with the interface between CdS and CdTe which sometimes needs to be reinforced by CdCl₂ treatment.³² In the present case since CdTe is directly grown on top of CdS through electrodeposition, intermixing and diffusion at the interface will be more pronounced compared to vapor phase growth, thereby reducing the need for further treatments.

Additional experiments were carried out to determine photoconversion efficiency from detailed photoelectrochemical measurements by considering the open circuit potential (V_{oc}), short circuit current density (J_{sc}), and fill factor (FF) for each device. It was observed that the photoconversion efficiency was highest with the tubular architectures of CdTe (9.6%), compared to that of the pillar-like structures (7.2%) as shown in Figure 9 and summarized in Table 1. It was observed that the V_{oc} for the film-like device was slightly higher than that with the nanostructured arrays. This can be explained as an effect of several factors including varying degree of crystallinity in the CdS–CdTe layers as well as different carrier recombination rate and series resistance across the

junctions in the film and nanostructure arrays, respectively. Typically, it has been observed that single crystalline Si shows a higher V_{oc} , while commercially available polycrystalline Si shows considerably lower V_{oc} .

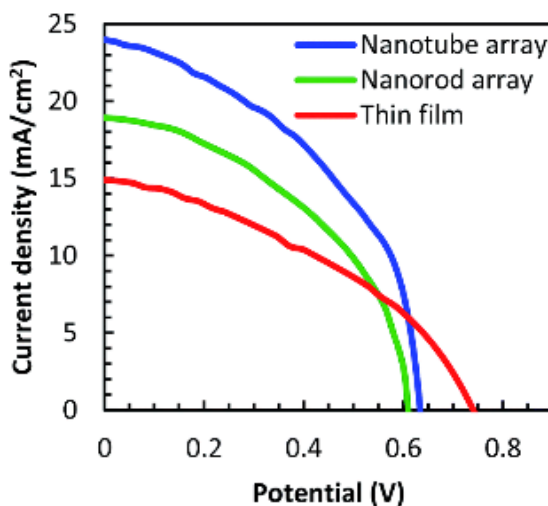


Figure 9. Photoconversion efficiency. A comparison of CdS–CdTe nanostructured devices containing CdTe nanotubes, nanorods, and thin film.

In the present case degree of crystallinity of CdTe in the tubes and rods is definitely lower than that obtained in the film morphology. Additionally, both of the nanostructured architectures showed higher conversion efficiency than the film-like morphology and typically, the efficiency was increased by almost 50% in changing the morphology of the CdTe layer from granular film to tubular structures. The obtained photoconversion efficiency with these nanostructured devices obtained from PEC measurements was considerably high and with proper device fabrication they can be possibly made comparable to the high quality CdTe solar cells being reported

recently.^{34,35} It should be noted that this photoconversion efficiency was obtained from the bare nanostructure arrays without applying any anti-reflective coating.

Interestingly, the photocurrent obtained from both the CdS–CdTe nanotube and nanorod devices were comparable to that obtained from the CdS–CdTe bulk film with a much higher coverage of the photoactive material as shown in Figure 10. Specifically, while the nanotube/nanorod arrays covered an area of $75 \times 75 \mu\text{m}^2$ on the electrode surface, the bulk film occupied an area of approximately $0.5 \times 0.5 \text{ mm}^2$ as represented in the schematic illustration shown in Figure 10c.

Table 1. Photovoltaic performance data of the fabricated devices

CdTe morphology	J_{sc}/mAcm^{-2}	V_{oc}/mV	FF%	$\eta\%$
Nanotube array	23.8	631	64.5	9.6
Nanorod array	18.8	609	63.2	7.2
Thin film	14.8	739	57.8	6.3

This essentially means that the active material coverage required for the heterojunction nanotube/nanorod device was less than 10% as compared to that of the planar film to produce an equivalent amount of photocurrent. This observation is very similar to the InP nanowire arrays reported recently by Wallentin et al. where the authors observed that even with 12% coverage, the nanowire arrays could produce 80% of the

current obtained from the thin film device.³³ When nanotube and nanorod arrays are compared, it was observed that same amount of photocurrent generated by nanorods can be generated from nanotubes with less coverage of the active material than nanorods. This is the true essence of miniaturization whereby, the same amount of efficiency can be achieved with drastically scaled down device. From a comparative point of view, it was observed that the photocurrent obtained from the nanotube arrays was maximum followed by the nanorod arrays, while the bulk film showed the minimum amongst the three.

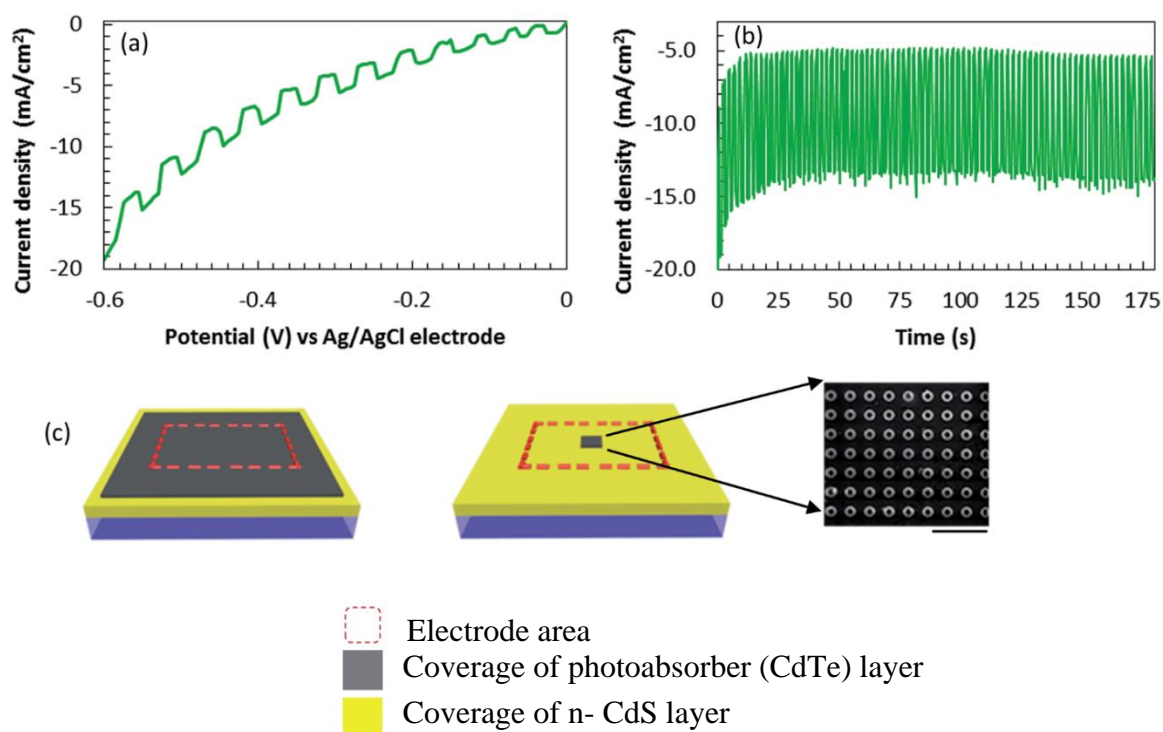


Figure 10. PEC study of thin films. (a) The on-off response of the photocurrent obtained under alternate illumination and dark conditions from the 1 μm thick CdTe thin film grown on CdS layer. (b) Stability of the photocurrent measured at a constant potential of -0.4 V for extended time under intermittent exposure to the light source for CdTe thin film grown on CdS. (c) Schematic representation of the coverage of the nanotube/nanorod compared to the thin film device. Scale bar is 10 μm.

This observation confirms that indeed the “holey” architecture as offered by the nanotube geometry provides additional opportunity for increasing the photoconversion efficiency through optimal tuning of the optical properties. Since the reported method provides ample opportunities to tune the pore size and the wall thickness of the nanotubes, this approach will be extremely useful to design these nanotube architectures with the aid of some simulation studies to optimize the optical properties thereby maximizing the efficiency.

Electrochemical Impedance Spectroscopy (EIS) was also measured with the pseudo-superstrate configuration of the CdS–CdTe devices and the corresponding Nyquist plots are shown in ESI Figure S8. The impedance data was analyzed based on Randles equivalent circuit model (inset in ESI Figure S8) to determine EIS parameters such as solution resistance (R_s), charge transfer resistance (R_{CT}) and constant phase element (CPE) representing double layer capacitance at the interphase (ESI Table ST1). It was observed that the device with CdTe tubular architecture showed minimum charge transfer resistance, thereby leading to the highest current density. The bulk film on the other hand, showed the highest charge transfer resistance, possibly due to inefficient junction geometry and inhibited transport.

5. CONCLUSIONS

In conclusion, we could successfully establish a simple yet versatile protocol for the fabrication of lateral p–n junction, CdS–CdTe nanotube and nanorod arrays on conducting ITO substrates. Photoelectrochemical measurements indicated the robustness

of the nanostructure–substrate interface and revealed that these nanotubes and nanorod arrays were capable of producing photocurrent which was comparable to that obtained with CdS–CdTe thin film albeit with much higher coverage of the active photoabsorber layer. Additionally, the nanotube array device showed a higher photoconversion efficiency compared to the nanorod device and the bulk films. Such enhancement of photocurrent can be caused either by increased absorption through resonant light trapping, reduced optical reflection due to the three dimensional nanostructure or simply by packing high density of nanostructures in parallel such that they act as parallel set of resistors, where the total current flowing through the device is the summation of current flowing through individual nanostructures. The influence of the “holey” architecture in the photoabsorber layer was also evident from the increased photocurrent of the nanotube devices compared to the nanorod devices, which also suggested that one of the major factors for varying efficiency was tuning of the optical properties between the nanotube and nanorod arrays. Further studies and simulations are being conducted to investigate whether these CdTe nanotubes and nanorods can exhibit resonant light trapping and to what extent. These results are of immense technological importance, since the photocurrent can be potentially amplified even further simply by increasing the packing density of the nanostructures. The simplicity and versatility of the protocol also implies that other types of vertically ordered photovoltaic nanostructure arrays with tuneable physical dimensions can also be grown as p–n heterojunctions on suitable window layers. This protocol will be especially useful to grow nanotube and nanorod/nanowire arrays of complex ternary and quaternary chalcogenides like copper indium gallium selenide (CIGS), copper zinc tin sulphide (CZTS) and copper indium selenide (CISe).

ACKNOWLEDGEMENTS

The authors would like to acknowledge University of Missouri Research Board for supporting this research and MRC for equipment usage.

SUPPLEMENTARY INFORMATION

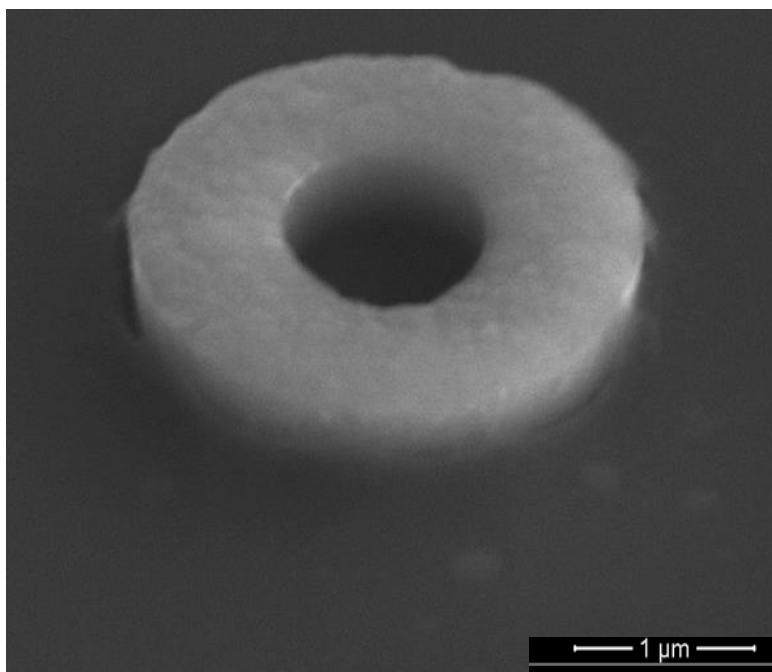


Figure S1. SEM image of a CdTe tube grown by pulsed electrodeposition. Compared to the continuous deposition, lateral growth has minimized and tubes can be grown beyond the thickness of the polymer by pulsed deposition.

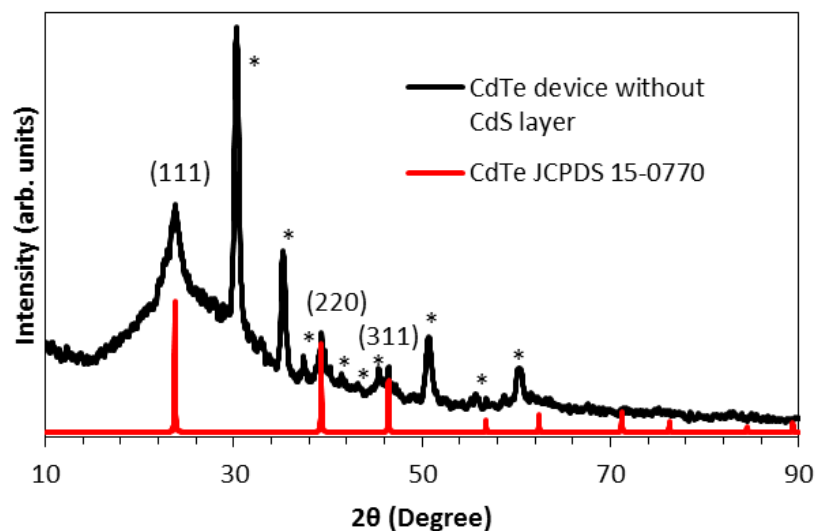


Figure S2. PXRD pattern of the electrodeposited CdTe layer before deposition of CdS layer. This pattern matched with the standard CdTe pattern [JCPDS 15-0770]. * indicates ITO peaks from the substrate.

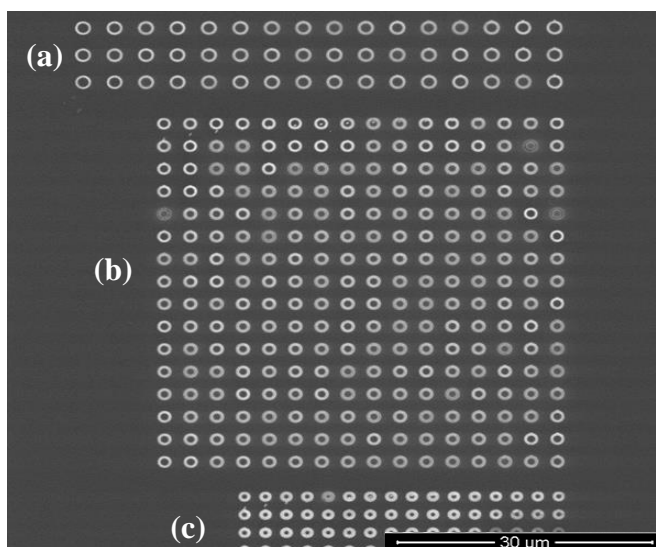


Figure S3. SEM image of one nanotube pattern written in three different sizes. It shows the versatility of the protocol to fine tune the nanotube diameter and wall thickness without changing the feature size of the original pattern used in EBL. When the pattern is written in a larger area (a) the tube diameter as well as the distance between adjacent tubes (pitch) becomes larger and the tube wall thickness becomes thinner. When the same pattern is written in a small area (c) the tube pore diameter as well as pitch become smaller and thickness of the nanotube wall becomes larger.

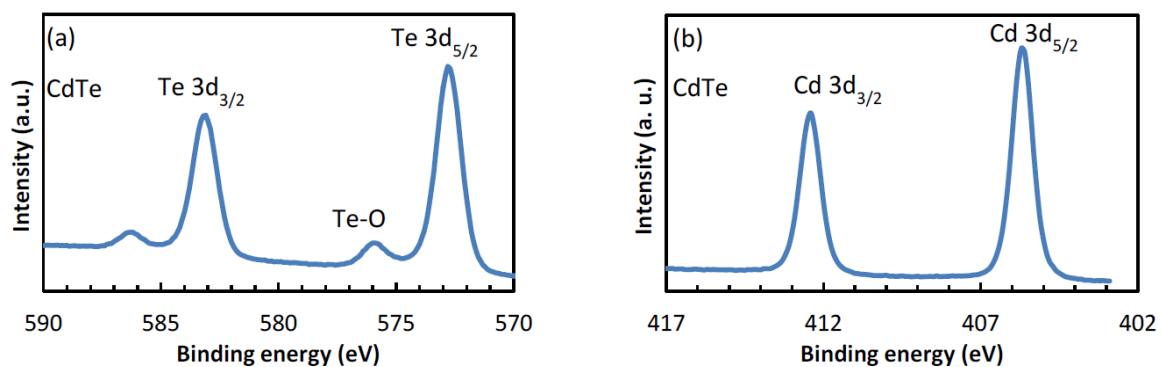


Figure S4. XPS analysis of the CdTe nanotube arrays. (a) Binding energy spectrum of Te 3d_{3/2} and 3d_{5/2} (d) Binding energy spectrum of Cd 3d_{3/2} and 3d_{5/2} confirms the presence of CdTe.

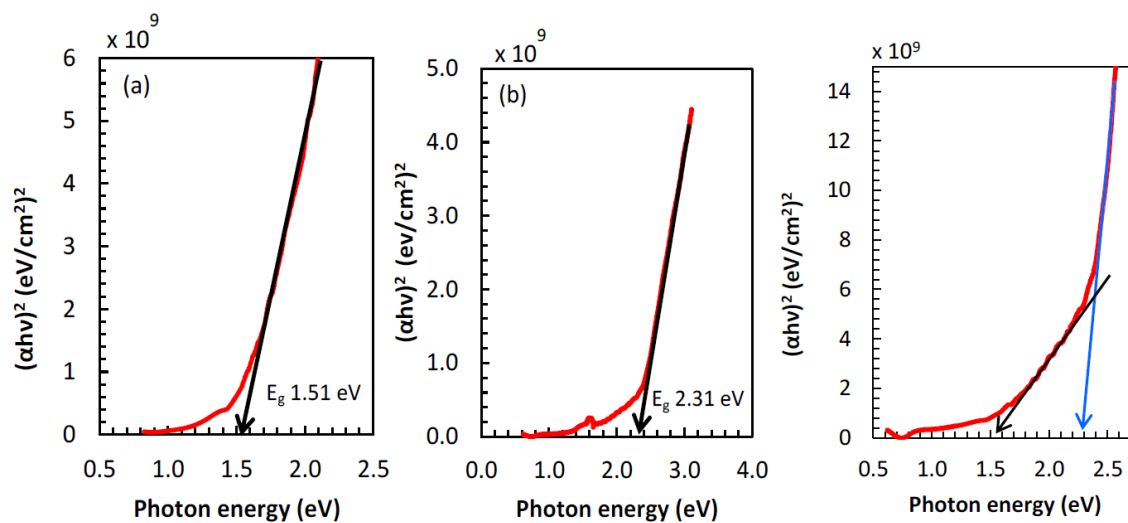


Figure S5. Optical band gap determination. (a) as-prepared nanotube arrays, (b) cadmium sulfide thin film and (c) CdS/CdTe nanotube combined device

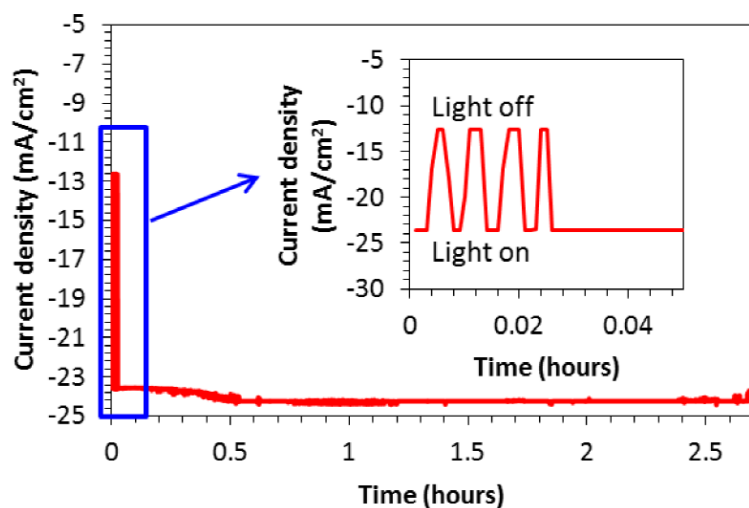


Figure S6. Stability of the photocurrent response of the CdTe on CdS device under photoelectrochemical testing conditions. Initially, the device response was monitored by periodically turning on and off the light source. Then light source was kept on and photocurrent was recorded. It can be seen that the photocurrent response was stable for more than 2 h of continuous illumination.

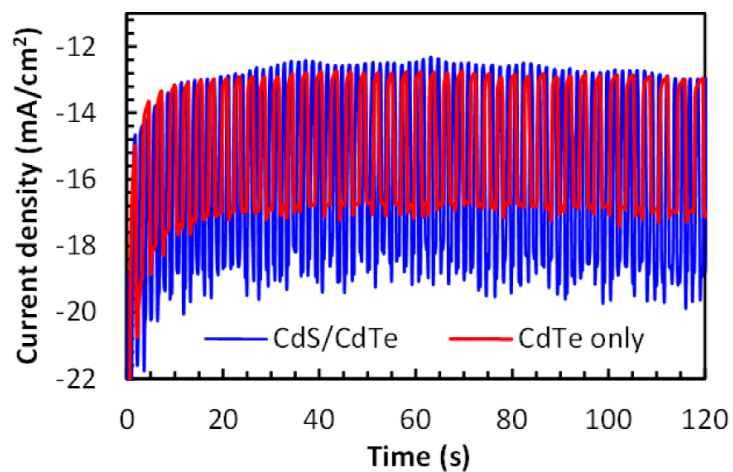


Figure S7. Comparison of light on-off response of the CdTe nanotube array with CdS/CdTe nanotube arrays. It was seen that there is ~25% increase of current density in the presence of n-type CdS layer.

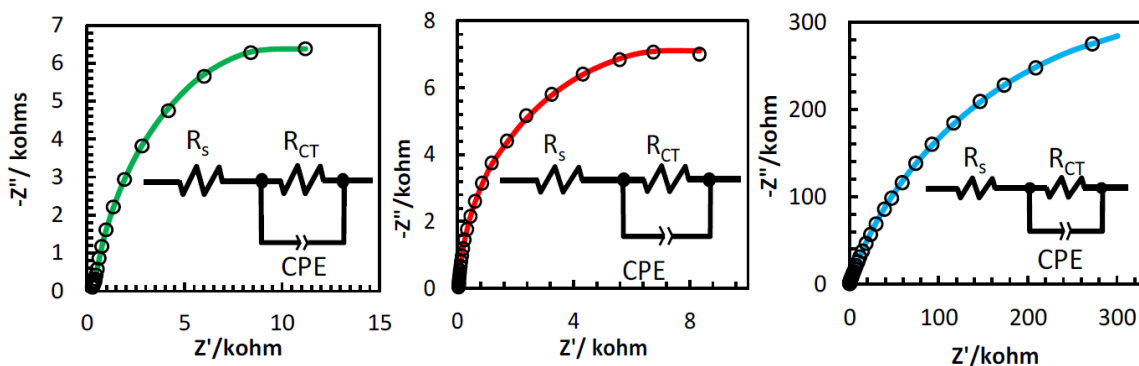


Figure S8. Impedance analysis. Nyquist plots of (a) CdS/CdTe nanotube arrays (b) CdS/CdTe nanorod arrays and (c) CdS/CdTe thin film. The inset shows the equivalent circuit diagram.

Table ST1. Evaluated EIS parameters of different geometries of the fabricated devices

CdTe morphology	R_s/ohm	R_{ct}/kohm	CPE/Fcm^{-2}
Nanotube array	0.28	15.02	5.80×10^{-2}
Nanorod array	0.38	18.52	7.02×10^{-6}
Thin film	0.44	819.10	1.65×10^{-6}

REFERENCES

1. S. G. Kumar and K. S. R. K. Rao, *Energy Environ. Sci.*, 2014, **7**, 45–102.
2. Z. Fang, X. C. Wang, C. W. Hong and C. Z. Zhao, *Int. J. Photoenergy*, 2011, Article ID 297350, 8 pages, DOI:10.1155/2011/297350 ; J. Britt and C. Ferekides, *Appl. Phys. Lett.*, 1993, **62**, 2851–2852; X. Wu, J. C. Keane, R. Dhere, C. DeHart, D. S. Albin, A. Duda, T. A. Gessert, S. Asher, D. H. Levi and P. Sheldon, *Proceedings of the 17th European Photovoltaic Solar Energy Conference*, 2001, 995–1000.
3. Steve Krum, February 23, 2016, First Solar Achieves, <http://investor.firstsolar.com/releasedetail.cfm?ReleaseID=956479>.

4. D. M. Oman, K. M. Dugan, J. L. Killian, V. Ceekala, C. S. Ferekides and D. L. Morel, *Appl. Phys. Lett.*, 1995, **67**, 1896–1898 N. Romeo, A. Bosio, V. Canevari and A. Podestà, *Sol. Energ.*, 2004, **77**, 795–801.
5. V. Krishnakumar, J. Han, A. Klein and W. Jaegermann, *Thin Solid Films*, 2011, **519**, 7138–7141.
6. J. Han, C. Spanheimer, G. Haindi, G. Fu, V. Krishnakumar, J. Schaffner, C. Fan, K. Zhao, A. Klein and W. Jaegermann, *Sol. Energy Mater. Sol. Cells*, 2011, **95**, 816–820.
7. N. W. Duffy, D. Lane, M. E. Ozsan, L. M. Peter, K. D. Rogers and R. L. Wang, *Thin Solid Films*, 2000, **361**, 314–320 .
8. E. Rakhshani, *J. Appl. Phys.*, 2001, **90**, 4265–4271.
9. N. W. Duffy, L. M. Peter, R. L. Wang, D. W. Lane and K. D. Rogers, *Electrochim. Acta*, 2000, **45**, 3355–3365.
10. S. J. C. Irvine, A. Hartley and A. Stafford, *J. Cryst. Growth*, 2000, **22**, 117–123.
11. E. Garnett and P. Yang, *Nano Lett.*, 2010, **10**, 1082–1087.
12. Z. Fan, H. Razavi and J. W. Do, *Nat. Mater.*, 2009, **8**, 648.
13. R. Kapadia, Z. Fan, K. Takei and A. Javey, *Nano Energy*, 2012, **1**, 132–144.
14. S. E. Han and G. Chen, *Nano Lett.*, 2010, **10**, 1012–1015; S. Jeong, S. Wang and Y. Cui, *J. Vac. Sci. Technol.*, 2012, **30**, 060801; R. Yu, Q. Lin, S.-F. Leung and Z. Fa, *Nano Energy*, 2012, **1**, 57 ; K.-Q. Peng, X. Wang, L. Li, X.-L. Wu and S.-T. Lee, *J. Am. Chem. Soc.*, 2010, **132**, 6872; H. Jeong, H. Song, Y. Pak, K. Kwon, K. Jo, H. Lee and G. Y. Jung, *Adv. Mater.*, 2014, **26**, 3445.
15. D. Gong, C. A. Grimes, O. K. Varghese, W. Hu, R. S. Singh, Z. Chen and E. C. Dickey, *J. Mater. Res.*, 2001, **16**, 3331–3334.
16. S. Mishra and M. Nath, *Nano Energy*, 2013, **2**, 1207–1213; W. P. R. Liyanage, J. S. Wilson, E. C. Kinzel, B. K. Durant and M. Nath, *Sol. Energy Mater. Sol. Cells*, 2015, **133**, 260–267.
17. W. P. R. Liyanage, J. S. Wilson, E. Kinzel and M. Nath, *Nanomater. Energy*, 2014, **3**(5), 167–176.
18. W. P. R. Liyanage and M. Nath, *ECS Trans.*, 2015, **66**(40), 1–7.
19. H. Khallaf, I. O. Oladeji and G. Chai, *Thin Solid Films*, 2008, **516**, 7306–7312.

20. P. K. Nair, M. T. S. Nair and V. M. Garcia, *Sol. Energy Mater. Sol. Cells*, 1998, **52**, 313–344.
21. M. Dharamdasa, P. A. Bingham, O. K. Echendu, H. I. Salim, T. Druffel, R. Dharamdasa, G. U. Sumanasekera, R. R. Dharmasena, M. B. Dergacheva, K. A. Mit, K. A. Urazov, L. Bowen, M. Walls and A. Abbas, *Coatings*, 2014, **4**, 380.
22. M. P. R. Panicker, M. Knaster and F. A. Kroger, *J. Electrochem. Soc.*, 1978, **125**, 566–572; M. Miyake, K. Murase, T. Hirato and Y. Awakura, *J. Electroanal. Chem.*, 2004, **562**, 247–253.
23. N. Romeo, A. Bosio, V. Canevari and A. Podesta, *Sol. Energ.*, 2004, **77**, 795–801.
24. L. Patterson, *Phys. Rev.*, 1939, **56**, 978–982.
25. W. J. Danaher, L. E. Lyons, M. Marychurch and G. C. Morris, *Appl. Surf. Sci.*, 1986, **27**(3), 338–354.
26. G. Fulop, M. Doty, P. Meyers, J. Betz and C. Liu, *Appl. Phys. Lett.*, 1982, **40**(4), 327–328.
27. Cortes, H. Gomez, R. E. Marotti, G. Riveros and E. A. Dalchiele, *Sol. Energy Mater. Sol. Cells*, 2004, **82**(1), 21–34.
28. N. Tiwari, G. Khrypunov, F. Kurdzesau, D. L. Bätzner, A. Romeo and H. Zogg, *Prog. Photovoltaics*, 2004, **12**, 33–38.
29. Kampmann, P. Cowache and J. Vedel, *J. Electroanal. Chem.*, 1995, **387**, 53–64.
30. T. Inoue, Y. Watanabe, A. Fujishima and K. Honda, *Proceedings of the Electrochemical Society*, 1977, **7–3**, 210.
31. D. Lincot and J. Vedel, *J. Electroanal. Chem.*, 1987, **220**, 179.
32. M. Dharamdasa, *Coatings*, 2014, **4**, 282.
33. Wallentin, N. Anttu and D. Asoli, *Science*, 2013, **339**, 1057–1060.
34. D. Major, R. E. Treharne, L. J Phillips and K. Durose, *Nature*, 2014, **511**(7509), 334–337.
35. G. Panthani, J. M. Kurley, R. W. Crisp, T. C. Dietz, T. Ezzyat, J. M. Luther and D. V. Talapin, *Nano Lett.*, 2014, **14**(2), 670–675.

V. CuInSe₂ NANOTUBE ARRAYS FOR EFFICIENT SOLAR ENERGY CONVERSION

Manuscript has been submitted to Materials Science and Engineering: B

Wipula Priya Rasika Liyanage, Manashi Nath*

Department of Chemistry, Missouri University of Science and Technology, Rolla, MO 65409 USA. * Corresponding author e-mail: nathm@mst.edu

ABSTRACT

Highly uniform and vertically aligned *p*-type CuInSe₂ (CISE) nanotube array were fabricated through a unique protocol, incorporating confined electrodeposition on lithographically patterned nanoelectrodes. This protocol can be readily adapted to fabricate nanotube arrays of other photoabsorber and functional materials with precisely controllable design parameters. Ternary CISE nanotube arrays were electrodeposited from a single electrolytic bath and the resulting nanotube arrays were studied through powder X-ray diffraction as well as elemental analysis which revealed compositional purity. Detailed photoelectrochemical (PEC) characterizations in a liquid junction was also carried out to investigate the photoenergy conversion properties. It was observed that the tubular geometry had a strong influence on the photocurrent response and a 29.9% improvement to the photo conversion efficiency was observed with the nanotube array compared to a thin film geometry fabricated by the same process while the photoactive material coverage of the nanotube morphology was only a fraction (~10%) of the thin film device. This technique provides ample opportunities to study novel photovoltaic

materials and device design architectures where structural parameters plays a key role such as resonant light trapping.

1. INTRODUCTION

There has been a rapid increase of nanostructured solar cell research over the past few years owing to their promising potential of increasing photoconversion efficiency. In this regard, nanoparticles have been widely explored as potential candidates for nanostructured photovoltaic (PV) solar cells due to their high surface area [1-4]. However, inefficient light scattering ability due to the small size of the nanostructured photoabsorbers (10-30nm) and increased charge recombination due to electron scattering at particle boundaries has prevented their efficiency improvement [5-7]. On the other hand, solar cells having high aspect ratio architectures of the photoabsorbers such as nanorods and nanowires (NW) have been reported to possess inherent advantages over conventional thin film devices [8-12]. The ability to fabricate solar cells with a larger tolerance of lattice-mismatched materials [13, 14] and the intrinsic strain relaxation property along with the greater absorption cross section make NWs prospective candidates for the fabrication of low-cost and highly efficient solar cells [15]. In addition, well aligned nanowires have shown outstanding charge transport properties in solar cell applications [16-21].

Likewise, porous geometry consisting of periodically arranged nanoholes has also attracted significant attention as a surface modification technique of solar cells since these types of architectures have demonstrated efficient light trapping [22-25] leading to

improved photoconversion efficiency. Such improvements have been numerically simulated and experimentally demonstrated in reports [26-29]. Therefore, a photovoltaic device that can combine high aspect ratio nanostructure along with the nanohole geometry can expectedly lead to enhanced efficiency by combining the advantages of both of those architectures.

A well oriented array of photoabsorber nanotubes can be considered to be a combined architecture of nanohole and nanowire arrays. However, one should be able fabricate such well-ordered vertically oriented nanotube arrays systematically with well controlled physical parameters such as nanotube wall thickness, diameter, length and distribution pattern to observe the changes of photoconversion efficiency as a function of variation of structural parameters in order to optimize efficiency. Nevertheless, there are only a few reports available for such fabrication methods for vertically oriented nanostructure arrays which often involves the assistance of a hard template such as anodized aluminum oxide (AAO) or ZnO. Removal of such hard templates for exposing full functionality of the nanostructure arrays requires harsh conditions similar to highly acidic or basic treatments that can be detrimental to the fabricated photovoltaic semiconductor performance. It must be noted here that although nanowire arrays using AAO membranes [30-33] and nanotube arrays have been reported in the literature previously [34-37], there is no reports of simple procedures for nanotube fabrication with pre-determined parameters.

In the present study, we report a facile route for the direct fabrication of highly oriented CuInSe₂ nanotube arrays to investigate the advantage of both the aspect ratio and the nanohole architecture on the photoconversion efficiency. Our fabrication technique

involving confined electrodeposition on lithographically patterned nanoelectrodes, allows us to precisely control structural parameters such as tube length, diameter, tube wall thickness, array distribution density and periodicity which can then be optimized for achieving maximum efficiency.

To the best of our knowledge, this is the first reports on CuInSe₂ nanotube arrays without numerous steps for fabrication and greatest flexibility on structure parameters for customized fabrication. Additionally, there is no need of template removal using highly acidic or basic conditions which limit their emergence as a scalable process. The results obtained from the photoelectrochemical characterization of the CuInSe₂ nanotube arrays in this report has been compared with a thin-film solar cell morphology fabricated by the same process under similar conditions. In addition, the investigation of morphology, structure, composition, and optical properties are reported.

2. EXPERIMENTAL SECTION

2.1. GROWTH OF NANOTUBES

The CISE nanotubes were grown on indium tin oxide (ITO) coated conducting glass substrates by electrodeposition technique using an Iviumstat potentiostat according to a protocol recently developed by the authors and refers to as confined electrodeposition on lithographically patterned nanoelectrodes (see ref. [38] for detailed process). In this protocol, first the desired array of nanoelectrodes with specific size and shape were patterned via electron beam lithography using Raith eLINE Plus nanolithography system.

The patterns were revealed on the surface of the ITO-glass after developing the substrate following e-beam exposure. A chemical bath containing Cu, In and Se precursors was prepared according to a reported procedure for CuInSe₂ thin film deposition [39] along with some modifications. A typical deposition bath consisted of 0.5 mM CuCl₂, 2.0 mM SeO₂ and 6.0 mM InCl₃ with 0.1 M KCl as the supporting electrolyte in deionized water. After the solution was prepared 0.5M HCl was added to adjust the solution pH to 2.

An IviumStat.h high power electrochemical set-up consisted of a conventional three electrode system comprising patterned substrate as the working electrode, a platinum mesh as the counter electrode and Ag/AgCl electrode as the reference was used. Electrodes were vertically dipped in the electrolytic bath and electrodeposition was carried out under chronoamperometric conditions in stirred solution at room temperature for 20 s. In our experimental conditions, an applied potential of -0.7 V vs Ag/AgCl produced the optimal composition. After growth, the nanotube arrays were thoroughly washed with deionized water to remove any residues from the precursor solution and dried under a stream of nitrogen gas.

A layer of CdS has been widely used as the n-type layer of thin film CuInSe₂ solar cells [40-44] to create a p-n junction to effectively separate photo-generated electron hole pairs and is typically fabricated by chemical bath deposition (CBD). A uniform layer of CdS was thus obtained under well-controlled CBD conditions using a reported procedure [45]. The CBD process was carried out at 60 °C for 20 min to achieve a ~80 nm thick uniform layer. Low temperature or shorter time resulted in CdS films of

low thickness. CISE nanotube arrays having a p-n junction was obtained by growing these nanotube arrays on nanoelectrodes patterned on CdS coated ITO glass.

3. CHARACTERIZATION OF NANOTUBES

Morphology and composition analysis of the nanotube arrays were carried out by using Helios Nanolab-600 scanning electron microscope (SEM) equipped with Energy Dispersive Analysis of X-ray (EDAX) detector (Oxford instruments) for elemental analysis. High resolution transmission electron microscopy (HRTEM) images and selected area electron diffraction (SAED) patterns were obtained using Tecani F20 Transmission electron microscope. X-ray diffraction patterns were collected using PANalytical's X'Pert PRO Materials Research Diffractometer (MRD) employing Cu K α radiation ($\lambda = 1.5418 \text{ \AA}$) at grazing incidence angles for the analysis of the crystal structure. Optical properties were studied with Cary 5 UV-Vis-NIR spectrophotometer. Photoelectrochemical (PEC) characterization, impedance and Mott-Schottky measurements of the nanotube arrays were performed using the IviumStat.h potentiostat and the light irradiation was provided with a 400 W Xe lamp with a light intensity of 100 mW/cm². The electrolyte for photoelectrochemical measurement consisted of 0.1 M aqueous solutions of sodium sulfite, sodium sulfate, sodium acetate and the solution pH was adjusted to 4.6 with acetic acid [46]. Measurements were taken with the three electrode configuration as explained earlier using nanotube array as the working electrode.

4. RESULTS AND DISCUSSION

4.1. COMPOSITION, MORPHOLOGY AND CRYSTAL STRUCTURE

In general, the overall composition of the electrodeposited CISe depends on the relative concentrations of the precursor ions in the deposition bath and the applied potential. It has been reported previously that the deposition rates of Cu, In and Se varies with deposition time and applied potential [47]. Further, it has been reported that, under chronoamperometric conditions, during the first few minutes of deposition, there is a decrease in the In content while selenium content was increased in the deposition before achieving a constant composition. On the other hand, when the applied potential was increased the opposite trend was observed [47]. However, it has been shown that high quality CISe devices can be fabricated with a range of compositions around the stoichiometric point [48]. Nevertheless, in our experiments, the observed composition changes in the deposition were minimum (less than 3%) since the deposition time was much less (~60s) to observe such a change compared to longer deposition times used in thin film deposition [39,47]. The deposition bath was also stirred very well to avoid limitations due to diffusion. Shorter deposition time and constant stirring also helped to avoid local pH variations near the working electrode and hence, avoid evolution of gaseous hydrogen and formation of indium hydroxide on the working electrode. Therefore, complexing agents such as citrates to maintain constant composition of the deposition and pH buffers to avoid pH variations were not required during the deposition process. In addition, at pH 2.0, the 0.1 M KCl added to the deposition bath acted as a background electrolyte to increase conductivity of the bath and also low pH to help

prevent the formation of insoluble species such as indium hydroxide in the electrolytic bath.

An SEM image of as-deposited nanotube arrays has been presented in Figure 1 showing the formation of uniform nanotubes exclusively on the patterned nanoelectrodes without any sideward growth or inter-space. The polymer coverage adjacent to the patterned nanoelectrodes confines the formation of the nanotubes during electrodeposition of the CISE inside the columnar channels and perpendicular to the substrate thereby leading to the formation of a highly oriented, vertical array of uniform nanotubes.

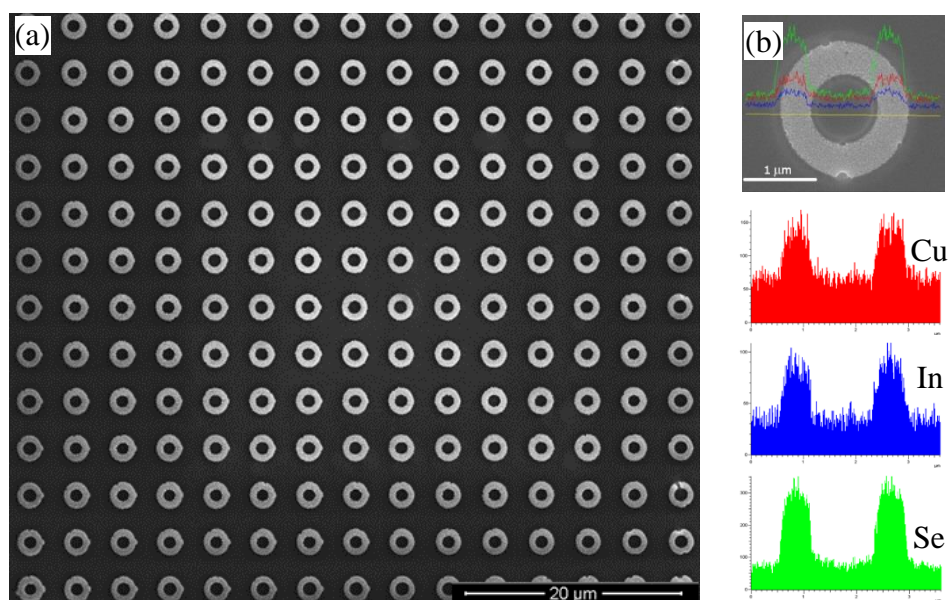


Figure 1. Morphology and composition. SEM image of (a) view from top of an array of fabricated CISE nanotubes. (b) EDAX line scan across a single nanotube indicating the Cu, In and Se elements.

The elemental analysis of as-deposited array by EDAX shows a near stoichiometric composition of CuInSe₂ with a slight excess of Cu which also indicates that the deposit is *p*-type [48, 49]. Figure S1(a) (supporting information) shows a tilted view of the pattern indicating the growth of these arrays up to the top surface of the polymeric resist and Figure S1(b) (supporting information) shows a pattern that is intentionally damaged to better demonstrate the cross sectional view of tubular nature and the vertical alignment of the structure. Figure S2 (supporting information) shows a pattern that is covering a larger area and indicate the uniformity of the array.

Furthermore, it can be seen that due to the presence of polymer on the substrate, no CISE deposition takes place in other areas except on patterned nanoelectrodes. Therefore, structural parameters of fabricated nanotube arrays such as tube diameter, thickness of the nanotube walls, packing density as well as the distribution pattern of the array can conveniently be controlled by making desired adjustments to the writing pattern defined during the e-beam lithography process.

This illustrates the novelty of this protocol to fabricate uniform nanotube arrays with pre-determined structure parameters. Analysis of the material from nanotube arrays under HRTEM and selected area electron diffraction (SAED) pattern shown in Figure 2 reveals the crystalline nanotubes are dominated by (112) planes. Crystal structure of the nanotube arrays was further examined by PXRD analysis. To obtain clean PXRD pattern, the CISE array was fabricated on Au coated glass substrates to avoid overlapping XRD peaks from the ITO background.

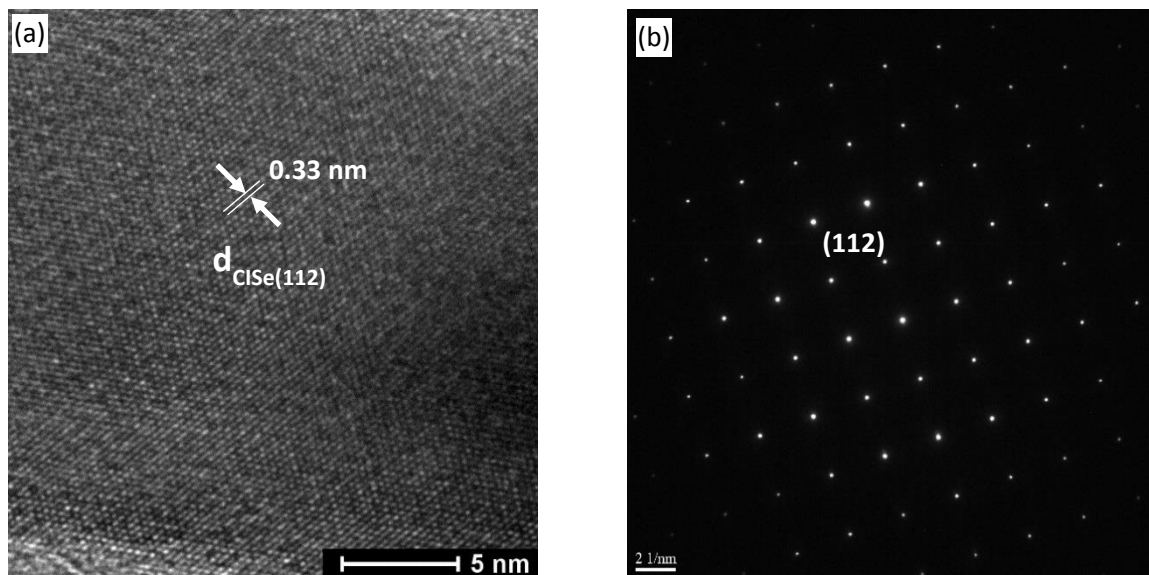


Figure 2. HRTEM image and SAED pattern showing dominant (112) crystal lattice fringes of CISe

Crystallinity of the deposition was further improved upon annealing at 400 °C for 10 minutes in N₂ saturated atmosphere [50, 51]. The crystallinity would improve further if annealing was carried out for an extended period of time however, it also can lead to the loss of Se from the structure and therefore, additional annealing was not carried out. As shown in Figure 3, the PXRD pattern matched with the standard chalcopyrite phase of CISe (JCPDS 35-1102).

Other secondary phases such as Cu₂Se, CuSe or In₂Se₃ or other impurity peaks were not observed in the PXRD pattern indicating the phase purity of the sample. In addition, an average crystalline domain size of 20 nm was calculated taking into consideration the observed peak broadening in the obtained PXRD pattern by using the Scherrer equation [52].

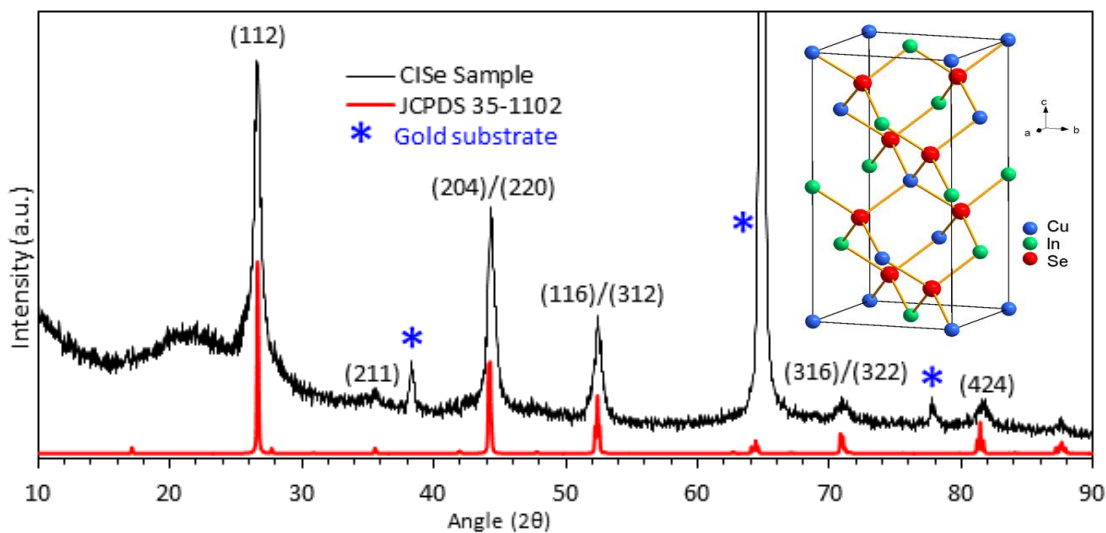


Figure 3. XRD pattern of an array of CISe nanotubes. The spectra of the sample matches well with the chalcopyrite structure of CISe (JCPDS 35-1102). The peaks labelled with an asterisk are from the gold substrate.

4.2. OPTICAL PROPERTIES

Prepared nanotube arrays were examined using UV-Vis-NIR absorption spectroscopy to investigate optical properties. The absorption spectrum as given in Figure 4 shows a significant absorption in the visible region, which has been reported previously as also originating from the nonbonding copper $3d$ localized states [53], suggesting suitability of the device for use in entire solar spectrum. Measured absorption coefficient values over the visible region is in the range of 10^4 cm^{-1} and that lies in the range of reported literature values for CISe [54-56]. The absorption curve has a characteristic tail in the long wavelength region which is typically observed in single crystalline and polycrystalline direct band gap materials such as CISe. Such auxiliary absorption was well explained using photon assisted transition and Dow-Redfield model referring to the electric fields emerging from grain boundaries in polycrystalline materials [57]. In

addition structural defects in grains and grain boundaries can also lead to gap states inside the band edges which shows transitions in longer wavelength regions. When CISE samples are substantially heat treated at high temperature, it is known that loss of selenium occurs leading to selenium vacancies in the structure. In this case, an additional transition has observed in the low energy absorption region [58] and this sub band response was not observed from our nanotube device.

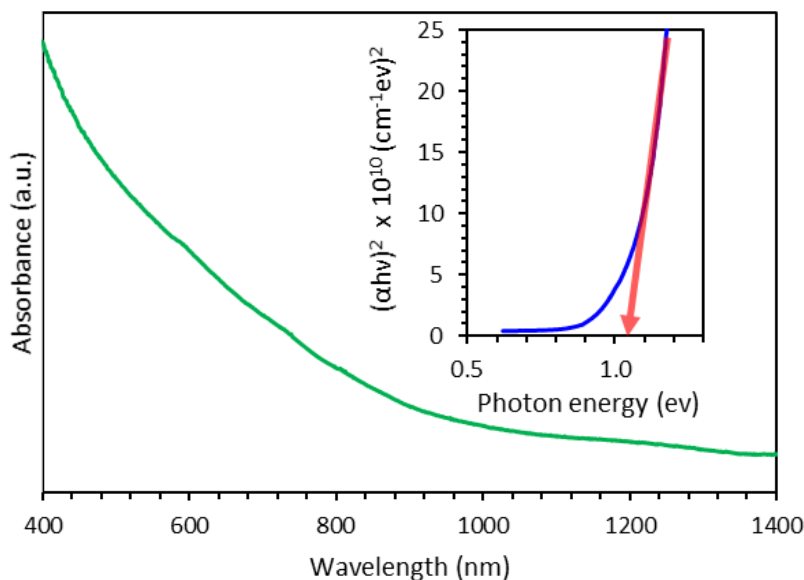


Figure 4. Absorption spectrum of the CISE nanotube arrays. It shows significant absorption over the visible region and the inset shows the corresponding plot prepared for optical band gap determination considering the variation of the absorption coefficient with the photon energy.

Optical bandgap, E_g , was determined considering the variation of absorption coefficient, α , with the photon energy, $h\nu$, using the plot of $(\alpha h\nu)^2$ vs $h\nu$ according to the classical relation $(\alpha h\nu)^2 = A(h\nu - E_g)$ where A is a constant and the other symbols have

their usual meaning. The linear region of the plot near the absorption edge was extrapolated to $(\alpha h\nu)^2 = 0$ to obtain the optical band gap energy as indicated in the inset of Figure 3. The band gap of the nanotube arrays was determined to be 1.04 eV which corroborates very well with the observed CISE band gap energies at room temperature as reported in literature [54, 59,60].

4.3. PHOTOELECTROCHEMICAL (PEC) STUDY OF THE NANOTUBE ARRAY

A PEC analysis of the nanotube array was carried out in an acetate buffered electrolyte solution following a reported procedure [46] where a redox couple forms a liquid junction with the top surface of the nanotubes. The presence of polymeric e-beam resist covering the inter-space of nanotube arrays provide an added advantage by providing a barrier between the liquid and the back contact layer of the nanotube arrays. Otherwise, a significant shunt conduction will produce as a result of the contact of the electrolyte and the back electrical contact. A typical electrochemical bath consisted of 0.1 M solutions of sodium acetate, sodium sulfite and sodium sulfate and the pH was adjusted to 4.6 with acetic acid. The conventional three electrode electrochemical set up with a platinum mesh as a counter electrode, Ag/AgCl as the reference electrode and the fabricated nanotube array as the working electrode was used in the experiment. The illumination for the nanodevice was provided with a Xenon lamp working in UVA zone (320 – 390 nm) with an intensity of 100 mW/cm². The photochemical activity of the nanotube arrays was compared with a CISE thin film deposited on ITO-coated glass using similar procedure as described above.

Figure 5 shows the photocurrent response of the nanotube arrays compared with a thin film geometry of CISE fabricated by the same process. Current response of the devices were monitored while a potential scan was applied from +0.3 V to -0.6 V vs Ag|AgCl at a scan rate of 5 mV/s. The illumination to the devices were turned off and on periodically to record the dark current and the photocurrent responses, respectively. When the devices are illuminated a rapid increase of the cathodic current was observed and when the illumination was turned off, a rapid decrease of the current was observed confirming the generation of photocurrent in response to illumination. Typically for *p*-type materials, cathodic current is observed under illuminated conditions since the photogenerated electron transfer take place from the conduction band of the semiconductor to the oxidant in the solution [61,62]. However, the origin of electrons for increased dark current under continues scan to the cathodic direction for *p*-type materials has explained to be through valance band and the mechanism by which they arrive at the surface has correlated to the band bending at the electrochemical interphase under reduction conditions[61,63]. The stability of the photocurrents were monitored by chronoamperometric method where the light source was turned on and off at constant intervals under a constant applied potential.

Stable photocurrent could be obtained from the nanotube array for an extended period of time as shown in Figure5(c) and it also was noted that the fabricated nanotube arrays were stable in the electrochemical bath and did not undergo degradation under the experimental conditions. It is known that the acetate buffer solution can act as an efficient hole scavenger to prevent degradation of semiconducting material [46].

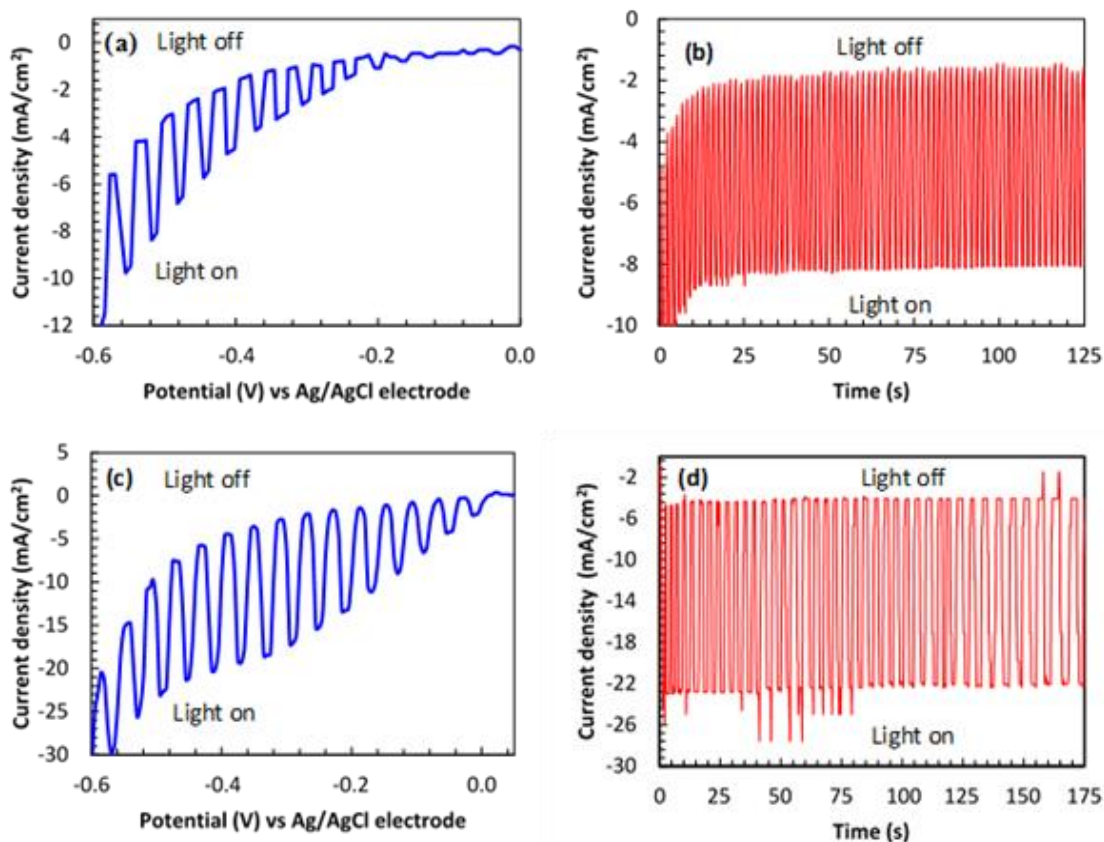


Figure 5. PEC characterization. (a) PEC response of the thin film devices when the light source was turned on and turned off periodically under a potential sweep (b) Stability of the photo response of the thin film measured at an applied potential of -0.5V. (c) On- off response of the nanotube device under a potential sweep (d) Stability of the photocurrent of the nanotube device measured under applied potential of -0.5V

Further analysis was carried out with nanotube arrays to understand photovoltaic behavior by fabricating PEC solar cell devices to measure photo conversion efficiency (η) taking into consideration the short circuit current density (J_{sc}), open circuit voltage (V_{oc}) and fill factor (FF). A heterojunction was made to the device by coating an *n-type* CdS buffer layer (~80nm) on ITO glass by CBD method before fabricating nanotube arrays to improve separation of photo generated electron-hole pairs and suppress the

recombination. As shown in the current density voltage (JV) plot given in Figure 6 and the summarized data given in Table 1, the cell fabricated with nanotube arrays could achieve a higher photo conversion efficiency (8.85%) compared to a thin film solar cell device (6.82%) fabricated by the same procedure. It can also be observed that even though the V_{oc} is very close to each other for the two types of solar cell geometries, when the morphology is changed to a tubular architecture, there is a notable enhancement of the J_{sc} and the FF for the nanotube array solar cell achieving ~30% increase in photo conversion efficiency compared to the thin film device. It should be noted that in addition to the improved performance, the nanotube array device has much less photo active material coverage (~10%) on the electrode surface area compared to the thin film device which covers the entire electrode surface area.

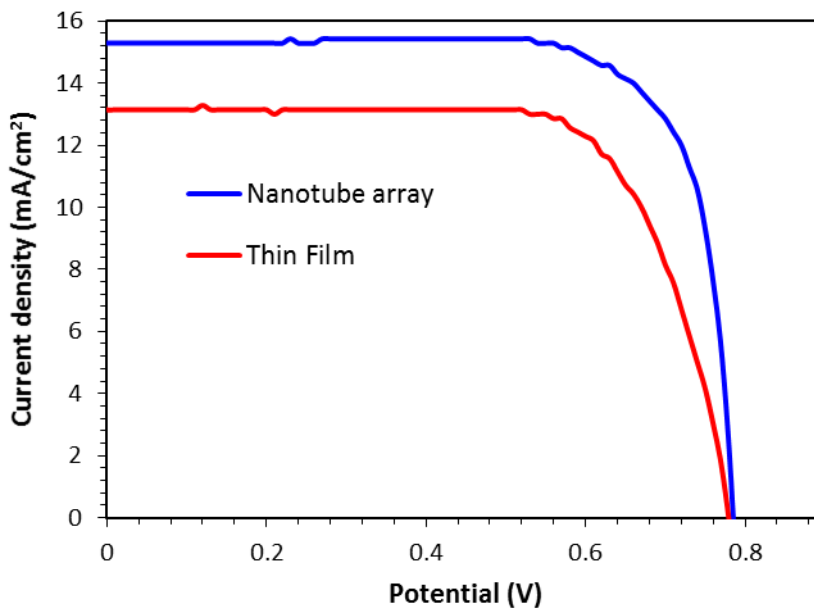


Figure 6. A comparison of the photo current voltage (JV) performance of the CISE nanotube array and thin film devices.

Table 1. Summary of PV performance and impedance parameters of the CISE devices

CISE geometry	$J_{SC}/mAcm^{-2}$	V_{OC}/mV	FF	$\eta\%$	R_s/ohm	$R_{ct}/kohm$	CPE/Fcm^{-2}
Nanotube array	15.28	78.5	75.78	8.86	11.69	1.22	7.1×10^{-3}
Thin film	13.14	77.9	67.26	6.82	15.95	2.84	5.5×10^{-5}

The enhanced performance is likely due to the shortened carrier transport length coupled with the better light scattering ability and enhanced light trapping of the nanotube array geometry which improve effective photoabsorption. Similar results have been previously reported for InP nanowire arrays where, 83% of the J_{SC} obtained from a thin film device was achieved by nanowire arrays despite material coverage of ~12% [15]. In addition, it has been demonstrated that CdSe nanowire arrays shows higher minority carrier collection efficiency and has the ability to absorb low energy photons more efficiently than thin film electrodes fabricated to the similar thickness [64].

Enhancement of the fill factor in the nanotube array device can be related to the enhanced charge transport across the junction which often produce a competition between minority carrier collection across the junction and the surface recombination [63]. The combination of one-electron transfer redox couple with the increased junction area due to the tubular architecture of the device therefore, improves charge transfer across the junction compared to the surface recombination because, at a given illumination intensity, the minority carrier flux density decreases as the surface area of the junction increases. This lead to an enhanced fill factor in the nanotube device compared to the thin film device as observed in this experiment. Our devices show a

proof of concept that CISE nanotube arrays can be fabricated by this method and shows a base line performance. The significantly improved photoconversion efficiency shown by the CISE nanotube array indicates that this tubular morphology can be further tuned to increase photoconversion efficiency by manipulating physical parameters such as nanotube pore diameter, wall thickness, and distribution pattern of the array to further improve light scattering, photoabsorption and light trapping with the aid of some simulation studies since this fabrication protocol has the capability to make arrays with pre-determined parameters.

Electrochemical Impedance Spectroscopy (EIS) analysis was carried out with the nanotube device which showed a typical Nyquist curve as shown in Figure 7a, and the charge transfer resistance (R_{ct}), solution resistance (R_s) and constant phase element (CPE) indicating the double layer capacitance was determined by fitting the measured impedance data in to an equivalent circuit model. Evaluated EIS parameters have been summarized in Table 1. The nanotube array showed a much less charge transfer resistance and higher double layer capacitance than that of thin film geometry which can in turn lead to a higher current density shown by the nanotube array due to the efficient carrier generation and transport provided by the tubular geometry.

Figure 7(b) shows the Mott-Schottky plot calculated from the EIS data by considering the capacitance, C , vs applied potential at 1000 Hz, 500 Hz and 250 Hz frequencies with a small AC amplitude (10mV) at each potential [62]. The analysis was carried out in the dark and the negative slope of the linear fit confirms that nanotube arrays are p -type supporting the observed cathodic photocurrent in the photoelectrochemical measurements.

The flat band potential was obtained from the intercept of the slope with the x-axis of the line drawn through the linear region of the 1000 Hz data. The flat band potential obtained at -0.03 V (vs Ag/AgCl electrode), is in good agreement with the observed photocurrent onset potentials of the photoelectrochemical measurements. Generally, there is an increase in the resistive component of the electrode with applied potential in the dark due to the formation of a depletion layer consisting of immobile charges in the double layer region.

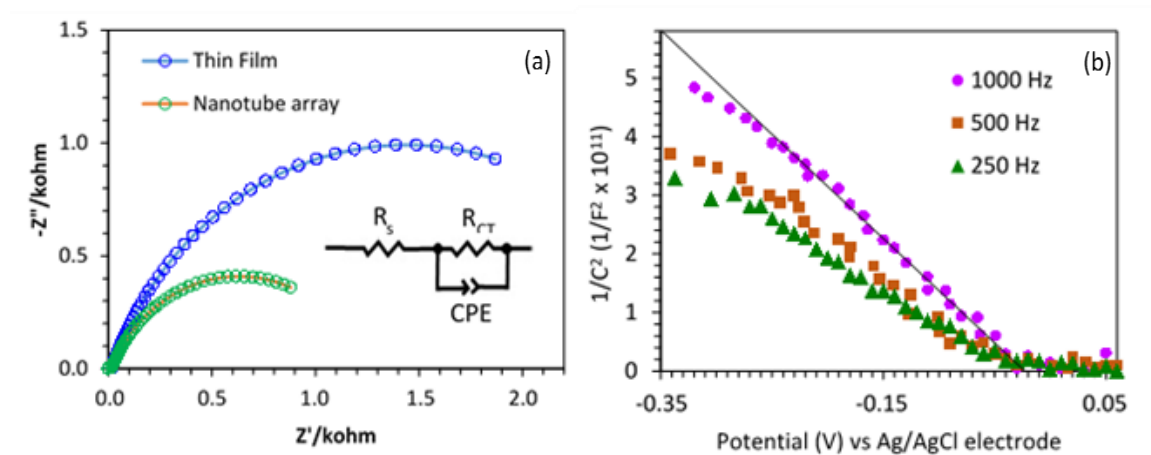


Figure 7. Electrochemical Impedance Spectroscopy. (a) Nyquist plots of nanotube array and the thin film device with the corresponding equivalent circuit as the inset. (b) Mottshottky plots of the CISe nanotube array in the dark. Data was recorded at 1000 Hz, 500 Hz and 250 Hz and the line was drawn considering the linear region of the 1000 Hz data.

Since free carriers are formed under illumination, this resistance is eliminated.

Therefore, the position of the flat band can be considered as the point where onset of the photocurrent starts eliminating this resistance [61].

5. CONCLUSIONS

We demonstrate a simple protocol for the direct fabrication of CISE nanotube arrays on a conducting substrate with controllable design parameters without using hard templates such as Anodic Aluminum Oxide or other sacrificial templates. Use of e-beam lithography on the patterning process enables one to utilize the potential of this ever-growing powerful technique to manipulate all the key design parameters of the nanotube array such as pore diameter, wall thickness, distribution pattern, distribution density, etc., for optimizing the photo absorption and maximizing the efficiency to obtain highly efficient photo devices. The e-beam resist used in the process provides a soft and flexible matrix for the growth of vertically aligned nanotube arrays and the thickness of the resist can be used to control the length of the nanotubes. The photoelectrochemical measurements showed that these nanotube arrays are capable of producing higher current densities despite the use of much less active material coverage compared to thin film devices making it is possible to use expensive materials for photo conversion at a lower cost. The strong influence for the photo conversion by nanotube array can be caused by the elongated effective absorption length through multiple scattering of light by tubular architecture of the array and short carrier transport distance. In general, we believe the present work as a source for further studies and this concept would be very useful in energizing nanodevices as well as fabricating highly sensitive photodetectors and various other optoelectronic devices. Further improvements to the PV performance can be made by the application of surface passivation layers and optimizing the thickness of the buffer layer to minimize recombination losses. Another avenue for improvement is the

introduction of Ga to the system so that the bandgap can be manipulated for a broad light harvesting range. These changes are continuing for further studies.

ACKNOWLEDGEMENTS

The authors would like to acknowledge University of Missouri Research Board for sponsoring this research and MRC for equipment usage.

SUPPLEMENTARY INFORMATION

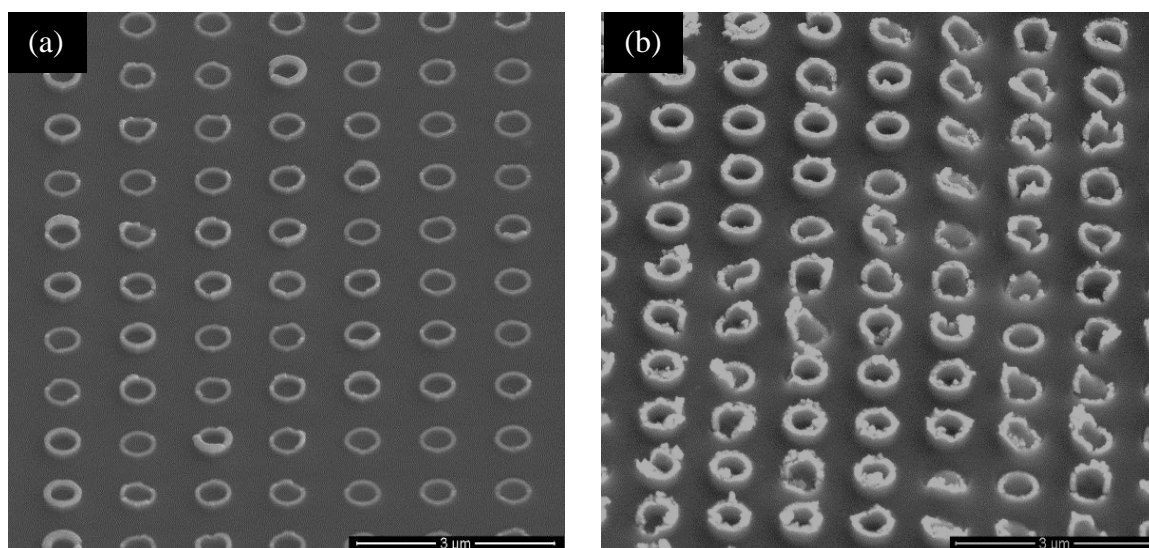


Figure S1. view from SEM at an angle. (a) a tilted view of a CIGSe nanotube array showing the growth of tubes to the top limit of the polymer layer. (b) an array of nanotubes was scratched and some polymer was removed to show the cross sectional view of tubes.

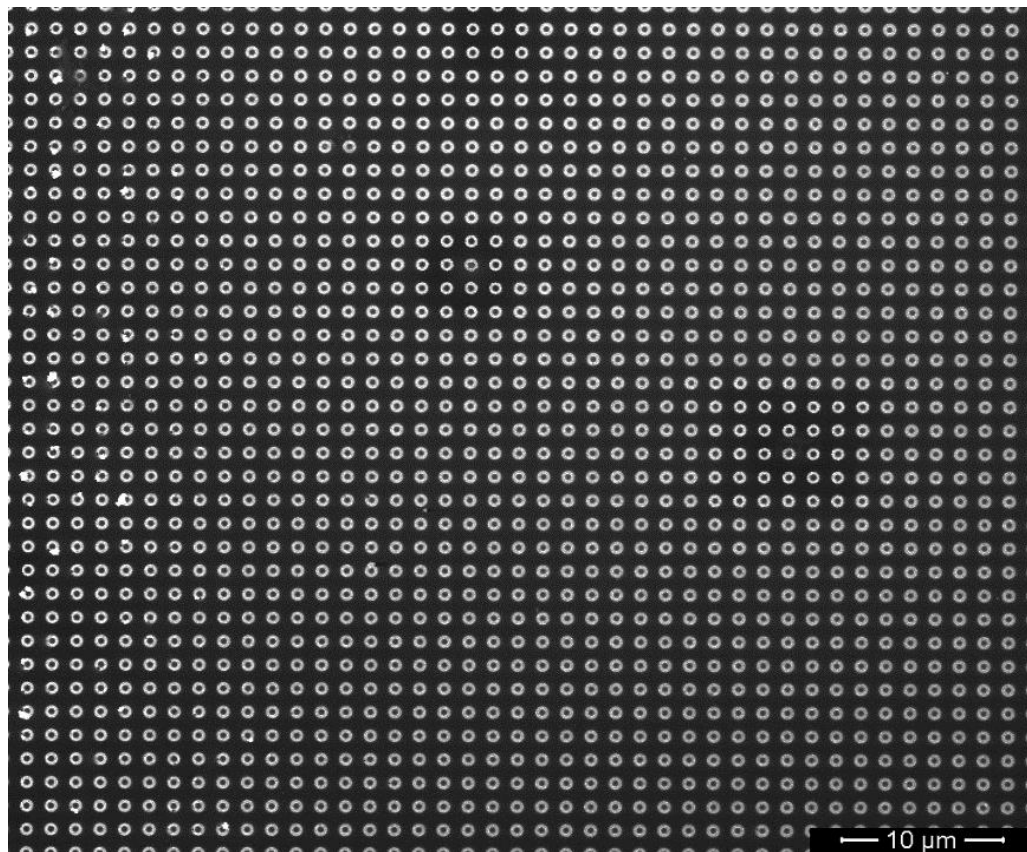


Figure S2. SEM image of a CISe nanotube array covering a larger area. It shows the uniformity of the array indicating the ability of this protocol to fabricate nanotube arrays with accurate structure parameters.

REFERENCES

1. Lin, X., Kavalakkatt, J., Ennaoui, A., & Lux-Steiner, M. C. (2015). Cu₂ZnSn(S, Se)₄ thin film absorbers based on ZnS, SnS and Cu₃SnS₄ nanoparticle inks: Enhanced solar cells performance by using a two-step annealing process. *Solar Energy Materials and Solar Cells*, 132, 221-229.
2. Li, S., Li, W., Liu, Q., Wei, H., Jin, E., Wang, H., & Wang, M. (2015). Spin-coated Ag nanoparticles onto ITO substrates for efficient improvement of polymer solar cell performance. *J. Mater. Chem. C*, 3(6), 1319-1324.

3. Lan, X., Voznyy, O., Kiani, A., García de Arquer, F. P., Abbas, A. S., Kim, G. H., & Yuan, M. (2016). Passivation Using Molecular Halides Increases Quantum Dot Solar Cell Performance. *Advanced Materials*, 28(2), 299-304.
4. Kim, H. J., Lee, H. D., Rao, S. S., Reddy, A. E., Kim, S. K., & Thulasi-Varma, C. V. (2016). Well-dispersed NiS nanoparticles grown on a functionalized CoS nanosphere surface as a high performance counter electrode for quantum dot-sensitized solar cells. *RSC Advances*, 6(35), 29003-29019.
5. Ye, M., Zheng, D., Lv, M., Chen, C., Lin, C., & Lin, Z. (2013). Hierarchically Structured Nanotubes for Highly Efficient Dye-Sensitized Solar Cells. *Advanced Materials*, 25(22), 3039-3044.
6. Docampo, P., Guldin, S., Steiner, U., & Snaith, H. J. (2013). Charge transport limitations in self-assembled TiO₂ photoanodes for dye-sensitized solar cells. *The journal of physical chemistry letters*, 4(5), 698-703.
7. Park, K., Zhang, Q., Myers, D., & Cao, G. (2013). Charge transport properties in TiO₂ network with different particle sizes for dye sensitized solar cells. *ACS applied materials & interfaces*, 5(3), 1044-1052.
8. Han, N., Yang, Z. X., Wang, F., Dong, G., Yip, S., Liang, X., & Ho, J. C. (2015). High-performance GaAs nanowire solar cells for flexible and transparent photovoltaics. *ACS applied materials & interfaces*, 7(36), 20454-20459.
9. Armstrong, J. C., & Cui, J. B. (2015). Three-dimensional structures based on ZnO/CdS and ZnO/(Zn, Mg) O core-shell nanowires embedded in Cu (In, Ga) S₂ for solar cell applications. *Solar Energy Materials and Solar Cells*, 141, 356-363.
10. Li, Y., Qian, F., Xiang, J., & Lieber, C. M. (2006). Nanowire electronic and optoelectronic devices. *Materials today*, 9(10), 18-27.
11. Caselli, D., Liu, Z., Shelhammer, D., & Ning, C. Z. (2014). Composition-graded nanowire solar cells fabricated in a single process for spectrum-splitting photovoltaic systems. *Nano letters*, 14(10), 5772-5779.
12. Nowzari, A., Heurlin, M., Jain, V., Storm, K., Hosseinnia, A., Anttu, N., & Samuelson, L. (2015). A comparative study of absorption in vertically and laterally oriented InP core-shell nanowire photovoltaic devices. *Nano letters*, 15(3), 1809-1814.
13. Heurlin, M., Wickert, P., Fält, S., Borgström, M. T., Deppert, K., Samuelson, L., & Magnusson, M. H. (2011). Axial InP nanowire tandem junction grown on a silicon substrate. *Nano letters*, 11(5), 2028-2031.

14. Mårtensson, T., Svensson, C. P. T., Wacaser, B. A., Larsson, M. W., Seifert, W., Deppert, K., & Samuelson, L. (2004). Epitaxial III– V nanowires on silicon. *Nano Letters*, 4(10), 1987-1990.
15. Wallentin, J., Anttu, N., Asoli, D., Huffman, M., Åberg, I., Magnusson, M. H. & Xu, H. Q. (2013). InP nanowire array solar cells achieving 13.8% efficiency by exceeding the ray optics limit. *Science*, 339 (6123), 1057–1060
16. Wu, J. J., Chen, G. R., Yang, H. H., Ku, C. H., & Lai, J. Y. (2007). Effects of dye adsorption on the electron transport properties in ZnO-nanowire dye-sensitized solar cells. *Applied physics letters*, 90(21), 213109.
17. Adachi, M., Sakamoto, M., Jiu, J., Ogata, Y., & Isoda, S. (2006). Determination of parameters of electron transport in dye-sensitized solar cells using electrochemical impedance spectroscopy. *The Journal of Physical Chemistry B*, 110(28), 13872-13880.
18. Meng, S., Ren, J., & Kaxiras, E. (2008). Natural dyes adsorbed on TiO₂ nanowire for photovoltaic applications: enhanced light absorption and ultrafast electron injection. *Nano letters*, 8(10), 3266-3272.
19. Law, M., Greene, L. E., Johnson, J. C., Saykally, R., & Yang, P. (2005). Nanowire dye-sensitized solar cells. *Nature materials*, 4(6), 455-459.
20. Mishra, S., & Nath, M. (2013). Growth of vertically aligned CdTe nanorod arrays through patterned electrodeposition. *Nano Energy*, 2(6), 1207-1213.
21. Liyanage, W. P. R., & Nath, M. (2015). Growth of Ordered Nanostructure Arrays including Nanotubes and Nanorods for High Efficiency Solar Cells. *ECS Transactions*, 66(40), 1-7.
22. Zhang, A., & Guo, Z. (2016). Efficient light trapping in tapered silicon nanohole arrays. *Optik-International Journal for Light and Electron Optics*, 127(5), 2861-2865.
23. Verschuuren, M. A., de Dood, M. J. A., Stolwijk, D., & Polman, A. (2015). Optical properties of high-quality nanohole arrays in gold made using soft-nanoimprint lithography. *MRS Communications*, 5(04), 547-553.

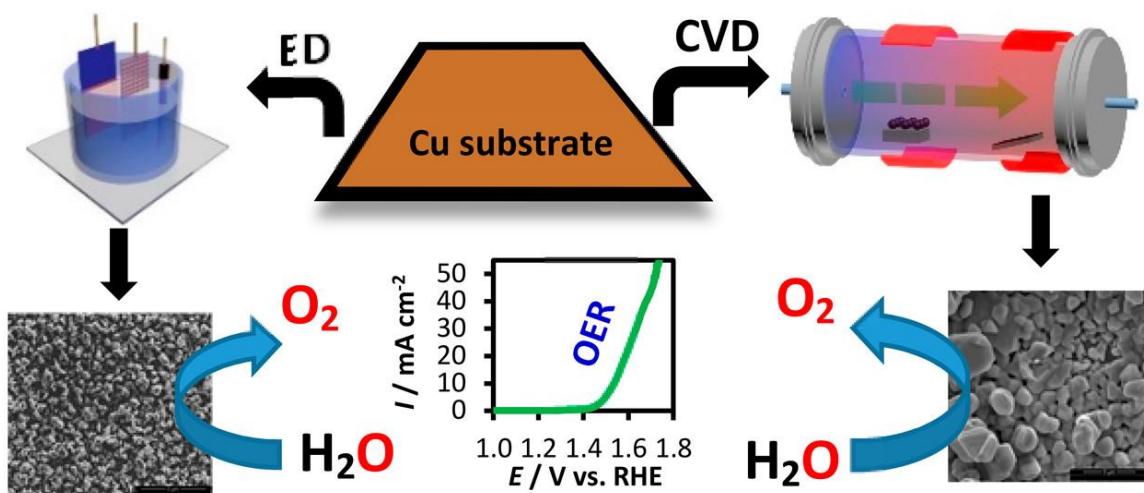
24. Tsakalakos L, Balc J, Fronheiser J, Korevaar BA, Sulima O, Rand J. (2007). Silicon nanowire solar cells. *Applied Physics Letters*; **91**(23): 233117.
25. Buencuerpo, J., Llorens, J. M., Zilio, P., Raja, W., Cunha, J., Alabastri, A., & Versloot, T. (2015). Light-trapping in photon enhanced thermionic emitters. *Optics Express*, 23(19), A1220-A1235.
26. Lin QF, Hua B, Leung SF, Duan XC, Fan ZY. (2013). Efficient light absorption with integrated nanopillar/nanowell arrays for three-dimensional thin-film photovoltaic applications. *ACS Nano* ; **7**(3): 2725–2732.
27. Tan H, Psomadaki E, Isabella O, Fischer M, Babal P, Vasudevan R, Zeman M, Smets AHM. (2013). Micro-textures for efficient light trapping and improved electrical performance in thin-film nanocrystalline silicon solar cells. *Applied Physics Letters* ; **103**(17): 173905.
28. Hu L, Chen G. (2007). Analysis of optical absorption in silicon nanowire arrays for photovoltaic applications. *Nano Letters*; **7**(11): 3249–3252.
29. Li J, Yu H, Wong SM, Li X, Zhang G, Lo PGQ, Kwong DL. (2009). Design guidelines of periodic Si nanowire arrays for solar cell application. *Applied Physics Letters* ; **95**(24): 243113.
30. Neetzel, C., Ohgai, T., Yanai, T., Nakano, M., & Fukunaga, H. (2017). Uniaxial Magnetization Performance of Textured Fe Nanowire Arrays Electrodeposited by a Pulsed Potential Deposition Technique. *Nanoscale research letters*, 12(1), 598.
31. An, B. H., Orabi, L., Lee, J. S., Mansouri, M. S., Al-Mansoori, M., Kim, Y. K., & Choi, D. S. (2018). Electrochemical synthesis of CuIn (1– x) Ga_xSe₂ nanowires with controlled stoichiometry. *Materials Letters*, 211, 149-152.
32. Wang, C. E., Tanaka, S., Shimizu, T., & Shingubara, S. (2014). Fabrication of vertical Cu₂ZnSnS₄ nanowire arrays by two-step electroplating method into anodic aluminum oxide template. *Journal of Materials Science & Nanotechnology*, 1, S103.
33. Wen, L., Xu, R., Mi, Y., & Lei, Y. (2017). Multiple nanostructures based on anodized aluminium oxide templates. *Nature nanotechnology*, 12(3), 244.

34. Wang, Q., Qiao, J., Zhou, J., & Gao, S. (2015). Fabrication of CuInSe₂ quantum dots sensitized TiO₂ nanotube arrays. *Electrochimica Acta*, *167*, 470-475.
35. Schoen, D. T., Peng, H., & Cui, Y. (2013). CuInSe₂ nanowires from facile chemical transformation of In₂Se₃ and their integration in single-nanowire devices. *Acs Nano*, *7*(4), 3205-3211.
36. Xu, J., Luan, C. Y., Tang, Y. B., Chen, X., Zapien, J. A., Zhang, W. J. & Lee, C. S. (2010). Low-temperature synthesis of CuInSe₂ nanotube array on conducting glass substrates for solar cell application. *ACS nano*, *4*(10), 6064-6070.
37. Peng, H., Xie, C., Schoen, D. T., McIlwrath, K., Zhang, X. F., & Cui, Y. (2007). Ordered vacancy compounds and nanotube formation in CuInSe₂-CdS core-shell nanowires. *Nano Letters*, *7*(12), 3734-3738.
38. Liyanage, W. P. R., & Nath, M. (2016). CdS-CdTe heterojunction nanotube arrays for efficient solar energy conversion. *Journal of Materials Chemistry A*, *4*(38), 14637-14648.
39. Li, Y., Shaikh, S. S., & Menezes, S. (2012). Film growth mechanism for electrodeposited copper indium selenide compounds. *Thin Solid Films*, *524*, 20-25.
40. Hauschild, D., Kreikemeyer-Lorenzo, D., Jackson, & Weinhardt, L. (2017). Impact of RbF Postdeposition Treatment on the Electronic Structure of the CdS/Cu (In, Ga) Se₂. *ACS Energy Letters*, *2*(10), 2383-2387.
41. Kapur, V. K., Basol, B. M., & Tseng, E. S. (1987). Low cost methods for the production of semiconductor films for CuInSe₂/CdS solar cells. *Solar cells*, *21*(1-4), 65-72.
42. Naghavi, N., Spiering, S., Powalla, M., Cavana, B., & Lincot, D. (2003). High-efficiency copper indium gallium diselenide (CIGS) solar cells (ALCVD). *Progress in Photovoltaics: Research and Applications*, *11*(7), 437-443.
43. Bukowsky, C. R., Grandidier, J., Fountaine, K. T., Callahan, D. M., Stanbery, B. J., & Atwater, H. A. (2017). Photon and carrier management design for nonplanar thin-film copper indium gallium selenide photovoltaics. *Solar Energy Materials and Solar Cells*, *161*, 149-156.

44. Bailie, C. D., Christoforo, M. G., Mailoa, J. P., Bowring, A. R., Unger, E. L., Nguyen, W. H., & Noufi, R. (2015). Semi-transparent perovskite solar cells for tandems with silicon and CIGS. *Energy & Environmental Science*, 8(3), 956-963.
45. Khallaf, H., Oladeji, I. O., Chai, G., & Chow, L. (2008). Characterization of CdS thin films grown by chemical bath deposition using four different cadmium sources. *Thin Solid Films*, 516(21), 7306-7312.
46. Kampmann, A., Cowache, P., Vedel, J., & Lincot, D. (1995). Investigation of the influence of the electrodeposition potential on the optical, photoelectrochemical and structural properties of as-deposited CdTe. *Journal of Electroanalytical Chemistry*, 387(1-2), 53-64.
47. Phok, S., Rajaputra, S., & Singh, V. P. (2007). Copper indium diselenide nanowire arrays by electrodeposition in porous alumina templates. *Nanotechnology*, 18(47), 475601.
48. Rockett, A., & Birkmire, R. W. (1991). CuInSe₂ for photovoltaic applications. *Journal of Applied Physics*, 70(7), R81-R97.
49. Wagner, S.; Bridenbaugh, P. M. (1977). Multicomponent Tetrahedral Compounds for Solar Cells *Journal of Crystal Growth*, 39, 151– 159.
50. Dagan, G., Abou-Elfotouh, F., Dunlavy, D. J., Matson, R. J., & Cahen, D. (1990). Defect level identification in copper indium selenide (CuInSe₂) from photoluminescence studies. *Chemistry of Materials*, 2(3), 286-293.
51. Guillemoles, J. F., Lusso, A., Cowache, P., Massaccesi, S., Vedel, J., & Lincot, D. (1994). Recrystallization of electrodeposited copper indium diselenide thin films in an atmosphere of elemental selenium. *Advanced Materials*, 6(5), 376-379.
52. Patterson, A. L. (1939). The Scherrer formula for X-ray particle size determination. *Physical review*, 56(10), 978.
53. Xiao, J., Xie, Y., Xiong, Y., Tang, R., & Qian, Y. (2001). A mild solvothermal route to chalcopyrite quaternary semiconductor CuIn (SexS_{1-x})₂ nanocrystallites. *Journal of Materials Chemistry*, 11(5), 1417-1420.

54. Sadigov, M. S., Özkan, M., Bacaksiz, E., Altunbaş, M., & Kopya, A. I. (1999). Production of CuInSe₂ thin films by a sequential processes of evaporations and selenization. *Journal of materials science*, 34(18), 4579-4584.
55. Coutts, T. J., and C. R. Osterwald. (1987). The quantum efficiency of CdS/CuInSe₂ solar cells. *Solar Cells* 22.3: 195-209.
56. Kondrotas, R., Colina, M., Guc, M., Neuschitzer, M., Giraldo, S., Alcobé, X., & Pérez-Rodríguez, A. (2017). Towards In-reduced photovoltaic absorbers: Evaluation of zinc-blende CuInSe₂-ZnSe solid solution. *Solar Energy Materials and Solar Cells*, 160, 26-33.
57. Dow, J. D., & Redfield, D. (1970). Electroabsorption in semiconductors: the excitonic absorption edge. *Physical Review B*, 1(8), 3358
58. Khare, N., Razzini, G., & Bicelli, L. P. (1991). Photoelectrochemical, electrolyte electroreflectance and topological characterization of electrodeposited CuInSe₂ films. *Solar cells*, 31(3), 283-295
59. Tuttle, J. R., Albin, D., Matson, R. J., & Noufi, R. (1989). A comprehensive study on the optical properties of thin-film CuInSe₂ as a function of composition and substrate temperature. *Journal of applied physics*, 66(9), 4408-4417.
60. Herrero, J., & Guillen, C. (1991). Study of the optical transitions in electrodeposited CuInSe₂ thin films. *Journal of applied physics*, 69(1), 429-432.
61. Laser, D., & Bard, A. J. (1976). Semiconductor electrodes. IV. Electrochemical behavior of n-and p-type silicon electrodes in acetonitrile solutions. *The Journal of Physical Chemistry*, 80(5), 459-466.
62. Ye, H., Park, H. S., Akhavan, V. A., Goodfellow, B. W., Panthani, M. G., Korgel, B. A., & Bard, A. J. (2010). Photoelectrochemical Characterization of CuInSe₂ and Cu (In_{1-x}Ga_x) Se₂ Thin Films for Solar Cells. *The Journal of Physical Chemistry C*, 115(1), 234-240.
63. Tufts, B. J., Abrahams, I. L., & Lewis, N. S. (1989). Studies of the gallium arsenide/potassium hydroxide-selenium ion (Se²⁻)/selenide semiconductor/liquid junction. *The Journal of Physical Chemistry*, 93(8), 3260-3269.
64. Spurgeon, J. M., Atwater, H. A., & Lewis, N. S. (2008). A comparison between the behavior of nanorod array and planar Cd (Se, Te) photoelectrodes. *The Journal of Physical Chemistry C*, 112(15), 6186-6193.

VI. COPPER SELENIDES AS HIGH-EFFICIENCY ELECTROCATALYSTS FOR OXYGEN EVOLUTION REACTION



ACS Applied Energy Materials, 2018, 1 (8), pp 4075–4083

Jahangir Masud, Wipula P. R. Liyanage, Xi Cao, Apurv Saxena, Manashi Nath*

Department of Chemistry, Missouri University of Science & Technology, Rolla, MO 65409, USA.

*email: nathm@mst.edu

KEYWORDS: OER, Copper Selenides, Water Splitting, CVD, Transition Metal Chalcogenides.

ABSTRACT

Designing high-efficiency water oxidation catalysts from earth-abundant resources have attracted significant attention in the last couple of years owing to the potential application of this technology in several energy conversion devices. Among the transition metals, copper is one of the cheapest earth-abundant non-precious element which can enhance its electrocatalytic activity due to heavily occupied *d*-orbitals. In this article we have shown electrocatalytic activity of copper selenide for the first time for water oxidation reaction. The copper selenide phases were synthesized by direct electrodeposition on electrodes, as well as by hydrothermal and chemical vapor deposition (CVD) techniques. Structure and morphology characterization through powder X-ray diffraction, Raman, X-photoelectron spectroscopy, and electron microscopy revealed that all the synthesized phases were pure crystalline copper selenide of composition Cu_2Se and comprising nanostructured granular morphology. Electrocatalytic performance for water oxidation was investigated in alkaline solution (1M KOH) and it was observed that Cu_2Se showed a low overpotential of only 270 mV to achieve 10 mA cm^{-2} . This catalyst also displayed a low Tafel slope of 48.1 mV dec^{-1} . Interestingly Cu_2Se showed comparable electrocatalytic activity irrespective of the method of synthesis indicating that it is indeed an intrinsic property of the material. Chronoamperometric studies revealed that the catalyst retained its activity for prolonged period of continuous oxygen evolution exceeding 6 h, while post-activity characterization revealed that crystallinity and surface composition was preserved after catalytic activity. Copper

selenides being found in nature as stable minerals, this article can initiate new concept for efficient catalyst design.

1. INTRODUCTION

Electrochemical oxygen evolution reaction (OER) representing the challenging anodic half-cell reaction in both H₂ evolution through water splitting and conversion of CO₂ to fuel, has received considerable and persistent attention over the last several decades.¹⁻⁴ Water splitting and CO₂ electroreduction are considered as two of the most promising reactions for sustainable generation of renewable fuels. However, the kinetically sluggish 4e⁻ oxidation process in OER ($4\text{OH}^- \rightarrow \text{O}_2 + 2\text{H}_2\text{O} + 4\text{e}^-$) requires high energy and is the most challenging aspect for large-scale deployment of these energy conversion processes.⁵⁻⁸ One approach to address this problem is the development of efficient catalysts for OER. Although iridium dioxide (IrO₂)⁹ and ruthenium dioxide (RuO₂)¹⁰ has been known as state-of-the-art OER electrocatalysts with low overpotential, their high cost and scarcity of the elements makes these catalysts unsuitable for economically feasible hydrogen production in a practically usable scale.

Recently, many efforts have been devoted to improve the OER electrocatalytic activity by exploring noble-metal free electrocatalysts.¹¹⁻¹⁷ Indeed, a variety of non-noble metal-based compounds with attractive catalytic efficiency and stability have been explored in recent years. Particularly, earth abundant transition metals comprising Ni, Fe and Co, and their oxides were widely studied as OER catalyst in alkaline media.^{13,17} Among these the transition metal chalcogenides (M_xE_y , M – Ni, Fe, Co and E = S, Se)

have gained considerable attention due to their exceptional electrocatalytic activity towards OER, ORR (oxygen reduction reaction) and HER in alkaline media.¹⁸⁻²⁵ Research from several groups including our own have shown high catalytic activity for Ni-chalcogenides such as NiSe,¹⁸ Ni₃Se₂,²⁰ NiSe₂,²² Ni₃S₂,²⁶ Ni₃Te₂,²⁷ cobalt selenides, Co₇Se₈,^{19, 28} CoSe₂,²⁹ for OER, HER and ORR. However, apart from enhanced performance, reducing the electrocatalyst cost without compromising performance has still been the focus of further research and tremendous efforts have been devoted by many researchers in that direction. One of the easiest way to reduce the cost is to design the catalyst from the most earth abundant and cheap elements.

Copper is widely available in the earth crust and cheaper than most metals including Ir, Ni, Co etc. Copper and its oxides can be easily synthesized via electrodeposition and hydrothermal methods. Despite the lower price and earth-abundancy, copper is rarely used as water splitting catalyst due to the poor catalytic activity. Yang et al.³⁰ synthesized Cu₂O/CuO bilayered composites by electrodeposition and a subsequent thermal reduction and showed the high photochemical HER activity and stability. In another report, OER activity of Cu(OH)₂ based nanowire grown on Cu foil³¹ was reported, where 530 mV overpotential was required to achieve the current density at 10 mA cm⁻². Unfortunately, the high overpotential renders it economically unsuitable as a replacement for Ir. Previously we have observed that the catalyst activity can be enhanced by increasing covalency in the metal-anion bond.²⁷ Hereby, we propose that Cu-based chalcogenides will show better electrocatalytic activity compared to the oxides since covalency increases down the chalcogenide series away from oxygen.

In this work we have reported the highly efficient electrocatalytic activity of copper selenide (Cu_2Se) nanostructures obtained via different synthesis routes, such as electrodeposition, hydrothermal method and chemical vapor deposition. These simple binary copper selenides show improved oxygen evolution with high efficiency in alkaline medium and exhibit high stability for prolonged period of time. The overpotential (η) at a current density of 10 mA cm^{-2} , was obtained at 270 mV, which was significantly lower than the oxide-based catalysts including state-of-the-art RuO_2 and IrO_2 , and is among the lowest overpotentials observed till date. The low Tafel slopes (48.1 mV dec^{-1}) also indicate better OER kinetics for these copper selenide electrocatalyst. It should be also noted that there are very few reports of binary copper compounds as OER electrocatalyst with Cu being the catalytically active site. Additionally, this is one of the first reports of OER catalytic activity in the family of binary copper chalcogenides.

2. EXPERIMENTAL SECTION

2.1. MATERIALS

All the chemicals used for the synthesis were of analytical grade and were used without further purification. All solutions were prepared using deionized water (DI : resistivity $18 \text{ M}\Omega \text{ cm}$). Copper sulfate (CuSO_4) was purchased from Fisher Scientific, Selenium dioxide (SeO_2) and hydrazine hydrate ($\text{N}_2\text{H}_4 \cdot \text{H}_2\text{O}$, 100%) were purchased from the Acros Organics. Au coated glass slides (Au-glass, hereafter) were bought from Deposition Research Lab Incorporated (DRLI) Lebanon, Missouri.

2.2. ELECTRODEPOSITION OF COPPER SELENIDE (Cu₂Se)

Conventional three-electrode system was used for the electrodeposition of copper selenide films on different conducting substrates (e.g. Cu, Au-glass, glassy carbon (GC), etc.). Ag|AgCl and Pt mesh were used as the reference and counter electrode, respectively. Substrates were cleaned by micro-90 detergent followed by sonication in mixture of isopropanol, ethanol, and deionized water. The clean and air dried substrates were masked with a scotch tape, leaving a circular exposed geometric area of known dimensions (0.08 cm²) for the electrodeposition. Electrodeposition of copper selenide films were carried from an electrolytic bath containing 10 mM CuSO₄, 10 mM SeO₂ and 25 mM LiCl at 25 °C. Dilute HCl was added to adjust the pH at 2.4 . Before electrodeposition, N₂ gas was purged through the solution for 30 min to remove all dissolved O₂ from the electrochemical bath. Electrodeposition was carried out for 300 s at -0.7 and -0.8 V (vs Ag|AgCl). After deposition the films were thoroughly washed with DI water to remove any adsorbents from the surface of the film.

2.3. HYDROTHERMAL SYNTHESIS OF COPPER SELENIDE (Cu₂Se)

In a typical synthesis, Cu₂O (1.0 mM) was dissolved in 5.0 ml of deionized water under magnetic stirring to form a homogeneous solution. After mixing the solution for 10 min, Se powder (1.0 mM) was added and stirred vigorously for 20 min. Finally, N₂H₄.H₂O (2.0 ml) was added to the mixture and stirred continuously for another 10 min. The resulting solution was transferred to a Teflon-lined stainless-steel autoclave. The autoclave was sealed and maintained at 185 °C for 24 h, then naturally cooled to room temperature. The black product formed was centrifuged, washed several times with DI

water and then with mixture of ethanol and DI water to remove impurities. The product was dried in a vacuum oven at 25°C for 12 h.

2.4. CHEMICAL VAPOR DEPOSITION (CVD) OF COPPER SELENIDE

Cu₂Se sample synthesized by chemical vapor deposition (CVD) technique were carried out in a horizontal tube furnace at 700 °C under a constant flow of N₂ as carrier gas. Flow rate of N₂ was maintained throughout the reaction at 120 sccm with the help of mass flow controllers. Growth was carried out using Cu coated Si wafer cut into 1cm x 2 cm pieces as the substrate and typically substrates were placed at the middle region of the furnace at 700 °C. Since Se sublimates at elevated temperatures, the Se shots were kept near the inlet of the reaction tube such that the temperature of selenium exceeds the sublimation temperature when the central zone of the furnace reaches 700 °C. Initially, Se (0.5g of selenium shots) was kept outside of the heating zone by pushing the ceramic liner of the furnace to the extreme left. Once the central zone of the furnace reached 700 °C, the ceramic liner was pushed to the right such that the Se shots were in the 400 °C zone. This is a crucial step for the reproducibility of the reaction as this step prevents the escape of Se before the growth zone at the center of the furnace reaching the intended reaction temperature (700 °C). The reaction was carried out for 30 minutes and the furnace was cooled down to room temperature at a rate of 8 °C min⁻¹. As prepared samples were further annealed at 140 °C for 60 minutes under nitrogen atmosphere before further characterization.

2.5. ELECTRODE PREPARATION

The electrodeposited and CVD synthesized samples were prepared directly on the electrode which were used as-synthesized for electrochemical measurements. To analyze the activity of hydrothermally synthesized Cu_2Se , a homogeneous catalyst ink was prepared by adding 5.0 mg of catalyst powder in 250.0 μL of Nafion solution (50 μL of 1 % nafion solution in 50 μL of 50% IPA in water) followed by ultrasonication for 30 min. 20 μL of the dispersion was drop casted on a confined area (0.08 cm^2) on Cu substrate. The drop-casted film was then dried at room temperature and finally heated at $130 \text{ }^\circ\text{C}$ for 30 mins in an oven.

In this article, we have reported copper selenide (Cu_2Se) catalyst by using different synthetic routes and hereafter electrochemically deposited catalysts will be denoted as Cu_2Se (ED-1) and Cu_2Se (ED-2) for the deposition potential at -0.8 and -0.7 V vs $\text{Ag}|\text{AgCl}$, respectively, hydrothermally synthesized catalyst as Cu_2Se (HD), and chemical vapor deposited catalyst as Cu_2Se (CVD).

3. RESULTS AND DISCUSSION

3.1. STRUCTURAL AND MORPHOLOGICAL CHARACTERIZATION

The variation of phase compositions of copper selenide synthesized by different methods were investigated by powder X-ray diffraction (pxrd). Figure 1a shows the pure, crystalline pxrd patterns of hydrothermally synthesized copper selenide which is nicely consistent with the standard diffraction pattern for Cu_2Se (PDF# 00-006-0680). The electrochemically deposited Cu_2Se (ED-1) (deposited at -0.8V vs $\text{Ag}|\text{AgCl}$) on the other

hand, showed lesser degree of crystallinity as shown in supporting Figure S1. It has been reported previously that electrodeposition frequently produces poorly crystalline or even amorphous films. The crystallinity of the electrodeposited films was greatly affected by the change of deposition potential in the same electrochemical bath. Crystalline Cu_2Se (PDF # 00-06-0680) was obtained at a deposition potential of -0.7 V (vs. $\text{Ag}|\text{AgCl}$) with some Cu_3Se_2 (PDF# 01-071-0045) present as a minor impurity phase.

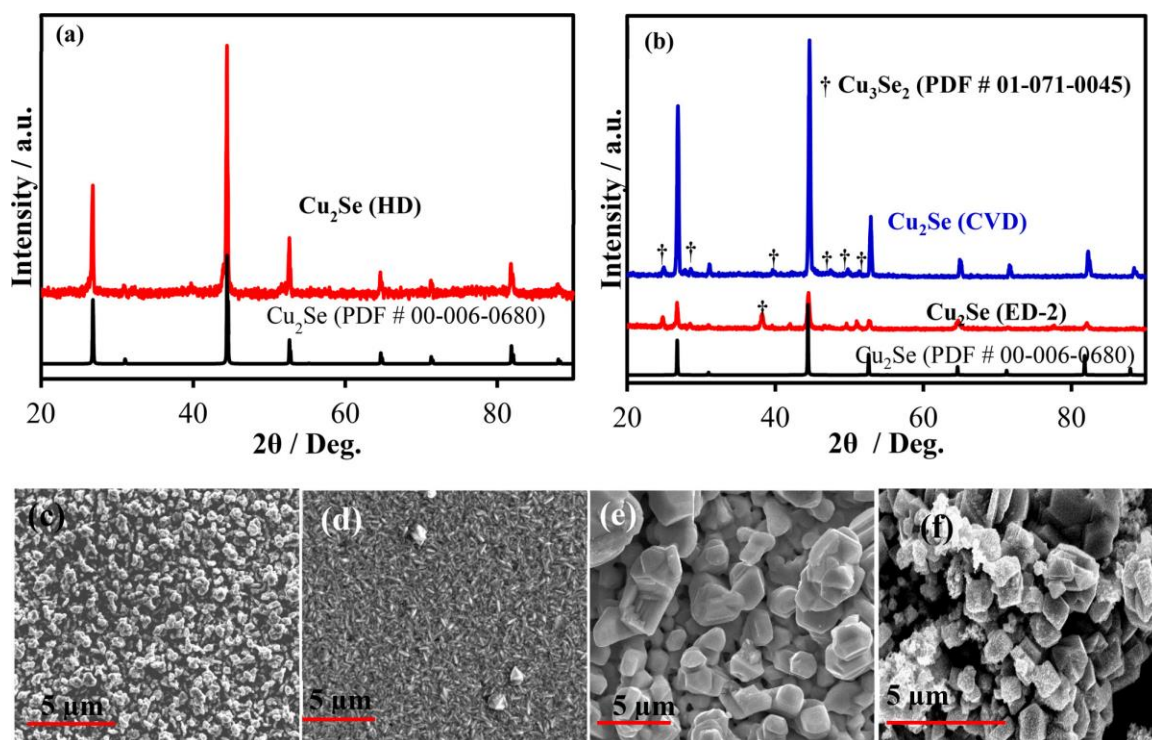


Figure 1. PXRD patterns of Cu_2Se . (a) hydrothermally synthesized Cu_2Se and (b) CVD (blue) and electrodeposited (red) Cu_2Se catalysts along with the corresponding reference spectra. SEM images of (c) electrodeposited Cu_2Se (ED-1 at -0.8 V), (d) electrodeposited Cu_2Se (ED-2 at -0.7 V), (e) chemical vapor deposited Cu_2Se (CVD), and (f) hydrothermally synthesized Cu_2Se (HD) catalysts.

For CVD synthesis, the pattern also showed mainly Cu_2Se phase with minor presence of Cu_3Se_2 as shown in Figure 1b. The closeness of the pXRD patterns with the Cu_2Se and Cu_3Se_2 confirmed that copper selenide was a major product for all of these synthesis procedures. The morphology of as prepared copper selenide films were studied by SEM. Figure 1c-f show SEM images of Cu_2Se (ED-1), Cu_2Se (ED-2), Cu_2Se (CVD) and Cu_2Se (HD), respectively. It was revealed that the electrodeposited films (Figure 1c and 1d) are relatively uniform, well-dispersed and composed of randomly oriented nanoparticles. This type of morphology may lead to a very rough surface with high porosity which is beneficial for enhanced catalytic activity. The CVD, Cu_2Se (ED-2) film and hydrothermally synthesized Cu_2Se powder showed different morphologies as can be seen in Figure 1e and 1f. These are mainly granular with size distribution of nanometer to few micrometers. The chemical compositions of these films, as analyzed by EDS, are shown in supporting Figure S2a, 2b, 2c and 2d. The EDS confirms the presence of Cu and Se in the all samples and absence of even trace amount of oxygen. The atomic ratio of Cu : Se was calculated as approximately 2.0 : 1.0, 2.0 : 1.0, 1.9 : 1.0 and 2.0 : 1.0 for Cu_2Se (ED-1), Cu_2Se (CVD), Cu_2Se (ED-2) and Cu_2Se (HD), respectively which also confirmed that the major phase was Cu_2Se in all these samples. The EDS measurements were performed at several locations on the sample surface to confirm uniform chemical compositions.

Transmission electron microscopy (TEM) images of the representative Cu_2Se (ED-1) and Cu_2Se (CVD) catalyst has been shown in Figure 2a and 2d, respectively. It can be seen (Figure 2a) that the Cu_2Se (ED-1) are nanoparticles with smooth surfaces have relatively symmetrical shapes with size in the range of 20-40 nm. On the other hand,

chemical vapor deposited Cu₂Se (CVD) shows interconnected nanoparticles (Figure 2d). HRTEM image of Cu₂Se (ED-1) showed multiple lattice fringes as shown in Figure 2b with measured d-spacings of 3.38, 1.76 Å corresponding to the (111) and (311) planes of Cu₂Se, respectively. Lattice fringes correspond to (220) plane (spacing of 2.03 Å) could be easily indexed from HRTEM of Cu₂Se (CVD) catalyst (Figure 2e). In addition, the crystallinity of catalysts was further confirmed by selected area electron diffraction (SAED) patterns. A characteristic SAED pattern of Cu₂Se (inset of Figure 2b) was indexed to the (111), (220) and (311) planes while SAED pattern for Cu₂Se (CVD) showed spots corresponding to (020), (220), (040) reflections of Cu₂Se, thereby corroborating the indexed HRTEM (inset of Figure 2e).

The oxidation state of the elements in copper selenide samples were investigated by X-ray photoelectron spectroscopy (XPS). Figure 2c represents the deconvoluted Cu 2p XPS peak for Cu₂Se (ED-1) catalyst where the strong fitting of peaks at 932.2 and 952.2 eV for Cu¹⁺ 2p_{3/2} and 2p_{1/2} peaks and 934.2 eV and 954.3 eV for Cu²⁺ 2p_{3/2} and 2p_{1/2} peaks, respectively confirmed the presence of Cu in +1/+2 mixed oxidation states. Obvious satellite peaks were observed at 943.2 and 962.4 eV possibly due to the overlapping of antibonding orbital between the Cu and Se. Similar oxidation states of Cu could be assigned for Cu₂Se (CVD) catalyst as shown in Figure 2f where peaks at 932.1 and 952.2 eV for Cu¹⁺ 2p_{3/2} and 2p_{1/2} peaks and binding energies at 934.2 eV and 954.4 eV for Cu²⁺ 2p_{3/2} and 2p_{1/2} peaks. These binding energy values nicely matched with previous report of Cu₂Se.³²⁻³⁴ It should be mentioned that Cu at the surface of both electrodeposited and CVD synthesized Cu₂Se showed mixed oxidation states of +1 and +2. The coexistence of +1 and +2 mixed valence is well-known in Cu₂Se.³² The

deconvoluted Se 3d XPS spectra of Cu₂Se (inset of Figure 2c) and chemically vapor deposited Cu₂Se (inset of Figure 2f) catalysts showed peaks at 54.1 and 55.0 eV for the Se 3d_{5/2} and Se 3d_{3/2}, respectively, in accordance with previously reported for Cu₂Se.³⁴ The weaker shoulder peaks in Se 3d at 56.5 eV may result from the oxidation of Se²⁻ ions on the surface of the catalyst.³⁴

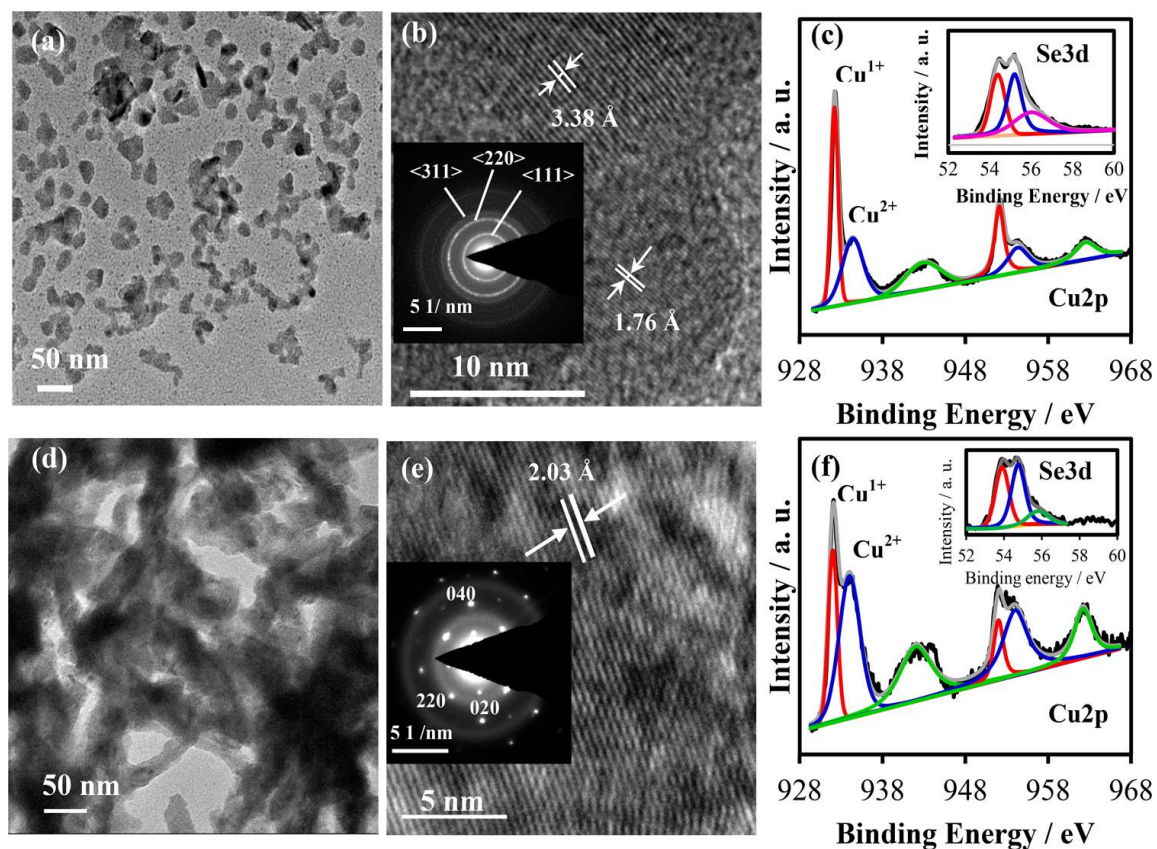


Figure 2. TEM images of Cu₂Se. (a & b) Cu₂Se (ED-1) and (d & e) Cu₂Se (CVD). The insets (of b & e) show SAED of Cu₂Se (ED-1) and Cu₂Se (CVD), respectively. Figures (c) and (f) are the XPS of Cu 2p of Cu₂Se (ED-1) and Cu₂Se (CVD), respectively. Insets (of c & f) show the corresponding Se 3d spectra.

The Cu to Se atomic ratio of $\sim 2.0 : 1.0$ was calculated from the initial Cu2p_{3/2} and Se3d_{5/2} peak areas, demonstrating that the catalyst indeed of Cu₂Se. Hydrothermally synthesized pure Cu₂Se also exhibited similar XPS spectra as shown in supporting information Figure S3 confirming the presence of mixed valent Cu coordinated to Se²⁻. Raman shift of Cu₂Se (ED-1) and Cu₂Se (CVD) is shown in Figure S4. The only intense peak observed at 260 cm⁻¹, can be assigned to the Se-Se stretch vibration in Se²⁻ and is in good agreement with the value previously reported for Cu₂Se.³⁵ The absence of peaks at 141 and 235cm⁻¹ confirm that the film contains no elemental Se. It has also been noted that there is no evidence of oxidic phases as there is no substantial peak observed at about 500 cm⁻¹, characteristic of the oxide phase.

The electrocatalytic OER activity of Cu₂Se catalyst was investigated in 1M KOH solution. Typical three electrode system electrochemical cell was used in this study where Cu₂Se modified Cu and/or GC substrate served as working electrode, KCl saturated Ag|AgCl as reference and glassy carbon (GC) plate as counter electrodes. The reference Ag|AgCl electrode was calibrated by using open circuit potential (OCP, -0.199 V) with Pt wire in H₂-saturated H₂SO₄ solution and converted to a reversible hydrogen electrode (RHE) using the following equation, Eq. 1:

$$E_{\text{RHE}} = E_{\text{Ag|AgCl}} + 0.059\text{pH} + E_{\text{Ag|AgCl}}^{\circ} \quad \text{---(1)}$$

where E_{RHE} is the converted potential vs. RHE, $E_{\text{Ag|AgCl}}$ is the experimentally obtained potential vs. Ag|AgCl reference electrode, and $E_{\text{Ag|AgCl}}^{\circ}$ is the standard potential of Ag|AgCl (0.199 V).

The linear sweep voltammetry (LSV) was performed in N₂-saturated 1M KOH solution at a scan rate of 10 mV s⁻¹. Figure 3a and 3b shows the OER polarization curves

recorded for different catalysts. It can be seen that Cu itself exhibits poor OER activity in alkaline medium. However, the simple modification of Cu substrates by chemical vapor deposition, hydrothermally synthesized and/or electrodeposition of copper selenide demonstrates exceptionally high OER activity. The OER onset potentials for Cu₂Se (CVD), Cu₂Se (ED-2), Cu₂Se (HD) and Cu₂Se (ED-1) were obtained as 1.45, 1.45, 1.50 and 1.53 V vs. RHE, respectively. Surprisingly, both of electrochemically (ED-2) and chemical vapor deposited Cu₂Se catalyst shows the similar onset potential which confirms the intrinsic properties of catalyst which is independent of synthesis history and surface morphology.

The slower rise in oxidation current density for the hydrothermally synthesized sample compared to the electrodeposited one can be attributed to the fact that while the electrodeposited Cu₂Se grew directly on the electrode and produced a binder-free film, the hydrothermally synthesized sample was assembled on the electrode with the help of Nafion that limited exposure of the active sites as well as introduced contact resistance between the catalyst and electrode. Such reduction in activity between the hydrothermally synthesized and electrodeposited catalyst has also been observed for other OER electrocatalysts.²⁷ The efficiency of OER catalysts were obtained by measuring the overpotential (η) required to get the geometric current density of 10 mA cm⁻² which is believed to be equivalent of 10% solar energy conversion efficiency.³⁵ It was found that the current density of 10 mA cm⁻² was almost unreachable for the bare Cu electrode over the span of applied potential range. On the other hand, only 270, 290, 300 and 320 mV overpotentials were needed to achieve the current density of 10 mA cm⁻² for Cu₂Se (ED-2), Cu₂Se (HD), Cu₂Se (CVD) and Cu₂Se (ED-1), respectively. The lower overpotential

(by ~ 30 mV) in electrochemically synthesized Cu₂Se (ED-2) catalyst compared to CVD catalyst implies that the surface morphology and nanostructuring also plays a vital role in OER activity.

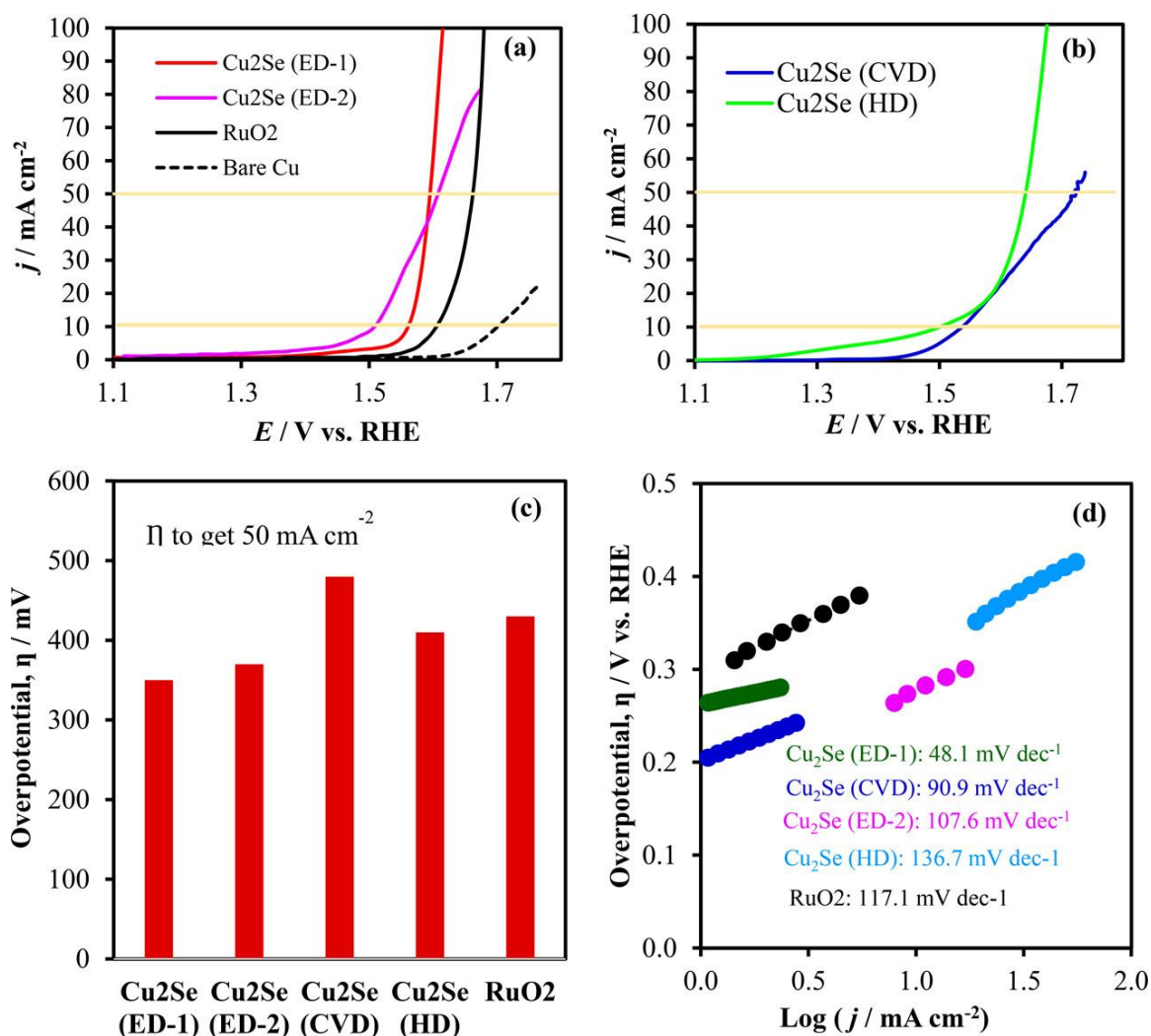


Figure 3. OER polarization curves of Cu₂Se. (a & b) in N₂ saturated 1M KOH solution for different catalysts. c) OER overpotential, η to achieve 50 mA cm⁻² at different catalysts and d) Tafel plots of catalysts.

In addition, coexistence of Cu_3Se_2 as a minor phase in the Cu_2Se (CVD) and Cu_2Se (ED) may also play a synergistic role in the enhancing the catalytic activity. The effect of surface morphology, substrate effect as well as growth conditions can also be seen when comparing the overpotential at higher current densities (50 mA cm^{-2}) as shown in Figure 3c. Surprisingly the lowest overpotentials were required for the electrodeposited samples, Cu_2Se (ED-1) and Cu_2Se (ED-2) catalysts.

The rationale for this observation might be attributed to the highly porous morphology and smaller nanoparticles in the catalytic film compared to other copper selenide catalysts, as well as the advantages of direct electrodeposition of the catalyst which produces a binder-free catalytic film with direct electrical contact with the electrode and containing no non-active components thereby maximizing charge transport and catalytic efficiency. The hydrothermally synthesized sample on the other hand was attached to the electrode with the help of Nafion, which reduces the exposure of the active sites to the electrolyte as well as inhibits charge transport. The difference observed in catalytic activity between samples produced from different synthetic routes can also be attributed to the difference in particle/grain size apart from the direct adherence of the film to the electrode as well as surface morphology. It is also possible that degree of crystallinity of the catalytic film plays an influential role on its activity. While Cu_2Se (ED-1) showing best catalytic activity was amorphous, the other films were crystalline. Generally, amorphous catalytic films show better catalytic activity due to more exposure of the active sites to the electrolyte. Apart from this, the onset potential as well as Tafel slopes of Cu_2Se (ED-2), Cu_2Se (HD) and Cu_2Se (CVD) were almost similar. The catalytic performance was also normalized with respect to catalyst loading as shown in

Figure S5. It was observed that the electrodeposited samples showed the best gravimetric current density at a fixed overpotential compared to the CVD-grown and hydrothermally synthesized samples, respectively. This observation further confirms that the electrodeposited sample owing to its direct attachment to the electrode, smaller grain size and lower degree of crystallinity, exhibits enhanced catalytic performance even with low loading. Note that the OER activity of the copper selenide nanostructures was better than state-of-the-art of RuO₂ as well as other reported CuO based catalyst.^{31,36-37} The greatly improved electrocatalytic OER activity of Cu₂Se (ED-1) compared to CuO can be ascribed to the effect of lower electronegativity of Se vs O leading to increase in covalency of the Cu-Se bond. Similar observations have been reported previously for transition metal chalcogenides-based catalysts where more covalent metal-selenide bond enhanced catalytic activity of the binary and ternary selenides.^{20-22,27} The OER activities of different Cu-based electrocatalyst are shown in Table 1.

The Tafel slope is an important factor for the evaluation of catalyst kinetics which describes the influence of potential, or overpotential on steady-state current density. To gain further insight into the OER activities of these catalysts, Tafel slopes, were retrieved from the LSVs and are presented in Figure 3d. A linear dependency of η vs $\log(j)$ was achieved for all copper selenide catalysts and slopes were presented in Table 1. The lowest Tafel slopes was obtained for Cu₂Se (ED-1) catalyst (48.1 mV dec⁻¹) indicating better OER kinetics, highlighting the effect of nanostructure of catalyst along with porous network. Impressively, the estimated Tafel slopes of Cu₂Se is lower than well studied RuO₂ (117.1 mV dec⁻¹) catalyst. The OER activity tested for RuO₂ in Figure 3 is in good agreement with recently reported results in literature and it further validate our

electrochemical measurements.⁴²⁻⁴³ Both electrochemically and chemical vapor deposited Cu₂Se (ED-2 and CVD) catalyst exhibited almost similar slopes which indicated that the reaction mechanism followed a similar pathway. The higher Tafel slope for hydrothermally synthesized Cu₂Se can be attributed as due to the effect of non-catalytic Nafion which was used to adhere the catalyst film on the electrode surface.

Table 1. Comparison of OER activities at different Cu-based electrocatalysts.

Catalysts	Electrolyte	Onset Potential / V vs. RHE	η at 10 mA cm ⁻² / mV	Catalyst loading / mgcm ⁻²	Tafel slopes/ mV dec ⁻¹	References
Cu(OH) ₂ NWS/CF	0.1 M NaOH	1.625	530	0.8	86	31
CuO NWS/CF	0.1 M NaOH	1.627	590	0.8	84	31
CuO _x NWS/CF	0.1 M NaOH	1.67	630	0.8	108	31
Annealed CuO	1.0 M KOH	1.58	430 (1 mA cm ⁻²)	-	61.4	36
H ₂ O ₂ treated CuO	0.1 M KOH	1.57	520 (2.5 mA cm ⁻²)	-	-	37
Cu _{0.3} Ir _{0.7} O ₈	0.1 M KOH	-	415	-	105	38
CuC ₂ O ₄ -SSM	1.0 M KOH	1.55	400	0.2	-	39
CuRhO ₂	1.0 M KOH	1.56	410	0.8	-	40
Cu ₃ P /CF	0.1 M KOH	-	412 (50 mA cm ⁻²)	68.5	63	41
Cu ₂ Se (ED-1)	1.0 M KOH	1.53	320	0.8	48.1	This work
Cu ₂ Se (CVD)	1.0 M KOH	1.45	300	2.0	90.9	This work
Cu ₂ Se (ED-2)	1.0 M KOH	1.45	270	0.7	107.6	This work
Cu ₂ Se (HD)	1.0 M KOH	1.50	290	5.0	136.7	This work

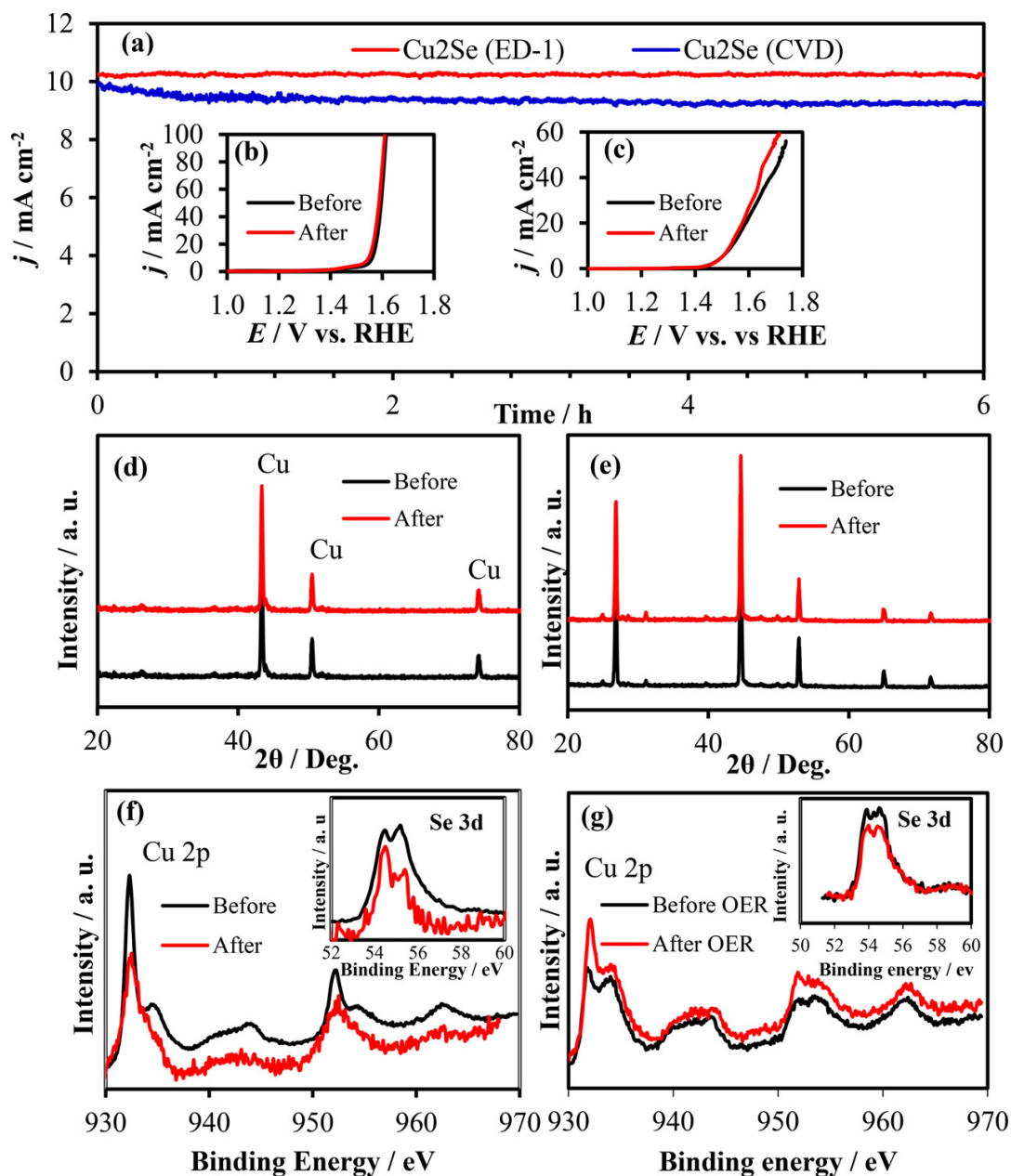


Figure 4. Stability studies of the catalyst. (a) OER stability in 1M KOH solution at a constant overpotential of 320 mV for Cu₂Se (ED-1) and 300 mV for Cu₂Se (CVD). Comparison of LSVs of (b) Cu₂Se (ED-1) and (c) Cu₂Se (CVD) after chronoamperometry. XRD (d) & XPS (f) for Cu₂Se (ED-1) and XRD (e) & XPS (g) for Cu₂Se (CVD) after stability.

The stability of the Cu₂Se (ED-1) and Cu₂Se (CVD) electrocatalysts were investigated with chronoamperometric studies whereby, the catalytic film was maintained at a constant potential to generate oxygen in 1M KOH solution for an extended period of time. The potential to achieve 10 mA cm⁻² current density was selected for the chronoamperometric studies as shown in Figure 4a.

The potentials of 1.53 V and 1.55 V vs. RHE were chosen for the stability study and the electrolyte was continuously stirred at 1200 rpm to get rid of accumulated O₂ bubbles from the electrode surface. It was observed that both catalysts (electrodeposited and CVD synthesized) showed exceptional stability of the OER catalytic activity in 1 M KOH and the current density did not show any degradation (Figure 4a). The comparison of LSVs before and after 6 h of oxygen generation were used to check the catalyst stability and has been shown in Figure 4b and 4c for electrodeposited Cu₂Se (ED-1) and Cu₂Se (CVD) catalyst, respectively. Interestingly, the LSV curves for both catalysts OER did not show any noticeable decrease of onset potential and overpotential compared to the as-synthesized catalysts, and the LSVs before and after chronoamperometric studies were almost superimposable.

Composition of the catalysts following catalytic activity was investigated through pXrd, XPS, and SEM analyses. Figure 4d and 4e show the comparison of pXrd patterns of Cu₂Se (ED-1) and Cu₂Se (CVD) catalyst, respectively after stability test. There was no change of pXrd patterns for both the samples after stability. Structural and compositional integrity of both of the catalysts was further confirmed by XPS spectra of Cu 2p and Se 3d after OER activity and presented in Figure 4f and 4g. Surface morphology of the both

catalyst checked through SEM imaging after activity did not reveal major changes in morphology (Figure S6) for both Cu₂Se (ED-1) and Cu₂Se (CVD) catalysts.

3.2. TESTING OF EVOLVED GAS AND FARADAIC EFFICIENCY

Rotating ring disk electrode (RRDE) set up was used in bipotentiostat mode to monitor and quantify the gas evolved at the anodic reaction as shown in Figure 5 and Figure S7. For this procedure Cu₂Se was electrodeposited on GC disk electrode in a RRDE set-up and scanned at the anodic potential range while Pt ring was held a potential of 0.2 V (vs. RHE). The idea was to hold the Pt ring potential suitable for ORR such that if any O₂ was being produced at the disk electrode, it will be collected and reduced at the ring electrode resulting in an increase of the ring current.

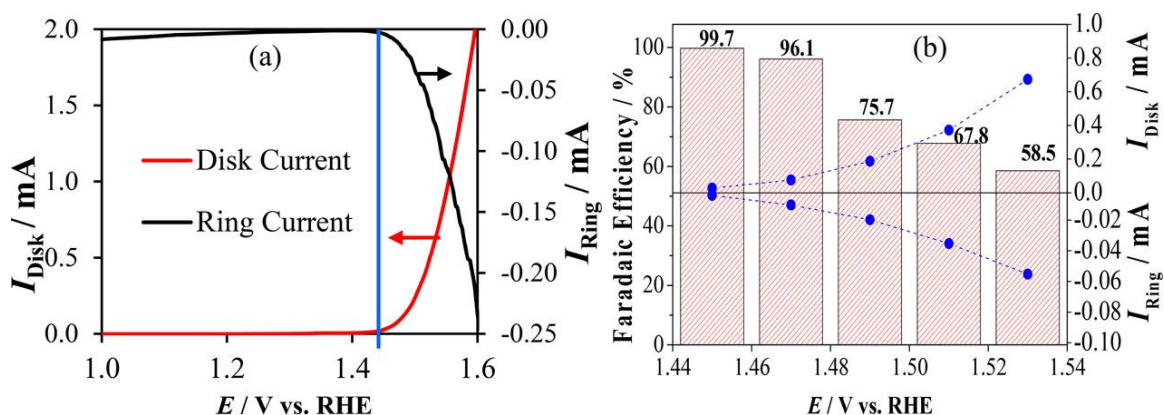


Figure 5. Plots for the ORR-OER reaction. (a) showing OER current density at Cu₂Se (ED-1)/GC disk electrode in N₂-saturated 1.0 M KOH and ORR current density at Pt ring electrode maintained at 0.2 V vs. RHE as a function of applied disk potential. Blue line indicates the onset potential for OER at the disk electrode corresponding with the onset of ORR at the ring electrode. (b) Faradaic efficiency of catalyst measured in N₂ saturated 1.0 M KOH at 1600 rpm rotation speed.

Both the ring current and disk current were measured as function of applied disk potential. Initially 1M KOH solution was purged with N₂ gas for 30 min before starting the reaction to remove dissolved O₂ and blanketed in N₂ atmosphere. The disk electrode was scanned from 1.0 to 1.5 V (vs. RHE) at a scan rate of 10 mV s⁻¹ at 1600 rpm. Initially, the ring current was measured to be almost zero current when disk current was almost zero. As soon as the disk current started to increase, the ring current also increased proportionately, indicating that there was indeed oxygen reduction happening at the Pt ring electrode and this O₂ was being generated at the disk electrode. Such OER-ORR coupled reaction also leads to precise determination of the onset potential for OER. From Figure 5a the onset potential of OER was obtained as 1.44 V vs. RHE. The OER faradaic efficiency of the catalyst was calculated from the ratio of ring and disk current and has been presented in Figure 5b. The highest Faradaic efficiency was obtained to be about 99.7% at the applied disk potential of 1.45 V (vs. RHE), and decreased to 58.5% with the disk voltage increasing to 1.53 V (vs. RHE).

Copper has been known as catalytically active center for several chemical conversion processes such as carbon dioxide reduction and hydrogenation catalysts.⁴⁴⁻⁵⁰ Nevertheless, reports for electrocatalytic activity for Cu-based compounds towards water splitting is limited.³⁶⁻⁴¹ The presence of Cu²⁺ along with Cu⁺ in this case is believed to be responsible for enhancement of OER catalytic activity by redistribution of electronic charge around the catalytic site through inductive effect of the neighboring metal atoms. In Cu₂Se, the bond between Cu¹⁺ and Se²⁻ has a certain degree of polarization due to the electrostatic interactions between the anion and the cation. However, when Cu²⁺ ions are also present in the solid, the degree of covalency in the Cu-Se bonds can increase due to

change in oxidation state of the metal (Cu^{2+} being more electronegative). Hence co-existence of Cu^{1+} and Cu^{2+} makes the anion-cation bonds non-identical leading to inductive effects. Such inductive effect will lead to redistribution of electron density around the metal centers and can generate sites where OH group can bind more preferentially. Additionally, the heavily occupied *d*-orbitals along with the increased covalency in the Cu-Se bonds can be expected to push the occupied electronic states to be closer to the water oxidation level leading to lower overpotential and faster charge transfer across the catalyst (electrode)-electrolyte interface. Such an effect has recently been observed in the Ni-selenide and Ni-telluride series. It is encouraging to observe such influence of increased covalency on the OER catalytic activity in the Cu-based chalcogenides also. It must be mentioned here that copper selenides are found in nature as selenide minerals.⁵¹ Cu_2Se in particular is known as berzelianite. Identifying such naturally occurring ores as stable and highly efficient water splitting electrocatalysts will lead to better catalyst design and have far-reaching implications for this energy conversion technology.

4. CONCLUSIONS

In summary, we have synthesized copper selenide nanostructure based electrocatalysts by electrodeposition, hydrothermal and CVD techniques and have comprehensively evaluated their catalytic activities for OER in alkaline conditions. The OER activity observed for all copper selenide samples which has been synthesized by different routes, suggests that the catalytic activity is indeed an intrinsic property of the

material and independent of synthesis procedure. Electrodeposited Cu₂Se catalyst exhibits enhanced catalytic activity that could afford a current density of 10 mA cm⁻² at a overpotential as low as 270 mV and with a low Tafel slope of 48.1 mV dec⁻¹. This catalyst shows excellent stability and structural integrity under continuous O₂ evolution condition for extended period of time (6 h). Cu being one of the cheapest and most earth-abundant element available to mankind, this work makes an important contribution in identifying high-performance catalysts that can be used for practical applications in water splitting devices to produce sustainable and renewable energy for future need.

ACKNOWLEDGEMENTS

The authors would also like to acknowledge Materials Research Center for equipment usage and Dr. Richard Brow for help with Raman measurements. The authors would like to acknowledge NSF (DMR-1710313) and American Chemical Society Petroleum Research Fund (54793-ND10) for financial support.

SUPPLEMENTARY INFORMATION

1. CHARACTERIZATION

1.1. Powder X-ray Diffraction (PXRD). The catalysts were characterized using powder X-ray diffraction (PXRD) using Philips X-Pert X-ray diffractometer (PANalytical, Almelo, The Netherlands) with a CuK α (1.5418 Å) radiation.

For the electrodeposited film the PXRD pattern was collected from the as-synthesized Cu₂Se layer on the Cu substrate.

1.2. Scanning Electron Microscopy (SEM). The SEM image was obtained using a FEI Helios NanoLab 600 FIB/FESEM at an accelerating voltage of 10 kV and a working distance of 4.5 mm. Energy dispersive spectroscopy (EDS) along with line scan analysis was also obtained from the same SEM.

1.3. Transmission Electron Microscopy (TEM). High resolution TEM images (HRTEM) and selected area electron diffraction (SAED) patterns of catalyst was obtained using FEI Tecnai F20. The spot size was less than 2 nm and probe current was 1.2 nA. STEM mode in the TEM was also used for imaging with camera length of 30 mm and the convergence angle of 13 mrad. Oxford ultra-thin (UTW) window EDS detector was used to detect the elements in TEM mode.

1.4. X-ray Photoelectron Spectroscopy (XPS). XPS measurements of the copper selenide were obtained through a KRATOS AXIS 165 X-ray Photoelectron Spectrometer (Kratos Analytical Limited, Manchester, United Kingdom) using the monochromatic Al X-ray source.

The spectrum was collected as is and after sputtering with Ar for 2 min which removes immediate oxide layer from surface of the catalyst. C1s signal at 284.5 eV was used as a reference to correct all the XPS binding energies.

1.5. Raman Spectra. Horiba Jobin Yvon Lab Raman ARAMIS model was used to perform Raman microspectroscopy on the *as-deposited* catalyst films. The laser used was He-Ne with a power of about 1.7 mW over a range of 100 – 2000 cm⁻¹. The spectra were iterated over an average of 25 scans.

1.6. Tafel Plots. The Tafel slope is the important parameter to explain the electrocatalytic activity and kinetics of a given reaction and can be expressed as follows:

$$\eta = a + \frac{2.3RT}{\alpha nF} \log j \quad (\text{S1})$$

where η is the overpotential, α is transfer coefficient, n is number of electron involved in the reaction, F is Faraday constant and j is the current density and slope is given by $2.3RT/\alpha nF$.

Faradaic efficiency of the Cu_2Se catalytic film was estimated by combined ORR–OER studies obtained from bipotentiostat mode of the IviumStat using a Rotating Ring Disk Electrode (RRDE) set-up where Pt and glassy carbon (GC) were used as ring and disk electrodes, respectively. The Faradaic efficiency was calculated using equation S2.

$$\text{Faradaic efficiency} = \frac{2i_r}{i_d N} \quad (\text{S2})$$

where i_r and i_d are the measured ring and disk currents, respectively, and N is the collection efficiency of RRDE, 0.17 in this work.

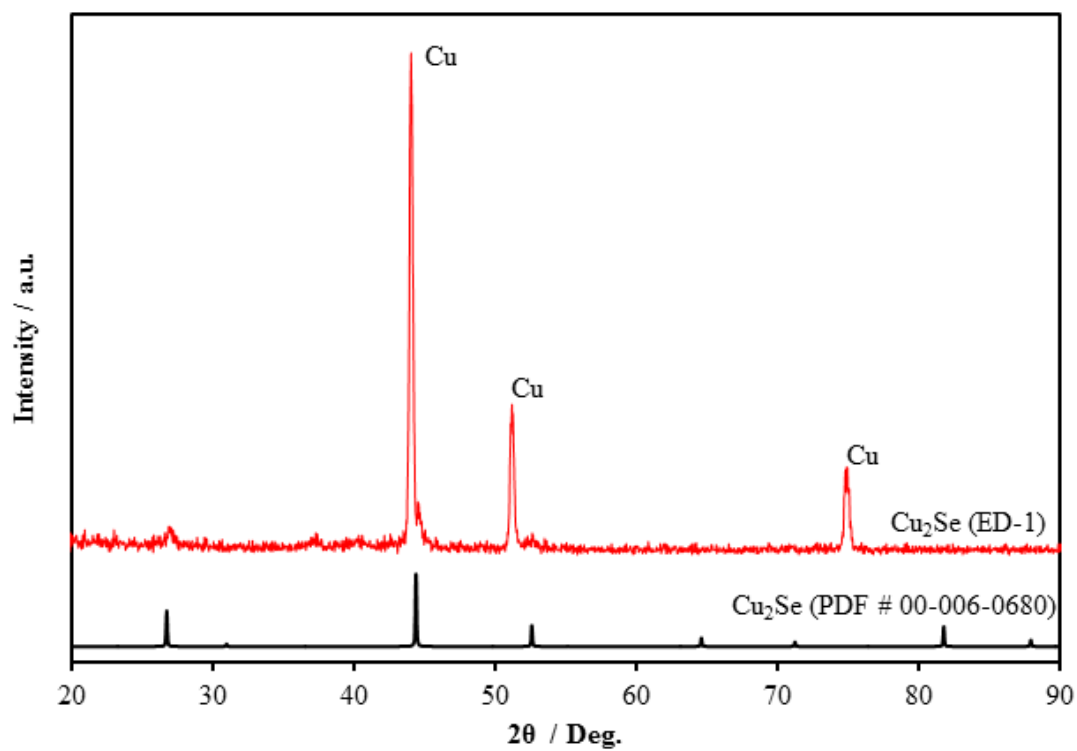


Figure S1. XRD patterns. XRD of Cu₂Se @ Cu (ED-1) along with standard pattern of Cu₂Se (PDF # 00-006-0680)

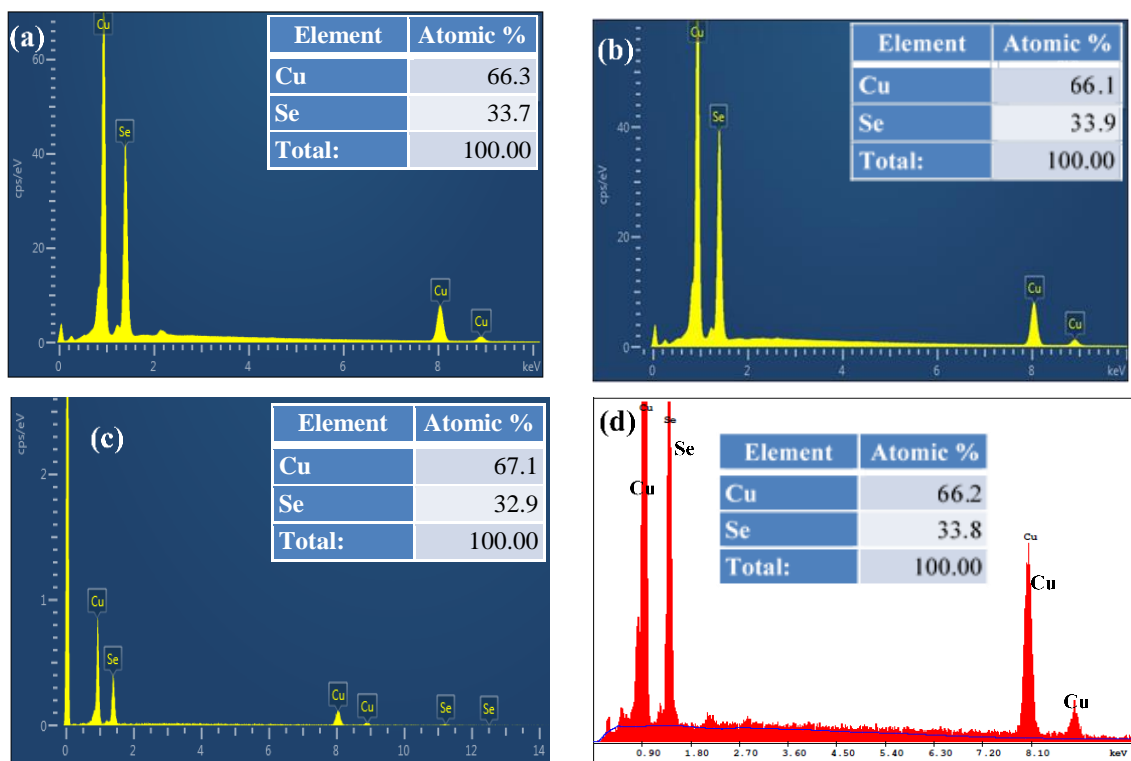


Figure S2. SEM EDX of different Cu_2Se catalysts. a) Cu_2Se (ED-1); b) Cu_2Se (ED-2); c) Cu_2Se (CVD) and d) Cu_2Se (HD)

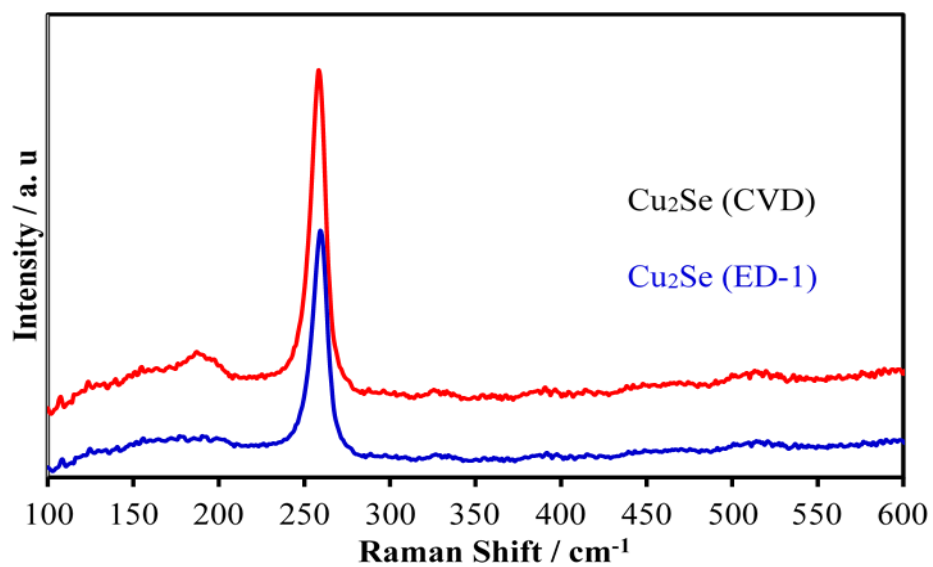


Figure S3. Raman spectra of Cu_2Se catalysts.

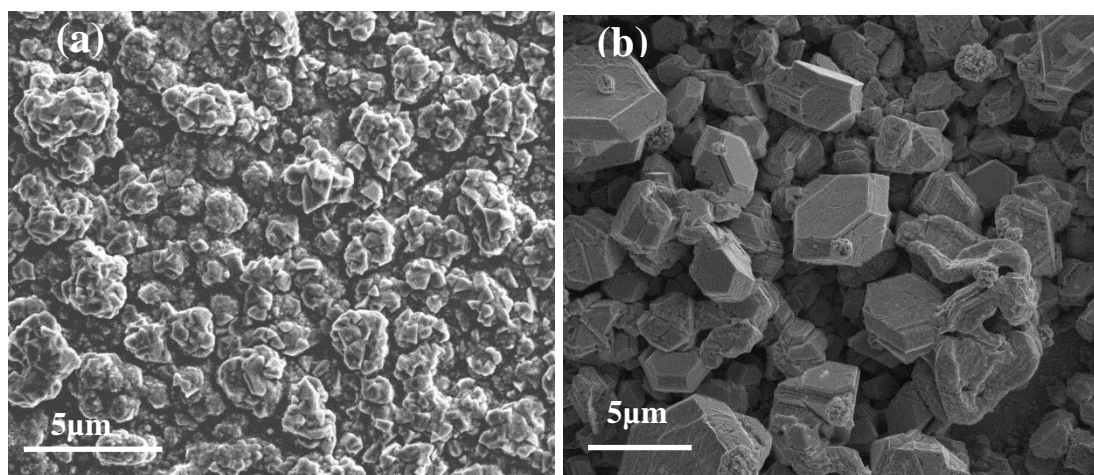


Figure S4. SEM images of catalyst after chronoamperometry. (a) Cu₂Se (ED-1) and (b) Cu₂Se (CVD)

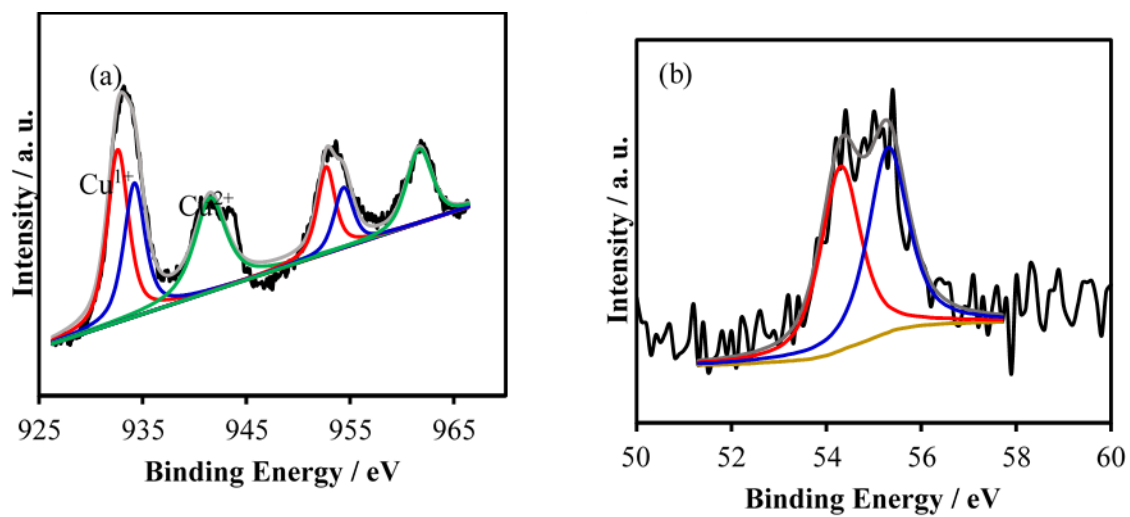


Figure S5. XPS of hydrothermally synthesized Cu₂Se. (a) Cu 2p and (b) Se 3d

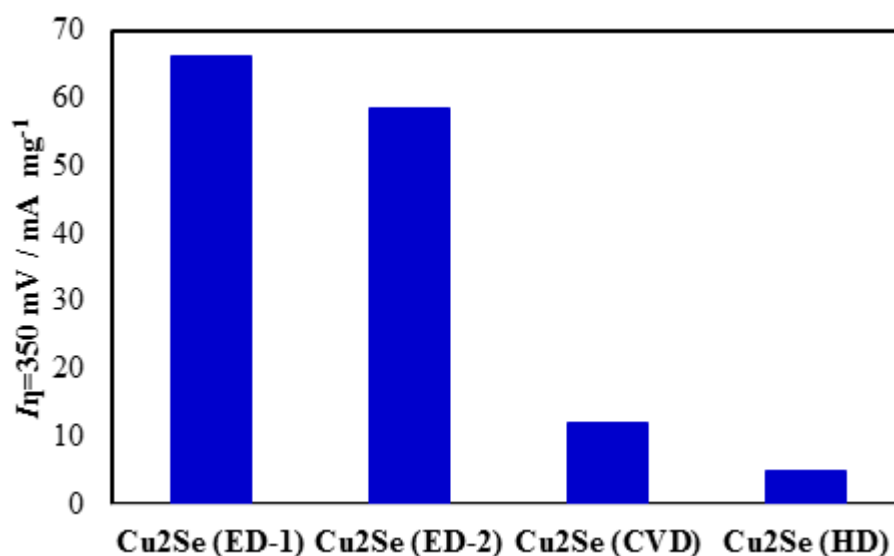


Figure S6. Mass activity of the catalysts made by different methods at over potential of 350 mV.

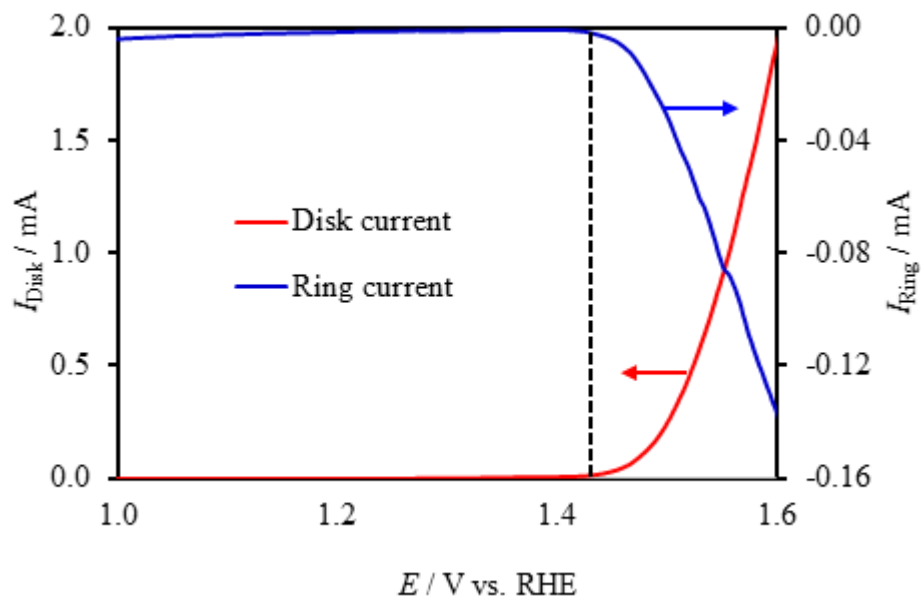


Figure S7. Plots for the ORR-OER reaction. OER current density at Cu₂Se (ED-2)/GC disk electrode in N₂-saturated 1.0 M KOH and ORR current density at Pt ring electrode maintained at 0.2 V vs. RHE as a function of applied disk potential. Dashed vertical line indicates the onset potential for OER at the disk electrode corresponds with the onset of ORR at the ring electrode.

REFERENCES

1. Kauffman, D. R.; Alfonso, D.; Deng, X.; Lee, J.; Jang, H.; Lee, J. Kumar, S.; Matranga, C. Electrocatalytic Oxygen Evolution with an Atomically Precise Nickel Catalyst. *ACS Catal.* **2016**, *6*, 1225–1234.
2. Huan, T. N.; Rouse, G.; Zanna, S.; Lucas, I. T.; Xu, X., Menguy, N.; Mougel, V.; Fontecave, M. A Dendritic Nanostructured Copper Oxide Electrocatalyst for the Oxygen Evolution Reaction. *Angew. Chem. Int. Ed.* **2017**, *56*, 4792-4796.
3. Vermaas, D. A.; Smith, W. A. Synergistic Electrochemical CO₂ Reduction and Water Oxidation. *ACS Energy Lett.* **2016**, *1*, 1143–1148.
4. Han, L.; Tang, P.; Carmona, A. R.; Garcia, B. R.; Torrens, M.; Morante, J. R.; Arbiol, J., Mascaros, J. R. G, Enhanced Activity and Acid pH Stability of Prussian Blue-type Oxygen Evolution Electrocatalysts Processed by Chemical Etching. *J.Am.Chem.Soc.* **2016**, *138*, 16037 – 16045.
5. Ma, W.; Ma, R.; Wang, C.; Liang, J.; Liu, X.; Zhou, K.; Sasaki, T. A Superlattice of Alternately Stacked Ni-Fe Hydroxide Nanosheets and Graphene for Efficient Splitting of Water. *ACS Nano* **2015**, *9*, 1977-1984.
6. Hong, W. T.; Risch, M.; Stoerzinger, K. A.; Grimaud, A.; Suntivich, J.; Shao-Horn, Y. Toward the Rational Design of Non-Precious Transition Metal Oxides for Oxygen Electrocatalysis. *Energy Environ. Sci.* **2015**, *8*, 1404-1427.
7. Lyu, F.; Bai, Y.; Li, Z.; Xu, W.; Wang, Q.; Mao, J.; Wang, L.; Zhang, X.; Yin, Y. Self-Templated Fabrication of CoO-MoO₂ Nanocages for Enhanced Oxygen Evolution. *Adv. Funct. Mater.* **2017**, *27*, 1702324.
8. Chen, H.; Gao, Y.; Sun, L. Highly Active Three-Dimensional NiFe/Cu₂O Nanowires/Cu Foam Electrode for Water Oxidation, *ChemSusChem* **2017**, *10*, 1475-1481.
9. Seitz, L. C.; Dickens, C. F.; Nishio, K.; Hikita, Y.; Montoya, J.; Doyle, A.; Kirk, C.; Vojvodic, A.; Hwang, H. Y.; Norskov, J. K.; Jaramillo, T. F. A highly active and stable IrO_x/SrIrO₃ catalyst for the oxygen evolution reaction. *Science* **2016**, *353*, 1011-1014.
10. Lee, Y.; Suntivich, J.; May, K. J.; Perry, E.E.; Shao-Horn, Y. Synthesis and Activities of Rutile IrO₂ and RuO₂ Nanoparticles for Oxygen Evolution in Acid and Alkaline Solutions. *J. Phys. Chem. Lett.* **2012**, *3*, 399-404.

11. Masud, J.; Umapathi, S.; Ashokaan, N.; Nath, M. Iron phosphide nanoparticles as an efficient electrocatalyst for the OER in alkaline solution. *J. Mater. Chem. A* **2016**, *4*, 9750-9754.
12. Silva, U. D.; Liyanage, W. P. R.; Nath, M. Magnetic Multifunctional Nanostructures as High-efficiency Catalysts for Oxygen Evolution Reactions. *MRS Advances*, **2016**, 1-7.
13. Jiao, F.; Frei, H. Nanostructured Cobalt Clusters in Mesoporous Silica as Efficient Oxygen-Evolving Catalysts. *Angew. Chem., Int. Ed.* **2009**, *48*, 1841-1844.
14. Amin, B. G.; Swesi, A. T.; Masud, J.; Nath, M. CoNi₂Se₄ as an efficient bifunctional electrocatalyst for overall water splitting, *Chem. Commun.*, **2017**, *53*, 5412-5415.
15. Tian, J.; Liu, Q.; Asiri, A. M.; Sun, X. Self-Supported Nanoporous Cobalt Phosphide Nanowire Arrays: An Efficient 3D Hydrogen-Evolving Cathode Over the Wide Range of pH 0–14. *J. Am. Chem. Soc.* **2014**, *136*, 7587-7590.
16. Ledendecker, M.; Calderon, S. K.; Shalom, M. The synthesis of nanostructured Ni₅P₄ films and their use as a non-noble bifunctional electrocatalyst for full water splitting. *Angew. Chem. Int. Ed.* **2015**, *127*, 12538–12542.
17. Peng, Z.; Jia, D.; Al-Enizi, A.; Elzatahry, A.; Zheng, G. From water oxidation to reduction: homologous Ni–Co based nanowires as complementary water splitting electrocatalysts. *Adv. Energy Mater.* **2015**, *5*, 1402031-1402038.
18. Tang, C.; Cheng, N.; Pu, Z.; Xing, W.; Sun, X. NiSe Nanowire Film Supported on Nickel Foam: An Efficient and Stable 3D Bifunctional Electrode for Full Water Splitting. *Angew. Chem. Int. Ed.* **2015**, *54*, 9351 – 9355.
19. Masud, J.; Swesi, A. T.; Liyanage, W. P. R.; Nath, M. Cobalt Selenide Nanostructures: An Efficient Bifunctional Catalyst with High Current Density at Low Coverage. *ACS Appl. Mater. Inter.* **2016**, *8*, 17292-17302.
20. Swesi, A. T.; Masud, J.; Nath, M. Nickel selenide as a high-efficiency catalyst for oxygen evolution reaction. *Energy & Environ. Sci.* **2016**, *9*, 1771-1782.
21. Masud, J.; Ioannou, P. C.; Levesanos, N.; Kyritsis, P.; Nath, M. A Molecular Ni-complex Containing Tetrahedral Nickel Selenide Core as Highly Efficient Electrocatalyst for Water Oxidation. *Chem. Sus. Chem.* **2016**, *9*, 3128-3132.
22. Swesi, A. T.; Masud, J.; Liyanage, W. P. R.; Umapathi, S.; Bohannan, E.; Medvedeva, J.; Nath, M. Textured NiSe₂ Film: Bifunctional Electrocatalyst for Full Water Splitting at Remarkably Low Overpotential with High Energy Efficiency, *Sci. Rep.* **2017**, *7*, 2401.

23. Gao, M. R.; Cao, X.; Gao, Q.; Xu, Y. F.; Zheng, Y. R.; Jiang, J.; Yu, S. H. Nitrogen-doped graphene supported CoSe₂ nanobelt composite catalyst for efficient water oxidation. *ACS Nano* **2014**, *8*, 3970-3978.
24. Wang, C.; Jiang, J.; Ding, T.; Chen, G.; Xu, W.; Yang, Q. Monodisperse Ternary NiCoP Nanostructures as a Bifunctional Electrocatalyst for Both Hydrogen and Oxygen Evolution Reactions with Excellent Performance. *Adv. Mater. Interfaces* **2016**, *3*, 1500454.
25. Zhang, J. J.; Su, H.; Wang, H. H.; Xue, Z. H.; Zhang, B.; Wei, X.; Lia, X.; Hirano, S. I.; Chen, J. S. Constructing Ohmic contact in cobalt selenide/Ti dyadic electrode: The third aspect to promote the oxygen evolution reaction. *Nano Energy* **2017**, *39*, 321–327.
26. Wu, Y.; Li, G. D.; Liu, Y.; Yang, L.; Lian, X.; Asefa, T.; Zou, X. Overall Water Splitting Catalyzed Efficiently by an Ultrathin Nanosheet-Built, Hollow Ni₃S₂-Based Electrocatalyst. *Adv. Funct. Mater.* **2016**, *26*, 4839-4847.
27. Silva, U. D.; Masud, J.; Zhang, N.; Hong, Y.; Liyanage, W. P. R.; Zaeem, M. A.; Nath, M., Nickel telluride as a bifunctional electrocatalyst for efficient water splitting in alkaline medium. *J. Mater. Chem. A*, **2018**, *6*, 7608-7622.
28. Masud, J.; Nath, M. Co₇Se₈ Nanostructures as Catalysts for Oxygen Reduction Reaction with High Methanol Tolerance. *ACS Energy Lett.* **2016**, *1*, 27–31.
29. Kwak, I. H.; Im, H. S.; Cha, E. H.; Park, J. CoSe₂ and NiSe₂ Nanocrystals as Superior Bifunctional Catalysts for Electrochemical and Photoelectrochemical Water Splitting. *ACS Appl. Mater. Interfaces*, **2016**, *8*, 5327–5334.
30. Yang, Y.; Xu, D.; Wu, Q.; Diao, P. Cu₂O/CuO Bilayered Composite as a High-Efficiency Photocathode for Photoelectrochemical Hydrogen Evolution Reaction. *Sci. Rep.* **2016**, *6*, 35158.
31. Hou, C. C.; Fu, W. F.; Chen, Y. Self-Supported Cu-Based Nanowire Arrays as Noble-Metal-Free Electrocatalysts for Oxygen Evolution. *ChemSusChem* **2016**, *9*, 2069-2073.
32. Riha, S. C.; Johnson, D. C.; Prieto, A. L. Cu₂Se Nanoparticles with Tunable Electronic Properties Due to a Controlled Solid-State Phase Transition Driven by Copper Oxidation and Cationic Conduction. *J. Am. Chem. Soc.* **2011**, *133*, 1383–1390.
33. Xu, J.; Yang, Q.; Kang, W.; Huang, X.; Wu, C.; Wang, L.; Luo, L.; Zhang, W.; Lee, C. S. Water Evaporation Induced Conversion of CuSe Nanoflakes to Cu_{2-x}Se Hierarchical Columnar Superstructures for High-Performance Solar Cell Applications. *Part. Part. Syst. Charact.* **2015**, *32*, 840–847.

34. Liu, X.; Duan, X.; Peng, P.; Zheng, W. Hydrothermal synthesis of copper selenides with controllable phases and morphologies from an ionic liquid precursor. *Nanoscale* **2011**, *3*, 5090-5095.
35. Lee, W.; Myung, N.; Rajeshwar, K.; Lee, C. W. Electrodeposition of Cu₂Se Semiconductor Thin Film on Se-Modified Polycrystalline Au Electrode. *J. of Electrochemical. Sci & Tech.* **2013**, *4*, 140-145.
36. Liu, X.; Cui, S.; Sun, Z.; Ren, Y.; Zhang, X.; Du, P. Self-Supported Copper Oxide Electrocatalyst for Water Oxidation at Low Overpotential and Confirmation of Its Robustness by Cu K-Edge X-ray Absorption Spectroscopy, *J. Phys. Chem. C* **2016**, *120*, 831–840.
37. Handoko, a. d.; Deng, S.; Deng, Y.; Cheng, A. W. F.; Chan, K. W.; Tan, H. R.; Pan, Y.; Tok, E. S.; Sowb, C. H.; Yeo, B. S. Enhanced activity of H₂O₂-treated copper(II) oxide nanostructures for the electrochemical evolution of oxygen, *Catal. Sci. Technol.* **2016**, *6*, 269-274.
38. Sun, W.; Song, Y.; Gong, X. Q.; Cao, L.; Yang, J. An efficiently tuned d-orbital occupation of IrO₂ by doping with Cu for enhancing the oxygen evolution reaction activity, *Chem. Sci.* **2015**, *6*, 4993-4999.
39. Serov, A.; Andersen, N. I.; Roy, A. J.; Matanovic, I.; Artyushkova, K.; Atanassov, P. CuCo₂O₄ ORR/OER Bi-Functional Catalyst: Influence of Synthetic Approach on Performance. *J. Electrochem. Soc.* **2015**, *162*, F449-F454.
40. Hinogami, R.; Toyoda, K.; Aizawa, M.; Kawasaki, T.; Gyoten, H. Copper Delafossite Anode for Water Electrolysis. *ECS Trans.* **2013**, *58*, 27-31.
41. Hou, C. C.; Chen, Q. Q.; Wang, C. J.; Liang, F.; Lin, Z.; Fu, W. F.; Chen, Y. Self-Supported Cedarlike Semimetallic Cu₃P Nanoarrays as a 3D High-Performance Janus Electrode for Both Oxygen and Hydrogen Evolution under Basic Conditions. *ACS Appl. Mater. Interfaces* **2016**, *8*, 23037 – 23048.
42. Li, H.; Li, Q.; Wen, O.; Williams, T. B.; Adhikari, S.; Dun, C.; Lu, C.; Itanze, D.; Jiang, L.; Carroll, D. L.; Donati, G. L.; Lundin, P. M.; Qiu, Y.; Geyer, S. M. Colloidal Cobalt Phosphide Nanocrystals as Trifunctional Electrocatalysts for Overall Water Splitting Powered by a Zinc-Air Battery. *Adv. Mater.* **2018**, *30*, 1705796.
43. Zhang, Z.; Ma, X.; Tang, J. Porous NiMoO_{4-x}/MoO₂ Hybrids as Highly Effective Electrocatalyst for Water Splitting Reaction. *J. Mater. Chem. A*, **2018**. DOI: 10.1039/C8TA03047B.

44. Li, C. W.; Kanan, M. W. CO₂ Reduction at Low Overpotential on Cu Electrodes Resulting from the Reduction of Thick Cu₂O Films. *J. Am. Chem. Soc.* **2012**, *134*, 7231–7234.
45. Zhang, X.; Liu, J. X.; Zijlstra, B.; Pilot, I. A. W.; Zhou, Z.; Sun, S.; Hensen, E. J. M. Optimum Cu nanoparticle catalysts for CO₂ hydrogenation towards methanol. *Nano Energy* **2018**, *43*, 200-209.
46. Gawande, M. B.; Goswami, A.; Felpin, F. X.; Asefa, T.; Huang, X.; Silva, R.; Zou, X.; Zboril, R.; Varma, R. S. Cu and Cu-Based Nanoparticles: Synthesis and Applications in Catalysis, *Chem. Rev.*, **2016**, *116*, 3722-3811.
47. Shimkin K. W.; Watson, D. A. Recent developments in copper-catalyzed radical alkylations of electron-rich π -systems, *Beilstein J. Org. Chem.* **2015**, *11*, 2278-2288.
48. Van Der Berg, R.; Prieto, G.; Korpershoek, G.; van der Wal, L. I.; van Bunningen, A. J.; Lægsgaard-Jørgensen, S.; de Jongh, P. E.; de Jong, K. P. Structure sensitivity of Cu and CuZn catalysts relevant to industrial methanol synthesis, *Nature Commun.* **2016**, *7*, 13057.
49. Chemler, S. R. Copper's Contribution to Amination Catalysis, *Science*, **2013**, *341*, 624-626.
50. Yang, H.; Chen, Y.; Cui, X.; Wang, G.; Cen, Y.; Deng, T.; Yan, W.; Gao, J.; Zhu, S.; Olsbye, U.; Wang, J.; Fan, W. A Highly Stable Copper-Based Catalyst for Clarifying the Catalytic Roles of Cu⁰ and Cu⁺ Species in Methanol Dehydrogenation, *Angew. Chem. Int. Ed.* **2018**, *57*, 1836-1840.
51. Murray, R. M.; Heyding, R. D. The Copper–Selenium System at Temperatures to 850 K and Pressures To 50 Kbar. *Can J. Chem.* **1975**, *53*, 878-887.

VII. FABRICATION OF MULTIFUNCTIONAL FERROMAGNETIC Au₃Pd–CoSe NANOPARTICLES

RSC Advances, 2014, 4, 28140

Wipula P. R. Liyanage,^{‡a} Sukhada Mishra,^{‡a} Kai Song^{§b} and Manashi Nath^{*a}

^aDepartment of Chemistry, Missouri University of Science and Technology, 400 W 11th Street, Rolla, MO 65409, USA. E-mail: nathm@mst.edu; Tel: (573)341-7160

^bMaterials Research Centre, Missouri University of Science and Technology, Rolla, MO 65409, USA

[‡] These authors contributed equally to this conducted research.

[§] Current address: FEI Company, 5350 NE Dawson Creek Drive, Hillsboro, Oregon 97124, USA; Tel: (860)768-8121.

ABSTRACT

We have synthesized multifunctional anisotropic Au₃Pd–CoSe nanoparticles on Si substrate through a catalyst aided chemical vapour deposition technique. The technique utilized volatile cobalt acetylacetonate and elemental selenium as precursors while sputter coated Au–Pd (3 : 2) film acted as a catalyst. The typical growth conditions led to clear segregation of the hetero-compositions (i.e. Au₃Pd and CoSe) in the product nanostructures thereby preserving the functionality of both the phases. The degree of crystallinity of the individual phases in the composite nanostructure was fairly high. The bifunctional nanoparticles show soft ferromagnetic behaviour at room temperature and optical activity making them ideal for opto-magnetic applications.

1. INTRODUCTION

Multifunctional nanostructures are explored extensively for their various applications including those in biosciences such as molecular imaging, magnetic separation, fluorescent label-ling and other theranostic uses.^{1,2} The capability to tune the size, shape and morphology in addition to the composition of these multifunctional nanomaterials provides them with even more versatility. Multifunctional nanomaterials can be categorized according to their morphologies as core–shell (where hetero-composition is expressed radially),³ dumbbell shaped (where heterocompositions are segregated along the long axis of the nanostructure)⁴ and barcode structures.⁵ The functionalities of the individual regions can be varied to obtain various types of multifunctional nanomaterials. The dumbbell shaped nano- particles containing two compositions of widely different functionalities sharing a common interface is especially lucrative since it provides opportunities to fully utilize both the functionalities in the nanoparticle ensemble. These types of multifunctional particles are also referred to as Janus particles when they are more spherical than elongated.⁶ Amongst these, nanostructures including a metallic and a magnetic composition have been of considerable interest due to their promising applications in magneto-optic and optoelectronic devices. Development in the field of nanotechnology has also contributed to the advancement of practical applications of the multifunctional nanoparticles in nanomedicine as theranostic agents.⁷ Owing to its, biocompatibility and localized surface plasmon resonance (SPR) properties, Au nanoparticles have been very well analyzed component of the multifunctional nanoparticle assemblies.^{7,8} The optical properties of the

Au imparts major advantages, as the SPR peak of the Au nanoparticles can be adjusted to near-infrared region, by tuning the size of the nanoparticles where the biological tissues being 'nearly transparent' at these wavelengths, do not absorb in these regions thus reducing background noise. Accordingly, various multifunctional nanoparticles containing Au, such as Au-Fe₂O₃, Au-FePt, Au-Fe₃O₄ has been synthesized by different techniques involving solution-based chemistry.⁸⁻¹⁰

The transition metal chalcogenides (MEx) [M = Fe, Co, Mn; E = Se, S, Te] have attracted the solid state chemists for a long time owing to their interesting electronic and magnetic properties.¹¹ Among them, CoSe is a semiconducting material with the band gap of 1.52 eV. Cobalt selenides typically show compositions ranging from the stoichiometric CoSe, CoSe₂ phases to the non-stoichiometric Co_{0.85}Se phase.¹²⁻¹⁵ Cobalt selenide is known to be a metallic conductor and exchange enhanced Pauli paramagnet in its ground state with a T_c of approximately 125 K.¹²⁻¹⁵ Recently cobalt selenides have shown lot of promise as catalysts for oxygen reduction, decomposition of hydrazine hydrate, magnetic refrigeration and as electrodes for Li-ion batteries.¹⁶ CoSe in bulk form has been synthesized through electrochemical deposition technique,¹⁷ high pressure solid-state synthesis¹⁸ and through mechanical alloying.¹⁹ However, reports of cobalt selenide nanostructures are very limited.²⁰⁻²² CoSe nanoparticles have been synthesized through microwave assisted methods²⁰ while CoSe nanocrystals were also formed using metal acetate-paraffin approach, in the presence of oleylamine,²¹ and by hydrothermal method in presence of hydrazine, cobalt chloride and selenium.²²

In this article, we report the synthesis, characterization and properties of Au₃Pd-CoSe bifunctional nanoparticles, which show magnetic ordering as well as optical

activity. These nanoparticles have been produced by a simple chemical vapour deposition (CVD) reaction and are the first of its kind. The bifunctional nature of these composite nanoparticles was characterized through optical and magnetic properties. The fusion of optical and magnetic properties in these nanoparticles will be useful for applications in various fields like opto-magnetic devices, biomedical and bio-imaging platforms.

2. EXPERIMENTAL

2.1. MATERIALS & METHODS

Si substrates used for chemical vapour deposition were purchased from Si quest international. These Si substrates were cut into pieces of 1 x 1 cm² and prewashed with isopropanol and acetone in order to remove dirt particles. No extra precautionary step was taken to remove the native oxide layer. The substrates were then sputter coated with Au–Pd (3 : 2) for 120 seconds creating a thick layer (approximately 100 nm) of Au–Pd over the substrates. Cobalt acetylacetonate [Co(C₅H₇O₂)₃, Co(acac)₃] and Se shots, used as precursors for Co and Se, respectively were obtained from Sigma-Aldrich and used as such, without further purification.

2.2. SYNTHESIS OF Au₃Pd–CoSe COMPOSITE NANOPARTICLES

Au₃Pd–CoSe nanoparticles were synthesized by catalyst aided CVD reaction carried out in a horizontal tube furnace at 800 °C under a flow of N₂ as carrier gas (120 sccm). A Au–Pd (3 : 2) coated Si wafer used as the substrate for growth was kept at the central region of the horizontal furnace at 800 °C. With the help of a mass flow controller

the reaction assembly was maintained at a continuous N₂ flow of 120 sccm. Both the Co(acac)₃ and Se sublime at elevated temperatures and hence they were strategically placed within the reaction tube such that the temperature at the precursors just exceeded their sublimation temperature when the central zone of the furnace was at 800 °C. Selenium shots were positioned at 400 °C, while the Co(acac)₃ was kept at a 250 °C region. Initially, the Co(acac)₃ and Se were kept outside the heating zone by pushing the ceramic liner to the extreme left. Once the central zone of the furnace reached the reaction temperature (800 °C), the ceramic liner was pushed to the right such that the Se and Co(acac)₃ were at 400 °C and 250 °C respectively. These steps were crucial for reproducibility of the reaction, as it avoids the sublimation and escape of the reactants (Se and Co(acac)₃ vapors) before the Au/Pd catalyst reaches the melting temperature. The reaction was carried out for 30 minutes, and the furnace was cooled down at the rate of 8 °C min⁻¹. After completion of the reaction a golden brown deposition was observed on the Si substrate. This deposition was further characterized for elucidation of the morphology and composition of the product.

2.3. CHARACTERIZATION TOOLS & TECHNIQUES

2.3.1. Powder X-ray diffraction. The product was characterized without any subsequent purification through powder X-ray diffraction (pxrd) with Philips X-Pert using CuK α (1.5418 Å) radiation.

Pxrd pattern was collected from the as-synthesized product spread on the Si substrate. Because the product formed a very thin layer on the Si substrate, the pxrd was collected at grazing angles in thin film geometry (GI mode with Gobel mirrors).

2.3.2. Electron microscopy characterizations. For transmission electron microscopy (TEM) imaging, the sample was prepared by loosening a small amount of product from the Si substrate (typically, the deposition on Si substrate was scratched) and dispersing it in ethanol. A drop from the “as prepared” dispersion was placed a holey carbon coated Cu TEM grid and dried in air thoroughly prior to TEM imaging and Energy dispersive X-ray spectroscopy (EDS). TEM images were obtained on FEI Tecnai F20 and Tecnai Osiris TEM operating at 200 kV. For FEI Tecnai Osiris TEM the probe current is 1 nA with a spot size of less than 1 nm. The convergence angle is 10.3 mrad and the camera length is 200 mm for HAADF imaging. High resolution TEM in Figure 3 was obtained with the Tecnai Osiris operated at 200 keV with a probe current of 2.5 nA. The Fast Fourier Transform (FFT) patterns generated from the lattice fringes clearly demonstrated the crystalline character of the individual regions, i.e. Au₃Pd and CoSe.

Scanning electron microscope (SEM) imaging was performed using FEI Helios NanoLab 600 FIB/FESEM directly onto the Si substrate covered with the nanoparticles. SEM and EDS imaging was also performed by isolating a small amount of powder from the Si substrate and putting it on the sample holder. The EDS line scan and mapping as shown in Figure 2 was conducted on an FEI Tecnai F20 TEM operated at 200 keV in STEM mode. The probe current is 1.2 nA with a spot size of less than 2 nm. The convergence angle is 13 mrad and the camera length is 30 mm for dark field imaging. This scope is equipped with an Oxford ultra-thin (UTW) window EDS detector, which allows detection of carbon. The X-ray transmission efficiency for carbon with this window is 42%.

2.3.3. Magnetic characterizations. A magnetic moment was collected from a SQUID magnetometer in the VSM mode. The Si-substrate containing large density of Au₃Pd–CoSe composite nanoparticles was loaded into a gel cap and was inserted into the magnetometer with the help of standard sample loader. The diamagnetic signal from the gel cap was collected separately and subtracted as a background from the signal obtained from the sample. The zero field cooled (ZFC) data was obtained after cooling the sample down to ~2K under 0 magnetic fields and then by measuring the magnetization under an applied field during the warming up cycle. The field cooled warming (FCW) data was collected by cooling the sample down from room temperature to 2 K under a non-zero magnetic field and then collecting the warming up data under an applied field. The magnetization of a blank Si substrate which was heat treated under similar conditions was also collected separately and used as a reference.

2.3.4. Optical characterizations. Varian Cary 50 UV-Vis Spectrophotometer was used for optical property measurements. Sample preparation for the UV-Vis spectroscopy involved two separate methods. In one method the composite nanoparticles were dislodged from the Si substrate and sonicated in ethanol for about 30 minutes. This dispersion was then loaded in a quartz cuvette and the absorbance spectra were recorded while the nanoparticles were still dispersed.

The second method involved functionalization of these bifunctional nanoparticles through the affinity of Au with thiol-based ligands. Typically the Au₃Pd–CoSe nanoparticles were dislodged from the Si substrate and added to an ethanolic solution of 1-octadecanethiol forming a stable dispersion. This dispersion was then dried on top of glass slides which were then loaded in the sample chamber of the UV-Vis spectrometer.

3. RESULTS & DISCUSSION

3.1. MORPHOLOGY AND STRUCTURAL CHARACTERIZATION

Figure 1a demonstrates the pXRD pattern obtained from the product, confirming the presence of hexagonal CoSe (JCPDS card no. 42541) and Au₃Pd (JCPDS no. 180872) formed from the catalyst. The intense and sharp pXRD peaks suggest highly crystalline nature of the formed product. Noticeably, the product purity was very high and it did not exhibit presence of any crystalline impurity from other cobalt selenide phases. Figure 1b shows the SEM image of the product, revealing a huge yield of the elliptical-shaped nanoparticle morphology. The shape and nature of these nanoparticles are very representative of the bifunctional Janus particles.⁶ The presence of hetero- composition zones in the nanoparticle was very apparent as can be seen from the different contrasts in the SEM images. The composite nanoparticles were mostly elliptical in shape with the short axis ranging from 100–150 nm while the catalyst tip was less than 100 nm. The nanoparticle size distribution was estimated by analyzing large number of these nanoparticles and the corresponding histogram is shown in Figure 1c (corresponding to the short axis of the elliptical particles) and 1d (corresponding to the catalyst tip/cap). Histogram analysis also showed that the particle sizes (along the long axis) were mostly in the range 200–250 nm. In almost all the nanoparticles, heterozones were observed longitudinally while radial hetero- junctions (core–shell) were not present. The size of these composite nanoparticles could be somewhat controlled by changing the size of the initial Au–Pd nanoalloy catalyst particles.

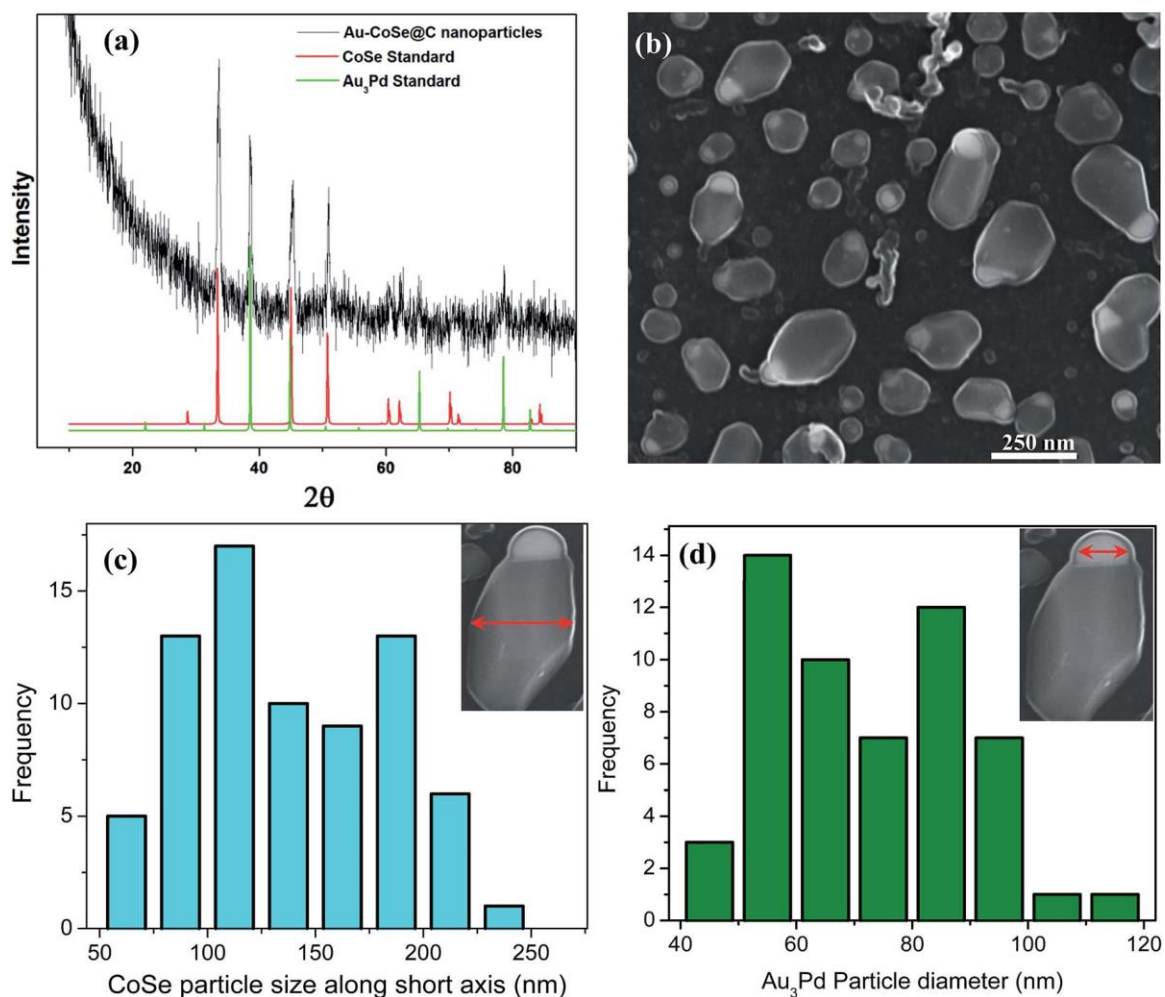


Figure 1. Crystal structure and morphology. (a) PXRD pattern of the Au₃Pd-CoSe nanoparticles showing presence of CoSe along with Au₃Pd. (b) SEM image of the bifunctional nanoparticles. Brighter tip represents Au₃Pd, while darker region contains CoSe. (c) Particle size distribution (along short axis) of Au₃Pd-CoSe nanoparticles. (d) Particle size distribution (i.e. diameter) of the Au-Pd region.

The elemental compositions of these bifunctional nanoparticles were investigated in details through extensive elemental analysis studies including EDS line scan and mapping in STEM mode. The elemental mapping from these individual nanoparticles showed that Co and Se were concentrated at the thicker end of the nanoparticle while Au and Pd was immobilized at the slender tip as shown in Figure 2.

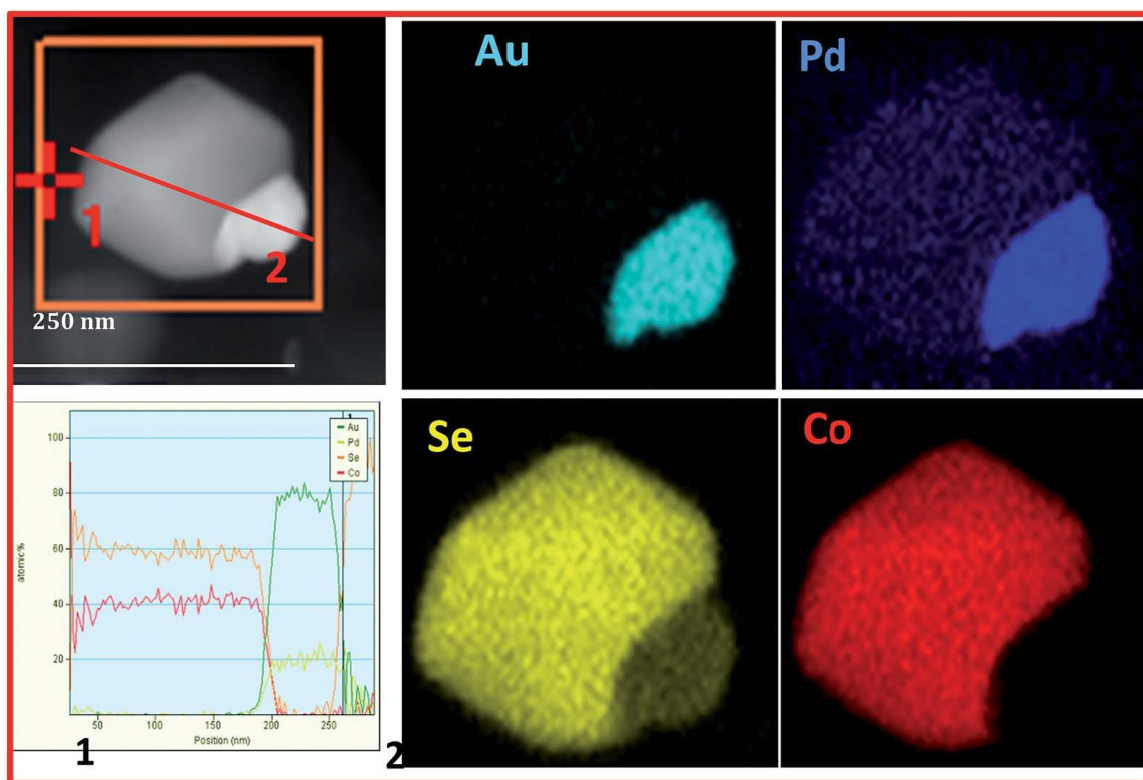


Figure 2. Elemental mapping of the Au–CoSe nanoparticles. As shown in upper left panel, preferential location and segregation of the Au, Pd, Co and Se are shown in the mapping images. The lower left panel shows elemental line scan across the same nanoparticle which corroborates with mapping.

The Au(Pd) and Co–Se regions shared a common interface. There was no noticeable mixing of Au in the Co–Se regions, and likewise there was almost no mixing of Co–Se in the Au region. This indicates that the phase purity of the individual phases in these bifunctional nanoparticles was very high. Although pXRD showed that the metallic part was mainly formed by Au_3Pd , there is a possibility that trace amounts of Au was also present. Au and Pd forms Au_3Pd alloy in a narrow temperature range.²³ The composition of these nanoparticles was also confirmed through X-ray photoelectron spectroscopy (XPS) which showed the presence of peaks corresponding to Co (2p) [778 eV] and Se

(3d) [54 eV] in addition to Au (4f) and Pd (4d) as shown in Figure S1 in supporting information (ESI). These values agree well with the reported values for CoSe.²⁴

These composite nanoparticles were studied through detailed high-resolution TEM microscopy (HRTEM) to get a better insight into the composition of individual regions of the bifunctional particles as well as nature of the interface between these. These HRTEM studies showed that the thicker portion was actually crystalline CoSe phase with lattice fringes corresponding to the [100] planes, while the darker region showed mostly the presence of crystalline Au₃Pd (Figure 3a and b). SAED pattern could also be collected from the CoSe region, which showed diffraction spots corresponding to (010), (1-01) and (1-11) lattice planes while the zone axis was along the <111> direction. HRTEM images collected near the interface revealed that the junction between CoSe and Au(Pd) phases were very clean and sharply defined (Figure 4a and b).

There was minimal mixing at the interface and there was no loss of crystalline order across the interface. The nature of the interface is very crucial since in these magnetic nanostructures pinning of magnetic flux at the interface by another magnetic material may lead to exchange bias interactions. However, in this case, the interface was very clean indicating that there was no major magnetic phase other than CoSe present in the interface.

3.2. OPTICAL PROPERTIES

Au nanostructures are well-known for their plasmonic property which gives a characteristic peak in the UV-Vis spectra.²⁵ It has been reported by other researchers that formation of Au₃Pd nanoparticles also shows surface plasmon bands similar to Au.^{26,27}

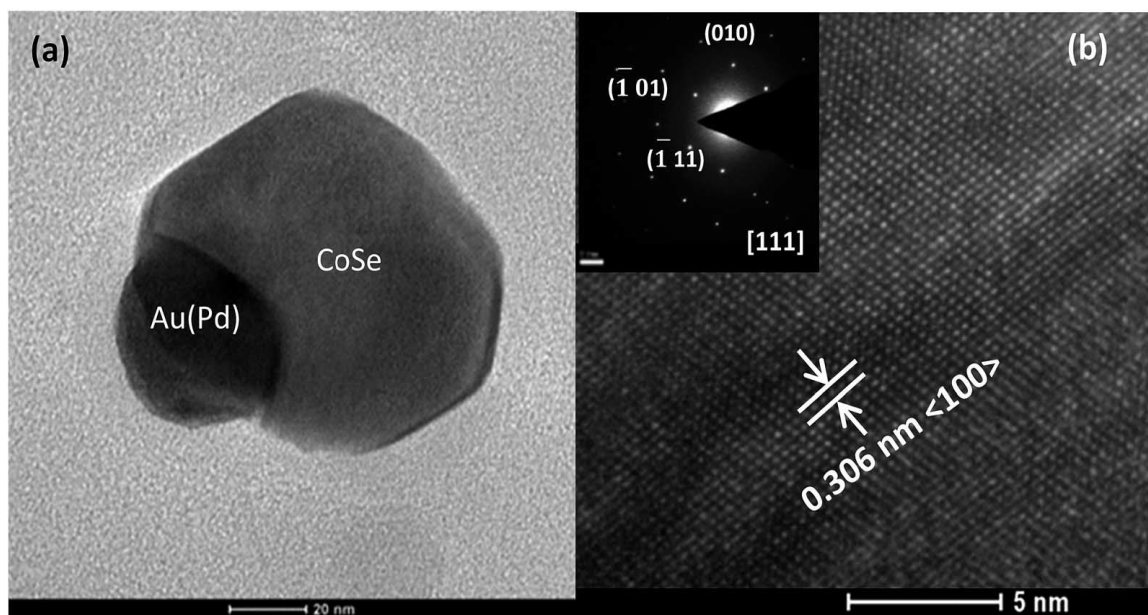


Figure 3. TEM images of nanoparticles. (a) Magnified view of the single nanoparticle, clearly showing the union of the two nanoparticles, through a common interface. (b) HRTEM image of the CoSe region showing the lattice fringes which could be matched with $\langle 100 \rangle$ lattice planes of CoSe phase. Inset showing the SAED pattern depicting high degree of crystallinity.

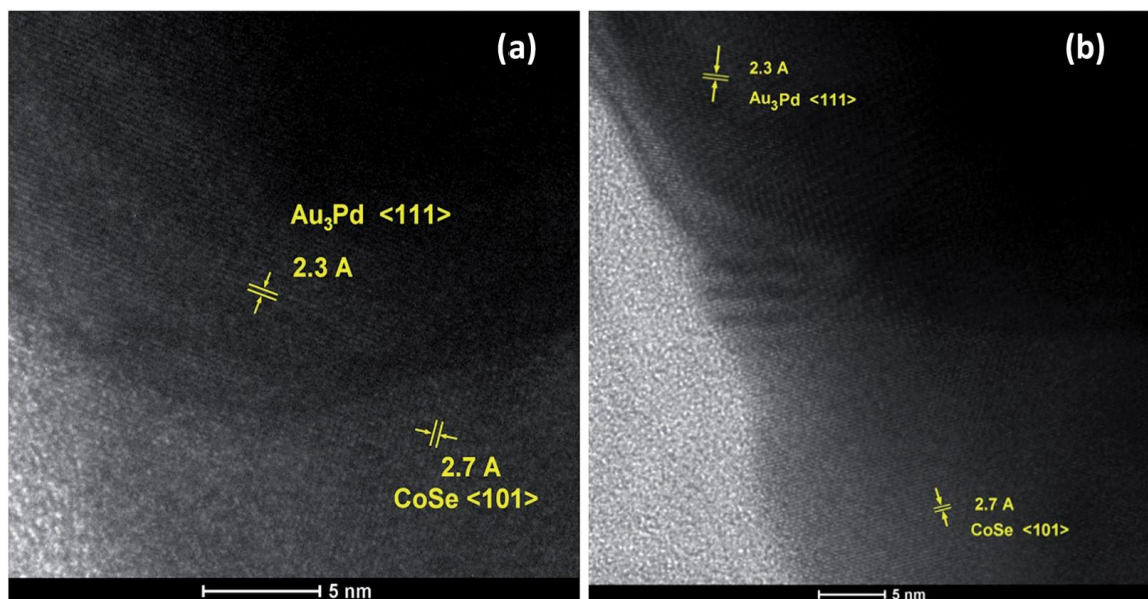


Figure 4. HRTEM images of a single nanoparticles. (a) and (b) shows clean interfaces and exhibits lattice fringes corresponding to Au_3Pd and CoSe on either sides.

Hence UV-Vis absorbance spectra and magnetization was collected from an ensemble of these Au₃Pd–CoSe nano- particles to study their opto-magnetic properties respectively. The UV-Vis spectra of Au₃Pd–CoSe nanoparticle ensemble show a peak around 565 nm which is characteristic of Au nano- structure with a size of ~90 nm (Figure 5a). The UV-Vis spectra also show a peak at 735 nm with a band-edge at ~750 nm corresponding to band gap energy of around 1.64 eV. This corresponds to the electronic excitation in the CoSe region, where bulk CoSe is reported to have a band-gap of 1.55 eV.^{12–15}

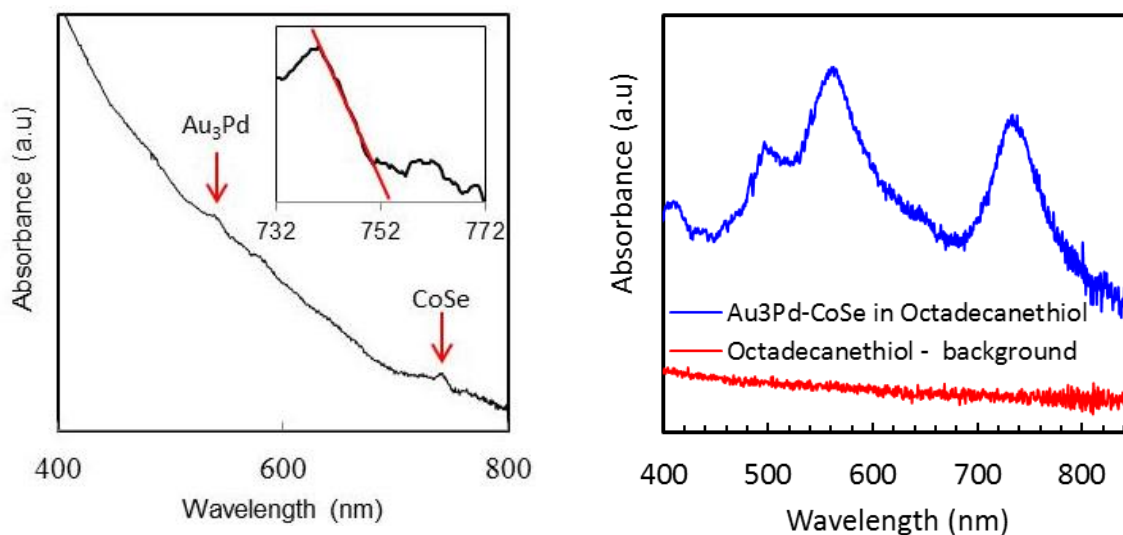


Figure 5. Absorbance spectra from Au₃Pd–CoSe bifunctional nanoparticles. (a) In ethanol and (b) as a film spread on glass slide.

It should be noted that the plasmonic property of Au is not dampened in these composite nanoparticles. The absorbance spectrum was also collected by dispersing the Au₃Pd–CoSe nanoparticles in solution in the presence of octadecanethiol which gave a

stable dispersion. This dispersion was then dried on a glass slide to form a uniform \square lm-like deposition. This slide was then subjected to UV-Vis spectroscopy and yielded a clean spectrum with peaks at 560 nm and 750 nm similar to the ones obtained in the ethanol (Figure 5b). It should be noted here that the octadecanethiol by itself does not show any well-defined feature in the 400–850 nm range of wavelength. Hence, the absorbance peaks obtained from the sample slide can be ascribed solely due to the Au₃Pd–CoSe nanoparticles.

3.3. MAGNETIC PROPERTY MEASUREMENT

While Au is the optically active component in these nano-structures, CoSe on the other hand is a magnetic solid which shows Pauli paramagnetism.^{12–15} Magnetic property of the composite nanoparticles was studied through temperature dependent magnetization and isothermal magnetization as a function of applied field. The magnetization as a function of temperature was collected both at zero-field (ZFC) and field cooled (FC) conditions. Both ZFC and FC plot shows characteristic of a ferromagnet-like interaction at low temperatures (<10 K) (Figure 6a). However, the data was a little bit noisy probably due to the composite nature of these nanoparticles and also the presence Si (from the substrate) in the ensemble used for magnetic measurement.

The magnetic signal from Si was also collected as background, which showed featureless M vs. T plot as would be expected (Figure S2). The isothermal magnetization vs. field for the composite nanoparticles was collected at 300 K and 5 K (Figure 6b).

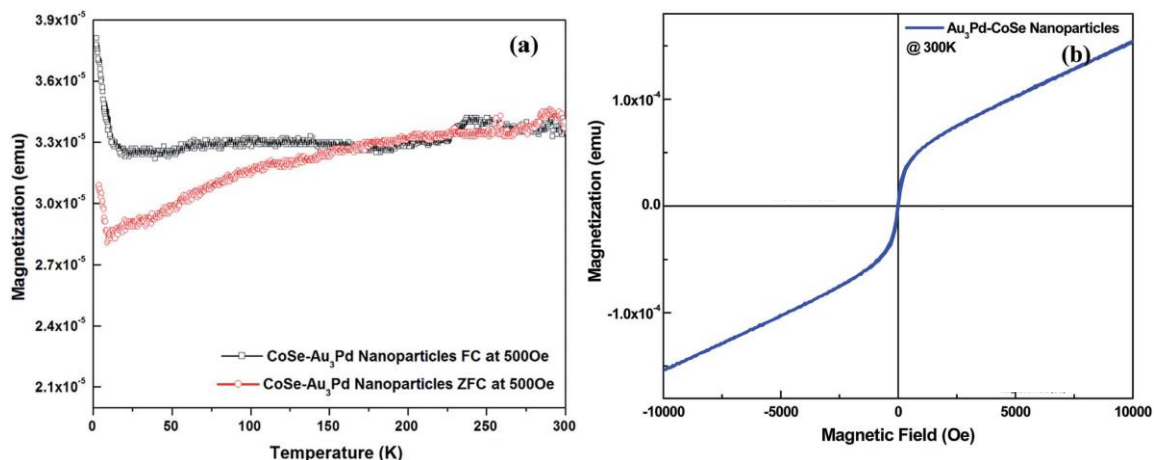


Figure 6. The magnetization behaviour of Au₃Pd–CoSe nanoparticles. (a) M vs. T plot of the nanoparticles under zero-field cooled and field-cooled conditions. (b) Isothermal M vs. H at 300 K. Lower right inset shows the zoomed in view showing the small coercivity. Upper left inset shows the M vs. H plot at 5 K.

The hysteresis plots were consistent with soft ferromagnetic behavior of the composite nanoparticles. At 300 K the hysteresis loop showed a very small coercive field of ~ 40 Oe (Figure 6b, right insert). At low temperatures (5 K) a clear hysteresis was also observed (Figure 6b, left insert). However, there was a marked absence of coercivity and the magnetization had a cross-over near 0 Oe. This kind of behavior has been observed in single molecule magnets and mesoscopic granular ferromagnetic particles.^{28,29} It is explained mainly by the occurrence of magnetic relaxation by quantum tunneling at low temperatures near zero fields. These kinds of magnetic relaxation are very dependent on the particle size and anisotropy. Also the presence of surface spin states causes anomalous behavior in the low temperature hysteresis loops of the nanosized magnetic particles. Hence, we suspect that the polydispersity of the CoSe regions along with varying degree of anisotropy between particles and the presence of interface with Au₃Pd give rise to competing magnetic interactions, especially at low temperatures, contributing

to the complex nature of the hysteresis curve. However, the nature of the hysteresis loops indicates that the nanoparticles have considerable ferromagnetic interactions within the ensemble. The very low value of the coercive field also suggests superparamagnetic behavior, which is expected for ferromagnetic nanoparticles with sizes below the critical limit for forming monodomain magnetic particles. It was also observed that the Au₃Pd–CoSe nanoparticle ensemble was weakly attracted to a common laboratory magnet and could be magnetically separated over several days. Hence it can be concluded that the Au₃Pd–CoSe nanoparticles have soft ferromagnetic interactions within the ensemble with low coercivity which makes them weakly responsive to external magnetic fields. Their diminishing hysteresis loop and nature of the ZFC–FC curves indicate that at 300 K they might be very near to the superparamagnetic blocking temperature separating the ordered state with the superparamagnetic state.

It was observed that the Au₃Pd–CoSe nanoparticles could be stabilized in solution by adding a thiol-based ligand (e.g. octadecanethiol) which shows affinity towards Au₃Pd-region. The dispersion formed by Au₃Pd–CoSe nanoparticles in ethanol in the presence of octadecanethiol was stable for several days. Interestingly, placing a magnet near the dispersion led to the very slow accumulation of Au₃Pd–CoSe nanoparticles near the magnet. This indicates that these nanoparticles reported here can be functionalized with appropriate head groups and will be ideal for application which requires multifunctional opto-magnetic components, where the magnetic part can be utilized for targeting and tracking, while the optical part aids in identification. Currently, the authors are trying to functionalize these nanoparticles with some peptide aptamers and use them for in vitro studies related to theranostic applications.

3.4. MECHANISM OF FORMATION

To elucidate the growth mechanism, the authors performed several experiments by varying the reaction parameters. It was realized that the first step in this reaction scheme was the formation of Au_3Pd alloy which is the stable phase in the Au–Pd binary phase diagram within the Pd rich zone.²³ This Au_3Pd then acts as the catalysts for further decomposition and growth of the Co-rich phases. The next stage in the nano-structure growth comprises of vaporization and transport of $\text{Co}(\text{acac})_3$ and Se. The $\text{Co}(\text{acac})_3$ pyrolyzes under the reaction condition and the Co-rich vapours generated dissolve and diffuses preferentially within the Au_3Pd region of the catalyst. As Se vapours are fed into the system, the Co end of the catalyst gets converted into CoSe which precipitates out from one end of the active catalyst region (Au_3Pd). The limited solubility of Co and Se in Au_3Pd , facilitates the anisotropic precipitation of the CoSe phase. It should be noted here that in the composite nanoparticle there was no evidence of elemental Co and the formation reaction of CoSe was complete.

The method for nanostructure growth reported here is similar to the growth of superconducting FeSe nanocables and entrapped nanoparticles by the current authors.^{30,31} In the case of FeSe nanostructures, however, the entire FeSe was encapsulated within a carbon nanofiber and carbonaceous shell, respectively, and the growing FeSe shared an interface with $\text{Pd}_{17}\text{Se}_{15}$, while Au did not take part in the reaction at all. There was no evidence of Au_3Pd formation in the case of FeSe. In the current case, however, the marked difference between the phase diagrams of Fe–Pd and Co–Pd results in completely different composition-zones in the nanostructures, viz. Au_3Pd alloy formation.

4. CONCLUSIONS

We have successfully synthesized, anisotropic, bifunctional Au₃Pd–CoSe nanoparticles, through facile, catalyst aided, chemical vapour deposition technique. The magnetic characterization of these bi-functional nanoparticles revealed their soft ferromagnetic nature. Optical activity of these nanoparticles was confirmed through observation of the plasmonic bands for Au and the absorbance peak corresponding to CoSe. The method described in this report can be used to synthesize new multifunctional nanostructures by carefully choosing various other metal-acetylacetonate precursors, and catalyst particles to synthesize metal selenide-noble metal multi-functional nanostructures.

ACKNOWLEDGEMENTS

The authors would like to acknowledge Materials Research Center for equipment usage, Dr. Kartik Ghosh, Dr. Jakub Koza and Dr. Jay Switzer for help with some magnetic measurements.

SUPPLEMENTARY INFORMATION

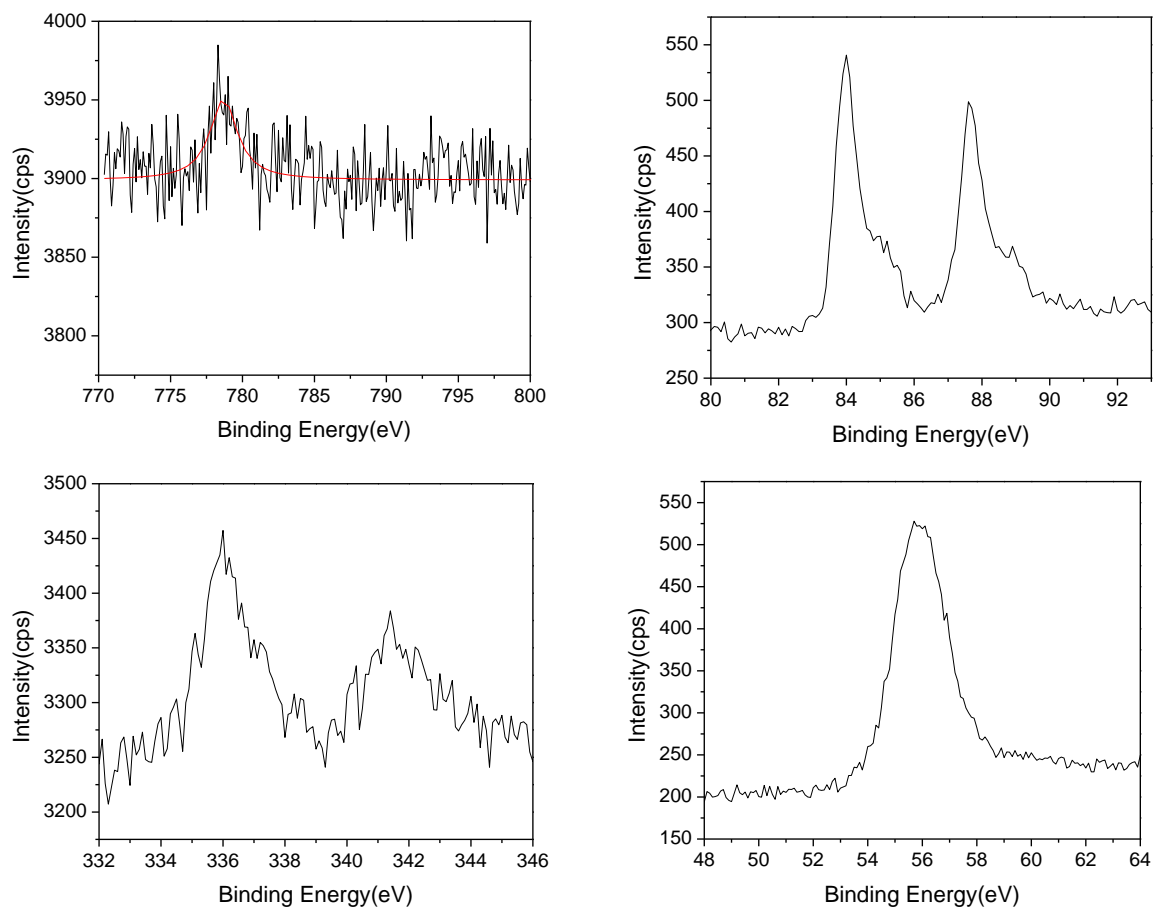


Figure S1. The XPS spectra collected from the Au₃Pd-CoSe composite nanoparticles after sputtering for 10 s.

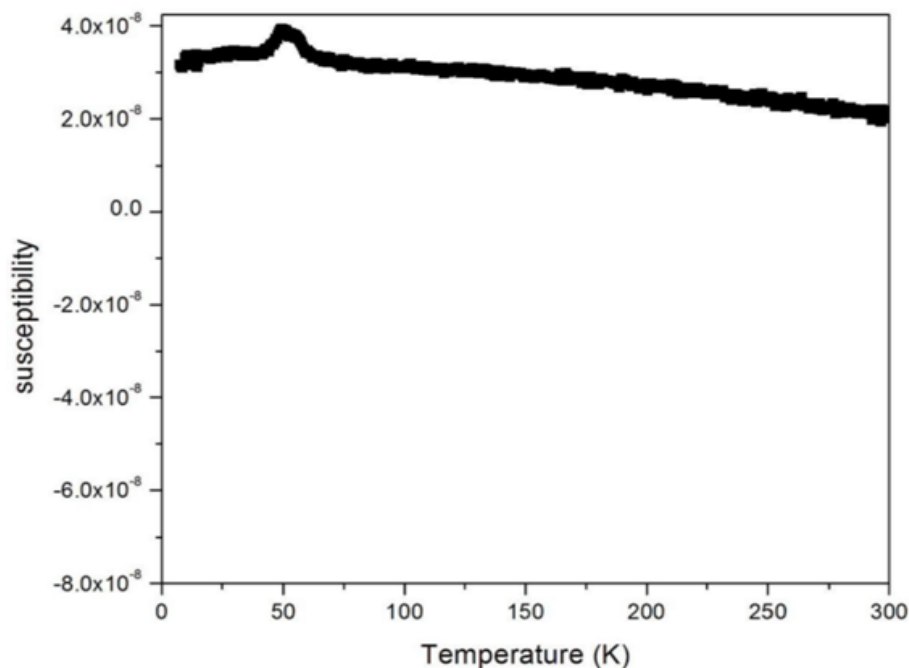


Figure S2. The susceptibility vs temperature plot of Si substrate (blank).

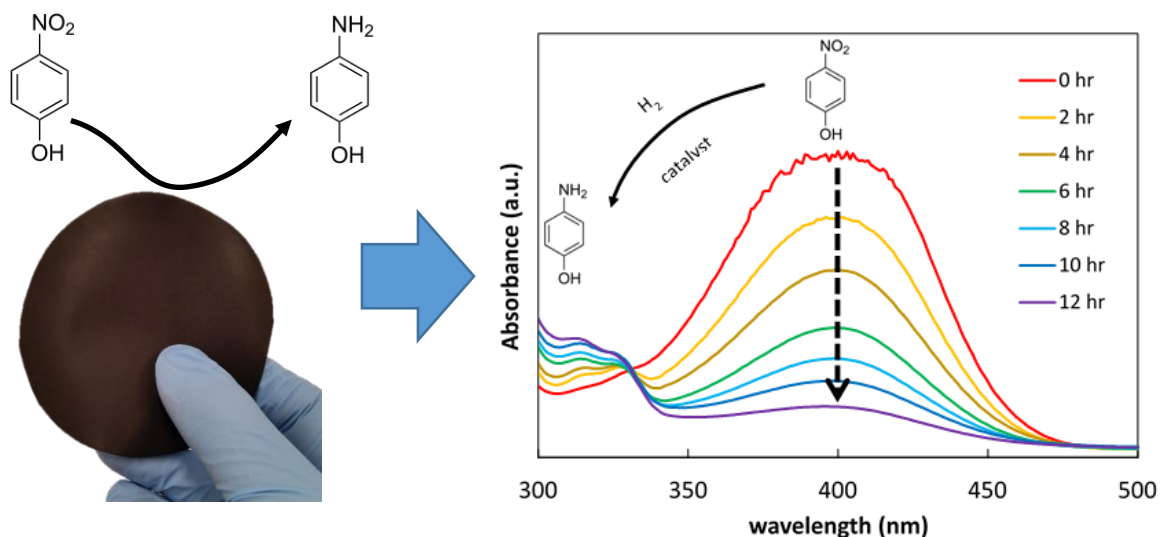
REFERENCES

1. H. Zeng and S. Sun, *Adv. Funct. Mater.*, 2008, **18**, 391
2. C. V. Durgadas, C. P. Sharma and K. Sreenivasan, *Nanoscale*, 2011, **3**, 4780
3. M. Kaur, J. S. McCloy, W. Jian, Q. Yao and Y. Qiang, *J. Phys. Chem. C*, 2012, **116**, 12875
4. C. Xu, D. Ho, J. Xie, C. Wang, N. Kohler, E. G. Walsh, J. R. Morgan, Y. E. Chin and S. Sun, *Angew. Chem., Int. Ed.*, 2008, **47**, 173
5. A. J. Mieszawska, R. Jalilian, G. U. Sumanasekera and F. P. Zamborini, *Small*, 2007, **3**, 72
6. C. Langlois, Z. L. Li, J. Yuan, D. Alloyeau, J. Nelayah, D. Bochicchio, R. Ferrando and C. Ricolleau, *Nanoscale*, 2012, **4**, 3381
7. G. A. Sotiriou, *WIREs Nanomed. Nanobiotechnol.*, 2013, **5**, 19–30

8. Z. Fan, M. Shelton, A. K. Singh, D. Senapati, A. S. Khan and P. C. Ray, *ACS Nano*, 2012, **6**, 1065
9. C. Wang, J. Chen, T. Talavage and J. Irudayaraj, *Angew. Chem., Int. Ed. Engl.*, 2009, **48**, 2759
10. X. Ji, R. Shao, M. A. Elliott, J. R. Stafford, E. Esparza-Coss, A. J. Bankson, G. Liang, P. Z. Luo, K. Park, T. J. Markert and C. Li, *J. Phys. Chem. C*, 2007, **111**, 6245
11. H. Ido and T. Itoh, *Electronic structure and Magnetism of 3d-Transition Metal Pnictides*, Springer, 2009
12. M. Hansen, *Constitution of Binary Alloys*, Geminuim Publ. Co., New York, 1985, p. 502
13. X. H. Liu, N. Zhang, R. Yi, G. Z. Qiu, A. G. Yan, H. Y. Wu, D. P. Meng and M. T. Tang, *Mater. Sci. Eng., B*, 2007, **140**, 38
14. J. H. Zhang, X. G. Yang, S. D. Li, Y. Xie, W. C. Yu and Y. Qian, *J. Solid State Chem.*, 2000, **152**, 537
15. J. F. Zhao, J. M. Song, C. C. Liu, B. H. Liu, H. L. Niu, C. J. Mao, S. Y. Zhang, Y. H. Shen and Z. P. Zhang, *Cryst. Eng. Comm*, 2011, **13**, 5681
16. L. Zhang and C. Zhang, *Nanoscale*, 2014, **6**, 1782–1789
17. F. Liu, B. Wang, Y. Lai, J. Li, Z. Zhang and Y. Liu, *J. Electrochem. Soc.*, 2010, **157**, D523
18. N. Umeyama, M. Tokumoto, S. Yagi, M. Tomura, K. Tokiwa, T. Fujii, R. Toda, N. Miyakawa and S. Ikeda, *Jpn. J. Appl. Phys.*, 2012, **51**, 053001
19. C. E. M. Camposa, J. C. de Lima, T. A. Grandia, K. D. Machado and P. S. Pizanib, *Phys. B*, 2002, **324**, 409
20. C. Wang, C. Xu, H. Zeng and S. Sun, *Adv. Mater.*, 2009, **21**, 3045
21. Y. Jin, C. Jia, S. Huang, M. O'Donnell and X. Gao, *Nat. Commun.*, 2010, **1**, 1
22. X. Liu, N. Zhang, R. Yi, G. Qiu, A. Yan, H. Wu, D. Meng and M. Tang, *Mater. Sci. Eng., B*, 2007, **140**, 38
23. H. Okamoto and T. B. Massalski, *Bull. Alloy Phase Diagrams*, 1985, **6**, 229

24. A. B. Mandale, S. Badrinarayanan, S. K. Date and A. P. B. Sinha, *J. Electron Spectrosc. Relat. Phenom.*, 1984, **33**, 61
25. M. Hu, J. Chen, Z. Li, L. Au, G. V. Hartland, X. Li, M. Marqueze and Y. Xia, *Chem. Soc. Rev.*, 2006, **35**, 1084
26. C. Shen, C. Hui, T. Yang, C. Xiao, J. Tian, L. Bao, S. Chen, H. Ding and H. Gao, *Chem. Mater.*, 2008, **20**, 6939
27. E. P. Tijerina, M. Garcia Pinilla, S. Mejia-Rosales, U. Ortiz-Mendez, A. Torres and M. Jose-Yacamán, *Faraday Discuss.*, 2008, **138**, 353
28. D. P. Mills, F. Moro, J. McMaster, J. Slageren, W. Lewis, A. J. Blake and S. T. Liddle, *Nat. Chem.*, 2011, **3**, 454
29. R. H. Kodama, C. L. Seaman, A. E. Berkowitz and B. Mapple, *J. Appl. Phys.*, 1994, **75**, 5639
30. S. Mishra, K. Song, J. A. Koza and M. Nath, *ACS Nano*, 2013, **7**, 1145
31. S. Mishra, K. Song, K. Ghosh and M. Nath, *ACS Nano*, 2014, **8**, 2077

VIII. A FREE STANDING CATALYST FILM FOR ELECTROCATALYTIC APPLICATIONS



Manuscript has been submitted to International Journal of Hydrogen Energy

Wipula Priya Rasika Liyanagea, Manashi Nath,*

Department of Chemistry, Missouri University of Science and Technology, 142 Schrenk Hall, 400 W. 11th St., Rolla, MO 65409

* Corresponding author e-mail: nathm@mst.edu

ABSTRACT

This research work describes a methodology for the fabrication and characterization of a free standing catalyst film prepared combining different catalytic materials such as nickel telluride (Ni₃Te₂), platinum/carbon (Pt/C) with carboxylated polyacrylonitrile styrene butadiene (cABS) copolymer dispersion, activated carbon and

other supportive ingredients. The aim of this work is to produce a low cost, flexible, standalone catalyst film with improved electrical conductivity, mechanical properties and durability for future electrocatalytic applications such as photo/electro catalytic water oxidation, membrane for reduction of gaseous carbon dioxide to useful chemicals, electrocatalytic water purification, etc. The catalyst film can be prepared from scalable common techniques such as dip coating, spray painting, roller painting and roll to roll coating. The prepared films were characterized for electrical conductivity, catalytic activity, scanning electron microscopy (SEM), thermal behavior through thermogravimetric analysis (TGA) and stress-strain test. Electrical properties observed to be varied depending on the amount of conducting carbon in the catalyst film. The minimum sheet resistance achieved was $180 \Omega/\text{sq}$ and the highest conductivity was 820 Sm^{-1} observed for the catalyst film having the composition of $\sim 70\%$ carbon in the film. Catalyst film was evaluated both under oxygen evolution reaction (OER) and hydrogen evolution reaction (HER) conditions and it was stable for more than three hours under OER conditions.

1. INTRODUCTION

Recent progress achieved in the field of nanoscience and technology has been made possible to make materials with controllable size, shape and composition. This is particularly interested in the field of catalysis research since it provide ample opportunities to study the influence of morphology and composition of catalyst particles towards interested reactions. Especially catalytic materials in the form of nanoparticles

exhibit surprisingly enhanced catalytic activity mainly due to the increase in surface reactivity¹⁻⁶. As a result, well dispersed catalytic materials in the reaction medium is preferred to carry out catalytically driven reactions since maximum contact between catalytic particles and the reactants can be achieved in this process. However, there is an immense difficulty of separating the catalyst from its products or unreacted reactants at the end of the catalytic cycle⁷⁻⁹. These types of systems, therefore, create problems of contamination of the product with catalytic materials and also greatly affects the recycling ability of the catalysts. In industry, heterogeneous catalysis is preferred over homogenous catalysis due to the same reasons.¹⁰ Recovery of the catalyst at the end of the catalytic cycle is a much greener approach in terms of cost, environmental concerns and the product quality. Use of nanofiltration¹¹, scavenging columns¹², complexing agents in solution¹³, use of liquid biphasic solutions¹⁴ have been demonstrated as some of the potential solutions. However, these problems can be addressed by anchoring catalytic materials to a solid support so that the process can be easier to handle, catalyst can be separated and recycled without additional complicated steps. One of the disadvantage in this method is that efficiency of the catalyst is compromised to some extent since the catalytic reaction takes place close to the interface region of the material and hence, porous supports are used to expose a maximum surface area of the material to the catalytic medium. Various types of supporting media such as porous organosilica¹⁵⁻¹⁷, stabilized magnesia and other oxides¹⁸⁻²⁰ and zeolites²¹⁻²³ has been investigated for this purpose. Additionally, the conductivity of the catalyst support is an important parameter in electro catalysis. In these instances, conducting substrates such as carbon fibers²⁴, carbon nanotubes and graphene²⁵⁻²⁸ has been shown promise. Pristine carbon nanotubes,

however, chemically inactive and need to be functionalized to introduce oxygen and other functional groups to make them more hydrophilic and improve the catalyst-support interaction. As a result, conducting polymeric materials have seen as a potentially attractive system to support catalytic materials since suitable functionalities can be introduced to the polymer to improve polymer-catalyst interactions in addition to their capability of electron and proton conductivity. Viologen based polymers^{29,30}, poly vinyl acetic acid (PVAA)³¹, poly(4-vinylpyridine) (PVP)³², polyaniline (PA)^{33,34}, polypyrrole (PPy)^{35,36} and perfluoro sulfonic acid containing polymers such as Nafion³⁷ are the most common polymers used for this purpose. These material has the potential to be ideal candidates with further developments in the future. However, an optimal material that combines low cost, mechanical strength, stability in acid and base environments and a simple fabrication method capable of expanding into industrial scale manufacturing process still remains challenging.

Carboxylated polyacrylonitrile butadiene is a commercially available aqueous based polymer dispersion and certain grades of these polymer are available as copolymers of styrene at a very reasonable cost but has not been studied extensively for these types of applications. Presence of carboxylic groups in the polymer may be advantageous since they can exert a strong interaction with catalyst particles to make them attach well with the polymer promoting the long term stability of the catalyst films. On the other hand, aqueous based polymeric systems are preferred in every possible instances because there is a greater flexibility of material processing and dispersion preparation and those processes are less complicated, scalable and much greener compared to organic solvent based polymer systems and thermoplastic resin based

systems. Presence of carboxylic groups make the polymer hydrophilic and similarly make it compatible with other polar additives in a composite. This study explores the capability of carboxylated polyacrylonitrile butadiene styrene (cABS) polymer dispersion to be used in a catalyst ink and to fabricate a free standing catalyst film to be employed in catalytic and electrocatalytic applications in aqueous medium. With the recent progress of research in the area of water oxidation to generate oxygen and hydrogen fuels, a flexible, conducting and free standing catalyst film with the capacity to fabricate in larger scale with simple techniques such as using a roller paint brush, spin coating, screen printing, dip coating or printing at a minimum cost is highly desirable. The large area fabrication of these free standing catalyst films were achieved with cABS dispersion and electrically conducting carbon to deliver substrate independent and low cost composite films suitable for electrodes operating under dry or wet conditions. This wet-based novel fabrication process is simple, scalable and contains inexpensive common materials.

2. EXPERIMENTAL

2.1. MATERIALS

Chemicals used in the current study i.e. Carboxylated polyacrylonitrile butadiene styrene polymer (Nychem® 1578x1) from Emerald Specialty Polymers, LLC (OH, USA), activated conducting carbon from Aldrich Chemical Company, Inc. (WI, USA), Sodium carboxymethyl cellulose (Mw~700,000) from Sigma-Aldrich Co. (MO, USA) and Triton® X-100 from Acros organics (NJ, USA) were used without further purification steps.

2.2. FABRICATION OF CATALYST FILM

2.2.1. Preparation of Conducting Carbon Dispersion. First, Triton® X-100 was diluted with deionized water to make a 5% (v/v) solution. Then, 1 mL of this solution was mixed into a 20 mL of deionized water while stirring with a magnetic stirrer. Activated carbon (3 g) was slowly added in small quantities into this solution and stirring was continued for further 30 minutes. A solution of Sodium carboxymethyl cellulose (10 mg/mL) was prepared by completely dissolving sodium carboxymethyl cellulose powder in deionized water at 90°C and 6 mL of this solution was added to the carbon mixture and stirring was continued for further 30 minutes.

2.2.2. Preparation of the Catalyst Dispersion. Hydrothermally synthesized catalytic materials in our lab including selenides, Ni_3Se_2 , NiSe , FeNi_2Se_4 , Co_7Se_8 , Cu_2Se , and telluride Ni_3Te_2 , etc. were dispersed in deionized water typically in 10mg/mL concentration. Finely divided catalyst powder was directly mixed into deionized water and sonicated in a Fisher Scientific FS20 sonicator to make a uniform dispersion. Then the mixture was stirred with a magnetic stir bar for 15 minutes to ensure complete homogenization of the catalyst and as-prepared dispersion was stored under ambient condition in air-tight vials. The dispersion was stirred again for 15 minutes prior to use to ensure homogeneous mixing.

2.2.3. Preparation of Catalyst Ink-Base. Figure 1 illustrates a typical process for fabricating the free standing catalyst film base.

cABS polymer (20 mL) was mixed with 0.5mL of 5% Triton® X-100 solution under stirring and stored in a closed vial at room temperature at least 24 hours before

using it to prevent formation of lumps and aggregations during further processing of the dispersion and labeled the mixture as stabilized polymer solution.

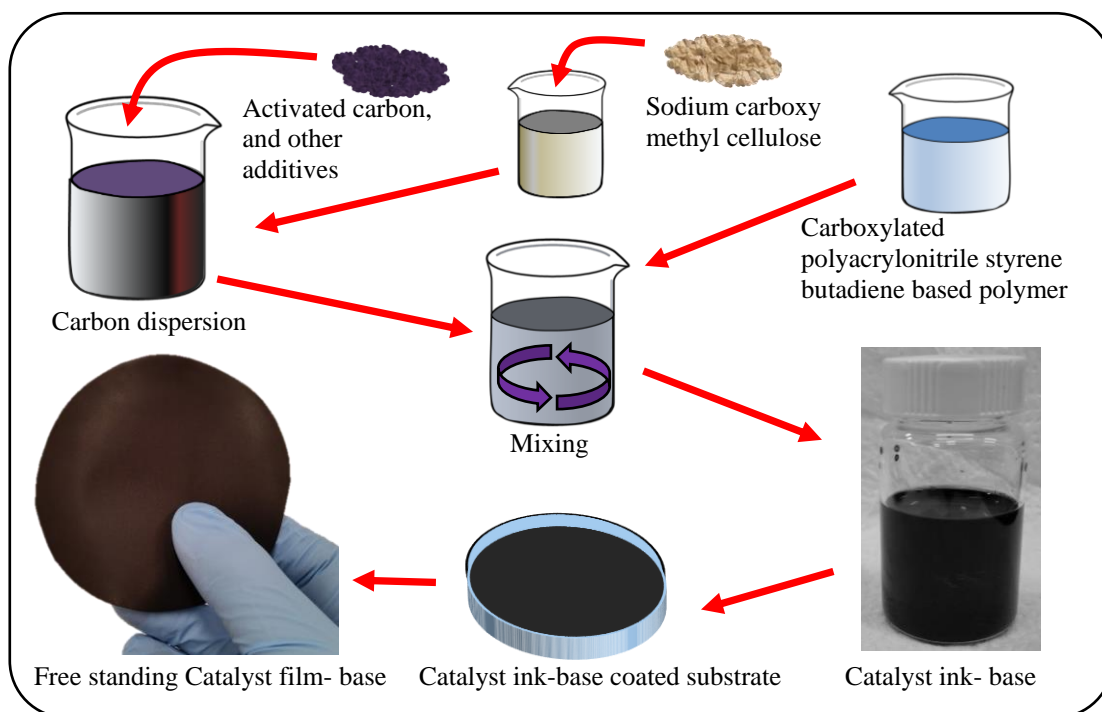


Figure 1. Schematic representation of preparing the free standing catalyst film-base

Catalyst ink base was typically prepared by mixing six parts of conducting carbon dispersion with one part (v/v) of the stabilized polymer solution at room temperature while stirring with a magnetic stirrer. This mixing ratio can be changed depending on the desired strength and conductivity of the finished layer. As an example, if high strength is preferred, the fraction of polymer solution can be increased.

Table 1 shows some typical example mixing ratios and the properties of resulting films. As prepared catalyst ink base could be applied onto a desired substrate such as

glass, metal, wood, paper, cloth, plastic, polymer films etc., by using a preferred application method such as with a paint brush, spin coating, spray painting, dip coating, drop casting, screen printing, roll-to-roll coating etc. and dried as described below to obtain a free standing catalyst film-base.

2.2.4. Preparation of Catalyst Ink. For the preparation of the catalyst ink, ten parts of the catalyst dispersion was mixed into four parts (v/v) of the conducting carbon dispersion while stirring with a magnetic stirrer. A diluted polymer solution was separately made by mixing 0.5mL of the stabilized polymer solution with 9.5 mL of deionized water.

Then one part (v/v) of this diluted polymer solution was mixed into the carbon/catalyst dispersion already prepared and stirring was continued for further 15 minutes at room temperature. This mixing ratio can be changed depending on the desired catalytic activity and conductivity of the catalyst ink. As an example, if more catalytic activity is preferred, the fraction of the catalyst dispersion in the ink can be increased. This catalyst ink also can be applied onto a given substrate in a similar manner described in catalyst ink-base.

2.2.5. Preparation of Substrate Supported Catalyst Films. In a typical sample preparation, a thin layer of catalyst ink-base was applied to a given substrate such as glass, fabric, etc. and completely dried in an oven at 70 °C.

After the sample was cooled to room temperature, catalyst ink was directly coated on the dried catalyst ink-base and placed in an oven at 70 °C to achieve complete drying. Drying time typically depends on the thickness of the catalyst film and the coated area.

After the catalyst film is completely dried, it was allowed to cool to room temperature. Another layer of same catalyst ink can be coated again if multiple coatings are desired.

2.2.6. Preparation of Free Standing Catalyst Film. First, a layer of catalyst ink-base was applied onto a smooth substrate such as glass Petridis and completely dried in an oven at 70 °C. After that it was allowed to cool to room temperature naturally, then a layer of catalyst ink was applied on top of the dry catalyst ink-base layer and dried and cooled similarly. The composite film can simply be peeled off from the substrate as a free standing catalyst film after dipping the sample in a hot water bath at ~90°C for about 5 minutes. Figure 2 shows a typical free standing catalyst film preparation process and as-prepared films.

2.2.7. Preparation of Free Standing Films with Electrodeposited Catalyst Layers. Although, the catalyst materials of interest were used as the powdered form to prepare free standing catalyst films, due to the conductivity of the catalyst ink-base layer, free standing catalyst films can also be prepared by electrodeposition of the catalyst of interest directly on the catalyst ink-base films.

First, a layer of catalyst ink base was applied onto a smooth substrate such as glass and completely dried in an oven at 70 °C. Then, these films were peeled off from the substrate after dipping the sample in a hot water bath maintained at ~90 °C. The films were dried again in the oven to get rid of water and insulated the films with clear tape leaving the area only for electrical contact with external circuit and the area for electrodeposition to take place.

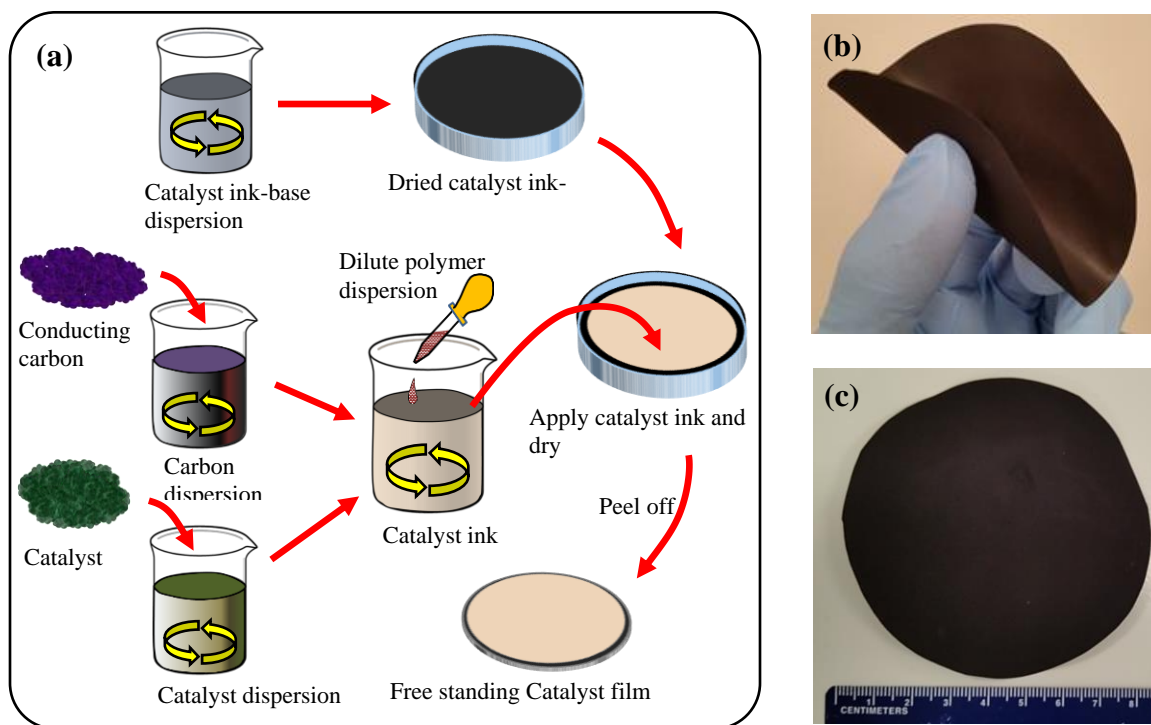


Figure 2. Free standing catalyst film. (a) Schematic illustration of preparing the catalyst ink and free standing catalyst film. The photographs shows the (b) flexibility and (c) a large composite film fabricated from this process

Then, electrodeposition of the catalysts were carried out on these films in a similar fashion to a normal conducting substrate, such as gold coated glass, using reported procedures^{38, 39}.

3. CHARACTERIZATION OF FREE STANDING CATALYST FILM

Helios Nanolab- 600 equipped with an Oxford INCA detector was used for Scanning electron microscopy (SEM) imaging and Energy Dispersive Spectrometry (EDS) for elemental analysis respectively. Powder XRD (pxrd) analysis was performed

on free standing films using PANalytical's X'Pert PRO Materials Research Diffractometer (Cu K α 1.5418 Å). UV-Vis absorption spectra were recorded using Varian Cary® 50 UV-Vis Spectrophotometer. Electrochemical measurements were carried out using an IviumStat potentiostat using three electrode system. Ag|AgCl, carbon cloth and the catalyst film were used as reference, counter and working electrodes, respectively. All potentials observed vs Ag|AgCl were converted to the reversible hydrogen electrode (RHE) by using the following equation.

$$E_{\text{RHE}} = E_{\text{Ag|AgCl}} + 0.059 \text{ pH} + E^0_{\text{Ag|AgCl}} \quad (1)$$

where, E_{RHE} is the calculated potential vs RHE, $E_{\text{Ag|AgCl}}$ is the experimentally measured potential vs Ag|AgCl reference electrode, and $E^0_{\text{Ag|AgCl}}$ is the standard thermodynamic potential of Ag|AgCl at 25 °C (0.197 V). Electrical conductivity, σ , of the samples were measured using the relationship, $\sigma = (LI/AV)$ where, L is the thickness of the sample, I is the measured current, A is the area of the sample and V is the voltage applied. A C4S 44/5S four-probe measurement system from Cascade Microtech, Inc. used for the measurements at room temperature. Current was applied using a Keithley 220 programmable current source and the voltage was measured using a HP 3457A multimeter.

3.1. EVALUATION OF CATALYTIC ACTIVITY

Performance of the free standing catalyst film towards the oxygen evolution reaction (OER) and hydrogen evolution reaction (HER) were monitored by linear sweep voltammetry (LSV) in 1M KOH solution. A Tafel plot was created to understand the

kinetic behavior of the catalyst when fabricated as a free standing films. Tafel slope, $(2.3RT/\alpha nF)$, can be obtained from the plot between η and $\log j$ of the Tafel equation;

$$\eta = a + (2.3RT/\alpha nF)\log j \quad (3)$$

where, η is the over potential, R is the universal gas constant, T is the room temperature, α is the transfer coefficient, n is the number of electrons involved in the reaction, F is faraday constant and j is the current density.

On demand hydrogen production for electrocatalytic reactions by free standing catalyst film was demonstrated by catalytic reduction of 20mL of 0.01M p-nitrophenol (PNP) to p-aminophenol (PAP) at room temperature (25 °C) in the presence of Pt/C (10%) catalysts loaded on the polymer composite. In a typical PNP reduction reactions NaBH_4 use as the source of hydrogen however, in this study HER was utilized to generate the required hydrogen for the reaction by applying a -0.6V to the working electrode under chronoamperometric conditions and Pt already available on the free standing film employed as a catalyst for the reaction. Aliquots of 50uL from the reaction mixture was taken at different time intervals and diluted 20 times with deionized water before taking the absorbance measurements.

Two control experiments were carried out using identical solutions by bubbling hydrogen gas from a different source in the absence of a catalyst film and in another experiment, dipping a catalyst film in an identical solution in the absence of hydrogen. Electrochemical accelerated durability test (ADTs) was employed to evaluate the long-term performance of the catalysts films. ADT has reported in literature as an inexpensive and convenient technique for evaluating catalysts for stability and performance⁴⁰. Using

the similar experimental set up as in a LSV test, ADT was conducted in the current study with cyclic voltammetry (CV) curves between 0.2 and 1.5 V (vs RHE).

4. RESULTS AND DISCUSSION

4.1. ELECTRICAL CONDUCTIVITY

Several catalyst ink base compositions were prepared by mixing different ratios of conducting carbon dispersion and the stabilized polymer solution according to the Table 1 to evaluate electrical conductivity, physical performance and morphology of the finished catalyst ink base films.

Since cABS is intrinsically non-conducting, it is important to bring the conductivity to the free standing film by mixing conducting materials such as conducting carbon to perform electrocatalytic activity. Conducting carbon is a well-known, inexpensive material to mix with insulating polymers to produce conducting composites⁴¹. Electrical conductivity of insulating polymers such as cABS is not sensitive to small changes of conducting carbon at low loading in the composite films.

However, at higher loadings of conducting particles, it has reported that conducting particles maintain contact with each other creating an uninterrupted conducting pathway. When the conducting particle loading is at this critical concentration, known as percolation threshold, a rapid increase of the conductivity of the film has been observed⁴².

Table 1. Electrical and mechanical properties of catalyst ink base films

Sample name	Carbon: polymer (dispersions, v/v)	Carbon % in the film	Electrical conductivity (Sm^{-1})	Sheet resistance (Ω/sq)
cABS-0.25	3:0.25	69.8	820.0	180
cABS-0.4	3:0.4	60.4	769.2	183
cABS-0.5	3:0.5	55.4	714.3	237
cABS-1	3:1	39.1	32.1	353
cABS-2	3:2	24.7	30.8	1183
cABS-3	3:3	18.0	20.0	6279
cABS-4	3:4	14.2	18.8	222E+3
cABS-5	3:5	11.7	1.1	Over limit
cABS- 0	0:1	0.0	0.0	Over limit

Similar observations has made during this study. Furthermore, some studies suggest that conductivity can also be facilitated by tunneling in the absence of continuous pathways if the proximity of conducting particles are small^{43,44}. Figure 3 shows the dependence of electrical conductivity as a function of conducting carbon content of the polymer films.

Apart from giving rise to conductivity to the composite polymer film, the presence of carbon alters the mechanical properties of the polymer. It should be noted that, in this study, when the carbon content of the films were beyond 60%, the films lost most of its elasticity and therefore, not suitable as free standing films without a support of a substrate such as a solid support or another low carbon loaded composite film as a support.

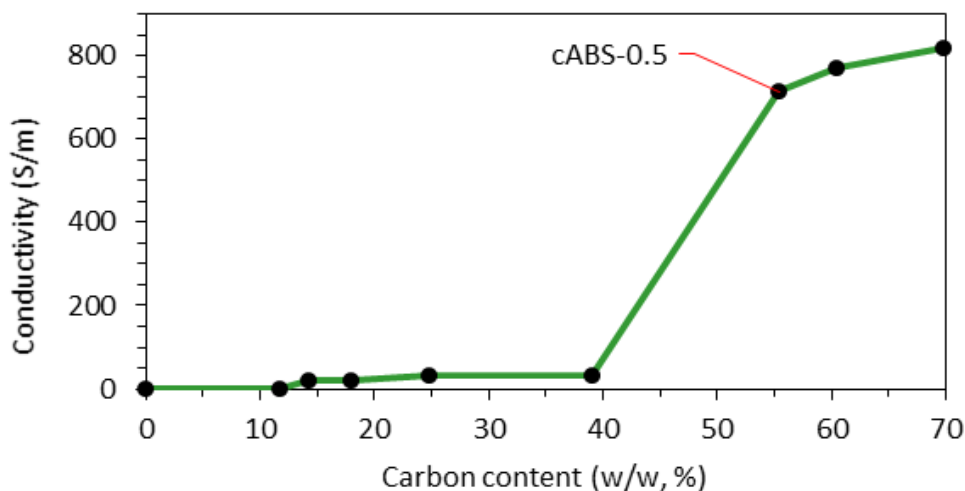


Figure 3. Effect of carbon content to the electrical conductivity of composite films. At low carbon content the conductivity of the films are much lower compared to the conductivity of the composite films beyond their percolation threshold.

This is because at this level of carbon percentages the available content of polymer is not sufficient to strongly bind the carbon particles together. However, electrical conductivity increases with the increase of the carbon content of the films. Considering both the mechanical strength and desired electrical conductivity cABS-0.5 was used as the free standing catalyst base film in all the electrochemical studies.

4.2. SCANNING ELECTRON MICROSCOPY (SEM)

Samples prepared in Table 1 was observed under the SEM as shown in Figure 4. It can be seen from the images that when the polymer content was gradually decreased the conducting carbon particles become in contact with each other creating a continuous path forming an excellent conductivity network. At high polymer contents the carbon particles become scattered in the polymer matrix and lose their interconnection. This evidence explains the observed high electrical conductivity of the composite films at

higher conducting carbon loading and diminished conductivity at low carbon loadings. Moreover, the observations are also in good agreement with reported explanations of enhancing the conductivity of insulating polymers in the literature⁴².

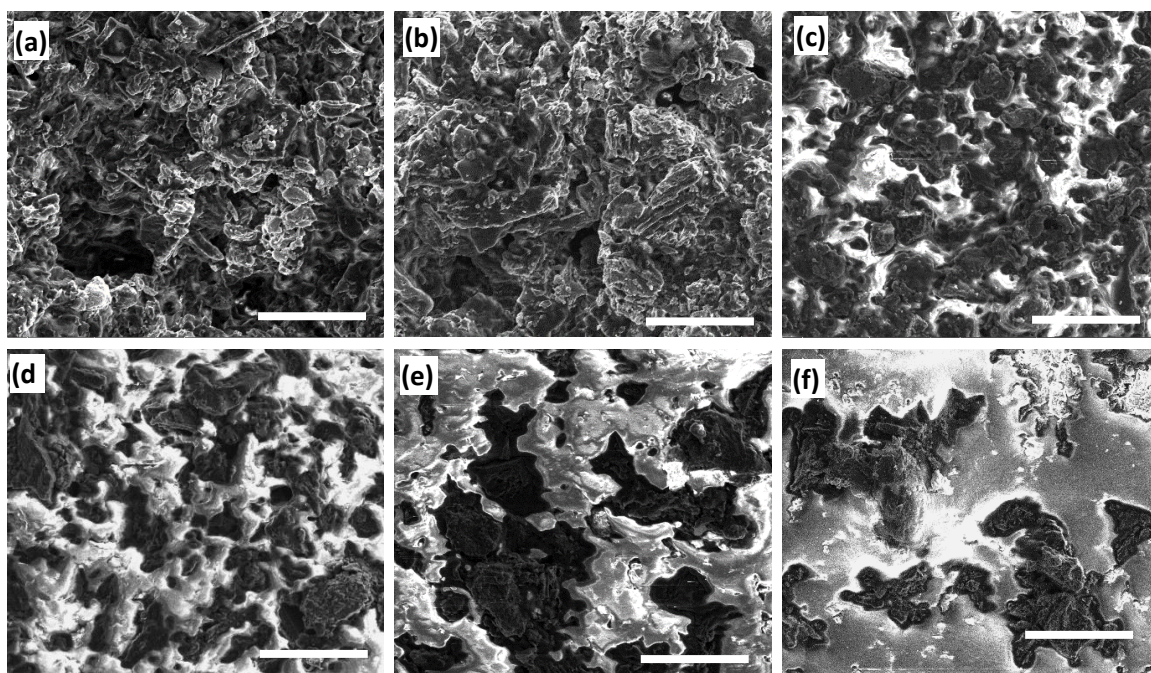


Figure 4. SEM images of free standing catalyst base films prepared in Table 1. (a) cABS-0.25, (b) cABS-0.5, (c) cABS-1, (d) cABS-2, (e) cABS-3 and (f) cABS-4. The image are arranged according to the increasing order of polymer (bright areas in images) content in the composite films. The length of the scale bar in 30 μm .

In addition, it was observed from the SEM images that when the carbon content was increased the roughness of the films were also increased introducing a porosity to the composite films. This intern, increases the effective surface area of these films and provide strong binding sites to the catalyst layer

Catalyst films loaded with different types of catalyst materials such as Ni_3Te_2 , Pt/C were prepared according to the illustration in Figure 2 and observed under SEM to understand the surface morphology of the catalyst films. It should be mentioned that those catalytic materials were made in our lab, has been fully characterized and previously reported in literature³⁸. EDAX mapping of catalyst films were done to identify the distribution of catalyst particles in the free standing catalyst film. A sample prepared with Ni_2Te_3 in Figure 5 shows the surface morphology of the free standing catalyst film and the distribution of catalyst particles in the film.

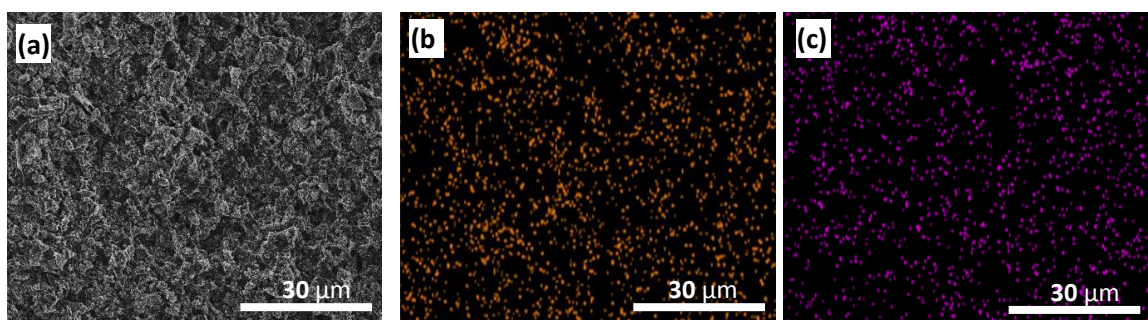


Figure 5. Free standing catalyst film prepared with Ni_3Te_2 catalyst. (a) SEM image (b) EDAX elemental map of the catalyst film showing the presence of (b) nickel and (c) tellurium. It should be noted that catalyst particles has dispersed well within the matrix without a significant segregation.

The catalyst films had a very rough morphology and a significant amount of porosity, which is an advantage in catalysis because it increases the contact area with the electrolyte and the catalyst film during electrochemical applications. SEM images and EDAX mappings of other catalyst films were shown in supplementary Figure S1.

4.3. EVALUATION OF CATALYTIC PROPERTIES

Free standing catalyst films prepared with Ni_3Te_2 catalysts were evaluated towards OER activity by recording polarization curves with linear sweep voltammetry (LSV) at a scan rate of 5 mV/S in nitrogen saturated 1M KOH solution with a catalyst loading maintained at 6.25 mg/cm². A controlled experiment of the free standing film was carried out without loading any catalyst for comparison. It can be seen from Figure 6(a) that LSV curve of the free standing catalyst film (FSF) with Ni_3Te_2 catalysts displays lower onset potential for starting the OER activity. Benchmark experiments with pristine catalyst materials drop casted on gold coated glass (Au glass), carbon fiber paper (CFP), carbon cloth (CC), nickel foam (NF), and glassy carbon (GC) were also carried out for comparing the effect of the substrate. Onset potentials of the catalysts showed similar trend however, the tafel slope of the polarization curve of the free standing film are much smaller indicating slow reaction kinetics of the catalysts on free standing catalyst films compared to other substrates. This can be attributed to the high sheet resistance, as indicated in table 1, of the free standing films compared to the other substrates which are typically in the range of ~10-20 Ω /sq.

However, there is lot of room for improving the charge transfer of the free standing film by incorporating materials such as other types of highly conducting carbon, carbon fibers, carbon nanotubes, graphene, etc. to the composite thereby to expedite the catalytic activity. Figure 6(b) shows a typical experiment carried out for evaluation of the stability of a catalyst.

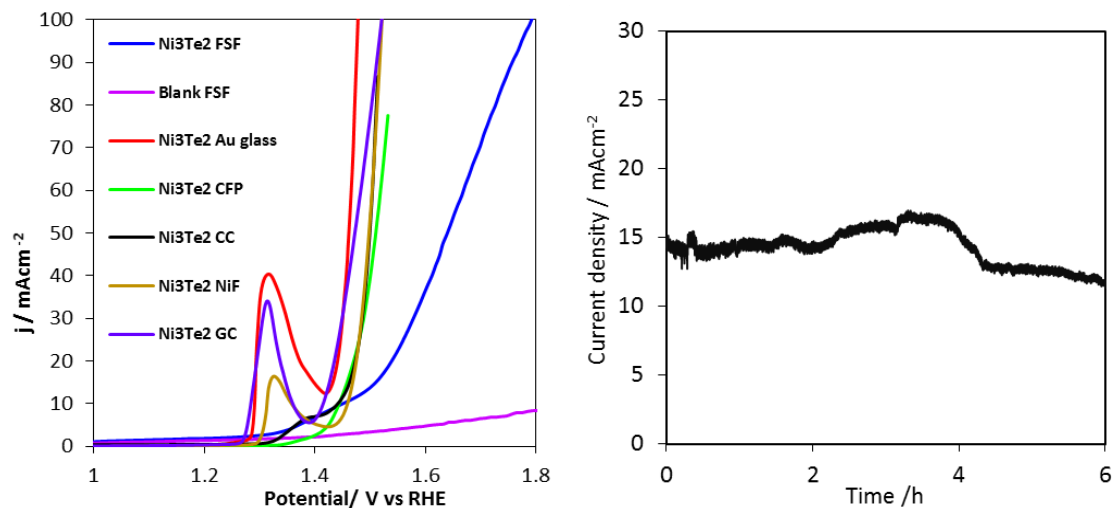


Figure 6. Evaluation of free standing catalyst film. (a) loaded with Ni₃Te₂ catalysts for OER activity using LSV curves (b) monitoring the long term stable current density of the catalyst film

A constant potential was applied to the free standing film to obtain a current density of ~ 15 mA/cm² and the current was monitored over extended period of time. The absence of a significant current degradation is an indication of the capability of the free standing film to carry out the catalytic reaction for an extended period of time.

Hydrogen evolution reaction (HER) capability of the free standing films were investigated to see the possibility of using these catalyst films to produce gaseous hydrogen on demand. Catalytic hydrogenation of p-nitrophenol (PNP) to p-aminophenol (PAP) was selected as a model reaction and Pt/C loaded (10%) free standing catalyst films under applied potential of -0.6V (HER conditions) was maintained to generate hydrogen as the source of hydrogen gas for the reaction. The chemical reduction of PNP can be conveniently monitored by UV-Vis spectroscopy.⁴⁵ Upon dissolution of PNP in the 1M KOH solution, a strong absorption peak at 400nm can be observed in the UV-Vis spectrum due to the formation of p-nitrophenolate ion. Previous research works report

that upon catalytic hydrogenation of PNP, intensity of this peak decreases rapidly and a new peak starts to appear at 300nm region corresponding to formation of PAP.⁵¹ Similar observations was made during this study as the HER starts. The light yellow color of the starting solution was diminished gradually and finally, the solution turned into colorless indicating the completion of the reduction reaction. The progress of the reaction was followed by monitoring the UV-Vis spectrum as shown in Figure 7(a). The rate of the reaction was calculated as shown in Figure 7(b) and the results agrees with the first order kinetics previously reported in literature.⁴⁵

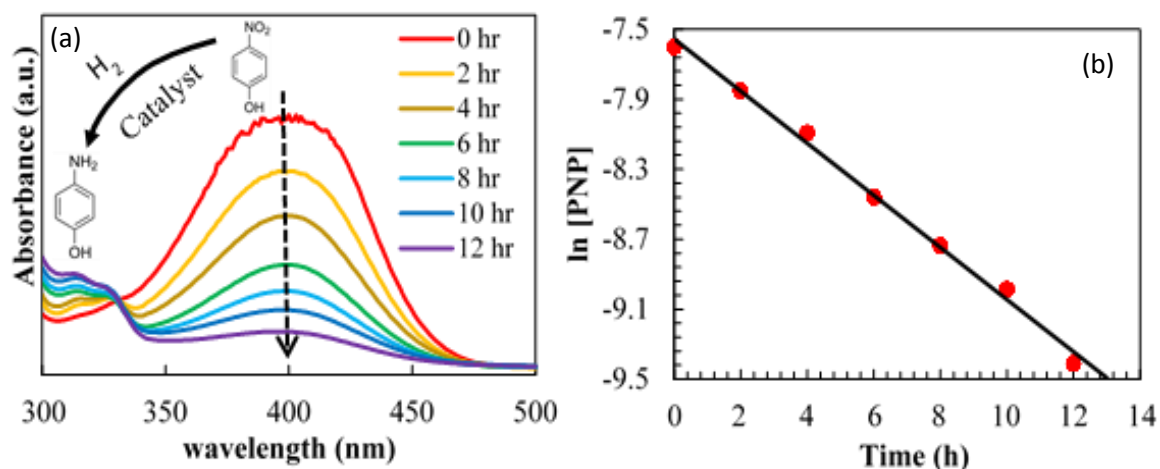


Figure 7. Evaluation of HER and catalytic activity of free standing catalyst film. (a) electrocatalytic conversion of PNP to PAP showing the production of hydrogen on demand (b) determination of the rate constant of the reaction

It also was confirmed using a separate source of hydrogen, when either hydrogen gas or the catalyst were absent in the reaction medium the conversion reaction does not take place. Hence it is evident that the free standing catalyst film is capable of producing hydrogen for a longer period of time under electrochemical reaction conditions.

5. CONCLUSIONS

This study shows a proof of a concept that these free standing catalyst films fabricated from cASB and catalytic materials have a significant potential to be used in electrocatalytic reactions such as water oxidation and on demand hydrogen production. These free standing catalytic films deserve a detailed investigation to improve them as flexible model electrodes for electrocatalytic applications by fine tuning the electrical conductivity and surface resistance especially taking into account the relatively low cost of the polymer and the other materials used and the simplicity of the fabrication process. Combination of this method with improved catalytic material synthesis techniques could create revolutionary changes in high performance, long lasting electrocatalytic applications. However, more detailed studies are still required to monitor the behavior of these films under ‘real’ application conditions. Outcome of this research provides very important insights into the fabrication process and properties so that these free standing films can be optimized use in promising electrocatalytic applications.

ACKNOWLEDGEMENTS

The authors would like to acknowledge University of Missouri Research Board for sponsoring this research and MRC for equipment usage.

REFERENCES

1. Haruta, M. and Daté, M., 2001. Advances in the catalysis of Au nanoparticles. *Applied Catalysis A: General*, 222(1-2), pp.427-437.
2. Szekely, G. A., & Faeth, G. M. (1982). Combustion properties of carbon slurry drops. *Aiaa Journal*, 20(3), 422-429.
3. Bachelet, G. B., Bassani, F., Bourg, M., & Julg, A. (1983). Surface and size effects on the electronic states of small metallic clusters: a model calculation. *Journal of Physics C: Solid State Physics*, 16(21), 4305.
4. Hwang, C. B., Fu, Y. S., Lu, Y. L., Jang, S. W., Chou, P. T., Wang, C. C., & Yu, S. J. (2000). Synthesis, characterization, and highly efficient catalytic reactivity of suspended palladium nanoparticles. *Journal of Catalysis*, 195(2), 336-341.
5. Chen, C. W., & Akashi, M. (1997). Synthesis, characterization, and catalytic properties of colloidal platinum nanoparticles protected by poly (N-isopropylacrylamide). *Langmuir*, 13(24), 6465-6472.
6. Sanchez, A., Abbet, U & Landman, U. (1999). When gold is not noble: nanoscale gold catalysts. *The Journal of Physical Chemistry A*, 103(48), 9573-9578.
7. Cornils, B. and Herrmann, W.A. eds., 2004. *Aqueous-phase organometallic catalysis: concepts and applications*. John Wiley & Sons., 2nd edition, pp3
8. Cornils, B. (1998). Industrial aqueous biphasic catalysis: status and directions. *Organic Process Research & Development*, 2(2), 121-127.
9. Helwani, Z., Othman, M. R., Aziz, N., Kim, J., & Fernando, W. J. N. (2009). Solid heterogeneous catalysts for transesterification of triglycerides with methanol: a review. *Applied Catalysis A: General*, 363(1-2), 1-10.
10. Mehnert, C. P., Mozeleski, E. J., & Cook, R. A. (2002). Supported ionic liquid catalysis investigated for hydrogenation reactions. *Chemical Communications*, (24), 3010-3011.
11. Ormerod, D., Bongers, B., Porto-Carrero, W., Giegas, S., Vijt, G., Lefevre, N. & Buekenhoudt, A. (2013). Separation of metathesis catalysts and reaction products in flow reactors using organic solvent nanofiltration. *RSC Advances*, 3(44), 21501-21510.

12. Wiles, C., & Watts, P. (2011). Recent advances in micro reaction technology. *Chemical communications*, 47(23), 6512-6535.
13. Gürsel, I. V., Noël, T., Wang, Q., & Hessel, V. (2015). Separation/recycling methods for homogeneous transition metal catalysts in continuous flow. *Green Chemistry*, 17(4), 2012-2026.
14. Hall, J. F., Han, X., Poliakoff, M., Bourne, R. A., & George, M. W. (2012). Maximising the efficiency of continuous photo-oxidation with singlet oxygen in supercritical CO₂. *Chemical Communications*, 48(25), 3073-3075.
15. Carrado, K. A. (2000). Synthetic organo- and polymer-clays: preparation, characterization, and materials applications. *Applied Clay Science*, 17(1-2), 1-23.
16. Patel, A. C., Li, S., Wang, C., Zhang, W., & Wei, Y. (2007). Electrospinning of porous silica nanofibers containing silver nanoparticles for catalytic applications. *Chemistry of materials*, 19(6), 1231-1238.
17. Sharma, S. K., Patel, H. A., & Jasra, R. V. (2008). Synthesis of jasminaldehyde using magnesium organo silicate as a solid base catalyst. *Journal of Molecular Catalysis A: Chemical*, 280(1-2), 61-67.
18. Schaper, H., Berg-Slot, J. J., & Stork, W. H. J. (1989). Stabilized magnesia: a novel catalyst (support) material. *Applied Catalysis*, 54(1), 79-90.
19. Freund, H. J., & Pacchioni, G. (2008). Oxide ultra-thin films on metals: new materials for the design of supported metal catalysts. *Chemical society reviews*, 37(10), 2224-2242.
20. Nong, H. N., Oh, H. S., Reier, T., Willinger, E., Willinger, M. G., Petkov, V. & Strasser, P. (2015). Oxide-Supported IrNiO_x Core-Shell Particles as Efficient, Cost-Effective, and Stable Catalysts for Electrochemical Water Splitting. *Angewandte Chemie International Edition*, 54(10), 2975-2979.
21. Hernadi, K., Fonseca, A., Nagy, J. B., Bemaerts, D., Fudala, A., & Lucas, A. A. (1996). Catalytic synthesis of carbon nanotubes using zeolite support. *Zeolites*, 5(17), 416-423.
22. Kang, J., Cheng, K., Zhang, L., Zhang, Q., Ding, J., Hua, W., & Wang, Y. (2011). Mesoporous zeolite-supported ruthenium nanoparticles as highly selective Fischer-Tropsch catalysts for the production of C₅-C₁₁ isoparaffins. *Angewandte Chemie International Edition*, 50(22), 5200-5203.

23. Corma, A., Nemeth, L. T., Renz, M., & Valencia, S. (2001). Sn-zeolite beta as a heterogeneous chemoselective catalyst for Baeyer–Villiger oxidations. *Nature*, 412(6845), 423.
24. Rodriguez, N. M., Kim, M. S., & Baker, R. T. K. (1994). Carbon nanofibers: a unique catalyst support medium. *The journal of physical chemistry*, 98(50), 13108-13111.
25. Li, W., Liang, C., Zhou, W., Qiu, J., Zhou, Z., Sun, G., & Xin, Q. (2003). Preparation and characterization of multiwalled carbon nanotube-supported platinum for cathode catalysts of direct methanol fuel cells. *The Journal of Physical Chemistry B*, 107(26), 6292-6299.
26. Lv, R., Cui, T., Jun, M. S., Zhang, Q., Cao, A., Su, D. S., ... & Kang, F. (2011). Open-Ended, N-Doped Carbon Nanotube–Graphene Hybrid Nanostructures as High-Performance Catalyst Support. *Advanced Functional Materials*, 21(5), 999-1006.
27. Gentil, S., Lalaoui, N., Dutta, A., Nedellec, Y., Cosnier, S., Shaw, W. J., & Le Goff, A. (2017). Carbon-Nanotube-Supported Bio-Inspired Nickel Catalyst and Its Integration in Hybrid Hydrogen/Air Fuel Cells. *Angewandte Chemie*, 129(7), 1871-1875.
28. Cao, J., Hu, Y., Chen, L., Xu, J., & Chen, Z. (2017). Nitrogen-doped carbon quantum dot/graphene hybrid nanocomposite as an efficient catalyst support for the oxygen reduction reaction. *International Journal of Hydrogen Energy*, 42(5), 2931-2942.
29. Dominey, R. N., Lewis, N. S., Bruce, J. A., Bookbinder, D. C., & Wrighton, M. S. (1982). Improvement of photoelectrochemical hydrogen generation by surface modification of p-type silicon semiconductor photocathodes. *Journal of the American Chemical Society*, 104(2), 467-482.
30. Bruce, J. A., Murahashi, T., & Wrighton, M. S. (1982). Synthesis and characterization of structured interfaces for hydrogen generation. Study of an N, N'-dialkyl-4, 4'-bipyridinium redox polymer/palladium catalyst system. *The Journal of Physical Chemistry*, 86(9), 1552-1563.
31. Kao, W. H., & Kuwana, T. (1984). Electrocatalysis by electrodeposited spherical platinum microparticles dispersed in a polymeric film electrode. *Journal of the American Chemical Society*, 106(3), 473-476.

32. Bartak, D. E., Kazee, B., Shimazu, K., & Kuwana, T. (1986). Electrodeposition and characterization of platinum microparticles in poly (4-vinylpyridine) film electrodes. *Analytical Chemistry*, 58(13), 2756-2761.
33. Kost, K. M., Bartak, D. E., Kazee, B., & Kuwana, T. (1988). Electrodeposition of platinum microparticles into polyaniline films with electrocatalytic applications. *Analytical Chemistry*, 60(21), 2379-2384.
34. García-Fernández, M. J., Pastor-Blas, M. M., Epron, F., & Sepúlveda-Escribano, A. (2018). Proposed mechanisms for the removal of nitrate from water by platinum catalysts supported on polyaniline and polypyrrole. *Applied Catalysis B: Environmental*, 225, 162-171.
35. Mazzotta, E., Caroli, A., Pennetta, A., De Benedetto, G. E., Primiceri, E., Monteduro, A. G., & Malitesta, C. (2018). Facile synthesis of 3D flower-like Pt nanostructures on polypyrrole nanowire matrix for enhanced methanol oxidation. *RSC Advances*, 8(19), 10367-10375.
36. Sapurina, I., Li, Y., Alekseeva, E., Bober, P., Trchova, M., Moravkova, Z., & Stejskal, J. (2017). Polypyrrole nanotubes: The tuning of morphology and conductivity. *Polymer*, 113, 247-258.
37. Peron, J., Shi, Z., & Holdcroft, S. (2011). Hydrocarbon proton conducting polymers for fuel cell catalyst layers. *Energy & Environmental Science*, 4(5), 1575-1591.
38. De Silva, U., Masud, J., Zhang, N., Hong, Y., Liyanage, W. P., Zaeem, M. A., & Nath, M. (2018). Nickel telluride as a bifunctional electrocatalyst for efficient water splitting in alkaline medium. *Journal of Materials Chemistry A*, 6, 7608-7622.
39. Swesi, A. T., Masud, J., & Nath, M. (2016). Nickel selenide as a high-efficiency catalyst for oxygen evolution reaction. *Energy & Environmental Science*, 9(5), 1771-1782.
40. Liu, C. W., Chen, H. S., Lai, C. M., Lin, J. N., Tsai, L. D., & Wang, K. W. (2014). Promotion of oxygen reduction reaction durability of carbon-supported PtAu catalysts by surface segregation and TiO₂ addition. *ACS applied materials & interfaces*, 6(3), 1589-1594.
41. Huang, J. C. (2002). Carbon black filled conducting polymers and polymer blends. *Advances in Polymer Technology*, 21(4), 299-313.

42. Ruschau, G. R., & Newnham, R. E. (1992). Critical volume fractions in conductive composites. *Journal of composite materials*, 26(18), 2727-2735.
43. Tang, H., Chen, X., Tang, A., & Luo, Y. (1996). Studies on the electrical conductivity of carbon black filled polymers. *Journal of Applied Polymer Science*, 59(3), 383-387.
44. Sherman, R. D., Middleman, L. M., & Jacobs, S. M. (1983). Electron transport processes in conductor-filled polymers. *Polymer Engineering & Science*, 23(1), 36-46.
45. Kuroda, K., Ishida, T., & Haruta, M. (2009). Reduction of 4-nitrophenol to 4-aminophenol over Au nanoparticles deposited on PMMA. *Journal of Molecular Catalysis A: Chemical*, 298(1-2), 7-11.

SECTION

2. CONCLUSION

This research work introduces a novel protocol that shows vast potential for growing vertically ordered semiconducting nanotube arrays of uniform dimensions over a large area. This in turn provides new directions and opportunities to explore innovative nanostructured architectures in solar energy harvesting and generation of solar fuels. The nanoelectrodes were defined on conducting substrates such as ITO coated glass slides through *e*-beam lithography and then semiconductor nanotubes arrays were electrodeposited from an electrochemical bath containing relevant precursors. Insulating matrix of the polymeric resist used (PMMA) confined electrodeposition to a columnar growth on the nanoelectrodes thereby producing nanotubes with very uniform diameter, length, composition and morphology. It was observed that the aspect ratio of these nanotubes was fully controllable by tuning the diameter of the nanoelectrode and thickness of the PMMA film. Electrodeposition took place only over the nanoelectrodes leaving the polymeric surface (PMMA) completely clean. PMMA could be removed by simple soaking of the nanotube device in acetone leaving the nanotubes on the substrate, indicating robustness of the nanostructure-substrate interface. It should be emphasized that the length of the nanotubes was dependent on the thickness of the resist with a thinner layer of the resist leading to more nanoshell-like geometry. The creation of nanotube arrays was unique and the most novel part of this research, and interestingly, preliminary photoelectrochemical measurements from the nanotubes device revealed that these nanotube arrays with less than 10 % coverage of the electrode surface were capable

of producing photocurrent densities in the mA/cm² range, which was even higher than that obtained with thin films of similar thickness. This is very important since photocurrent can be potentially amplified even further simply by manipulating physical parameters, packing density and pattern of the nanotubes and optimizing the optical properties. Interestingly, this protocol provides ample opportunities to make changes and identify the optimum geometry of the arrangement.

This methodology was used successfully to create p-n heterojunction assemblies where p-type CdTe nanotubes were either electrodeposited on n-type CdS layer or n-type CdS layer was deposited on p-type CdTe nanotubes. Additionally, the CdS-CdTe nanotube assembly also showed appreciable photocurrent. Most importantly, the tubular array architecture showed a better photoconversion efficiency compared to the planar device as well as the nanorod arrays. Similar methodology was used to create CISE tubular nanostructures with proper stoichiometry and crystallinity. The compositional purity of these ternary photovoltaic material obtained through this simple electrodeposition procedure was notable providing proof that indeed high-quality material deposition can be achieved. These nanotubes could be grown on different substrates including Mo-glass, FTO-glass as well as Cu-coated Si, underlying the versatility of the protocol.

Photoelectrochemical experiments carried out on CdS-CdTe and CdS-CISE devices to determine photoconversion efficiency shows that CISE cell fabricated with nanotube arrays could achieve a higher photo conversion efficiency (8.85%) compared to a thin film solar cell device (6.82%) fabricated by the same procedure. It was also observed that even though the V_{OC} was very close to each other for the two types of

photoabsorber geometries, when the morphology was changed to a tubular architecture, there was an enhancement of the J_{sc} and the FF. Similarly, for the CdS-CdTe device, it was observed that the tubular architectures showed highest photoconversion efficiency (9.6%), compared to that of the pillar-like structures (7.2%). It was also observed that the film-like device had a slightly higher V_{oc} than that of the nanostructured arrays. Several factors including varying degree of crystallinity in the CdS-CdTe layers as well as different carrier recombination rate and series resistance across the junctions in the film and nanostructure arrays, respectively, can cause such variance in V_{oc} .

Additionally, a method for making semiconducting nanoelectrode patterns over a much larger area was demonstrated taking the advantage of patterning capability of Nanosphere Photo Lithography (NPL) process. Since NPL can pattern large area in a single step, CdTe nanorod arrays were grown over cm^2 areas. This method is important for translating patterning process into a larger scale processing technique. This technique will also be very fruitful in substantially minimizing the use of chemical resources without compromising on the quality, since the arrays of nanowires potentially amplify optical absorption efficiency by many orders of magnitude. This is especially significant for CdTe based photoabsorbers, where, even though CdTe gives high efficiency, scaling of CdTe photovoltaic devices is limited by the availability of Te. The nanotube/nanowire arrays reduce the amount of CdTe needed to absorb all the sunlight.

For the purpose of fabricating a solar fuel generating architecture, this work also focused on developing Cu_2Se as a water oxidation catalyst and also fabrication of a free standing electrocatalytic membrane. The conclusions driven from each paper has been summarized in the following:

Copper selenide nanostructure based electrocatalysts was synthesized by different techniques such as electrodeposition, hydrothermal and CVD and evaluated catalytic activity for OER in alkaline media. Catalytic activity was observed by samples made by all the routes indicating the intrinsic property of the material. Electrodeposited Cu_2Se catalyst showed enhanced catalytic activity and a current density of 10 mA cm^{-2} was obtained at an overpotential as low as 270 mV . In addition a lower Tafel slope of 48.1 mV dec^{-1} was observed. Since Cu is one of the most earth-abundant material, this research provides contribution in identifying affordable catalytic materials that can be used for real-world applications in sustainable and renewable energy generation process.

A free standing catalyst membrane was fabricated to incorporate electrocatalytic materials to be used in renewable energy generation applications. The work shows proof of a concept that these free standing catalyst films made from readily available polymeric materials, conducting carbon and catalytic materials have a significant potential to be used in electrocatalytic applications. Initial results showed the capability of catalytic activity such as water oxidation and on demand hydrogen production. Incorporating this method with highly active catalytic materials can significantly advance the application of electrocatalysis since the electrode fabrication process strongly bind the catalysts to the film and hence catalyst can be protected for long term performance. However, more detailed studies are still required to improve conductivity, mechanical performance, etc. This research work reveals the detailed fabrication process and examples of catalytic performance hence these films can be further enhanced to be used in promising large scale electrocatalytic applications.

BIBLIOGRAPHY

1. Zhou, Y., Clarke, L., Eom, J., Kyle, P., Patel, P., Kim, S.H., Dirks, J., Jensen, E., Liu, Y., Rice, J. and Schmidt, L., 2014. Modeling the effect of climate change on US state-level buildings energy demands in an integrated assessment framework. *Applied Energy*, 113, pp.1077-1088.
2. Kumar, A., Baredar, P. and Qureshi, U., 2015. Historical and recent development of photovoltaic thermal (PVT) technologies. *Renewable and Sustainable Energy Reviews*, 42, pp.1428-1436.
3. Liu, D., Gangishetty, M.K. and Kelly, T.L., 2014. Effect of CH₃NH₃PbI₃ thickness on device efficiency in planar heterojunction perovskite solar cells. *Journal of Materials Chemistry A*, 2(46), pp.19873-19881.
4. Prince, M., 1955. Silicon solar energy converters. *Journal of Applied Physics*, 26(5), pp.534-540.
5. Grätzel, M., 2001. Photoelectrochemical cells. *nature*, 414(6861), p.338.
6. Cook, R.L., MacDuff, R.C. and Sammells, A.F., 1988. Photoelectrochemical carbon dioxide reduction to hydrocarbons at ambient temperature and pressure. *Journal of the Electrochemical Society*, 135(12), pp.3069-70.
7. Singh, G.K., 2013. Solar power generation by PV (photovoltaic) technology: A review. *Energy*, 53, pp.1-13.
8. Juarez-Perez, E.J., Wußler, M., Fabregat-Santiago, F., Lakus-Wollny, K., Mankel, E., Mayer, T., Jaegermann, W. and Mora-Sero, I., 2014. Role of the selective contacts in the performance of lead halide perovskite solar cells. *The journal of physical chemistry letters*, 5(4), pp.680-685.
9. https://ecee.colorado.edu/~bart/book/book/chapter4/ch4_2.htm, retrieved on 06-18-2017
10. Shockley, W. and Queisser, H.J., 1961. Detailed balance limit of efficiency of p-n junction solar cells. *Journal of applied physics*, 32(3), pp.510-519.
11. Green, M.A., 2009. The path to 25% silicon solar cell efficiency: history of silicon cell evolution. *Progress in Photovoltaics: Research and Applications*, 17(3), pp.183-189.

12. Green, M.A., Emery, K., Hishikawa, Y. and Warta, W., 2011. Solar cell efficiency tables (version 37). *Progress in photovoltaics: research and applications*, 19(1), pp.84-92.
13. Chen, W.M., Kim, H. and Yamaguchi, H., 2014. Renewable energy in eastern Asia: Renewable energy policy review and comparative SWOT analysis for promoting renewable energy in Japan, South Korea, and Taiwan. *Energy Policy*, 74, pp.319-329.
14. Beard, M.C., Luther, J.M. and Nozik, A.J., 2014. The promise and challenge of nanostructured solar cells. *Nature nanotechnology*, 9(12), p.951.
15. Alivisatos, A.P., 1996. Semiconductor clusters, nanocrystals, and quantum dots. *science*, 271(5251), pp.933-937.
16. Rahman, I.A. and Padavettan, V., 2012. Synthesis of silica nanoparticles by sol-gel: size-dependent properties, surface modification, and applications in silica-polymer nanocomposites—a review. *Journal of Nanomaterials*, 2012, p.8.
17. Roduner, E., 2006. Size matters: why nanomaterials are different. *Chemical Society Reviews*, 35(7), pp.583-592.
18. Wadia, C., Alivisatos, A.P. and Kammen, D.M., 2009. Materials availability expands the opportunity for large-scale photovoltaics deployment. *Environmental science & technology*, 43(6), pp.2072-2077.
19. Krogstrup, P., Jørgensen, H.I., Heiss, M., Demichel, O., Holm, J.V., Aagesen, M., Nygard, J. and i Morral, A.F., 2013. Single-nanowire solar cells beyond the Shockley–Queisser limit. *Nature Photonics*, 7(4), p.306.
20. Baker-Finch, S.C. and McIntosh, K.R., 2011. Reflection of normally incident light from silicon solar cells with pyramidal texture. *Progress in Photovoltaics: Research and Applications*, 19(4), pp.406-416.
21. Prevo, B.G., Hon, E.W. and Velev, O.D., 2007. Assembly and characterization of colloid-based antireflective coatings on multicrystalline silicon solar cells. *Journal of Materials Chemistry*, 17(8), pp.791-799.
22. Lalanne, P. and Morris, G.M., 1997. Antireflection behavior of silicon subwavelength periodic structures for visible light. *Nanotechnology*, 8(2), p.53.
23. Boden, S.A. and Bagnall, D.M., 2008. Tunable reflection minima of nanostructured antireflective surfaces. *Applied Physics Letters*, 93(13), p.133108.

24. Chao, Y.C., Chen, C.Y., Lin, C.A. and He, J.H., 2011. Light scattering by nanostructured anti-reflection coatings. *Energy & Environmental Science*, 4(9), pp.3436-3441.
25. Fazio, B., Artoni, P., Iatì, M.A., D'andrea, C., Faro, M.J.L., Del Sorbo, S., Pirotta, S., Gucciardi, P.G., Musumeci, P., Vasi, C.S. and Saija, R., 2016. Strongly enhanced light trapping in a two-dimensional silicon nanowire random fractal array. *Light: Science & Applications*, 5(4), p.e16062.
26. Garnett, E. and Yang, P., 2010. Light trapping in silicon nanowire solar cells. *Nano letters*, 10(3), pp.1082-1087.
27. Robel, I., Kuno, M. and Kamat, P.V., 2007. Size-dependent electron injection from excited CdSe quantum dots into TiO₂ nanoparticles. *Journal of the American Chemical Society*, 129(14), pp.4136-4137.
28. Kongkanand, A., Tvrđy, K., Takechi, K., Kuno, M. and Kamat, P.V., 2008. Quantum dot solar cells. Tuning photoresponse through size and shape control of CdSe–TiO₂ architecture. *Journal of the American Chemical Society*, 130(12), pp.4007-4015.
29. Pietryga, J.M., Schaller, R.D., Werder, D., Stewart, M.H., Klimov, V.I. and Hollingsworth, J.A., 2004. Pushing the band gap envelope: mid-infrared emitting colloidal PbSe quantum dots. *Journal of the American Chemical Society*, 126(38), pp.11752-11753.
30. Moreels, I., Lambert, K., Smeets, D., De Muynck, D., Nollet, T., Martins, J.C., Vanhaecke, F., Vantomme, A., Delerue, C., Allan, G. and Hens, Z., 2009. Size-dependent optical properties of colloidal PbS quantum dots. *ACS nano*, 3(10), pp.3023-3030.
31. Gao, J., Luther, J.M., Semonin, O.E., Ellingson, R.J., Nozik, A.J. and Beard, M.C., 2011. Quantum dot size dependent J–V characteristics in heterojunction ZnO/PbS quantum dot solar cells. *Nano letters*, 11(3), pp.1002-1008.
32. Zhang, J., Gao, J., Church, C.P., Miller, E.M., Luther, J.M., Klimov, V.I. and Beard, M.C., 2014. PbSe quantum dot solar cells with more than 6% efficiency fabricated in ambient atmosphere. *Nano letters*, 14(10), pp.6010-6015.
33. Chuang, C.H.M., Brown, P.R., Bulović, V. and Bawendi, M.G., 2014. Improved performance and stability in quantum dot solar cells through band alignment engineering. *Nature materials*, 13(8), p.796.
34. Ning, Z., Voznyy, O., Pan, J., Hoogland, S., Adinolfi, V., Xu, J., Li, M., Kirmani, A.R., Sun, J.P., Minor, J. and Kemp, K.W., 2014. Air-stable n-type colloidal quantum dot solids. *Nature materials*, 13(8), p.822.

35. Bang, J.H. and Kamat, P.V., 2009. Quantum dot sensitized solar cells. A tale of two semiconductor nanocrystals: CdSe and CdTe. *ACS nano*, 3(6), pp.1467-1476.
36. Zhao, K., Pan, Z., Mora-Seró, I., Cánovas, E., Wang, H., Song, Y., Gong, X., Wang, J., Bonn, M., Bisquert, J. and Zhong, X., 2015. Boosting power conversion efficiencies of quantum-dot-sensitized solar cells beyond 8% by recombination control. *Journal of the American Chemical Society*, 137(16), pp.5602-5609.
37. Panthani, M.G., Akhavan, V., Goodfellow, B., Schmidtke, J.P., Dunn, L., Dodabalapur, A., Barbara, P.F. and Korgel, B.A., 2008. Synthesis of CuInS₂, CuInSe₂, and Cu (In_xGa_{1-x})Se₂ (CIGS) nanocrystal “inks” for printable photovoltaics. *Journal of the American Chemical Society*, 130(49), pp.16770-16777.
38. Ball, J.M., Lee, M.M., Hey, A. and Snaith, H.J., 2013. Low-temperature processed meso-superstructured to thin-film perovskite solar cells. *Energy & Environmental Science*, 6(6), pp.1739-1743.
39. Robel, I., Subramanian, V., Kuno, M. and Kamat, P.V., 2006. Quantum dot solar cells. Harvesting light energy with CdSe nanocrystals molecularly linked to mesoscopic TiO₂ films. *Journal of the American Chemical Society*, 128(7), pp.2385-2393.
40. Garnett, E.C. and Yang, P., 2008. Silicon nanowire radial p–n junction solar cells. *Journal of the American Chemical Society*, 130(29), pp.9224-9225.
41. Christesen, J.D., Zhang, X., Pinion, C.W., Celano, T.A., Flynn, C.J. and Cahoon, J.F., 2012. Design principles for photovoltaic devices based on Si nanowires with axial or radial p–n junctions. *Nano letters*, 12(11), pp.6024-6029.
42. Conibeer, G., Green, M., Cho, E.C., König, D. and Huang, S., 2008. Silicon quantum dot nanostructures for tandem photovoltaic cells. *Thin Solid Films*, 516(20), pp.6748-6756.
43. Ren, S., Chang, L.Y., Lim, S.K., Zhao, J., Smith, M., Zhao, N., Bulovic, V., Bawendi, M. and Gradecak, S., 2011. Inorganic–organic hybrid solar cell. *Nano letters*, 11(9), pp.3998-4002.
44. Van Stryland, E.W., Woodall, M.A., Vanherzeele, H. and Soileau, M.J., 1985. Energy band-gap dependence of two-photon absorption. *Optics letters*, 10(10), pp.490-492.
45. King, R.R., Law, D.C., Edmondson, K.M., Fetzer, C.M., Kinsey, G.S., Yoon, H., Sherif, R.A. and Karam, N.H., 2007. 40% efficient metamorphic GaInP/GaInAs/Ge multijunction solar cells. *Applied physics letters*, 90(18), p.183516.

46. <https://www.ise.fraunhofer.de/en/press-media/press-releases/2014/new-world-record-for-solar-cell-efficiency-at-46-percent.html>, *retrieved* 06-09-2017
47. Wallentin, J., Anttu, N., Asoli, D., Huffman, M., Åberg, I., Magnusson, & Xu, H. Q. *Science*, 2013,339 (6123), 1057-1060.
48. Law, M., Greene, L.E., Johnson, J.C., Saykally, R. and Yang, P., 2005. Nanowire dye-sensitized solar cells. *Nature materials*, 4(6), p.455.
49. Cui, J. and Gibson, U.J., 2010. A simple two-step electrodeposition of Cu₂O/ZnO nanopillar solar cells. *The Journal of Physical Chemistry C*, 114(14), pp.6408-6412.
50. Shkondin, E., Takayama, O., Panah, M.A., Liu, P., Larsen, P.V., Mar, M.D., Jensen, F. and Lavrinenko, A.V., 2017. Large-scale high aspect ratio Al-doped ZnO nanopillars arrays as anisotropic metamaterials. *Optical Materials Express*, 7(5), pp.1606-1627.
51. Hsu, C.M., Battaglia, C., Pahud, C., Ruan, Z., Haug, F.J., Fan, S., Ballif, C. and Cui, Y., 2012. High-efficiency amorphous silicon solar cell on a periodic nanocone back reflector. *Advanced Energy Materials*, 2(6), pp.628-633.
52. Jeong, S., Garnett, E.C., Wang, S., Yu, Z., Fan, S., Brongersma, M.L., McGehee, M.D. and Cui, Y., 2012. Hybrid silicon nanocone-polymer solar cells. *Nano letters*, 12(6), pp.2971-2976.
53. Yan, R., Gargas, D. and Yang, P., 2009. Nanowire photonics. *Nature photonics*, 3(10), p.569.
54. Jean, J., Chang, S., Brown, P.R., Cheng, J.J., Rekemeyer, P.H., Bawendi, M.G., Gradečak, S. and Bulović, V., 2013. ZnO nanowire arrays for enhanced photocurrent in PbS quantum dot solar cells. *Advanced materials*, 25(20), pp.2790-2796.
55. Huang, N., Lin, C. and Povinelli, M.L., 2012. Broadband absorption of semiconductor nanowire arrays for photovoltaic applications. *Journal of Optics*, 14(2), p.024004.
56. Anttu, N., Dagtýè, V., Zeng, X., Otnes, G. and Borgström, M., 2017. Absorption and transmission of light in III-V nanowire arrays for tandem solar cell applications. *Nanotechnology*, 28(20), p.205203.
57. Link, S., Mohamed, M.B. and El-Sayed, M.A., 1999. Simulation of the optical absorption spectra of gold nanorods as a function of their aspect ratio and the effect of the medium dielectric constant. *The Journal of Physical Chemistry B*, 103(16), pp.3073-3077.

58. Li, J., Yu, H., Wong, S.M., Li, X., Zhang, G., Lo, P.G.Q. and Kwong, D.L., 2009. Design guidelines of periodic Si nanowire arrays for solar cell application. *Applied Physics Letters*, 95(24), p.243113.
59. Hu, L. and Chen, G., 2007. Analysis of optical absorption in silicon nanowire arrays for photovoltaic applications. *Nano letters*, 7(11), pp.3249-3252.
60. Han, S.E. and Chen, G., 2010. Optical absorption enhancement in silicon nanohole arrays for solar photovoltaics. *Nano letters*, 10(3), pp.1012-1015.
61. Han, S.E. and Chen, G., 2010. Toward the Lambertian limit of light trapping in thin nanostructured silicon solar cells. *Nano letters*, 10(11), pp.4692-4696.
62. Li, X., 2012. Metal assisted chemical etching for high aspect ratio nanostructures: A review of characteristics and applications in photovoltaics. *Current Opinion in Solid State and Materials Science*, 16(2), pp.71-81.
63. Zhu, J., Yu, Z., Burkhard, G.F., Hsu, C.M., Connor, S.T., Xu, Y., Wang, Q., McGehee, M., Fan, S. and Cui, Y., 2008. Optical absorption enhancement in amorphous silicon nanowire and nanocone arrays. *Nano letters*, 9(1), pp.279-282.
64. Greyson, E.C., Babayan, Y. and Odom, T.W., 2004. Directed growth of ordered arrays of small-diameter ZnO nanowires. *Advanced Materials*, 16(15), pp.1348-1352.
65. Peng, K.Q., Wang, X., Li, L., Wu, X.L. and Lee, S.T., 2010. High-performance silicon nanohole solar cells. *Journal of the American Chemical Society*, 132(20), pp.6872-6873.
66. Choi, W.K., Liew, T.H., Dawood, M.K., Smith, H.I., Thompson, C.V. and Hong, M.H., 2008. Synthesis of silicon nanowires and nanofin arrays using interference lithography and catalytic etching. *Nano letters*, 8(11), pp.3799-3802.
67. Boettcher, S.W., Spurgeon, J.M., Putnam, M.C., Warren, E.L., Turner-Evans, D.B., Kelzenberg, M.D., Maiolo, J.R., Atwater, H.A. and Lewis, N.S., 2010. Energy-conversion properties of vapor-liquid-solid-grown silicon wire-array photocathodes. *Science*, 327(5962), pp.185-187.
68. Kendrick, C.E., Yoon, H.P., Yuwen, Y.A., Barber, G.D., Shen, H., Mallouk, T.E., Dickey, E.C., Mayer, T.S. and Redwing, J.M., 2010. Radial junction silicon wire array solar cells fabricated by gold-catalyzed vapor-liquid-solid growth. *Applied Physics Letters*, 97(14), p.143108.
69. Kelzenberg, M.D., Turner-Evans, D.B., Kayes, B.M., Filler, M.A., Putnam, M.C., Lewis, N.S. and Atwater, H.A., 2008. Photovoltaic measurements in single-nanowire silicon solar cells. *Nano letters*, 8(2), pp.710-714.

70. Fan, H.J., Bertram, F., Dadgar, A., Christen, J., Krost, A. and Zacharias, M., 2004. Self-assembly of ZnO nanowires and the spatial resolved characterization of their luminescence. *Nanotechnology*, 15(11), p.1401.
71. Wang, Z.L., Kong, X.Y., Ding, Y., Gao, P., Hughes, W.L., Yang, R. and Zhang, Y., 2004. Semiconducting and piezoelectric oxide nanostructures induced by polar surfaces. *Advanced Functional Materials*, 14(10), pp.943-956.
72. Kanta, A.F., Schrijnemakers, A. and Decroly, A., 2016. Electrochemical characterisations of ZnO nanowires for dye-sensitised solar cells. *Materials & Design*, 95, pp.481-485.
73. Zheng, M.J., Zhang, L.D., Li, G.H. and Shen, W.Z., 2002. Fabrication and optical properties of large-scale uniform zinc oxide nanowire arrays by one-step electrochemical deposition technique. *Chemical Physics Letters*, 363(1-2), pp.123-128.
74. Zhao, A.W., Meng, G.W., Zhang, L.D., Gao, T., Sun, S.H. and Pang, Y.T., 2003. Electrochemical synthesis of ordered CdTe nanowire arrays. *Applied Physics A*, 76(4), pp.537-539.
75. Fan, Z., Razavi, H., Do, J.W., Moriwaki, A., Ergen, O., Reichertz, L.A. and Neale, S., 2009. Three-dimensional nanopillar-array photovoltaics on low-cost and flexible substrates. *Nature materials*, 8(8), p.648.
76. Fan, P., Zhong, M., Bai, B., Jin, G. and Zhang, H., 2016. Large scale and cost effective generation of 3D self-supporting oxide nanowire architectures by a top-down and bottom-up combined approach. *RSC Advances*, 6(51), pp.45923-45930.
77. Chueh, Y.L., Fan, Z., Takei, K., Ko, H., Kapadia, R., Rathore, A.A., Miller, N., Yu, K., Wu, M., Haller, E.E. and Javey, A., 2009. Black Ge based on crystalline/amorphous core/shell nanoneedle arrays. *Nano letters*, 10(2), pp.520-523.
78. Ergen, O., Ruebusch, D.J., Fang, H., Rathore, A.A., Kapadia, R., Fan, Z., Takei, K., Jamshidi, A., Wu, M. and Javey, A., 2010. Shape-controlled synthesis of single-crystalline nanopillar arrays by template-assisted vapor- liquid- solid process. *Journal of the American Chemical Society*, 132(40), pp.13972-13974.
79. Cheung, C.L., Nikolić, R.J., Reinhardt, C.E. and Wang, T.F., 2006. Fabrication of nanopillars by nanosphere lithography. *Nanotechnology*, 17(5), p.1339.
80. Kelzenberg, M.D., Boettcher, S.W., Petykiewicz, J.A., Turner-Evans, D.B., Putnam, M.C., Warren, E.L., Spurgeon, J.M., Briggs, R.M., Lewis, N.S. and Atwater, H.A., 2010. Enhanced absorption and carrier collection in Si wire arrays for photovoltaic applications. *Nature materials*, 9(3), p.239.

81. Sander, M.S., Prieto, A.L., Gronsky, R., Sands, T. and Stacy, A.M., 2002. Fabrication of High-Density, High Aspect Ratio, Large-Area Bismuth Telluride Nanowire Arrays by Electrodeposition into Porous Anodic Alumina Templates. *Advanced Materials*, 14(9), pp.665-667.
82. Rabin, O., Herz, P.R., Lin, Y.M., Akinwande, A.I., Cronin, S.B. and Dresselhaus, M.S., 2003. Formation of thick porous anodic alumina films and nanowire arrays on silicon wafers and glass. *Advanced Functional Materials*, 13(8), pp.631-638.
83. Routkevitch, D., Bigioni, T., Moskovits, M. and Xu, J.M., 1996. Electrochemical fabrication of CdS nanowire arrays in porous anodic aluminum oxide templates. *The Journal of Physical Chemistry*, 100(33), pp.14037-14047.
84. Li, Y., Meng, G.W., Zhang, L.D. and Phillipp, F., 2000. Ordered semiconductor ZnO nanowire arrays and their photoluminescence properties. *Applied Physics Letters*, 76(15), pp.2011-2013.
85. Fan, Z., Kapadia, R., Leu, P.W., Zhang, X., Chueh, Y.L., Takei, K., Yu, K., Jamshidi, A., Rathore, A.A., Ruebusch, D.J. and Wu, M., 2010. Ordered arrays of dual-diameter nanopillars for maximized optical absorption. *Nano letters*, 10(10), pp.3823-3827.
86. Fan, Z., Ruebusch, D.J., Rathore, A.A., Kapadia, R., Ergen, O., Leu, P.W. and Javey, A., 2009. Challenges and prospects of nanopillar-based solar cells. *Nano Research*, 2(11), p.829.
87. Gunawan, O. and Guha, S., 2009. Characteristics of vapor–liquid–solid grown silicon nanowire solar cells. *Solar Energy Materials and Solar Cells*, 93(8), pp.1388-1393.
88. Peng, K.Q. and Lee, S.T., 2011. Silicon nanowires for photovoltaic solar energy conversion. *Advanced Materials*, 23(2), pp.198-215.
89. Tang, Y.B., Chen, Z.H., Song, H.S., Lee, C.S., Cong, H.T., Cheng, H.M., Zhang, W.J., Bello, I. and Lee, S.T., 2008. Vertically aligned p-type single-crystalline GaN nanorod arrays on n-type Si for heterojunction photovoltaic cells. *Nano letters*, 8(12), pp.4191-4195.
90. Spurgeon, J.M., Atwater, H.A. and Lewis, N.S., 2008. A comparison between the behavior of nanorod array and planar Cd (Se, Te) photoelectrodes. *The Journal of Physical Chemistry C*, 112(15), pp.6186-6193.
91. McCune, M., Zhang, W. and Deng, Y., 2012. High efficiency dye-sensitized solar cells based on three-dimensional multilayered ZnO nanowire arrays with “caterpillar-like” structure. *Nano letters*, 12(7), pp.3656-3662.

92. Xu, Q., Qiao, S., Dutta, R., Le Thai, M., Li, X., Eggers, C.J., Chandran, G.T., Wu, Z. and Penner, R.M., 2015. A 30 μm Coaxial Nanowire Photoconductor Enabling Orthogonal Carrier Collection. *Nano letters*, 15(9), pp.5861-5867.
93. Zheng, B.Y., Zhao, H., Manjavacas, A., McClain, M., Nordlander, P. and Halas, N.J., 2015. Distinguishing between plasmon-induced and photoexcited carriers in a device geometry. *Nature communications*, 6, p.7797.
94. Im, J.H., Luo, J., Frankevičius, M., Pellet, N., Gao, P., Moehl, T., Zakeeruddin, S.M., Nazeeruddin, M.K., Grätzel, M. and Park, N.G., 2015. Nanowire perovskite solar cell. *Nano letters*, 15(3), pp.2120-2126.
95. Amato, M. and Rurali, R., 2016. Surface physics of semiconducting nanowires. *Progress in Surface Science*, 91(1), pp.1-28.
96. Putnam, M.C., Turner-Evans, D.B., Kelzenberg, M.D., Boettcher, S.W., Lewis, N.S. and Atwater, H.A., 2009. 10 μm minority-carrier diffusion lengths in Si wires synthesized by Cu-catalyzed vapor-liquid-solid growth. *Applied Physics Letters*, 95(16), p.163116.
97. Liyanage, W.P. and Nath, M., 2016. CdS–CdTe heterojunction nanotube arrays for efficient solar energy conversion. *Journal of Materials Chemistry A*, 4(38), pp.14637-14648.
98. Liyanage, W.P., Mishra, S., Wilson, J.A., Kinzel, E. and Nath, M., 2014. Patterned electrodeposition of CdTe nanorod and nanotube arrays for solar cells. *Nanomaterials and Energy*, 3(5), pp.167-176.
99. Liyanage, W.P., Wilson, J.S., Kinzel, E.C., Durant, B.K. and Nath, M., 2015. Fabrication of CdTe nanorod arrays over large area through patterned electrodeposition for efficient solar energy conversion. *Solar Energy Materials and Solar Cells*, 133, pp.260-267.
100. Liyanage, W.P.R. and Nath, M., 2015. Growth of Ordered Nanostructure Arrays including Nanotubes and Nanorods for High Efficiency Solar Cells. *ECS Transactions*, 66(40), pp.1-7.
101. Fujishima, A. and Honda, K., 1972. Electrochemical photolysis of water at a semiconductor electrode. *nature*, 238(5358), p.37.
102. Bard, A.J., 1980. Photoelectrochemistry. *Science*, 207(4427), pp.139-144.
103. Hodes, G., Cahen, D. and Manassen, J., 1976. Tungsten trioxide as a photoanode for a photoelectrochemical cell (PEC). *Nature*, 260(5549), p.312.

104. Ding, C., Shi, J., Wang, Z. and Li, C., 2016. Photoelectrocatalytic water splitting: significance of cocatalysts, electrolyte, and interfaces. *ACS Catalysis*, 7(1), pp.675-688.
105. Nozik, A.J., 1978. Photoelectrochemistry: applications to solar energy conversion. *Annual Review of Physical Chemistry*, 29(1), pp.189-222.
106. Walter, M.G., Warren, E.L., McKone, J.R., Boettcher, S.W., Mi, Q., Santori, E.A. and Lewis, N.S., 2010. Solar water splitting cells. *Chemical reviews*, 110(11), pp.6446-6473.
107. Osterloh, F.E., 2013. Inorganic nanostructures for photoelectrochemical and photocatalytic water splitting. *Chemical Society Reviews*, 42(6), pp.2294-2320.
108. Roger, I., Shipman, M.A. and Symes, M.D., 2017. Earth-abundant catalysts for electrochemical and photoelectrochemical water splitting. *Nature Reviews Chemistry*, 1(1), p.0003.
109. Cook, T.R., Dogutan, D.K., Reece, S.Y., Surendranath, Y., Teets, T.S. and Nocera, D.G., 2010. Solar energy supply and storage for the legacy and nonlegacy worlds. *Chemical reviews*, 110(11), pp.6474-6502.
110. Costi, R., Young, E.R., Bulović, V. and Nocera, D.G., 2013. Stabilized CdSe-CoPi composite photoanode for light-assisted water oxidation by transformation of a CdSe/cobalt metal thin film. *ACS applied materials & interfaces*, 5(7), pp.2364-2367.
111. Giménez, S. and Bisquert, J., 2016. *Photoelectrochemical solar fuel production* (pp. 403-407). Switzerland: Springer.
112. McKone, J.R., Lewis, N.S. and Gray, H.B., 2013. Will solar-driven water-splitting devices see the light of day?. *Chemistry of Materials*, 26(1), pp.407-414.
113. Yang, J., Wang, D., Han, H. and Li, C., 2013. Roles of cocatalysts in photocatalysis and photoelectrocatalysis. *Accounts of chemical research*, 46(8), pp.1900-1909.
114. Hisatomi, T., Kubota, J. and Domen, K., 2014. Recent advances in semiconductors for photocatalytic and photoelectrochemical water splitting. *Chemical Society Reviews*, 43(22), pp.7520-7535.
115. Lewis, N.S. and Nocera, D.G., 2006. Powering the planet: Chemical challenges in solar energy utilization. *Proceedings of the National Academy of Sciences*, 103(43), pp.15729-15735.

116. Birkmire, R.W. and Eser, E., 1997. Polycrystalline thin film solar cells: present status and future potential. *Annual Review of Materials Science*, 27(1), pp.625-653.
117. Wu, X., 2004. High-efficiency polycrystalline CdTe thin-film solar cells. *Solar energy*, 77(6), pp.803-814.
118. Chen, W.S., Stewart, J.M. and Mickelsen, R.A., 1985. Chemical deposition and characterization of Cu₃Se₂ and CuSe thin silms. *Appl. Phys. Lett*, 46, p.1095.
119. First Solar Press Release "First Solar sets world record for CdTe solar cell efficiency", <http://investor.firstsolar.com/releases.cfm> (Feb. 25, 2014).
120. Contreras, M.A., Egaas, B., Ramanathan, K., Hiltner, J., Swartzlander, A., Hasoon, F. and Noufi, R., 1999. Progress toward 20% efficiency in Cu (In, Ga) Se₂ polycrystalline thin-film solar cells. *Progress in Photovoltaics: Research and applications*, 7(4), pp.311-316.
121. Green, M.A., 2007. Thin-film solar cells: review of materials, technologies and commercial status. *Journal of Materials Science: Materials in Electronics*, 18(1), pp.15-19.
122. Beck, M.E., Swartzlander-Guest, A., Matson, R., Keane, J. and Noufi, R., 2000. CuIn (Ga) Se₂-based devices via a novel absorber formation process. *Solar Energy Materials and Solar Cells*, 64(2), pp.135-165.
123. Guo, Q., Ford, G.M., Hillhouse, H.W. and Agrawal, R., 2009. Sulfide nanocrystal inks for dense Cu (In_{1-x}Ga_x)(S_{1-y}Se_y)₂ absorber films and their photovoltaic performance. *Nano letters*, 9(8), pp.3060-3065.
124. Guillemoles, J.F., Kronik, L., Cahen, D., Rau, U., Jasenek, A. and Schock, H.W., 2000. Stability issues of Cu (In, Ga) Se₂-based solar cells. *The Journal of Physical Chemistry B*, 104(20), pp.4849-4862.
125. Ward, J.S., Ramanathan, K., Hasoon, T. and Noufi, R., 2002. A 21.5% efficient Cu (In, Ga) Se₂ thin-film concentrator solar cell. *Progress in Photovoltaics: Research and Applications*, 10(1), pp.41-46.
126. Rockett, A. and Birkmire, R.W., 1991. CuInSe₂ for photovoltaic applications. *Journal of Applied Physics*, 70(7), pp.R81-R97.
127. Park, H.S., Kweon, K.E., Ye, H., Paek, E., Hwang, G.S. and Bard, A.J., 2011. Factors in the metal doping of BiVO₄ for improved photoelectrocatalytic activity as studied by scanning electrochemical microscopy and first-principles density-functional calculation. *The Journal of Physical Chemistry C*, 115(36), pp.17870-17879.

128. Park, Y., McDonald, K.J. and Choi, K.S., 2013. Progress in bismuth vanadate photoanodes for use in solar water oxidation. *Chemical Society Reviews*, 42(6), pp.2321-2337.
129. Liu, X., Wang, F. and Wang, Q., 2012. Nanostructure-based WO₃ photoanodes for photoelectrochemical water splitting. *Physical Chemistry Chemical Physics*, 14(22), pp.7894-7911.
130. Mayer, M.T., Lin, Y., Yuan, G. and Wang, D., 2013. Forming heterojunctions at the nanoscale for improved photoelectrochemical water splitting by semiconductor materials: case studies on hematite. *Accounts of chemical research*, 46(7), pp.1558-1566.
131. Sivula, K., Le Formal, F. and Grätzel, M., 2011. Solar water splitting: progress using hematite (α -Fe₂O₃) photoelectrodes. *ChemSusChem*, 4(4), pp.432-449.
132. Klahr, B.M. and Hamann, T.W., 2011. Current and voltage limiting processes in thin film hematite electrodes. *The Journal of Physical Chemistry C*, 115(16), pp.8393-8399.
133. Hamann, T.W., 2012. Splitting water with rust: hematite photoelectrochemistry. *Dalton Transactions*, 41(26), pp.7830-7834.
134. Liu, G., Ye, S., Yan, P., Xiong, F., Fu, P., Wang, Z., Chen, Z., Shi, J. and Li, C., 2016. Enabling an integrated tantalum nitride photoanode to approach the theoretical photocurrent limit for solar water splitting. *Energy & Environmental Science*, 9(4), pp.1327-1334.
135. Li, Y., Zhang, L., Torres-Pardo, A., González-Calbet, J.M., Ma, Y., Oleynikov, P., Terasaki, O., Asahina, S., Shima, M., Cha, D. and Zhao, L., 2013. Cobalt phosphate-modified barium-doped tantalum nitride nanorod photoanode with 1.5% solar energy conversion efficiency. *Nature communications*, 4, p.2566.
136. He, Y., Ma, P., Zhu, S., Liu, M., Dong, Q., Espano, J., Yao, X. and Wang, D., 2017. Photo-induced performance enhancement of tantalum nitride for solar water oxidation. *Joule*, 1(4), pp.831-842.
137. Zhong, D.K., Sun, J., Inumaru, H. and Gamelin, D.R., 2009. Solar water oxidation by composite catalyst/ α -Fe₂O₃ photoanodes. *Journal of the American Chemical Society*, 131(17), pp.6086-6087.
138. Fan, K., Li, F., Wang, L., Daniel, Q., Chen, H., Gabrielsson, E., Sun, J. and Sun, L., 2015. Immobilization of a molecular ruthenium catalyst on hematite nanorod arrays for water oxidation with stable photocurrent. *ChemSusChem*, 8(19), pp.3242-3247.

139. Lewis, N.S., 2016. Developing a scalable artificial photosynthesis technology through nanomaterials by design. *Nature nanotechnology*, 11(12), p.1010.
140. Steinmiller, E.M. and Choi, K.S., 2009. Photochemical deposition of cobalt-based oxygen evolving catalyst on a semiconductor photoanode for solar oxygen production. *Proceedings of the National Academy of Sciences*, 106(49), pp.20633-20636.
141. Suntivich, J., May, K.J., Gasteiger, H.A., Goodenough, J.B. and Shao-Horn, Y., 2011. A perovskite oxide optimized for oxygen evolution catalysis from molecular orbital principles. *Science*, 334(6061), pp.1383-1385.
142. Lee, J.D., 1977. A new concise inorganic chemistry, billing & sons Ltd. *Guildford, London and Worcester*, 399.
143. Xu, Y. and Schoonen, M.A., 2000. The absolute energy positions of conduction and valence bands of selected semiconducting minerals. *American mineralogist*, 85(3-4), pp.543-556.
144. Rasmussen, F.A. and Thygesen, K.S., 2015. Computational 2D materials database: electronic structure of transition-metal dichalcogenides and oxides. *The Journal of Physical Chemistry C*, 119(23), pp.13169-13183.
145. Lauer, S., Trautwein, A.X. and Harris, F.E., 1984. Electronic-structure calculations, photoelectron spectra, optical spectra, and Mössbauer parameters for the pyrites MS_2 (M= Fe, Co, Ni, Cu, Zn). *Physical Review B*, 29(12), p.6774.
146. Swesi, A.T., Masud, J. and Nath, M., 2016. Nickel selenide as a high-efficiency catalyst for oxygen evolution reaction. *Energy & Environmental Science*, 9(5), pp.1771-1782.
147. Umaphathi, S., Masud, J., Swesi, A.T. and Nath, M., 2017. FeNi₂Se₄-Reduced Graphene Oxide Nanocomposite: Enhancing Bifunctional Electrocatalytic Activity for Oxygen Evolution and Reduction through Synergistic Effects. *Advanced Sustainable Systems*, 1(10), p.1700086.
148. Swesi, A.T., Masud, J., Liyanage, W.P., Umaphathi, S., Bohannan, E., Medvedeva, J. and Nath, M., 2017. Textured NiSe₂ Film: Bifunctional Electrocatalyst for Full Water Splitting at Remarkably Low Overpotential with High Energy Efficiency. *Scientific Reports*, 7(1), p.2401.
149. Golrokh Amin, B.; Swesi, A. T.; Masud, J.; Nath, M., 2017. CoNi₂Se₄ as an efficient bifunctional electrocatalyst for overall water splitting. *Chemical Communications*, 53(39), pp.5412-5415.

150. Masud, J., Ioannou, P.C., Levesanos, N., Kyritsis, P. and Nath, M., 2016. A Molecular Ni-complex Containing Tetrahedral Nickel Selenide Core as Highly Efficient Electrocatalyst for Water Oxidation. *ChemSusChem*, 9(22), pp.3128-3132.
151. Swesi, A.T., Masud, J. and Nath, M., 2016. Enhancing electrocatalytic activity of bifunctional Ni₃Se₂ for overall water splitting through etching-induced surface nanostructuring. *Journal of Materials Research*, 31(18), pp.2888-2896.
152. Masud, J., Swesi, A.T., Liyanage, W.P. and Nath, M., 2016. Cobalt selenide nanostructures: an efficient bifunctional catalyst with high current density at low coverage. *ACS applied materials & interfaces*, 8(27), pp.17292-17302.
153. De Silva, U., Masud, J., Zhang, N., Hong, Y., Liyanage, W.P., Zaeem, M.A. and Nath, M., 2018. Nickel telluride as a bifunctional electrocatalyst for efficient water splitting in alkaline medium. *Journal of Materials Chemistry A*, 6(17), pp.7608-7622.
154. De Silva, U., Liyanage, W.P.R. and Nath, M., 2016. Magnetic Multifunctional Nanostructures as High-efficiency Catalysts for Oxygen Evolution Reactions. *MRS Advances*, 1(34), pp.2401-2407.
155. Xia, C., Jiang, Q., Zhao, C., Hedhili, M.N. and Alshareef, H.N., 2016. Selenide-Based Electrocatalysts and Scaffolds for Water Oxidation Applications. *Advanced Materials*, 28(1), pp.77-85.
156. Ming, F., Liang, H., Shi, H., Xu, X., Mei, G. and Wang, Z., 2016. MOF-derived Co-doped nickel selenide/C electrocatalysts supported on Ni foam for overall water splitting. *Journal of Materials Chemistry A*, 4(39), pp.15148-15155.
157. Xu, X., Song, F. and Hu, X., 2016. A nickel iron diselenide-derived efficient oxygen-evolution catalyst. *Nature communications*, 7, p.12324.
158. Tang, C., Cheng, N., Pu, Z., Xing, W. and Sun, X., 2015. NiSe nanowire film supported on nickel foam: an efficient and stable 3D bifunctional electrode for full water splitting. *Angewandte Chemie*, 127(32), pp.9483-9487.
159. Liu, T., Asiri, A.M. and Sun, X., 2016. Electrodeposited Co-doped NiSe₂ nanoparticles film: a good electrocatalyst for efficient water splitting. *Nanoscale*, 8(7), pp.3911-3915.
160. Shi, J., Hu, J., Luo, Y., Sun, X. and Asiri, A.M., 2015. Ni₃Se₂ film as a non-precious metal bifunctional electrocatalyst for efficient water splitting. *Catalysis Science & Technology*, 5(11), pp.4954-4958.

161. Li, X., Han, G.Q., Liu, Y.R., Dong, B., Hu, W.H., Shang, X., Chai, Y.M. and Liu, C.G., 2016. NiSe@ NiOOH core-shell hyacinth-like nanostructures on nickel foam synthesized by in situ electrochemical oxidation as an efficient electrocatalyst for the oxygen evolution reaction. *ACS applied materials & interfaces*, 8(31), pp.20057-20066.
162. Wang, Z., Li, J., Tian, X., Wang, X., Yu, Y., Owusu, K.A., He, L. and Mai, L., 2016. Porous nickel-iron selenide nanosheets as highly efficient electrocatalysts for oxygen evolution reaction. *ACS applied materials & interfaces*, 8(30), pp.19386-19392.
163. Li, X., Han, G.Q., Liu, Y.R., Dong, B., Shang, X., Hu, W.H., Chai, Y.M., Liu, Y.Q. and Liu, C.G., 2016. In situ grown pyramid structures of nickel diselenides dependent on oxidized nickel foam as efficient electrocatalyst for oxygen evolution reaction. *Electrochimica Acta*, 205, pp.77-84.
164. Tang, C., Asiri, A.M. and Sun, X., 2016. Highly-active oxygen evolution electrocatalyzed by a Fe-doped NiSe nanoflake array electrode. *Chemical Communications*, 52(24), pp.4529-4532.
165. Wu, X., He, D., Zhang, H., Li, B., Lin, Z., Lei, L. and Zhang, X., 2016. Ni_{0.85}Se as an efficient non-noble bifunctional electrocatalyst for full water splitting. *International Journal of Hydrogen Energy*, 41(25), pp.10688-10694.
166. Xu, R., Wu, R., Shi, Y., Zhang, J. and Zhang, B., 2016. Ni₃Se₂ nanoforest/Ni foam as a hydrophilic, metallic, and self-supported bifunctional electrocatalyst for both H₂ and O₂ generations. *Nano Energy*, 24, pp.103-110.
167. Li, S., Peng, S., Huang, L., Cui, X., Al-Enizi, A.M. and Zheng, G., 2016. Carbon-coated Co³⁺-rich cobalt selenide derived from ZIF-67 for efficient electrochemical water oxidation. *ACS applied materials & interfaces*, 8(32), pp.20534-20539.
168. Kwak, I.H., Im, H.S., Jang, D.M., Kim, Y.W., E.H. and Park, J., 2016. CoSe₂ and NiSe₂ nanocrystals as superior bifunctional catalysts for electrochemical and photoelectrochemical water splitting. *ACS applied materials & interfaces*, 8(8), pp.5327-5334.
169. Hou, Y., Lohe, M.R., Zhang, J., Liu, S., Zhuang, X. and Feng, X., 2016. Vertically oriented cobalt selenide: an efficient 3D electrode for overall water splitting. *Energy & Environmental Science*, 9(2), pp.478-483.
170. Liu, Y., Cheng, H., Lyu, M., Fan, S., Liu, Q., Zhang, W., Zhi, Y., Wang, C., Xiao, C., Wei, S. and Ye, B., 2014. Low overpotential in vacancy-rich ultrathin CoSe₂ nanosheets for water oxidation. *Journal of the American Chemical Society*, 136(44), pp.15670-15675.

171. Yang, J., Shen, X., Ji, Z. and Zhu, G., 2013. Reduced graphene oxide/CoSe₂ nanocomposites: hydrothermal synthesis and their enhanced electrocatalytic activity. *Journal of materials science*, 48(22), pp.7913-7919.
172. Gao, M.R., Cao, X., Gao, Q., Xu, Y.F., Zheng, Y.R., Jiang, J. and Yu, S.H., 2014. Nitrogen-doped graphene supported CoSe₂ nanobelt composite catalyst for efficient water oxidation. *Acs Nano*, 8(4), pp.3970-3978.
173. Liao, M., Zeng, G., Luo, T., Jin, Z., Wang, Y., Kou, X. and Xiao, D., 2016. Three-dimensional coral-like cobalt selenide as an advanced electrocatalyst for highly efficient oxygen evolution reaction. *Electrochimica Acta*, 194, pp.59-66.
174. Fang, W., Liu, D., Lu, Q., Sun, X. and Asiri, A.M., 2016. Nickel promoted cobalt disulfide nanowire array supported on carbon cloth: an efficient and stable bifunctional electrocatalyst for full water splitting. *Electrochemistry Communications*, 63, pp.60-64.
175. Wu, J., Liu, M., Chatterjee, K., Hackenberg, K.P., Shen, J., Zou, X., Yan, Y., Gu, J., Yang, Y., Lou, J. and Ajayan, P.M., 2016. Exfoliated 2D transition metal disulfides for enhanced electrocatalysis of oxygen evolution reaction in acidic medium. *Advanced Materials Interfaces*, 3(9), p.1500669.
176. Gur, I., Fromer, N.A., Geier, M.L. and Alivisatos, A.P., 2005. Air-stable all-inorganic nanocrystal solar cells processed from solution. *Science*, 310(5747), pp.462-465.
177. Anttu, N. and Xu, H.Q., 2010. Coupling of light into nanowire arrays and subsequent absorption. *Journal of nanoscience and nanotechnology*, 10(11), pp.7183-7187.
178. Kannan, B., Castelino, K. and Majumdar, A., 2003. Design of nanostructured heterojunction polymer photovoltaic devices. *Nano Letters*, 3(12), pp.1729-1733.
179. Weickert, J., Dunbar, R.B., Hesse, H.C., Wiedemann, W. and Schmidt-Mende, L., 2011. Nanostructured organic and hybrid solar cells. *Advanced materials*, 23(16), pp.1810-1828.
180. Yoo, J., Nguyen, B.M., Campbell, I.H., Dayeh, S.A., Schuele, P., Evans, D. and Picraux, S.T., 2015. Si radial pin junction photovoltaic arrays with built-in light concentrators. *ACS nano*, 9(5), pp.5154-5163.
181. Zhu, P., Gu, S., Shen, X., Xu, N., Tan, Y., Zhuang, S., Deng, Y., Lu, Z., Wang, Z. and Zhu, J., 2016. Direct conversion of perovskite thin films into nanowires with kinetic control for flexible optoelectronic devices. *Nano letters*, 16(2), pp.871-876.

182. Dake, S., Lixin, C. and Suling, C., 2006. Preparation, Characterization and Applications of One-Dimensional Nanostructures [J]. *Chinese Journal of Rare Metals*, 1, p.019.
183. Castro, S.L., Bailey, S.G., Raffaele, R.P., Banger, K.K. and Hepp, A.F., 2003. Nanocrystalline chalcopyrite materials (CuInS₂ and CuInSe₂) via low-temperature pyrolysis of molecular single-source precursors. *Chemistry of Materials*, 15(16), pp.3142-3147.
184. Li, B., Xie, Y., Huang, J. and Qian, Y., 1999. Synthesis by a solvothermal route and characterization of CuInSe₂ nanowhiskers and nanoparticles. *Advanced Materials*, 11(17), pp.1456-1459.
185. Jiang, Y., Wu, Y., Mo, X., Yu, W., Xie, Y. and Qian, Y., 2000. Elemental solvothermal reaction to produce ternary semiconductor CuInE₂ (E= S, Se) nanorods. *Inorganic Chemistry*, 39(14), pp.2964-2965.
186. Schoen, D.T., Peng, H. and Cui, Y., 2009. Anisotropy of chemical transformation from In₂Se₃ to CuInSe₂ nanowires through solid state reaction. *Journal of the American Chemical Society*, 131(23), pp.7973-7975.
187. Jeong, S., Wang, S. and Cui, Y., 2012. Nanoscale photon management in silicon solar cells. *Journal of Vacuum Science & Technology A: Vacuum, Surfaces, and Films*, 30(6), p.060801.
188. Yu, R., Lin, Q., Leung, S.F. and Fan, Z., 2012. Nanomaterials and nanostructures for efficient light absorption and photovoltaics. *Nano energy*, 1(1), pp.57-72.
189. Qiu, Y., Hao, H.C., Zhou, J. and Lu, M., 2012. A close to unity and all-solar-spectrum absorption by ion-sputtering induced Si nanocone arrays. *Optics express*, 20(20), pp.22087-22094.
190. Watanabe, K., Yamamoto, J. and Tsuchiya, R., 2015. Broadband-antireflective hybrid nanopillar array for photovoltaic application. *Journal of Applied Physics*, 118(8), p.085102.
191. Hong, L., Wang, X., Zheng, H., Wang, J., Wang, H. and Yu, H., 2014. Optical absorption enhancement in a Si nanohole structure with hexagonal unit cell for solar cell application. *Nanotechnology*, 25(41), p.415303.
192. Dang, H., Singh, V.P., Guduru, S., Rajaputra, S. and Chen, Z.D., 2015. Nanotube photovoltaic configuration for enhancement of carrier generation and collection. *Nano Research*, 8(10), pp.3186-3196.

193. Li, J. and Yu, H., 2011. Texturing of crystalline Si thin film solar cells via nanostructure to boost efficiency. *International Journal of Nanoparticles*, 4(2-3), pp.284-306.
194. Wang, B. and Leu, P.W., 2012. Enhanced absorption in silicon nanocone arrays for photovoltaics. *Nanotechnology*, 23(19), p.194003.
195. Li, L., Peng, K.Q., Hu, B., Wang, X., Hu, Y., Wu, X.L. and Lee, S.T., 2012. Broadband optical absorption enhancement in silicon nanofunnel arrays for photovoltaic applications. *Applied Physics Letters*, 100(22), p.223902.
196. Junesch, J., Sannomiya, T. and Dahlin, A.B., 2012. Optical properties of nanohole arrays in metal–dielectric double films prepared by mask-on-metal colloidal lithography. *ACS nano*, 6(11), pp.10405-10415.
197. Montgomery, J. Boosting Solar Cells with Nanowires, RenewableEnergyWorld.com retrieved April 09, 2013.
198. Vega, V., Böhnert, T., Martens, S., Waleczek, M., Montero-Moreno, J.M., Görlitz, D., Prida, V.M. and Nielsch, K., 2012. Tuning the magnetic anisotropy of Co–Ni nanowires: comparison between single nanowires and nanowire arrays in hard-anodic aluminum oxide membranes. *Nanotechnology*, 23(46), p.465709.

VITA

Wipula Priya Rasika Liyanage received his Bachelor of Science (BS) degree in Chemistry in April 2004 from University of Peradeniya, Sri Lanka and the Master of Science (MS) degree in Polymer Technology in March 2010 from University of Moratuwa, Sri Lanka.

He joined Missouri University of Science and Technology to pursue Ph. D. in Chemistry. During the course of his research he published six journal articles, co-authored five journal articles, submitted two journal articles for publication and presented his research in six national conferences and four regional conferences. During his work as a Ph.D. fellow, he received a number of awards, among them Outstanding Graduate Researcher Award from the department of chemistry of the same institution and the Mid West Graduate Researcher Award from the American Chemical Society (ACS) may be mentioned. In May 2019, he received his Ph. D. in Chemistry from Missouri University of Science and Technology.